TUM School of Natural Sciences
Technische Universität München

Experimental and numerical investigation of helium exhaust at the ASDEX Upgrade tokamak with full-tungsten wall

Antonello Zito

Vollständiger Abdruck der von der TUM School of Natural Sciences der Technischen Universität München zur Erlangung des akademischen Grades eines

Doktors der Naturwissenschaften (Dr. rer. nat.)

genehmigten Dissertation.

Vorsitz:

Prof. Dr. Björn Garbrecht

Prüfer der Dissertation:

1. Prof. Dr. Ulrich Stroth
2. Prof. Dr. Christian Gabriel Theiler

Die Dissertation wurde am 20.09.2023 bei der Technischen Universität München eingereicht und durch die TUM School of Natural Sciences am 22.11.2023 angenommen.

MAX-PLANCK-INSTITUT
FÜR PLASMAPHYSIK

Doctoral Thesis in Physics

Technische Universität München
&
Max-Planck-Institut für Plasmaphysik

Experimental and numerical investigation of helium exhaust at the ASDEX Upgrade tokamak with full-tungsten wall

presented by

Antonello Zito

Advisor:

Prof. Dr. Ulrich Stroth

Co-advisors:

Dr. Marco Wischmeier

Dr. Athina Kappatou

Antonello Zito:
Experimental and numerical investigation of helium exhaust at the ASDEX Upgrade tokamak with full-tungsten wall.
| Doctoral Thesis in Physics, Technische Universität München.
| Research in collaboration with Max-Planck-Institut für Plasmaphysik, Garching, Germany.

This work has been carried out within the framework of the EUROfusion Consortium, funded by the European Union via the Euratom Research and Training Programme (Grant Agreement No 101052200 — EUROfusion). Views and opinions expressed are however those of the author(s) only and do not necessarily reflect those of the European Union or the European Commission. Neither the European Union nor the European Commission can be held responsible for them.

Technische Universität München:
www.tum.de

Max-Planck-Institut für Plasmaphysik:
www.ipp.mpg.de

EUROfusion:
www.euro-fusion.org

Contents

Abstract

In future fusion reactors, helium will be continuously generated in the core of the burning plasma as product of the D-T reaction. In order to avoid fuel dilution and degradation of the confinement properties, the helium concentration in the plasma must be kept within tolerable values. Therefore, an efficient removal of helium ash is mandatory. This requires the optimization of helium transport towards the divertor, which may impose constraints on edge and divertor plasma conditions, and an adequate design of the active pumping system. Extrapolations of the requirements of helium exhaust towards reactor-grade tokamaks rely on a deep understanding of the underlying physics mechanisms.

An experimental investigation of helium transport, recycling and pumping, aimed at the characterization of the basic physical processes determining helium exhaust, has been performed at the ASDEX Upgrade (AUG) tokamak. This is an ideal test environment thanks to the presence of an optimized divertor geometry, an extensive diagnostic coverage and plasma-facing components made of tungsten. The time evolution of the helium concentration was measured following a small helium gas injection during otherwise steady-state H-mode deuterium discharges, at the plasma midplane spectroscopically and in the exhaust neutral gas using an in-vessel optical Penning gauge. The exhaust efficiency, characterized by the helium compression in the divertor, was found to improve with increasing divertor neutral pressure but to degrade with detachment, in agreement with previous studies.

The experiments were complemented by a thorough numerical modelling. To interpret the experimentally observed exhaust dynamics, a novel multi-reservoir impurity particle balance model was developed. This simulates impurity ion transport in the plasma and plasma-wall interactions in a self-consistent way, and disentangles the contributions of active pumping and wall retention to the observed helium behavior. The limited performance of the AUG pumping systems and the high retention of helium atoms in the tungsten surfaces were found to have a strong and quantitatively similar impact in hindering an efficient exhaust. Extrapolating the modelled behavior towards reactor-grade tokamaks emphasizes the need for efficient active pumping systems to fulfil the requirements for stationary burning. Furthermore, it was concluded that the role of the main and divertor walls as particle reservoirs is critical for a proper interpretation of impurity transport, at least for short-pulsed tokamaks with metallic wall.

Additionally, the SOLPS-ITER code package was employed to identify the physics mechanisms which determine helium transport and recycling in the divertor. The simulations indicate a poor transport of helium atoms towards the pumps compared to that of deuterium and other impurities, in qualitative agreement with the experiments. This is mainly determined by the high first ionization energy of helium atoms, which strongly influences their recycling. It was also found that entrainment of helium atoms into the stronger deuterium gas flow is not negligible, but does not sufficiently enhance their transport towards the pumps to guarantee an efficient exhaust.

Kurzfassung

In zukünftigen Fusionsreaktoren wird im Kern des brennenden Plasmas kontinuierlich Helium als Produkt der D-T-Reaktion erzeugt. Um eine Verdünnung des Fusionsbrennstoffs und eine Verschlechterung der Einschlusseigenschaften zu vermeiden, muss die Heliumkonzentration im Plasma innerhalb tolerierbarer Werte gehalten werden. Daher ist eine effiziente Entfernung von Heliumasche zwingend erforderlich. Dies erfordert die Optimierung des Heliumtransports zum Divertor, was Einschränkungen bei den Rand- und Divertorplasmabedingungen mit sich bringt, sowie eine angemessene Auslegung des aktiven Pumpsystems. Die Extrapolation der Anforderungen an den Heliumabfuhr in Richtung reaktorfähiger Tokamaks setzt ein tiefes Verständnis der zugrunde liegenden physikalischen Mechanismen voraus.
Eine experimentelle Untersuchung des Heliumtransports, -recyclings und -pumpens, die auf die Charakterisierung der grundlegenden physikalischen Prozesse abzielt, die den Heliumabfuhr bestimmen, wurde am ASDEX Upgrade (AUG) Tokamak durchgeführt. Dank der optimierten Divertorgeometrie, der umfassenden diagnostischen Abdeckung und der Wandkomponenten aus Wolfram stellt dies eine ideale Testumgebung dar. Die zeitliche Entwicklung der Heliumkonzentration wurde nach einer geringen Injektion von Heliumgas während ansonsten stationärer H-Mode Deuteriumplasmen mittels Spektroskopie in der Plasmamittelebene und mit Hilfe von in-vessel optischen Penning-Vakuummetern im neutralen Abgas gemessen. Die Abfuhreffizienz, die durch die Heliumkompression im Divertor charakterisiert ist, verbesserte sich mit zunehmendem Divertor-Neutraldruck, verschlechterte sich jedoch mit dem Detachment, was mit früheren Studien übereinstimmt.
Die Experimente wurden durch eine umfassende numerische Modellierung ergänzt. Zur Interpretation der experimentell beobachteten Abfuhrdynamik wurde ein neuartiges Multireservoir-Verunreinigungsteilchen-Bilanzmodell entwickelt. Dieses simuliert den Transport von Verunreinigungsionen im Plasma und die Plasma-Wand-Wechselwirkungen auf selbstkonsistente Weise und entflechtet dabei die Beiträge des aktiven Pumpens und des Wandrückhaltevermögens zum beobachteten Heliumverhalten. Es wurde festgestellt, dass die begrenzte Fähigkeit der Pumpsysteme an AUG und das hohe Heliumrückhaltevermögen der Wolframoberflächen eine starke und quantitativ ähnliche Auswirkung auf die Verhinderung einer effizienten Abfuhr haben. Die Extrapolation des modellierten Verhaltens auf reaktortfähige Tokamaks unterstreicht die Notwendigkeit effizienter aktiver Pumpensysteme, um die Anforderungen für eine stationäre Fusionsreaktion zu erfüllen. Darüber hinaus wurde festgestellt, dass die Haupt- und Divertorwände als Teilchenreservoir für eine korrekte Interpretation des Verunreinigungstransports entscheidend sind, zumindest für kurz gepulste Tokamaks mit metallischer Wand.
Darüber hinaus wurde der SOLPS-ITER-Code eingesetzt, um die physikalischen Mechanismen zu ermitteln, die den Heliumtransport und -recycling im Divertor bestimmen. Die Simulationen deuten darauf hin, dass der Transport von Heliumatomen in Richtung der Pumpen im Vergleich zu Deuterium und anderen Verunreinigungen schlecht ist, was mit den Experimenten qualitativ übereinstimmt. Dies ist hauptsächlich auf die hohe erste Ionisierungsenergie der Heliumatome zurückzuführen, die ihr Recycling stark beeinflusst. Es wurde auch festgestellt, dass die Mitführung von Heliumatomen im stärkeren Deuteriumgasfluss nicht vernachlässigbar ist, aber dass dieser Effekt den Heliumtransport zu den Pumpen nicht ausreichend verstärkt, um eine effiziente Abfuhr zu gewährleisten.

Chapter 1

Introduction

In this Chapter a general overview of nuclear fusion research will be provided, and the motivation for studying helium exhaust will be discussed. First, in the Section 1.1 several key concepts of magnetic confinement fusion, which are of interest for this work, will be introduced. In the Section 1.2 the problems related to the presence of helium in fusion plasmas, which motivate the research performed in this thesis, will be addressed.

1.1 Magnetic confinement fusion

Nuclear fusion is a nuclear reaction in which two light nuclei combine to form one or more different nuclei and subatomic particles, resulting in a net release of energy. The advantages of exploiting fusion reactions for electric power generation, which motivate extensive theoretical and experimental research, include virtually unlimited fuel resources, low environmental impact and high intrinsic safety. Additionally, fuels for nuclear fusion feature the highest energy density: in terms of energy released, 10^6 tons of fossil fuel (for chemical combustion reactions) equate 0.8 tons of uranium (for nuclear fission reactions) or 0.14 tons of deuterium (for nuclear fusion reactions) [1].

1.1.1 Nuclear fusion reactions

Differently from what happens in fission reactors, a nuclear fusion chain reaction cannot be sustained, since no neutron-induced fusion reactions exist which present another neutron as reaction by-product. However, the fusion of two light nuclei may be achieved by making these collide. For this to happen, two nuclei must be brought very close to each other (at a distance of about one nuclear diameter), in order to activate the attractive force of the strong nuclear interaction. At such distance, a very strong electric repulsion exists between the two positively charged nuclei. Therefore, the fusion reaction can take place only if the nuclei have sufficient kinetic energy to overtake the Coulomb barrier through quantum tunnelling.
The most promising reaction for fusion electricity production involves the two heavier isotopes of hydrogen, namely *deuterium* and *tritium*, and generates as products a helium nucleus and a neutron:

$$\mathrm{D} + \mathrm{T} \rightarrow {}^4\mathrm{He} + \mathrm{n} + 17.6\ \mathrm{MeV}\ . \tag{1.1}$$

The net energy release of 17.6 MeV results from the mass defect of the reaction, according to the mass-energy equivalence $\Delta E = \Delta m c^2$. This is released in form of kinetic energy of the reaction products, and split between these obeying momentum conservation. Therefore, 3.5 MeV are given to the helium nucleus and 14.1 MeV are given to the neutron.
Exploiting such reaction requires continuous availability of the fusion fuel. While deuterium

may be extracted at low cost from oceanic water, tritium cannot be found in nature as it is radioactive with a relatively short half-life of 12.26 years. To solve this issue, it is foreseen to surround the region where fusion reactions occur with a lithium blanket. The released neutrons react indeed with lithium nuclei, resulting in further nuclear reactions which include tritium as by-product. Additionally, the heat released by the slowing down of the fast fusion-released neutrons within the blanket may be used to heat water flowing within the blanket and provide steam to be used in turbine generators.
In order to quantify the conditions which allow fusion reactions to take place, we can consider the trend of the most relevant reaction parameters. The probability that two nuclei fuse is quantified through the reaction *cross section* σ, which has the dimensions of a surface. This depends on the kinetic energy of the individual nuclei, and on their relative velocity. A global parameter quantifying the reaction rate in the whole system must, however, take into account the velocity distribution of the ensemble of nuclei. Assuming such system to be in thermodynamic equilibrium, a maxwellian distribution can be used [2], whose shape depends on the *temperature* T of the system.[1]

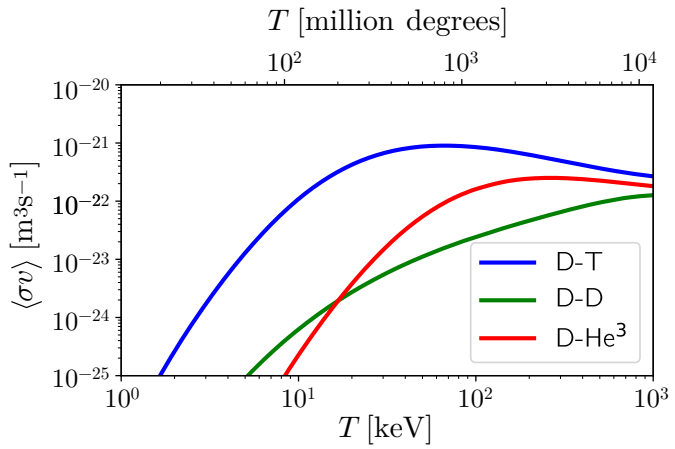

Figure 1.1: Rate coefficients for some relevant fusion reactions, as function of the temperature. The D-T rate coefficient is much larger than that for other reactions also at relatively low temperatures. Data extracted from [3].

The *rate coefficient* $\langle\sigma v\rangle$, measured in m^3/s, is obtained by averaging the quantity σv over a maxwellian distribution, where v is the relative velocity between two interacting nuclei. The resulting number of reactions in the system per unit of volume and per unit of time can be then written as $R = n_1 n_2 \langle\sigma v\rangle$, where n_1, n_2, are the *densities* of the interacting species, in m^{-3}. Figure 1.1 shows the rate coefficients for several fusion reactions, calculated from the experimental cross sections.
The temperatures required for a D-T gas, which has the highest rate coefficient, to maximize the fusion reactivity is of the order of tens of keV. This is more than 1000 times larger than the ionization potential of the deuterium and tritium atoms. This implies that the temperatures required for D-T gas in a fusion reactor will make it fully ionized, i.e. existing in form of free electrons and ions. In other words, a fusion fuel will need to be in the form of *plasma*. This is a state of matter in which particles mostly exhibit a collective behavior, being e.g. influenced by the application of external electromagnetic fields rather than by single-particle interactions [4].

1.1.2 Toroidal plasma confinement

In order to keep a hot fusion plasma far from the surrounding device materials, this can be confined by means of external magnetic fields with adequate configuration. This refers to the currently most exploited method for controlling fusion plasmas, i.e. the *magnetic confinement*.

[1] In the entire text, unless otherwise specified, the temperature is expressed in energy units, i.e. as $T \equiv k_B T_K$, in eV. Here $k_B \approx 8.617 \cdot 10^{-5}$ eV/K is the *Boltzmann constant* and T_K is the temperature of the reacting system in Kelvin. Saying that a system has a temperature (here, a thermal energy content) of 1 eV means that its classical temperature is about 11600 K.

The most convenient magnetic geometry to this aim is an axially symmetric closed field line geometry with toroidal shape (Figure 1.2) [6]. As electrons and ions follow field lines with closed path, they are confined within a finite torus-shaped volume. Such geometry is described by a *toroidal angle* φ and by local polar coordinates (θ, r), with θ the *poloidal angle* and r the *minor radius*. The distance R_0 between geometric axis and plasma center is called *major radius*.

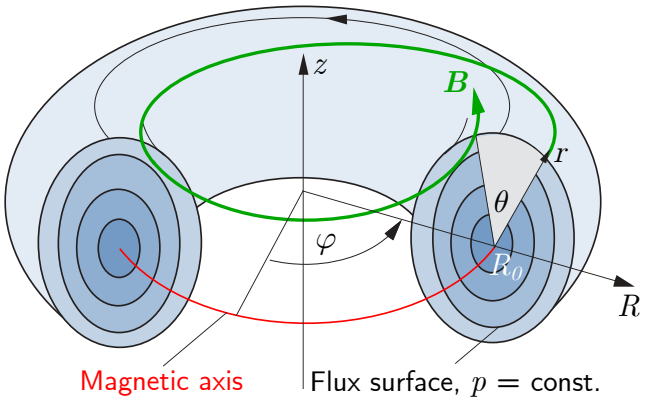

Figure 1.2: Geometric coordinates and magnetic field lines toroidal geometry, showing a set of nested magnetic flux surfaces at equilibrium. Adapted from [5].

A first source of confinement is a magnetic field $\boldsymbol{B}_\varphi$ characterized by field lines revolving in toroidal direction, with charged particles following field lines closing into themselves at each toroidal transit. With a purely toroidal field, however, particle drifts would induce fast radial losses of particles: field line curvature and a spatial gradient $B_\varphi \propto 1/R$ would generate a vertical drift of plasma particles (i.e. curvature and ∇B drifts), so that ions/electrons would drift towards the upper/lower side of the torus. The resulting net charge separation would produce an downwards-directed electric field and, in turn, an outwards-directed radial $\boldsymbol{E} \times \boldsymbol{B}$ drift of the plasma, resulting in a poor confinement.

A better confinement is achieved by twisting the field lines by adding a poloidal field component $\boldsymbol{B}_\theta$, i.e. whose field lines are circles projected on the poloidal planes. The total resulting field $\boldsymbol{B}_\varphi + \boldsymbol{B}_\theta$ has field lines winding helically around the torus, averaging out the vertical drifts. The result is a reduced vertical charge separation and radial drifts, obtaining equilibrium.

Each helical field line lies on one of a set of nested *magnetic flux surfaces* (Figure 1.2). Introducing a *magnetic flux function* ψ defined by $\boldsymbol{B} \cdot \nabla\psi = 0$, these can be defined as the contour surfaces where ψ is constant. So, the motion of plasma particles along the field lines, when projected on a poloidal cross section, will simply follow the contour of the flux surfaces projected on the poloidal plane, resulting in an electric current $\boldsymbol{J}$.

Force equilibrium for an effective confinement requires that a radially inwards-directed magnetic force equates the radially outwards-directed pressure force resulting from plasma thermal expansion due to the kinetic pressure p. Such balance is described by the relation $\boldsymbol{J} \times \boldsymbol{B} = \nabla p$. From this we deduce that $\boldsymbol{B} \cdot \nabla p = 0$, i.e. the pressure is constant on each magnetic flux surface. Moreover, from the charge conservation $\nabla \cdot \boldsymbol{J} = 0$ we deduce that also the current line vectors lie on the same flux surface.

In a future fusion reactor, the confinement must be good enough to minimize particle and, most importantly, energy losses. This would allow to keep the D-T plasma at a sufficiently high temperature to produce a high enough fusion reaction rate to provide a positive power balance, i.e. producing more power than the one externally required to maintain the plasma hot. The temperature necessary to reach this condition depends on the capability of the plasma to keep the produced energy confined within it against the heat transport losses (arising from transport processes) and radiation losses (arising from bremsstrahlung emission and line radiation). This capability is quantified by its *energy confinement time* τ_E. This is a characteristic time describing how quickly the heat is lost from the plasma, i.e. describes how efficiently it is thermally insulated.

Several approaches have been developed for confining a plasma in toroidal geometry. The most common one is the *tokamak* (Figure 1.3) [7].

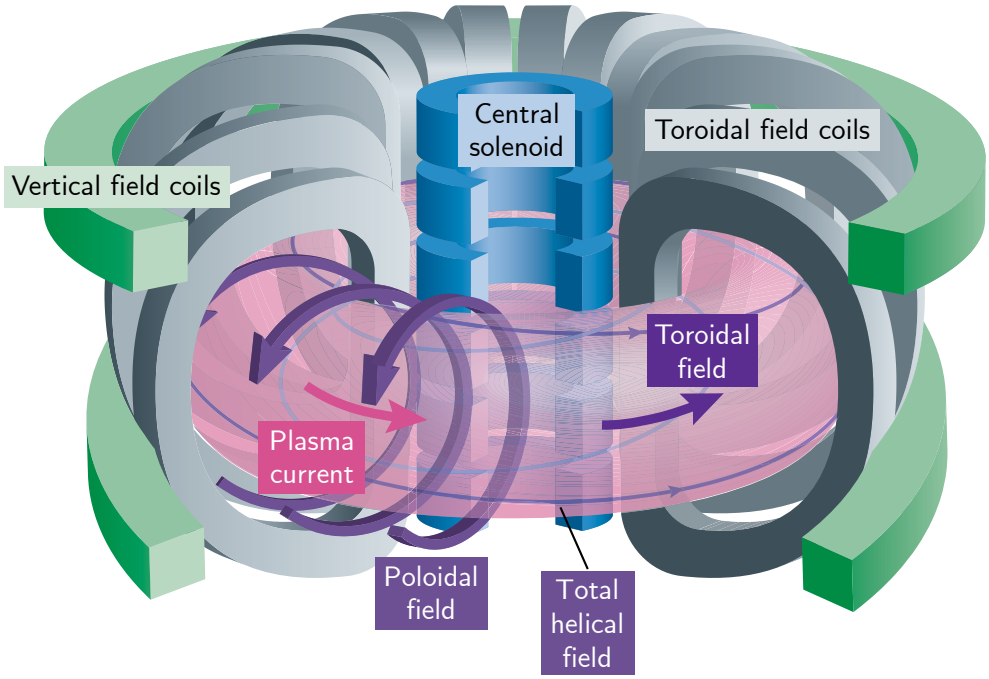

Figure 1.3: Schematic design of the main components of a tokamak. Adapted from [8].

In a tokamak the *toroidal field* is generated by currents flowing in an axially symmetric set of coils surrounding the vacuum chamber where the plasma is confined. A central solenoid, acting as the primary circuit of a transformer, is used to produce a time-varying poloidal magnetic flux which induces a toroidal loop voltage, and thus a net current flowing in toroidal direction, called *plasma current* I_p. This, in turn, generates the poloidal field as $B_\theta \approx \mu_0 I_p / 2\pi r$. This current also provides a heating source for the plasma, by means of the ohmic heating mechanism, due to a finite plasma resistivity R_p, with resulting heating power $P_{\text{ohm}} = R_p I_p^2$. Further coils are used to generate a vertical field which allows to create a wide range of plasma shapes and to perform a real-time control of plasma stability. Vertically elongated plasmas are typically produced in this way.
Typical operation of a tokamak discharge starts with the establishment of a steady toroidal field. Next, neutral fuel gas is injected into the tokamak chamber. The transformer-induced current is then ramped up, and the resulting heating ionizes the gas taking it to the plasma state. The plasma current keeps its maximum and constant value for the "flat top" portion of the plasma discharge. The poloidal field produced by the plasma current is much smaller than the toroidal field. During flat top operation, usually, an additional external heating source, in the form of radiofrequency waves or neutral particle beams, is applied to the plasma. The transformer cannot inductively drive a current for an infinite time. Therefore, for a tokamak to operate in steady state, external current drive is also required.
Other toroidal confinement concepts have been developed, e.g. the *stellarator*, in which the magnetic field components are solely produced by external coils, without any induced electric current. It is with tokamaks which, however, the best confinement properties and the highest plasma temperatures have been achieved so far.

1.1.3 The divertor concept

One of the main open issues in tokamak research is constituted by fulfilling the physics and engineering requirements for *particle* and *power exhaust* [9, 10, 11]. The research area which covers these aspects focuses on the behavior of the boundary region of tokamak plasmas. This is because of the dangers arising from the interaction between the plasma and the surrounding solid surfaces

[12, 13, 14]. In case of uncontrolled contact of the plasma with the *plasma-facing components (PFCs)*, severe problems would arise due to the resulting exceedingly large *heat loads* onto the materials. The maximum tolerable loads for steady-state operation are about $5-10\ \mathrm{MW/m^2}$, in order to prevent melting of the materials [15]. A further issue is the *erosion* of the materials, which would lead to a contamination of the plasma with the eroded heavy atoms. If uncontrolled, such impurities would strongly radiate in the plasma, leading to large energy losses and hence worsening the plasma performance. An acceptable exhaust concept should aim to keep the maximum heat loads onto the materials within tolerable engineering limits, and to hold the plasma-material interaction as far as possible from the confinement region, in order to minimize plasma contamination.

The most widely adopted strategy consists in a modification of the magnetic field geometry by means of an additional external coil, placed below the main plasma, which carries a current in the same direction as the plasma current [16, 17]. This is what is called a *divertor configuration* (Figure 1.4). The topology of the magnetic flux surfaces around the plasma edge region is distorted, and a null in the poloidal field, called *X-point*, is created. The flux surface passing through it will separate two topologically distinct regions. For this reason, such surface is called *separatrix*.

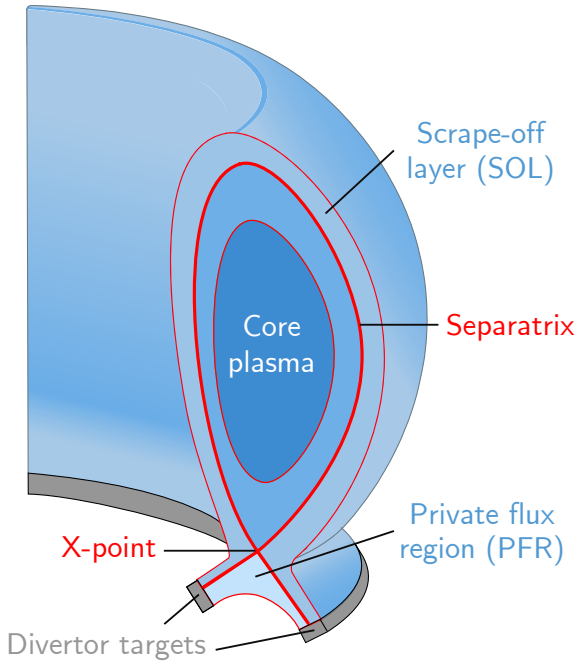

Figure 1.4: Schematic illustration of a diverted plasma configuration, highlighting the various topologically distinct regions.

The region enclosed by the separatrix constitutes the actual confinement region for the plasma, as only here particles follow field lines nested around closed flux surfaces. This is usually called the *core plasma*. The region outside the separatrix, characterized by open field lines, is called *scrape-off layer (SOL)*, and constitutes the boundary region of diverted plasmas. The region inside the separatrix but below the X-point is called *private flux region (PFR)*.

The advantage of such a configuration is to move the plasma-material interaction far from the core plasma, by concentrating it on solid material plates, placed below the X-point, which cut the flux surfaces in the SOL region. These are called *divertor targets*. Particles diffusing across the separatrix will indeed rapidly flow towards the targets along the field lines. As the ratio of parallel to perpendicular particle transport, w.r.t. the direction of the field lines, is very high, the portion of the SOL filled with the plasma is very thin, of the order of few mm. This makes the plasma-material interaction concentrated on a relatively small portion of the targets. For this reason, they must be designed to withstand extremely severe heat loads from the incoming plasma flow. By positioning the divertor targets in relative vicinity of the X-point, i.e. in a region where the poloidal field component is small w.r.t. the total field, the resulting *magnetic flux expansion* may be exploited. In this way the flux surfaces cutting the targets are spread over a wider region of the targets, mitigating the impinging particle and heat flux densities.

A further advantage of a divertor configuration is the possibility to easily control the fuel gas density in the main chamber and efficiently remove impurities, in order to avoid fuel dilution and radiation cooling. This can by done through active *pumps* located near the targets, i.e. towards the region where the largest particle fluxes are directed.

1.1.4 Plasma confinement regimes

Several different *confinement regimes* have been characterized in diverted tokamak plasmas, resulting in different quality of energy and particle confinement. It was experimentally discovered that, above a certain threshold of external heating power, a sudden regime transition occurs, in which an increase of the energy confinement time of about a factor of two takes places w.r.t. lower heating power [18]. This allowed a distinction between a "low-confinement mode" (*L-mode*) and a "high-confinement mode" (*H-mode*). In the edge region of H-mode plasmas, inside of the separatrix, turbulent radial transport is seen to be suppressed, allowing the existence of a steep plasma pressure profile, which is called *pedestal* (Figure 1.5). The region with suppressed transport is called *edge transport barrier (ETB)* [19]. This allows the achievement of larger densities and temperatures in the inner core, and hence an increased amount of stored thermal energy. The improved confinement properties of the H-mode make it a favourable operational regime for future fusion reactors.

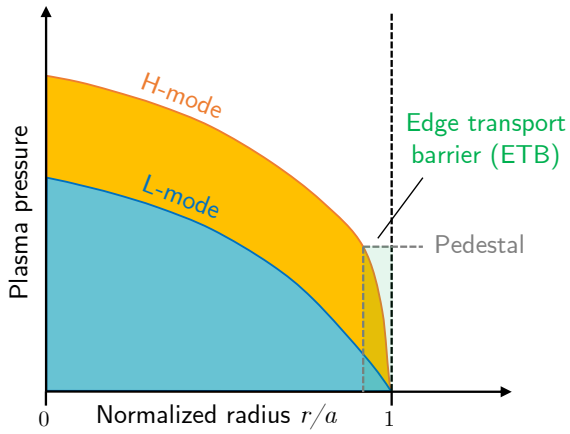

Figure 1.5: Qualitative typical radial plasma pressure profiles in L-mode and H-mode.

The power threshold for the L-H transition has been experimentally characterized as depending on several factors, including e.g. main plasma species, line averaged density, magnetic field and materials of the PFCs [20]. Since a complete physics-based model for the L-H transition is still missing, scaling laws derived from multi-device databases are generally employed for making predictions in this regard.

The access to the H-mode is accompanied by a feature which carries one of the most problematic engineering issues for future devices: the *edge localized modes (ELMs)* [21]. These are cyclic relaxations of the plasma profiles in the pedestal, with typical duration of hundreds µs, caused by instability phenomena in the plasma edge. They cause periodic abrupt ejections of particles and energy from the core plasma into the SOL, and lead to transient enormous loads onto the divertor targets.

Different types of ELMs have been experimentally characterized. The most relevant ones in current experiments are type-I ELMs and type-III ELMs. The former, generated by ideal MHD instabilities, appear as large and isolated bursts occurring at high heating powers with a frequency which ranges from 10 to 150 Hz. The latter, generated by resistive MHD instabilities, occur at heating power closer to the L-H transition threshold, and have higher frequencies up to 10 kHz.

1.1.5 Divertor operating regimes

A critical process characterizing the behavior of the divertor is the plasma-material interaction at the targets. When striking the target surfaces, incident ions recombine with electrons from the surface and are released again towards the plasma in the form of neutrals. Consecutively, depending on plasma density and temperature, they will be ionized again. This process is called *recycling*. The plasma behavior in terms of parallel particle flux $\Gamma_{\parallel}$ and heat flux $q_{\parallel}$ along the SOL, governed by recycling, defines several operating regimes for the divertor [16].

For low plasma densities, the recycled neutrals can penetrate the plasma far away from the targets without undergoing ionization, as their mean free path is longer than the X-point-to-target distance. Therefore, they are ionized in the core plasma or at the SOL upstream (i.e. around the plasma midplane). Such scenario is called *low recycling regime* (top panel in Fig. 1.6). The do-

minant particle source will then be located upstream in the SOL, and the upstream flow is stagnant up to the sheath entrance. Since roughly no ionization takes place along the SOL, there are negligible energy losses, and so no or small temperature drop along the SOL, resulting in a high temperature in front of the target plate. Since no power can be conducted in such a situation, the parallel heat flux from upstream to target is carried predominantly by convection.
If the plasma density is raised, the mean free path of the recycled neutrals in the SOL is decreased, so they are re-ionized in a thin layer in proximity of the targets. Therefore, the dominant particle source for the SOL is located in such a layer, resulting in a relatively weak plasma flow along the SOL, and a very strong flow in front of the targets, which is amplified by the particles suffering multiple recycling/re-ionization cycles. Such a scenario is called *high recycling regime* (middle panel in Fig. 1.6). The ionization processes cause large energy losses, resulting in lower temperatures in front of the targets w.r.t. those at the SOL upstream. Because of the consequently large temperature drop along the SOL, the parallel heat flux is carried predominantly by conduction, as $q_{\parallel,\mathrm{cond}} \propto T^{5/2} \frac{dT}{ds_\parallel}$, rather than by convection.
In order to reduce particle and heat loads onto the targets even further, energy losses must be achieved along the SOL. This can be done by increasing the plasma density even more, or by introducing radiating impurities. This brings the plasma temperature in front of the targets to values low enough to initiate several types of atomic processes. At temperatures less than about 5 eV, charge-exchange collisions between plasma and recycled neutrals become more effective than ionizations. Therefore, recycled neutrals collide with the plasma multiple times before being ionized, inducing strong pressure losses by friction. Additional energy is removed from the plasma as the energetic ions are converted to neutrals in such collisions. This decreases the parallel heat flux w.r.t. its upstream value. If the temperature is decreased even more, to less than about 1 eV, a region with dominant recombination arises in front of the targets. As most ions are now converted to neutrals, not only energy is removed from the plasma flow, but also the particle flux itself decreases. The resulting decrease of the plasma density makes the divertor region transparent to the recycled neutrals, bringing again the ionization front towards a more upstream location. Such scenario is usually called *detachment* [22, 23] (bottom panel in Fig. 1.6), and is the most desirable divertor regime for fusion reactors since it minimizes both particle and heat loads onto the targets.

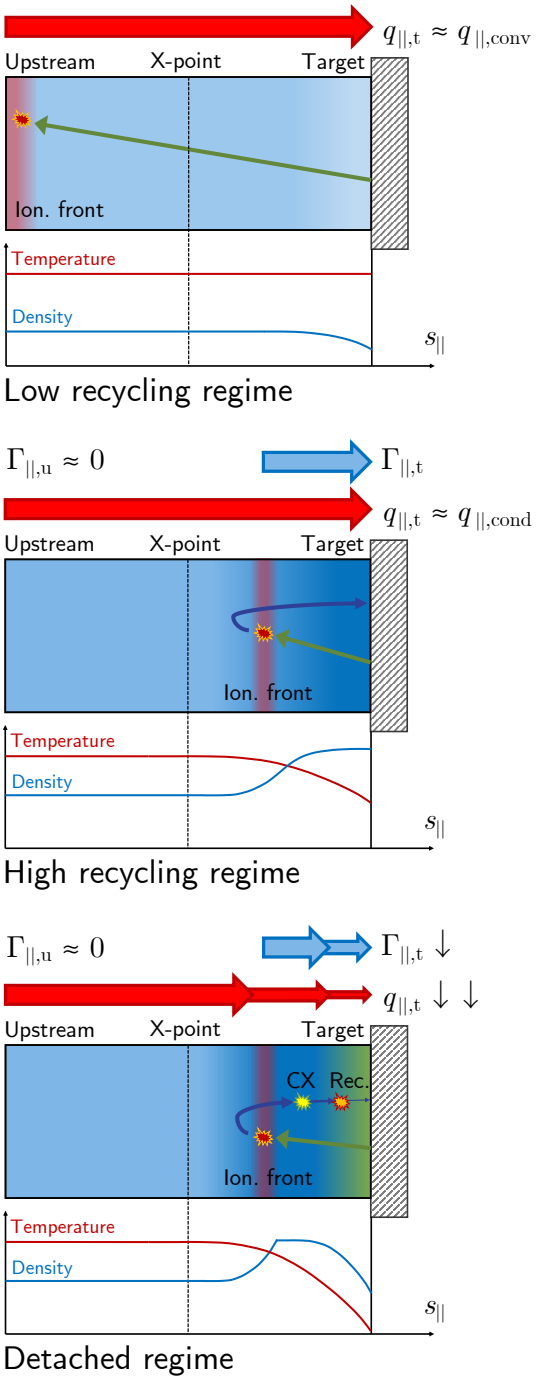

Figure 1.6: Qualitative representation of parallel fluxes and SOL plasma parameters in the various different divertor operating regimes in a "straightened" SOL. $s_\parallel$ represent the parallel distance from the targets along the SOL. The subscript "u" stands for upstream, while the subscript "t" stands for target.

1.2 The problem of helium in nuclear fusion

Understanding the behavior of *helium* in burning plasmas is critical for the design of fusion devices. In a D-T plasma alpha particles, i.e. He ions, will be continuously produced by the fusion reactions with a kinetic energy of 3.5 MeV. These are mainly confined, and quickly thermalize colliding with the other plasma species. Therefore, they provide the only direct mechanism for self-heating of the plasma.

1.2.1 Impact of fuel dilution on plasma ignition

A first trivial consequence of the presence of helium in a burning plasma is the reduction of the relative concentration of the D-T mixture, i.e. a dilution of the fusion fuel. The operational conditions for stationary burning, i.e. a situation in which the fusion power is sufficient to keep the plasma hot enough for sustaining a constant fusion reaction rate, are affected by the grade of fuel dilution.
The operational window for fusion, i.e. in which a stationary power balance for the plasma may be achieved, is usually expressed in terms of the *ignition parameter* $n_e\tau_\mathrm{E}$ as function of the plasma temperature. As a figure of merit for the impact of fuel dilution, we introduce the ratio between a *helium confinement time*, i.e. a characteristic time describing how quickly helium is removed from the system, and the energy confinement time, i.e.

$$\rho_\mathrm{He} \equiv \frac{\tau_\mathrm{He}}{\tau_\mathrm{E}} \ . \tag{1.2}$$

This is usually called *helium confinement ratio*. Figure 1.7 shows the curves inside which the ignition parameter must lie for ignition to be achievable in a D-T plasma for various values of the parameter ρ_He. These are derived by solving coupled particle and power balances for a burning plasma. The interested reader may find a full derivation in the references [24, 25, 26].

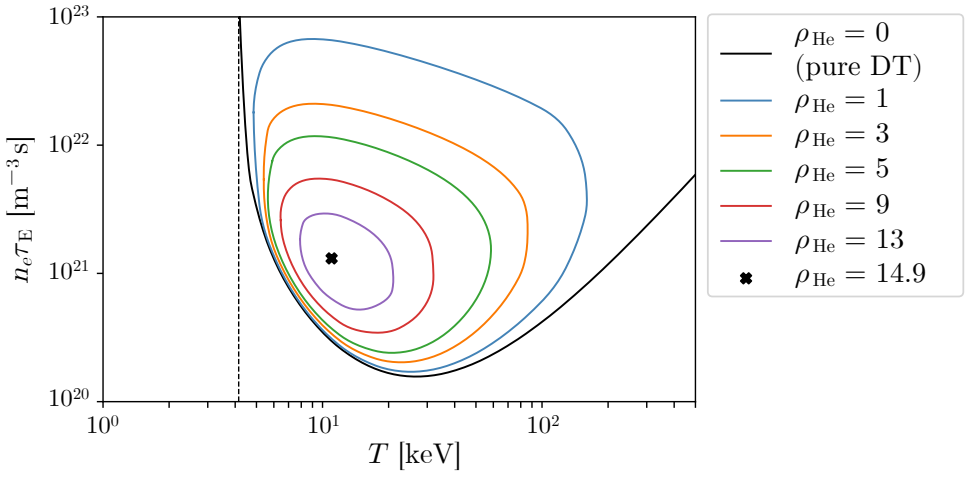

Figure 1.7: Allowed values of the ignition parameter as function of the temperature, for different values of ρ_He, for stationary burning of a D-T plasma.

The open black curve represents the ideal case in which $\tau_\mathrm{He} = 0$, therefore $\rho_\mathrm{He} = 0$, equivalent to the Lawson criterion [27], in which the He ions are assumed to be removed instantaneously from the burning plasma. With $\rho_\mathrm{He} > 0$ (i.e. considering a non instantaneous removal of He ions) the minimum allowed value for the ignition parameter increases. Additionally, the allowed operational window becomes restricted from its top. This happens because more fusion reactions would imply more dilution. Therefore the curves become closed, with the accessible temperature range being limited from both left and right. With increasing ρ_He (i.e. decreasing the efficiency of the removal of He ions) the operational window becomes smaller and smaller, until it closes at

a critical value $\rho_{\mathrm{He,crit}}$ which is about 14.9 for the case of a D-T plasma. This means that, if the characteristic time with which He ions are removed from the plasma is longer than about 14.9 times the energy confinement time, fuel dilution would be intolerable, and a stationary burning scenario would not be accessible. Additionally, the operational window would be even more reduced, and the value of $\rho_{\mathrm{He,crit}}$ would be even lower, if intrinsic or seeded radiating impurities are included [28].
Consequently, the successful operation of a fusion reactor depends largely on the minimization of ρ_{He}. In the design of ITER, for example, a maximum value of $\rho_{\mathrm{He}} = 10$ is foreseen [9].

1.2.2 Impact of helium on plasma confinement and L-H power threshold

A degradation of the core performance with increasing He content has been also systematically seen in current tokamaks. He seeding in hydrogenic plasmas causes a reduction of the energy confinement time of more than 10 % for a core He concentration of 5 % [29]. A similar confinement degradation is also observed in pure He plasmas w.r.t. to comparatively similar hydrogenic plasmas [30, 31, 32]. On the other hand, contrasting results exist on the impact of the presence of helium on the power threshold for the L-H transition [33, 34].

1.2.3 Scope and outline of the thesis

The accumulation of He ash in the core of a burning plasma must be kept within tolerable values, in order to avoid core dilution and not to degrade the confinement properties. This implies the necessity of exhausting helium from a burning plasma as efficiently as possible. This necessity motivates a thorough study of helium transport and exhaust in reactor-relevant plasma scenarios.
A mechanism to flush the plasma from He ash arises from the recycling of He ions at the plasma-facing material surfaces and the subsequent pumping of these in form of neutral atoms. For this to occur, He particles must be:

1. *Quickly transported from the core towards the divertor.* The exhaust is enhanced if He ions are efficiently transported to the plasma edge across the separatrix and towards the divertor [35]. This is closely related to the employed core confinement regime and the plasma edge characteristics [36].
2. *Neutralized and recycled at the plasma-facing material surfaces.* An efficient recycling of He ions allows to convert these to neutral atoms which are not anymore confined and can be pumped away. However, when ions strike the plasma-facing materials, they may be promptly recycled or, alternatively, penetrate the material lattice to be implanted into it, constituting a long-term storage inventory of particles in the proximity of the plasma. This was seen to be particularly efficient for He atoms in tungsten [37], which is the most promising candidate as wall material in fusion reactors [38]. Because of their very low solubility in metals, He atoms precipitate and cluster within vacancies in the material lattice, caused e.g. by displacement damage [39]. Implanted atoms may be released in a following time during plasma exposure, due to ion-bombardment-driven erosion and thermally-driven effusion [40]. This could potentially cause an effective delay in a permanent removal of the particles present in the system.
3. *Retained within the subdivertor volume.* Improving divertor retention of recycled He atoms allows to maintain large neutral He pressures in front of the pumping surfaces, which are typically located behind the divertor target plates. The pumping efficiency is enhanced if the recycled He atoms are directly scattered towards the pumps and do not leak to the main chamber [41]. Whether the recycled He atoms are preferentially transported

towards the pumps or escape the subdivertor region is mostly influenced by the properties of the He ion flow in the SOL and the recycling pattern of He atoms from the target plates [42, 43, 44]. Therefore, this is closely related to the employed divertor operating regime (cf. Section 1.1.5).

4. *Efficiently collected by an active pumping system.* The employment of efficient pumps is a necessary ingredient to ensure particle control in tokamaks [9]. Cryopumps constitute the most widely used solution for this. However, despite their efficiency in removing main fuel and impurities [45], they are not effective in removing He atoms as these do not condense on standard cryopanel surfaces (unless employing activated charcoal coating [46] or argon spraying to form a frosted cryotrapping layer [47]). He atoms can only be removed by turbomolecular pumps. However, their efficiency is typically much weaker than that of cryopumps.

The requirements (1) and (3) are mostly linked with transport physics, and nearly independent from the technical characteristics of the device. Additionally, they are constrained by the requirements of core confinement and power exhaust, which must be simultaneously fulfilled [10]. The requirements (2) and (4) instead are linked with the technical characteristics of the device, depending on the choice of geometry and materials for the PFCs and on the design of the pumping system. Therefore they allow for a wider room for optimization.

In this work the behavior of helium exhaust in tokamaks was experimentally investigated. This was complemented by a thorough numerical study aimed to interpret the experimental findings and characterize the related phenomena. A comprehensive knowledge of the physics mechanisms which affect helium exhaust is necessary for performing reasonable extrapolations towards future fusion reactors. This allows to develop operational scenarios for burning plasmas which are compatible with the requirements of helium exhaust, together with core confinement and power exhaust [10]. Additionally, it supports the choice of wall materials and geometry for the PFCs, and the design of the pumping systems in future fusion reactors [48, 49].

The experiments were performed at the ASDEX Upgrade (AUG) tokamak. This is an ideal test environment for such studies thanks to the presence of an ITER-like divertor geometry, an extensive diagnostic coverage and PFCs made of tungsten. The experiments featured He injection through gas puff into otherwise steady-state D plasmas in H-mode. This allowed to characterize the efficiency of helium exhaust in terms of global parameters, and to observe the dynamic behavior of the decay of the He content in the plasma after the injection phase. Different divertor scenarios were investigated, namely with varying neutral pressure and detachment state. Different types of numerical modelling were performed in order to interpret the experimental findings. The observed dynamic behavior of helium during AUG discharges, and the relative impact of long-term wall storage and active pumping, were interpreted through a newly developed numerical framework. This comprises the self-consistent coupling of the plasma impurity transport code Aurora [50] with a wall recycling and retention model, which features realistic assumptions on the plasma-wall interaction mechanisms. The mechanisms determining helium transport and recycling in the divertor were instead identified through realistic plasma edge simulations performed with the SOLPS-ITER code package [51].

Chapter 2 presents the main phenomena determining impurity transport, recycling and pumping in the various regions of a tokamak plasma, with focus on helium. Chapter 3 introduces the ASDEX Upgrade tokamak and the diagnostics which were employed for collecting the experimental data, and reports the performed experiments. Chapter 4 presents the modelling aimed to interpret the experimentally observed exhaust dynamics in terms of impact of wall storage and active pumping. Chapter 5 presents the simulations performed to characterize helium transport and recycling in the divertor. Chapter 6 finally gives the summary of the results and an outlook.

Chapter 2

Theoretical aspects of impurity transport, recycling and pumping

Figure 2.1 shows how impurity transport in tokamaks concerns three regions with different properties: the *core plasma* inside the separatrix, the *edge region* where the plasma interacts with the material walls and can be neutralized, and the *divertor* where the neutral gas is exhausted towards the pumping systems. In the core plasma impurity ions are radially transported across the magnetic flux surfaces, either via collisions or by turbulence. As soon as impurity ions cross the separatrix and enter the SOL, transport becomes dominated by the parallel plasma flow along the magnetic field lines, which drives them towards the divertor targets. When impurity ions strike the target plates they recycle, i.e. are released again as neutral atoms, through a number of different mechanisms. The same process takes place also for those ions which are radially transported to the main chamber wall. Recycled impurity neutral atoms may re-enter the plasma and be re-ionized or, alternatively, may escape the plasma region and travel towards the pumps (which are usually located behind the divertor targets), and be permanently removed from the system.

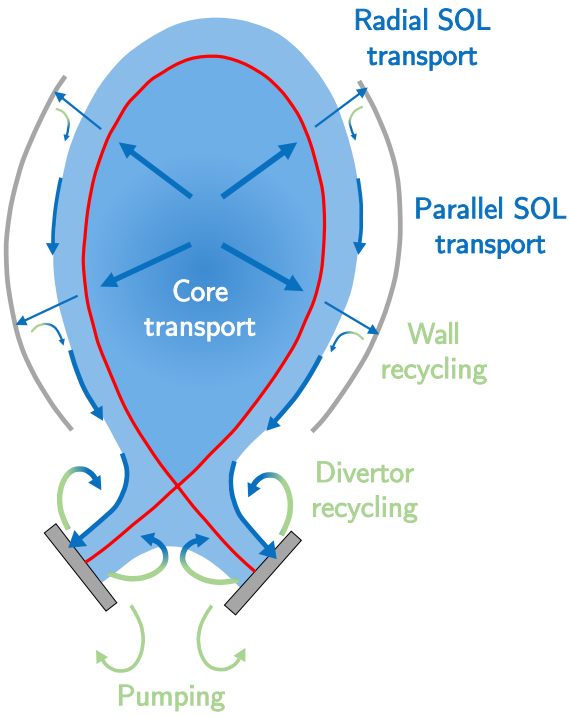

Figure 2.1: Overview of impurity particle transport in the various regions of a tokamak. Blue colors describe ion regions/fluxes, while green colors describe neutrals regions/fluxes. This color code for ions and neutrals applies for all the figures present in the text.

For the different regions of a tokamak different models which describe impurity transport have been developed. In this Chapter a theoretical description of such models is provided. In the Section 2.1 core transport is described, and an overview of the processes describing the different transport components is given. In the Section 2.2 the phenomena characterizing impurity transport and recycling in the plasma edge are discussed. In the Section 2.3 an overview of neutral gas transport is given. Finally, in the Section 2.4 the definition of several relevant parameters quantifying impurity exhaust, widely employed in the rest of this thesis, is given.

2.1 Core transport

The *core plasma* is characterized by temperatures which range from hundreds of eV close to the edge up to several keV in the center. Therefore, light impurities such as helium are typically fully ionized. Impurity accumulation in the core plasma, and consequently the amount of impurities which escape it travelling across the separatrix, are governed by radial, i.e. cross-field, transport.

2.1.1 Radial impurity transport in the core plasma

The radial impurity fluxes in the core plasma can be analytically and numerically described by means of transport equations. This allows to evaluate the time evolution of the radial impurity profiles, as a function of transport coefficients and boundary conditions. It also allows to calculate the fractional abundance of each ionization stage, solving a system of coupled equations for each stage including the atomic processes.
The mechanisms leading to radial transport of impurities are Coulomb collisions and turbulence caused by micro-instabilities. Whereas the collisional contributions to the transport can be usually analytically calculated, an accurate treatment of turbulence is challenging. Therefore its contribution is usually empirically inferred from experiments or estimated through advanced (e.g. gyrokinetic) numerical models. Especially for light impurities, turbulence provides the dominant contribution to radial transport in the core plasma [52].
The microscopic time evolution of the distribution function of a plasma species is given by the kinetic Boltzmann equation. The equation describing the macroscopic *particle conservation* is obtained by the zeroth moment of the kinetic equation for impurities:

$$\frac{\partial n_{\mathrm{imp},z}(\boldsymbol{x},t)}{\partial t} + \nabla \cdot \boldsymbol{\Gamma}_{\mathrm{imp},z}(\boldsymbol{x},t) = Q_{\mathrm{imp},z}(\boldsymbol{x},t) \ . \tag{2.1}$$

Eq. (2.1) describes the space and time dependence of the *impurity ion density* $n_{\mathrm{imp},z}$, in m^{-3}, of an impurity species 'imp' with charge state z, with $0 \leq z \leq Z_{\mathrm{imp}}$. $\boldsymbol{\Gamma}_{\mathrm{imp},z}$ is the corresponding *impurity ion flux density*, in $\mathrm{m}^{-2}\mathrm{s}^{-1}$, while $Q_{\mathrm{imp},z}$ is the sum of impurity particle *sources* and *sinks* due to processes such as ionization, recombination, CX collisions, or fusion for the case of helium. Source and sink terms also connect neighbouring charge states.
Since radial transport is the dominant transport mechanism for impurity ions in the core plasma, the impurity ion density for each charge state is approximately constant on a flux surface. It is therefore possible to reduce such a model to a simple one-dimensional description as function of a radial coordinate. Defining a radial coordinate as $r \equiv \sqrt{V/(2\pi^2 R_0)}$, where V is the volume enclosed by the corresponding flux surface, a *radial impurity transport equation* in cylindrical coordinates may be derived averaging Eq. (2.1) over flux surfaces [53]:

$$\frac{\partial n_{\mathrm{imp},z}(r,t)}{\partial t} + \frac{1}{r}\frac{\partial}{\partial r}\left(r\Gamma_{r,\mathrm{imp},z}(r,t)\right) = Q_{\mathrm{imp},z}(r,t) \ , \tag{2.2}$$

where $\Gamma_{r,\mathrm{imp},z} \equiv \boldsymbol{\Gamma}_{\mathrm{imp},z} \cdot \boldsymbol{e}_r$ is the radial flux component.
The commonly employed ansatz for characterizing the radial impurity ion fluxes is through the sum of a diffusive component and a convective component, i.e. as

$$\Gamma_{r,\mathrm{imp},z} = -D_{\mathrm{imp},z}\frac{\partial n_{\mathrm{imp},z}}{\partial r} + v_{\mathrm{imp},z} n_{\mathrm{imp},z} \ , \tag{2.3}$$

where $D_{\mathrm{imp},z}$ is a *diffusion coefficient*, in m^2/s, and $v_{\mathrm{imp},z}$ is a *convective velocity*, in $\mathrm{m/s}$. Both in general depend on the charge state z and are function of the radial coordinate r. Substituting Eq. (2.3) into Eq. (2.2), the radial impurity transport equation will read

$$\frac{\partial n_{\mathrm{imp},z}(r,t)}{\partial t} + \frac{1}{r}\frac{\partial}{\partial r}\left[r\left(-D_{\mathrm{imp},z}(r)\frac{\partial n_{\mathrm{imp},z}(r,t)}{\partial r} + v_{\mathrm{imp},z}(r) n_{\mathrm{imp},z}(r,t)\right)\right] = Q_{\mathrm{imp},z}(r,t) \ . \tag{2.4}$$

In spite of the assumption of $n_{\mathrm{imp},z}$ being constant on the flux surfaces, the radial component of the impurity ion flux may still show a variation with the poloidal angle θ. Reasons for this are the poloidally varying distance between flux surfaces, being shorter at the outboard side because of the Shafranov shift, and the $1/R$ dependence of the toroidal magnetic field. Indeed, poloidal variations of the radial density and temperature gradients and of the magnetic field cause a poloidal variation of the transport coefficients $D_{\mathrm{imp},z}$ and $v_{\mathrm{imp},z}$ as well. If, however, the poloidal variation of such coefficients is known, Eq. (2.4) may be still solved for the *flux-surface-averaged* transport coefficients [53]:

$$\begin{aligned} D_{\mathrm{imp},z} &= \frac{1}{4\pi^2 R_0 r}\int_0^{2\pi} D_{\mathrm{imp},z}(\theta)|\nabla r|\frac{dS}{d\theta}\,\mathrm{d}\theta\ , \\ v_{\mathrm{imp},z} &= \frac{1}{4\pi^2 R_0 r}\int_0^{2\pi} v_{\mathrm{imp},z}(\theta)\frac{dS}{d\theta}\,\mathrm{d}\theta\ . \end{aligned} \tag{2.5}$$

Impurity confinement in the core plasma may be described through an *impurity confinement time* τ_{imp}. This quantifies the time variation of the total impurity ion content $N_{\mathrm{imp}} = \int_{\mathrm{core}} n_{\mathrm{imp}}(\boldsymbol{x})\,\mathrm{d}^3\boldsymbol{x}$ in the core plasma as

$$\frac{dN_{\mathrm{imp}}}{dt} = -\frac{N_{\mathrm{imp}}}{\tau_{\mathrm{imp}}}\ . \tag{2.6}$$

Since, in equilibrium, the time variation of the total impurity ion content must be equal to a constant total impurity ion source rate, it follows that

$$\tau_{\mathrm{imp}} \equiv \frac{\int_{\mathrm{core}} n_{\mathrm{imp}}(\boldsymbol{x})\,\mathrm{d}^3\boldsymbol{x}}{\int_{\mathrm{core}} Q_{\mathrm{imp}}(\boldsymbol{x})\,\mathrm{d}^3\boldsymbol{x}}\ . \tag{2.7}$$

Equilibrium solutions of the radial transport equation

Analytic solutions of Eq. (2.4) exist only for very few cases. Each solution for the impurity ion density must, however, satisfy the symmetry condition at the plasma center

$$\left.\frac{\partial n_{\mathrm{imp}}}{\partial r}\right|_{r=0} = 0\ . \tag{2.8}$$

For purpose of qualitative illustration, approximated but physically relevant solutions can be obtained using a boundary condition

$$\left.\frac{\partial n_{\mathrm{imp}}}{\partial r}\right|_{r=a} = -\frac{n_{\mathrm{imp}}(a)}{\lambda_{\mathrm{SOL,imp}}} \tag{2.9}$$

relating the impurity ion density gradient at the separatrix to an empirical density decay length $\lambda_{\mathrm{SOL,imp}}$ in the SOL, and employing the following assumptions:

- A boundary condition $n_{\mathrm{imp}}(a) = 0$, i.e. impurity ion density dropped to zero at the separatrix. This reflects the fact that n_{imp} should be much lower at the separatrix than at the plasma center.
- Constant transport coefficients D_{imp}, v_{imp} over the plasma cross-section for all ionization stages.
- All the impurity neutrals being ionized at a distance λ_i from the wall, at the radial location $r = r_0$.

Solving Eq. (2.4) employing such simplifications gives the qualitative total impurity ion density profiles as shown in Fig. 2.2.
The total impurity ion density profile inside the ionization region ($r < r_0$) is determined by the direction of the convective velocity. For an inward-directed (i.e. negative) convective velocity

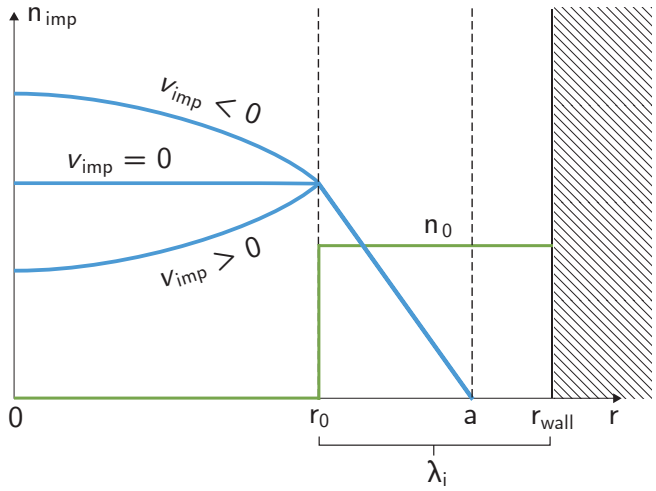

Figure 2.2: Qualitative illustration of the spatial distribution of the total equilibrium impurity ion density n_{imp} and the impurity neutral density n_0 as function of the radial coordinate r for negative, zero and positive convective velocities v_{imp}.

we obtain a peaked profile, while for an outward-directed (i.e. positive) convective velocity we obtain a hollow profile. If, instead, radial transport is dominated by diffusion only (i.e. radial velocity equal to zero), we obtain a plateau for the total impurity ion density. In any case, physically meaningful solutions are only achieved with positive diffusion coefficients.
For the simplified case here described, in which the particle source by ionization is located at $r = r_0$ as a point source, i.e. in the form $Q_{\mathrm{imp}}(r) = \Phi \frac{\delta(r-r_0)}{2\pi r_0}$, employing the further simplification of $v_{\mathrm{imp}} = 0$, the equilibrium density may be calculated as [53]

$$\begin{aligned} n_{\mathrm{imp}}(r) &= \frac{\Phi}{2\pi D_{\mathrm{imp}}} \left(\frac{\lambda_{\mathrm{SOL,imp}}}{a} - \ln(r_0/a) \right) \quad \text{for } r \leq r_0 \ , \\ n_{\mathrm{imp}}(r) &= \frac{\Phi}{2\pi D_{\mathrm{imp}}} \left(\frac{\lambda_{\mathrm{SOL,imp}}}{a} - \ln(r/a) \right) \quad \text{for } r > r_0 \ . \end{aligned} \tag{2.10}$$

Figure 2.3 shows the analytical time evolution of the total impurity ion density profile rising from zero towards the equilibrium solution after the start of a constant point source at $r = r_0$ (left) and decaying from the equilibrium profile after the source has been shut down (right).

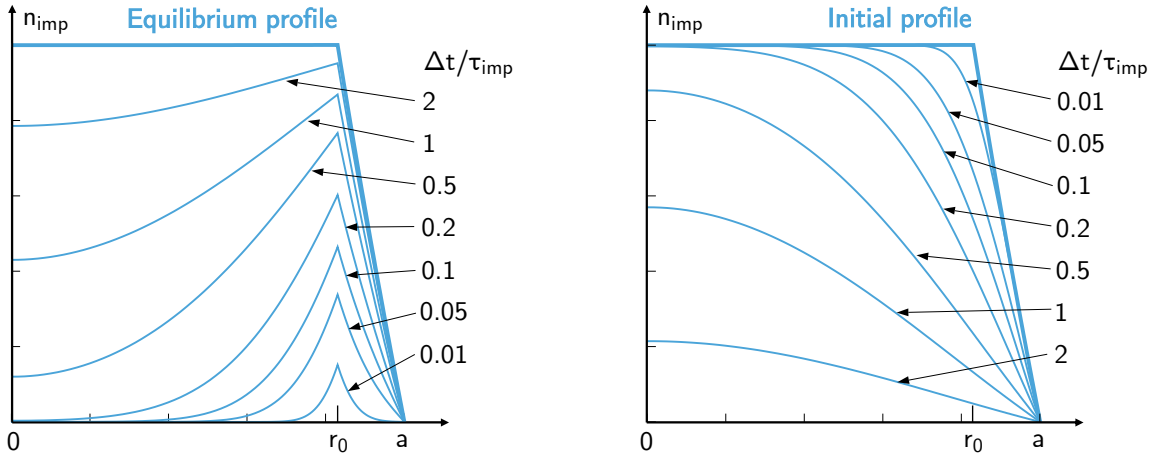

Figure 2.3: Temporal variation of the radial profile of the total impurity ion density in the core, in case of uniform diffusion coefficient and no convective velocity, starting from zero after a point source has been switched on at $r = r_0$ (left), and starting from the equilibrium solution after the source has been switched off (right), at different time delays normalized to the time τ_{imp}, analytically calculated solving Eq. (2.4) using the assumptions discussed in this paragraph. Adapted from [53].

Integrating the equilibrium solution, the particle confinement time may be then expressed as [53]

$$\tau_{\mathrm{imp}} = \frac{1}{2}\frac{a^2}{D_{\mathrm{imp}}}\left(\frac{\lambda_{\mathrm{SOL,imp}}}{a} + \frac{1-(r_0/a)^2}{2}\right) . \tag{2.11}$$

Atomic processes and charge state distribution

For the case of impurities, which have an atomic number $Z > 1$, the charge state distribution in the core plasma is mainly determined by the background electron density and temperature. The resulting charge state distribution comes from the balance of the various atomic processes involving the impurity ions, according to the so-called *collisional radiative model* [54].
Ionization processes are due to the impact of impurity particles $\mathrm{A}^z_{\mathrm{imp}}$ with fast plasma electrons, after which the impurity particles gain sufficient energy to transit to a higher charge state, i.e.

$$\mathrm{A}^z_{\mathrm{imp}} + \mathrm{e} \rightarrow \mathrm{A}^{z+1}_{\mathrm{imp}} + 2\mathrm{e} . \tag{2.12}$$

Recombination processes, after which impurity ions transit to a lower charge state, can be due to multiple reactions. Namely, radiative recombination, in which an electron is captured by an impurity ion and the surplus energy is released through radiation, i.e.

$$\mathrm{A}^z_{\mathrm{imp}} + \mathrm{e} \rightarrow \mathrm{A}^{z-1}_{\mathrm{imp}} + h\nu , \tag{2.13}$$

or dielectric recombination, in which two electrons are involved and the surplus energy is given to one electron, i.e.

$$\mathrm{A}^z_{\mathrm{imp}} + 2\mathrm{e} \rightarrow \mathrm{A}^{z-1}_{\mathrm{imp}} + \mathrm{e} , \tag{2.14}$$

or CX-assisted recombination, in which an impurity ion captures one electron from one neutral atom of the main plasma species through a charge-exchange collision, i.e.

$$\mathrm{A}^z_{\mathrm{imp}} + \mathrm{A}^0_{\mathrm{main}} \rightarrow \mathrm{A}^{z-1}_{\mathrm{imp}} + \mathrm{A}^+_{\mathrm{main}} . \tag{2.15}$$

CX reactions between ions and neutrals of the same impurity species can be neglected as a first approximation, assuming that their impact is much less than that of the collisions with the neutrals of the main species.
Therefore, for any charge state z, the total source term in the radial transport equation may be written as

$$\begin{aligned} Q_{\mathrm{imp},z}(r) = & -\left[n_e(r)\langle\sigma v\rangle^{\mathrm{ion}}_{\mathrm{imp},z}(r) + n_e(r)\langle\sigma v\rangle^{\mathrm{rec,RDR}}_{\mathrm{imp},z}(r) + n_n(r)\langle\sigma v\rangle^{\mathrm{rec,CX}}_{\mathrm{imp},z}(r)\right] n_{\mathrm{imp},z}(r) \\ & + \left[n_e(r)\langle\sigma v\rangle^{\mathrm{ion}}_{\mathrm{imp},z-1}(r)\right] n_{\mathrm{imp},z-1}(r) \\ & + \left[n_e(r)\langle\sigma v\rangle^{\mathrm{rec,RDR}}_{\mathrm{imp},z+1}(r) + n_n(r)\langle\sigma v\rangle^{\mathrm{rec,CX}}_{\mathrm{imp},z+1}(r)\right] n_{\mathrm{imp},z+1}(r) . \end{aligned} \tag{2.16}$$

The first line in Eq. (2.16) expresses sinks due to ionization towards a higher charge state and recombination (radiative + dielectric and CX-assisted) towards a lower charge state, and the second line a source due to ionization from a lower charge state. The third line accounts for sources due to recombination (radiative + dielectric and CX-assisted) from a higher charge state. $n_e(r)$ is the background electron density profile, while $n_n(r)$ is the background neutral profile of the main plasma species. Figure 2.4 shows the calculated rate coefficients for the case of helium in a hydrogenic background plasma, for all its charge state transitions.
Neglecting transport effects on the charge state distribution, the ratio of impurity densities for two adjacent ionization stages is

$$\frac{n_{\mathrm{imp},z+1}(r)}{n_{\mathrm{imp},z}(r)} = \frac{n_e(r)\langle\sigma v\rangle^{\mathrm{ion}}_{\mathrm{imp},z}(r)}{n_e(r)\langle\sigma v\rangle^{\mathrm{rec,RDR}}_{\mathrm{imp},z}(r) + n_n(r)\langle\sigma v\rangle^{\mathrm{rec,CX}}_{\mathrm{imp},z}(r)} . \tag{2.17}$$

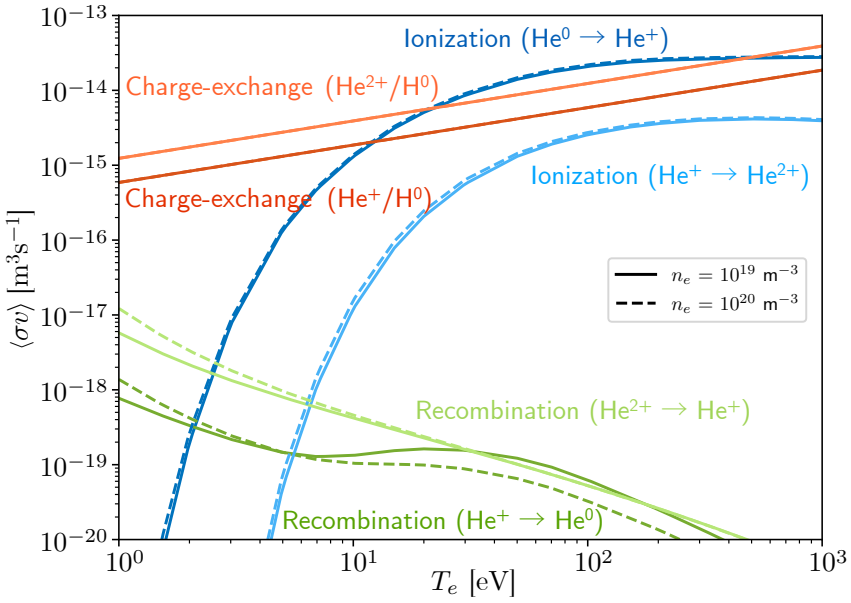

Figure 2.4: Calculated ionization rates $\langle\sigma v\rangle_{\mathrm{He}}^{\mathrm{ion}}$ (blue curves), radiative+dielectric recombination rates $\langle\sigma v\rangle_{\mathrm{He}}^{\mathrm{rec,RDR}}$ (green curves) and CX-assisted recombination rates $\langle\sigma v\rangle_{\mathrm{He}}^{\mathrm{rec,CX}}$ (red curves), for all the charge transitions of helium. ADAS data [55].

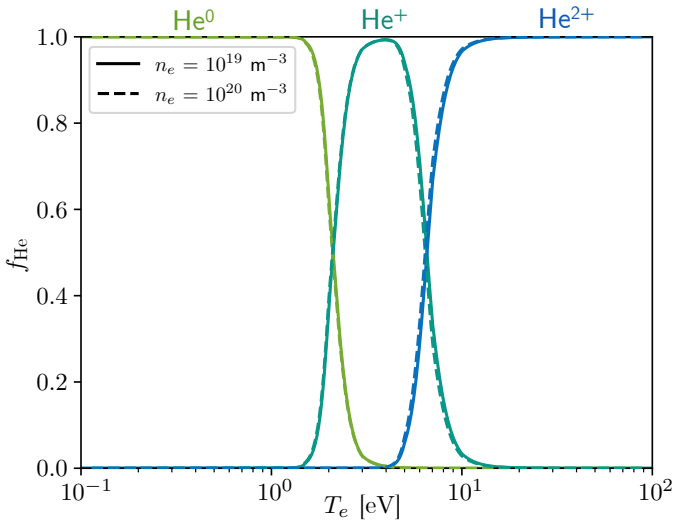

Figure 2.5: Calculated fractional abundances of He according to the collisional radiative model, employing the rates shown in Fig. 2.4.

This situation is usually referred to as *coronal equilibrium*. The ionization rates have the strongest dependence on the electron temperature. Although the charge-exchange rates are comparable to the ionization rates at high temperatures, the CX contribution to coronal equilibrium is usually very small, because the neutral main species density is low. Therefore, going from the edge towards the inner core plasma (i.e. from lower to higher temperatures), the *fractional abundances* $f_{\mathrm{imp},z} \equiv n_{\mathrm{imp},z}/\sum_z n_{\mathrm{imp},z}$ of the various charge state populations will form radial shells with increasing mean charge state. Figure 2.5 shows the calculated fractional abundances for the case of helium in a hydrogenic plasma.

However, taking into account radial transport, the local balance of ionization and recombination processes is usually not reached, as the characteristic equilibration times can be longer than the characteristic transport times. Impurity ions can be transported indeed to plasma regions with higher/lower temperature before they ionize/recombine. Therefore, the shell of any charge state is usually more radially extended than predicted by the coronal equilibrium, and is shifted inwards. This is particularly true in proximity of the plasma edge, where steep temperature gradients exist.

2.1.2 Collisional transport processes

One mechanism for impurity ion transport in magnetized plasmas is given by *Coulomb collisions* between particles. Such collisions cause friction forces acting on the ion fluid. Ions can be scattered while gyrating around field lines, and shifted towards a different magnetic flux surface.
The theory describing collisional transport in a cylindrical plasma, in presence of a homogeneous magnetic field, is usually referred to as *classical transport*. This takes into account the effect of friction forces which are perpendicular to the magnetic field. Additional phenomena in tokamaks arise because of the toroidal geometry. The resulting corrections to the classical transport theory form the *neoclassical transport* theory. This takes into account the additional effect of parallel friction forces, which are a consequence of the toroidal geometry. Therefore, radial particle fluxes in a tokamak plasma driven by collisional transport processes may be derived as the sum of a classical and a neoclassical part. A detailed treatment of the derivation of the collisional impurity transport transport coefficients may be found in [56, 57].

Classical transport

Within the classical theory, the radial density and temperature gradients lead to a diamagnetic particle flow in a direction perpendicular to the magnetic field. Since this flow is different for different plasma species, Coulomb collisions will cause friction between different species. Therefore, a radial particle flux for a given species is given by the friction exerted from all other species.
Balancing magnetic and pressure forces, it can be shown that the drift velocity caused to a plasma species a because of friction exerted by all other plasma species, i.e. due to the forces $\boldsymbol{F}_{\perp,ab}$ acting in perpendicular direction w.r.t. the magnetic field, is [53]

$$\boldsymbol{v}_{\perp,a} = \frac{1}{Z_a n_a B^2} \sum_{b\neq a} \boldsymbol{F}_{\perp,ab} \times \boldsymbol{B} \approx \frac{m_a}{Z_a B^2} \sum_{b\neq a} \nu_{ab} \left(\frac{\nabla p_b}{Z_b n_b} - \frac{\nabla p_a}{Z_a n_a} \right) . \tag{2.18}$$

Here, n, p, m and Z are ion density, ion pressure, atomic mass and atomic charge of a given plasma species, and ν_{ab} is the collision frequency between the species b and the species a, which is

$$\nu_{ab} = \frac{4\sqrt{2\pi}}{3(4\pi\varepsilon_0^2)} \frac{\sqrt{m_{ab}}}{m_a} \frac{Z_a^2 Z_b^2 \ln\Lambda}{T_i^{3/2}} n_b , \tag{2.19}$$

where $m_{ab} \equiv m_a m_b/(m_a + m_b)$, and $\ln\Lambda$ is the Coulomb logarithm.
The radial ion flux density of the species a is defined as $\boldsymbol{\Gamma}_{\perp,a} \equiv \boldsymbol{v}_{\perp,a} n_a$. The pressure gradients in Eq. (2.18) can be separated into the relative density and temperature gradients. Therefore, we can extract a term proportional to the density gradient of the considered species a, i.e. we can define a diffusive flux as $\boldsymbol{\Gamma}_{\text{diff},a} \equiv -D_a \nabla n_a$. The relative proportionality factor, i.e. [53]

$$D_{\text{CL},a} = \frac{m_a T_i}{Z_a^2 B^2} \sum_{b\neq a} \nu_{ab} = \frac{1}{2} \rho_a^2 \nu_a , \tag{2.20}$$

is the classical diffusion coefficient, where ρ_a is the gyroradius of the species a and $\nu_a \equiv \sum_{b\neq a} \nu_{ab}$. The remaining terms in Eq. (2.18) depend on the weighted sum of the density gradients of all other plasma species and to the temperature gradient. They are summarized in a convective flux $\boldsymbol{\Gamma}_{\text{conv},a} \equiv \boldsymbol{v}_a n_a$, where the proportionality factor, which can be shown to be [53]

$$\boldsymbol{v}_{\text{CL},a} = \sum_{b\neq a} D_{\text{CL},a} \frac{Z_a}{Z_b} \left[\frac{\nabla n_b}{n_b} - \frac{\nabla T_i}{T_i} \left(\frac{3m_{ab}}{2m_b} - 1 - \frac{Z_b}{Z_a} \left(\frac{3m_{ab}}{2m_a} - 1 \right) \right) \right] \tag{2.21}$$

is the classical convective velocity.

Since $\boldsymbol{v}_{\mathrm{CL},a}$ is proportional to the charge ratios Z_a/Z_b, radial transport becomes increasingly convective for heavier impurities. The impurity flux is driven in the same direction of the density gradient, i.e. inwards, and in the opposite direction of the ion temperature gradient, i.e. outwards.

Neoclassical transport

Additional transport in toroidal magnetic geometries is caused by curvature and inhomogeneity of the magnetic field. It arises from the parallel component of the friction force exerted on a given plasma species.
A first effect is caused by the fact that, in toroidal geometry, the diamagnetic flows perpendicular to the magnetic field are not divergence-free. Therefore, parallel flows arise to ensure that the total flow has a zero divergence. Such parallel flows are called *Pfirsch-Schlüter flows*. Similarly to the classical flows, different ion species have different Pfirsch-Schlüter flows, therefore friction occurs between different plasma species. It can be shown that this effect is described by an additional diffusivity component which is roughly [57]

$$D_{\mathrm{PS},a} \approx 2q^2 D_{\mathrm{CL},a} \ . \tag{2.22}$$

Another effect is caused by the fact that ions moving in a toroidal magnetic field may be trapped in magnetic mirrors because of the $1/R$ dependence of the magnetic field. Particles with large parallel velocity can complete a poloidal round, and are then called *passing particles*. During the poloidal round, the curvature drift leads to a displacement of the orbit of such particles from their "original" flux surface, with maximum magnitude approximately equal to $\varepsilon\rho_{\mathrm{p},a}$, with $\varepsilon \equiv \frac{r}{R_0}$ the inverse aspect ratio and $\rho_{\mathrm{p},a}$ poloidal gyroradius. Instead, particles which have sufficiently low parallel velocity will not complete a poloidal round, but will oscillate back and forth between the turning points in an effective magnetic mirror, being thus called *trapped particles*. The peculiar shape of the resulting orbits of the trapped particles, when viewed on a poloidal cross section, brought them the name of *banana orbits* (see Fig. 2.6). The width of the banana orbits is approximately equal to $\sqrt{\varepsilon}\rho_{\mathrm{p},a}$. Trapped ions travel along the banana orbit in such a way that they move against the electric current when they are at the inner side of the orbit (center of Fig. 2.6), and in the same direction of the electric current when they are at the outer side (right of Fig. 2.6). Therefore, radial density and temperature gradients lead to a further flow component for trapped particles in diamagnetic direction. Again, different ion species have different banana-driven flows, therefore Coulomb collisions cause further friction forces between different species, thus a further radial flux component. The additional diffusivity component due to this effect, usually called *banana-plateau* component, can be shown to be roughly [57]

$$D_{\mathrm{BP},a} \approx \frac{q^2}{\varepsilon^{3/2}} D_{\mathrm{CL},a} \ . \tag{2.23}$$

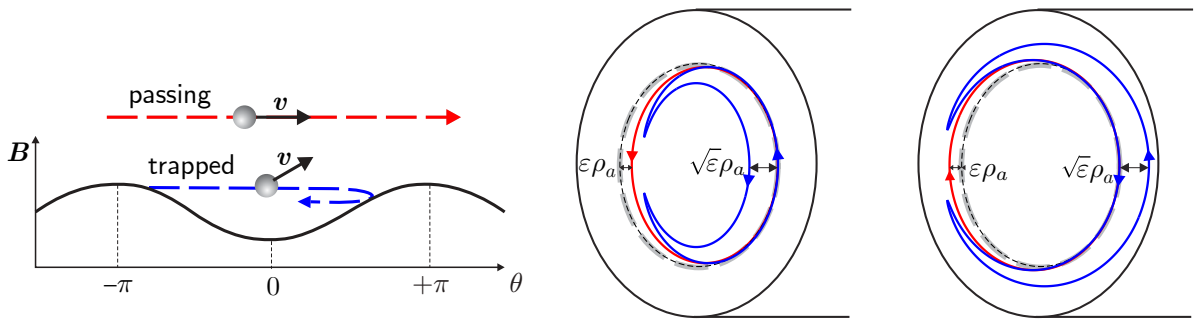

Figure 2.6: Particle orbits resulting from the motion of passing ions (in red) and trapped ions (in blue). Right: orbits for ions starting towards opposite directions at same radius. Adapted from [5].

Overview of collisional transport coefficients

According to the presented overview, the collisional transport coefficients can be split into three components: a *classical term*, caused by perpendicular friction forces, a *Pfirsch-Schlüter term* and a *banana-plateau term*, the last two caused by parallel friction forces. Each component has a diffusive and a convective term. In the trace limit, i.e. when only the collisions with the main ion species are considered, the radial impurity ion flux can be generally written as [53]

$$\Gamma_{r,\mathrm{imp}} = \sum_{x=\mathrm{CL,PS,BP}} D_{x,\mathrm{imp}} \left[-\frac{dn_{\mathrm{imp}}}{dr} + \frac{Z_a}{Z_b} \left(\frac{d \ln n_{\mathrm{main}}}{dr} + H_{x,\mathrm{imp}} \frac{d \ln T_i}{dr} \right) n_{\mathrm{imp}} \right] . \tag{2.24}$$

According to the notation of Eq. (2.24), for each transport component two parameters are sufficient to describe radial transport: a diffusion coefficient $D_{x,\mathrm{imp}}$ which quantifies the dependence on radial density gradients, and a temperature screening factor $H_{x,\mathrm{imp}}$ which quantifies the dependence on the radial temperature gradient.

The relative importance of the various neoclassical flows can be deduced comparing the collision frequency ν_{imp} (i.e., in the trace limit, the collision frequency, Eq. (2.19), between impurity ions and main ions) with the particle bounce frequency $\nu_b = \varepsilon^{3/2} v_{\mathrm{imp}}/qR$ (i.e. the frequency with which trapped ions travel between outer and inner side of the banana orbit), through the ratio $\nu^* \equiv \nu_{\mathrm{imp}}/\nu_b$, usually called normalized collisionality. If $\nu^* > \varepsilon^{-3/2}$ then passing impurity ions undergo collisions faster than the time needed to complete an orbit, which is qR/v_{imp}. In this case the banana-driven flows are negligible w.r.t. the Pfirsch-Schlüter flows, and we are in the so-called *Pfirsch-Schlüter regime*. If $1 < \nu^* < \varepsilon^{-3/2}$, the collisionality is low enough to make passing impurity ions complete their orbit before undergoing collisions. However, trapped particles, which require the longer time $qR/v_{\mathrm{imp}}\sqrt{\varepsilon}$ to complete an orbit, still undergo collisions. Here we are in the so-called *plateau regime*. Finally, if $\nu^* < 1$, the collisionality is so low that also trapped particles can complete their orbits. In this case the banana-related flows are dominant, and we are in the so-called *banana regime*.

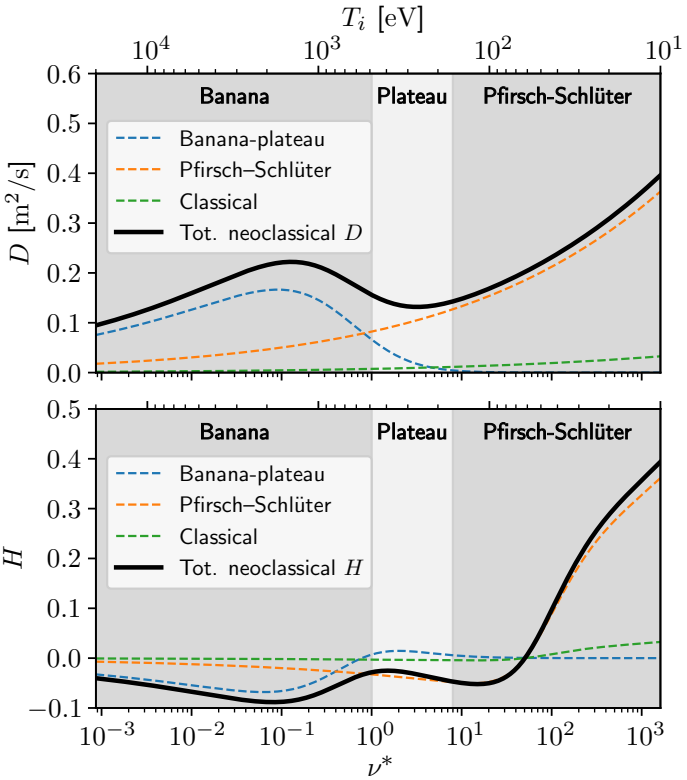

Figure 2.7: Calculated collisional transport coefficients (individual components as dashed colored lines and total sum as solid black line) for He^{2+} ions in trace limit in a background plasma with D^+ main ion species, as function of the normalized collisionality ν^*. A magnetic field $B_t = 2.5$ T, a safety factor $q = 2.5$, an inverse aspect ratio $\varepsilon = 0.25$ and an electron density $n_e = 10^{20}$ m^{-3} are assumed. The calculation was performed with the FACIT program [58].

Typically, for light impurities, in the inner core the banana-plateau terms are dominant, while transport towards the edge is mostly in the Pfirsch-Schlüter regime. Figure 2.7 shows the calculated neoclassical transport coefficients (D and H) for the case of trace amounts of He^{2+} ions in a background plasma with D^+ main ion species, as function of the normalized collisionality ν^*.

2.1.3 Anomalous transport processes

Although the neoclassical theory predicts transport coefficients much larger than the classical ones, neoclassical coefficients are still not sufficiently large to explain the experimentally observed radial particle transport in tokamak plasmas. This "anomaly" cannot be addressed by means of collisions between particles, therefore such a dominant component is usually called *anomalous transport* [59].
This can be attributed to *turbulence phenomena* driven by microinstabilities. Such non-linear processes lead to the formation of coherent structures in the plasma. The collective propagation of these structures, caused by the long-range nature the electrostatic interactions, typically results in a strongly enhanced particle transport in radial direction.

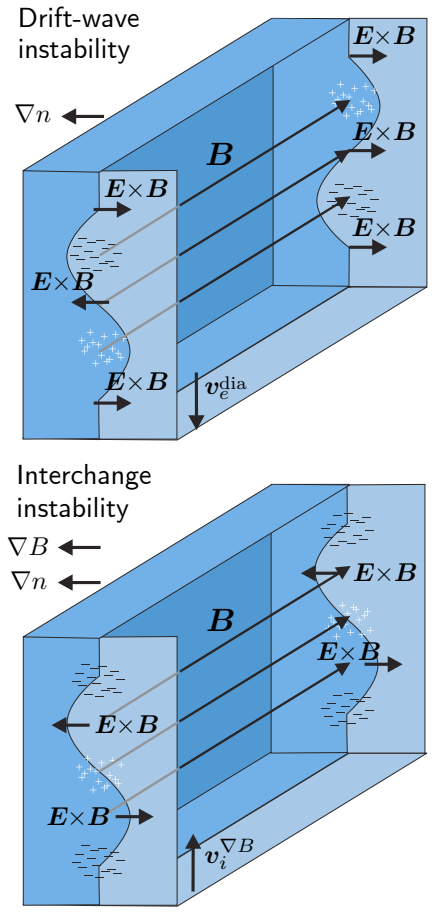

Figure 2.8: Microscopic phenomena leading to the drift-wave instability (top) and to the interchange instability (bottom). Adapted from [5].

In a magnetized plasma we find different sources of microinstabilities, due to interactions and fluctuations of different fields (density, temperature, electric potential and magnetic field), which can be described by different time and length scales. Two fundamental instabilities relevant for plasma turbulence are the *drift-wave instability* (top panel in Fig. 2.8) and the *interchange instability* (bottom panel in Fig. 2.8) [60].
Drift waves, occurring in arbitrary magnetic fields, are initiated by a three-dimensional perturbation of the pressure equilibrium which is elongated parallel to the field direction. The faster response of the electrons to the parallel pressure gradient creates positive charges in the region of positive density perturbation, and vice versa. Hence, a perturbation of the electric charges which is in phase with the original density perturbation. The consequent electric field creates an $\boldsymbol{E}\times\boldsymbol{B}$ drift which advects the background density, resulting in a net radial transport of particles in case of phase delay between density perturbation and electric potential perturbation, and a propagation of the perturbation in the electron diamagnetic direction.
The interchange instability takes place instead only in regions of bad magnetic field curvature, i.e. at the low field side of a toroidal equilibrium, and is initiated by a two-dimensional density perturbation which is constant along the field lines. Here the curvature drift moves the ions from a region of high density upwards towards a region of low density, while electrons are moved from a region of low density downwards towards a region of high density. In this way, an excess of positive charges is created at the border between low and high density where the density gradient is downwards-directed. On the other hand, an excess of negative charges is created at the border between low and high density where the density gradient is upwards-directed. The result is a perturbation of the electric charges which is out of phase by $\pi/2$ w.r.t. the density fluctuation. The net effect is an amplification of the original density perturbation and a strong radial transport.
Several different modes associated with the above mentioned instabilities are seen as responsible for the observed level of impurity transport in tokamak plasmas [53]. These are, for example, *ion temperature gradient (ITG) modes* [61], caused by the faster drift of hot ions w.r.t. that of cold

ions, and *trapped electron modes (TEM)* [62], caused by the accumulation of electric charges at the low-field side of the torus because of the toroidal precession of the banana electrons.

2.2 Plasma edge phenomena

Once impurity ions have crossed the separatrix driven by radial core transport, their transport in the SOL is dominated by the strong plasma flow parallel to the magnetic field lines directed towards the divertor. Several phenomena arise which determine the strength and direction of such flow, hence defining how efficiently impurities are transported towards the divertor region, from which they can be pumped. Additionally, the interaction of the impurity ions with the target surfaces, and the behavior of the subsequently recycled impurity atoms, must be accounted for a full description of the plasma edge phenomena.

2.2.1 Scrape-off layer force balance model

The transport of impurity ions in the SOL parallel to the magnetic field can be described in terms of the equation of motion for the impurity ions within a background plasma with given density and temperature. At a first approximation, interactions of impurity ions with each other and their influence on the plasma background may be neglected. This is reasonable because of the relatively low concentrations of impurities, i.e. assuming that $n_{\mathrm{imp}} Z_{\mathrm{imp}}^2 \ll n_e$.
The presented treatment is based on [16]. Several forces act on impurity ions moving along the field lines in the SOL. Some of them are directed towards the targets, i.e. flush the impurity ions towards the divertor, while others are directed upstream, i.e. drive them towards the midplane. Parallel ion transport in the SOL can be treated as purely collisional. Therefore, the motion of impurity ions in the SOL can be described through a *parallel force balance* applying the Braginskii equations [63], in particular the momentum balance equation. According to this, the motion of the impurities along a curvilinear coordinate s (which follows a magnetic field line), with ion density n_{imp} and parallel ion flow velocity $v_{\parallel,\mathrm{imp}}$, in a given background plasma with main ion density n_{main} and parallel main ion flow velocity $v_{\parallel,\mathrm{main}}$, is described by [16]

$$n_{\mathrm{imp}} m_{\mathrm{imp}} \left(\frac{\partial v_{\parallel,\mathrm{imp}}}{\partial t} + \frac{1}{2} \frac{\partial}{\partial s} v_{\parallel,\mathrm{imp}}^2 \right) = -\frac{\partial}{\partial s}(n_{\mathrm{imp}} T_{\mathrm{imp}}) + n_{\mathrm{imp}} m_{\mathrm{imp}} \frac{v_{\parallel,\mathrm{main}} - v_{\parallel,\mathrm{imp}}}{\tau_{\mathrm{coll}}} + n_{\mathrm{imp}} Z_{\mathrm{imp}} e E + C_{\mathrm{th},e} n_{\mathrm{imp}} \frac{\partial T_e}{\partial s} + C_{\mathrm{th,imp}} n_{\mathrm{imp}} \frac{\partial T_i}{\partial s} \,. \tag{2.25}$$

The left-hand side of Eq. (2.25) expresses the acceleration exerted on the impurity ions due to the forces present on the right-hand side. It is assumed here that the impurity ions in the SOL are in thermal equilibrium with the main ions (i.e. they have the same temperature), and diamagnetic and $\boldsymbol{E} \times \boldsymbol{B}$ drift terms and forces arising due to viscosity are neglected.
The individual forces which act on the impurity ions, according to the order in which they appear in the right-hand side term of the Eq. (2.25), are:

- The *impurity pressure gradient force*, arising from a difference of static pressure of the impurity ion species (i.e. $p_{\mathrm{imp}} = n_{\mathrm{imp}} T_{\mathrm{imp}}$) along the direction of the field line.
- The *friction force* exerted on the impurity ions due to collisions with the main ions, arising because of the difference in their parallel flow velocities. The time τ_{coll} is the average time between two collisions, and is defined as the reciprocal of the collision frequency for momentum transfer (Eq. (2.19)) between main ions and impurity ions. In general, the background plasma flow is directed towards the targets, so that the friction force also acts towards the targets. This term expresses then the contribution of the background

plasma flow, which is assumed to be more intense than the impurity flow, in "dragging" the impurity ions in the same direction.

- The *electrostatic force* caused by the parallel electric field due to the pre-sheath potential drop in the SOL. Applying Ohm's law, the strength of this force is approximately given by the electron pressure and temperature gradients, i.e. [16]

$$n_e e E \approx -\frac{\partial(n_e T_e)}{\partial s} - 0.71\, n_e \frac{\partial T_e}{\partial s} \ . \tag{2.26}$$

  Since the temperature decreases while travelling towards the targets, this force is directed towards the targets.

- The *thermal forces* for the electron and ion temperatures, respectively, which are due to the parallel temperature variation in the SOL. These are caused by the temperature dependence of the collisional momentum transfer. Less momentum is indeed transferred at higher temperatures. Therefore, the background electrons and ions which collide with impurity ions coming from the "cold" side of a flux tube exert a larger force than those colliding them from the "hot" side. The resulting net force will push the impurities up to the temperature gradient, i.e. towards upstream where temperatures are higher than in the divertor region, effectively acting against friction and electrostatic forces. The coefficients are given by [16]

$$C_{\mathrm{th},e} \approx 0.71 Z_{\mathrm{imp}}^2 \ , \tag{2.27}$$

$$C_{\mathrm{th,imp}} \approx \frac{3[\mu + 5\sqrt{2} Z_{\mathrm{imp}}^2 (1.1\mu^{5/2} - 0.35\mu^{3/2}) - 1]}{2.6 - 2\mu + 5.4\mu^2} \ , \tag{2.28}$$

  in which μ is

$$\mu \equiv \frac{m_{\mathrm{imp}}}{m_{\mathrm{imp}} + m_{\mathrm{main}}} \ . \tag{2.29}$$

The friction force and the ion thermal force are often the dominating terms of Eq. (2.25) for usual SOL temperatures of the order of tens of eV. Therefore, an effective motion of the impurity ions towards the divertor can be achieved provided that the friction force is larger than the ion thermal force.
In the divertor region, when approaching the targets, where there is a strong increase in the background plasma flow because of particle recycling, a strong friction force arises which drives the impurities towards the targets. On the other hand, the strongest temperature gradients occurring in this region give rise to strong upwards-directed thermal forces as well. Therefore, the force balance is greatly sensitive to the divertor plasma conditions, rather than to the upstream ones.
Different criteria have been deduced in terms of the SOL plasma parameters to conveniently estimate when the friction force prevails over the ion thermal force (thus the impurity flow is directed towards the divertor). For example, it can be shown that this is attained when

$$|M_{\mathrm{main}}| > \frac{\lambda_{\mathrm{main}}}{\lambda_T} \tag{2.30}$$

with M_{main} the Mach number of the main ion parallel plasma flow, λ_{main} the mean free path for collisions between main plasma ions and λ_T the characteristic length for temperature variation along the parallel coordinate s [64].
Although such parallel force balance (Eq. (2.25)) qualitatively accounts for the key mechanisms governing parallel impurity transport in the SOL, a realistic treatment may be achieved only through 2D edge transport codes. For example, the friction term of Eq. (2.25) may be heavily affected by the presence of *flow reversal* of the main ion flux, which is an intrinsically 2D phenomenon, resulting in an impurity ion flow which is mostly directed towards upstream until a certain parallel distance from the divertor targets.

2.2.2 Recycling behavior of impurities

When the impurity ion flux in the SOL reaches the surfaces of the divertor targets, multiple plasma-material interactions occur. After such interactions, impurity particles may be released again towards the plasma in form of neutral atoms, and re-ionized after travelling a distance corresponding to their ionization mean free path. These processes together constitute the *particle recycling*. A more exhaustive description of such processes may be found in [65].

Plasma-material interactions

The type of occurring plasma-material interactions strongly depends on the *incidence angle* and on the *impact energy* of the ion projectiles onto the materials. The impurity ion acceleration across the sheath tends to make these move almost unidirectionally and monoenergetically to the surface. The resulting impact energy depends on the electron and ion temperatures at the plasma-material interface and on the mean charge state $\overline{Z}_{\mathrm{imp}}$ through the formula [16]

$$E_{0,\mathrm{imp}} = 3T_e\overline{Z}_{\mathrm{imp}} + 2T_i \ . \tag{2.31}$$

The contribution $2T_i$ comes from the original kinetic energy of the ion projectiles. The contribution $3T_e\overline{Z}_{\mathrm{imp}}$ comes from the additional acceleration of the ions due to the sheath potential.
Energetic impurity ions which strike a solid surface penetrate it, and undergo elastic collisions with the lattice atoms, which alter their trajectories. If, during the collision cascade, the trajectory of an impinging projectile gets to be directed outside the surface before transferring its entire energy to the lattice, this will be promptly released in form of a fast neutral (since during the collision cascade the ions capture electrons from the lattice). This process is known as *reflection* (or backscattering). The reflection probability is given by the *particle reflection coefficient* $R_{N,\mathrm{imp}}$, defined in such a way that, if the impinging impurity flux onto the surface is $\Gamma_{\mathrm{imp,wall}}$, the reflected flux is

$$\Gamma_{\mathrm{imp,refl}} = R_{N,\mathrm{imp}} \cdot \Gamma_{\mathrm{imp,wall}} \ . \tag{2.32}$$

The mean energy of the reflected impurity atoms can be specified as

$$\langle E_{\mathrm{imp,refl}} \rangle = E_{0,\mathrm{imp}} \cdot \frac{R_{E,\mathrm{imp}}}{R_{N,\mathrm{imp}}} \ , \tag{2.33}$$

with $R_{E,\mathrm{imp}}$ the *energy reflection coefficient*. An empirical relation which expresses the reflection coefficients as function of the projectile impact energy is given by the Eckstein fit formula [66]

$$R_{(N/E),\mathrm{imp}} = \frac{a_1\varepsilon^{a_2}}{1 + a_3\varepsilon^{a_4}} \ , \tag{2.34}$$

with a_1, a_2, a_3, a_4 as fit coefficients, and $\varepsilon \equiv E_0/E_{\mathrm{TF}}$ the reduced energy. Here, E_{TF} is the Thomas-Fermi energy, which depends on projectile and surface material. Figure 2.9 shows the reflection coefficients and the relative fitting curves for He ions impinging on tungsten.
Alternatively, if a projectile loses its entire energy before being backscattered, it thermalizes and becomes *implanted* into the lattice, e.g. in vacancies caused by displacement damage or by trapping through chemical bonding. In this way, a certain concentration of implanted impurity atoms will build up in the material surface, until a saturation level is reached. The maximum amount of impurity atoms which may be implanted into a given material depends on the material itself, and on the energy of the impinging impurity ions (which determines in turn the mean penetration depth into the lattice). If the material is close to saturation, the implantation of an impurity projectile implies the consequent displacement and *thermal release* of a previously implanted impurity atom.
Other mechanisms exist which lead to the release of implanted impurity atoms from a material surface. Thermally-driven diffusion of impurity atoms within the lattice, as a result of heating

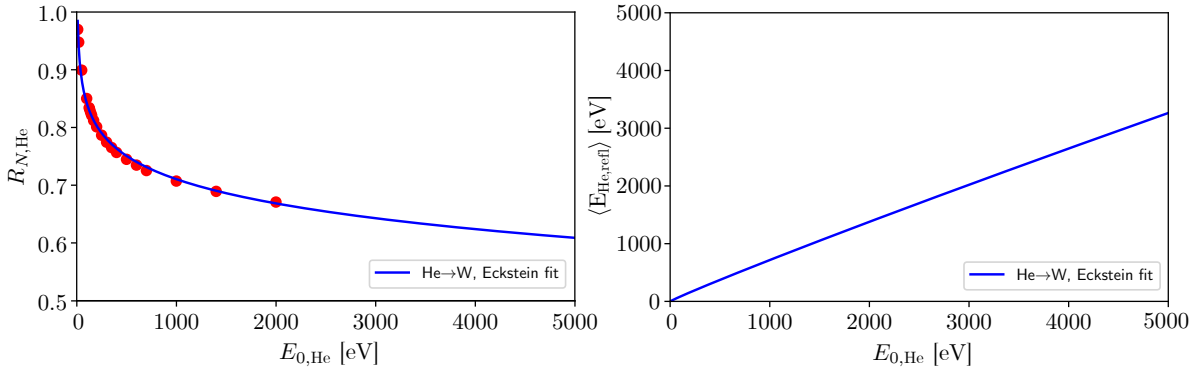

Figure 2.9: Calculated values of the reflection coefficient (left) and the mean reflected energy (right), as functions of the projectile impact energy and assuming an impact angle of 65° (which is reasonable for light impurities at magnetic fields typical of tokamaks [67]), as well as the fitting curves, for the case of He ions impinging on tungsten. The calculation was performed with the TRIM.SP program [68, 69].

the material, results into spontaneous *outgassing*. Alternatively, when the material is bombarded by other energetic ions, the collision cascade causes energy transfer from the projectiles to the implanted atoms. If the transferred energy is higher than their binding energy in the lattice, they are ejected from the material as fast particles. This may occur either via direct impact or via energy transfer from the surrounding lattice. This process is known as *physical sputtering*. The amount of ejected atoms is proportional to the impurity atom concentration implanted within the material lattice $f_{\mathrm{imp}} \equiv N_{\mathrm{imp}}/(N_{\mathrm{bulk}} + N_{\mathrm{imp}})$ and to the nuclear stopping power $S_n = [0.5 \cdot \ln(1 + 1.2288 \cdot \varepsilon)]/[\varepsilon + 0.1728 \cdot \sqrt{\varepsilon} + 0.008 \cdot \varepsilon^{0.1504}]$. This allows to calculate the sputtered impurity flux, from the projectile species s with impinging flux $\Gamma_{s,\mathrm{wall}}$, through a normalized *sputtering yield* $Y_{s\to\mathrm{imp}}/f_{\mathrm{imp}}$ as

$$\Gamma^{s}_{\mathrm{imp,sput}} = \frac{Y_{s\to\mathrm{imp}}}{f_{\mathrm{imp}}} \cdot f_{\mathrm{imp}} \cdot \Gamma_{s,\mathrm{wall}} \ . \tag{2.35}$$

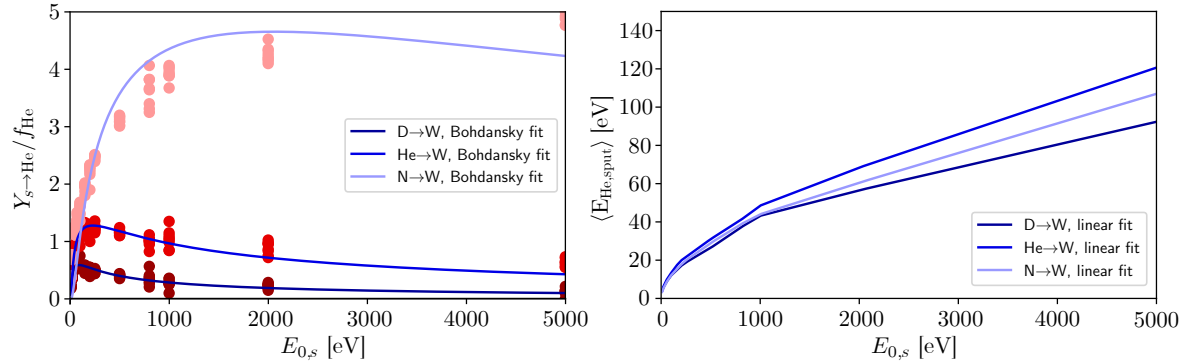

Figure 2.10: Calculated values of the normalized sputtering yields (left) and the mean sputtered energies (right) as functions of the projectile impact energy, assuming an impact angle of 65°, as well as the fitting curves, for the case of He atoms implanted in tungsten eroded by different ion projectiles (D, He, N). For the calculation, He atoms are assumed to be uniformly implanted and with no surface binding energy to the bulk lattice W atoms. The calculation was performed with the TRIM.SP program [68, 69].

An empirical relation which expresses the normalized sputtering yield as function of the above described parameters is given by the Bohdansky fit formula [66]

$$\frac{Y_{s\to\mathrm{imp}}}{f_{\mathrm{imp}}} = Q \cdot S_n \cdot \left[1 - \left(\frac{E_{\mathrm{th}}}{E_{0,s}}\right)^{2/3}\right] \cdot \left(1 - \frac{E_{\mathrm{th}}}{E_{0,s}}\right)^{2} \ , \tag{2.36}$$

where Q, E_{th} are fit coefficients (with E_{th} having the physical meaning of a threshold energy). Figure 2.10 shows the sputtering yields, the mean sputtered energies, and the corresponding fitting curves, for He atoms implanted in tungsten eroded by different ion projectile species.

Neutral-plasma interactions

Once impurities are re-emitted from the divertor targets in form of neutral atoms, either via reflection, thermal release or sputtering, they can interact with the energetic ions and electrons constituting the background plasma in multiple different ways.
At high plasma temperatures, for most of the recycled neutral atoms the first interaction with the plasma is an *ionization*, which occurs through electron-impact collision. In this case, impurity atoms undergo a ballistic motion from the recycling location until they are ionized. At low plasma temperatures, of the order of few eV, *CX collisions* between plasma ions and recycled impurity atoms also play a role. In case of non-resonant CX collisions (i.e. with the main plasma ions), the effect on the impurity species is the same as ionization after one single collision. Therefore, this contribution may be summed up to the electron-impact ionization, assuming $n_{\text{main}} \approx n_e$. In case of resonant CX collisions (i.e. with the impurity ions), one impurity atom remains because of the charge transfer. Therefore, if these dominate over ionization, many collisions occur before the neutral atoms are effectively ionized, and their motion in the plasma is not ballistic anymore. Figure 2.11 shows on the left the calculated rate coefficients for the above mentioned processes for the case of He atoms in a background plasma with D^+ main ion species, and on the right the resulting reaction rates, assuming $n_{He^{2+}} = 0.1\, n_e$. At temperatures higher than about $4 - 5$ eV, recycled He atoms ballistically travel before being ionized at the first interaction with the plasma, while at lower temperatures they will likely collide many times with He ions before being ionized.

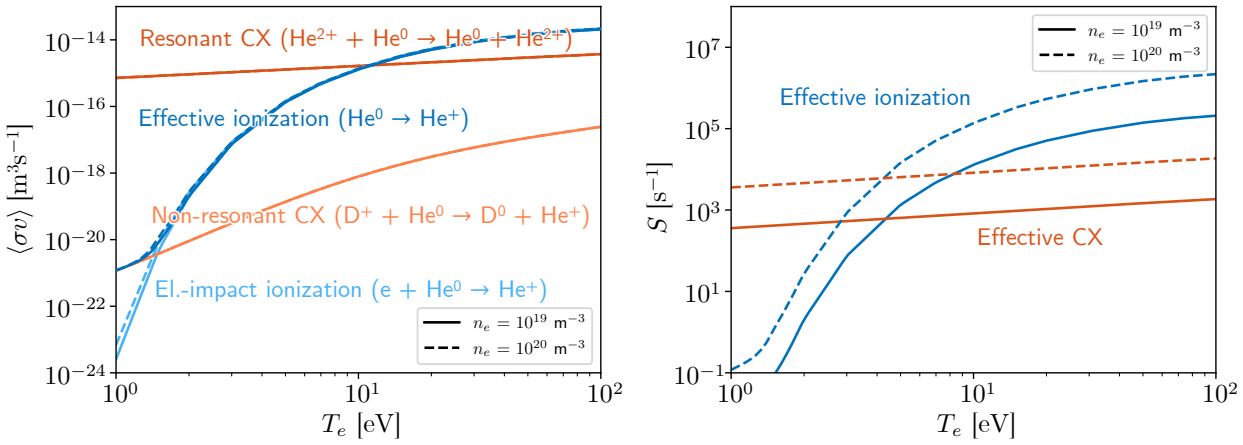

Figure 2.11: Left: rate coefficients for electron-impact ionization, resonant and non-resonant CX collision for He atoms in a background plasma with D^+ main ion species. Only the resonant CX collisions with He^{2+} ions are considered for simplicity, i.e. those with He^+ ions is neglected. Right: resulting effective ionization and CX reaction rates, assuming $n_{He^{2+}} = 0.1\, n_e$ and $n_{D^+} \approx n_e$. HYDHEL data [70].

How far the recycled impurity atoms can penetrate into the plasma can be quantified estimating the *mean free paths* for the above mentioned processes. The presented treatment is based on [71].
If the path of recycled impurity atoms is purely ballistic until their first ionization event, the mean free path may be estimated as

$$\lambda = \frac{\overline{v}_{\text{imp},0}}{n_e \langle \sigma v \rangle_{\text{imp}}^{\text{ion,eff}}} \,, \tag{2.37}$$

where $\overline{v}_{\text{imp},0} = \sqrt{T_{\text{wall}}/m_{\text{imp}}}$ is the average velocity of the impurity atoms, according to the temperature T_{wall} of the surface from which they are released, and $\langle \sigma v \rangle_{\text{imp}}^{\text{ion,eff}}$ is the total ionization rate coefficient (sum of electron-impact ionization and non-resonant CX contributions).
If, however, resonant CX collisions are dominant over ionizations (i.e. the reaction rate of

the former is much larger, namely $n_e\langle\sigma v\rangle_{\text{imp}}^{\text{ion,eff}} \ll n_{\text{imp}}\langle\sigma v\rangle_{\text{imp}}^{\text{CX}}$), an "effective" mean free path travelled before an ionization event may be estimated, following simple diffusion considerations, as

$$\lambda_{\text{eff}} = \frac{\overline{v}_{\text{imp,th}}}{\sqrt{n_e\langle\sigma v\rangle_{\text{imp}}^{\text{ion,eff}} \cdot \left(n_e\langle\sigma v\rangle_{\text{imp}}^{\text{ion,eff}} + n_{\text{imp}}\langle\sigma v\rangle_{\text{imp}}^{\text{CX}}\right)}} \,. \tag{2.38}$$

Here, we use $\overline{v}_{\text{imp,th}} = \sqrt{T_i/m_{\text{imp}}}$ as we assume that impurity atoms are thermalized with the plasma after the many CX collisions.

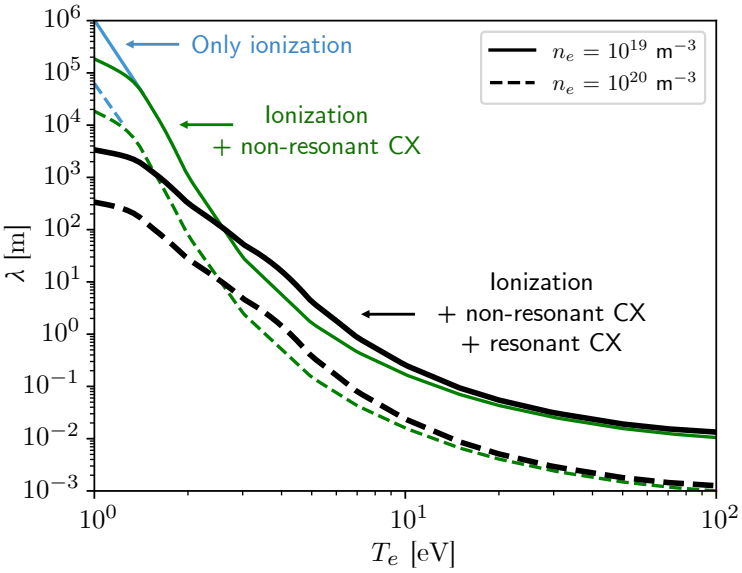

Figure 2.12: Mean free path for recycled He atoms in a deuterium plasma, with and without the effect of CX collisions, assuming $n_{\text{He}^{2+}} = 0.1\,n_e$ and $n_{\text{D}^+} \approx n_e$ and taking 0.1 eV as the average velocity of He atoms, calculated using the data in Fig. 2.11.

Figure 2.12 shows the calculated mean free paths for He atoms emitted in a background plasma with D^+ main ion species, assuming $n_{\text{He}^{2+}} = 0.1\,n_e$, when considering or neglecting the CX collisions.
At high temperatures (> 10 eV) the impact of CX collisions is negligible. At temperatures between 3 eV and 10 eV, resonant CX collisions become more frequent, and few impurity atoms gain energy with the thermalization with the plasma: in this way the few bounces will make impurity atoms travel, on average, slightly further deep into the plasma. At temperatures below 3 eV, resonant CX collisions become dominant, but the energy gained by the impurity atoms with the thermalization is lower: in this way the effect of multiple bounces is to decrease the mean free path. How much resonant CX collisions impact the mean free path strongly depends on the He ion density. In the case displayed in Fig. 2.12 (i.e. with $n_{\text{He}^{2+}} = 0.1\,n_e$), their impact on the mean free path at temperatures above 3 eV is small but visible, while at temperatures below 3 eV is major. In case of even lower He ion densities (e.g. $n_{\text{He}^{2+}} < 0.01\,n_e$), they have no impact on the mean free path at temperatures above 3 eV, while at temperatures below 3 eV their impact is smaller but still visible.
Non-resonant CX collisions do not cause the He atoms to bounce and be scattered, but remove one electron from these. The result is the same as for an electron-impact ionization. The resulting effective ionization decreases therefore further the mean free path. However, the range in which this is non negligible is limited to very low temperatures (< 1.5 eV). The impact of non-resonant CX collision does not depend on the He ion density, but on the main ion density.

2.2.3 Mechanisms of divertor retention of recycled impurities

The impurity ion flow in the SOL and the impurity recycling behavior define how efficiently impurities which reach the divertor region are there *retained*. Good retention implies higher impurity concentrations in the divertor w.r.t. a given core concentration, i.e. better pumping, if the pumps are located behind the divertor target plates. The following description is inspired by [41, 72].
One first factor affecting divertor retention of recycled impurities is the extent of the impurity ion *flow reversal* region in the near SOL in proximity of the divertor target plates. A flow reversal

region in the near SOL is caused by the larger parallel temperature gradient in this region. This can make the thermal forces dominate over the friction force, causing the impurity flux to be driven in the upstream direction rather than towards the targets. In high recycling divertor regimes, the main ion flux amplification created in the main ion recycling layer in front of the targets causes a strong friction which usually prevails over the thermal forces. Therefore, in the near SOL we usually find a region in front of the divertor target plates with downstream-directed impurity ion flux whose extent is determined by the extension of the main ion recycling layer, and "above" it a region with upstream-directed impurity ion flux. The boundary between these two regions will constitute the *stagnation surface* of the impurity ion flow (see Fig. 2.13). For a given background main ion flux, the location of the impurity stagnation surface mainly depends on the plasma temperature.

Divertor retention of recycled impurities also depends on the location where the recycled impurity atoms are re-ionized, i.e. the distance of the impurity *ionization front* from the target plates. This is regulated by the variation of the effective ionization mean free path of recycled impurity atoms in the divertor plasma which, as shown in the previous Section, is also mostly a function of the divertor plasma temperature. Reducing the divertor plasma temperatures the ionization front moves higher upstream, because of the increase of the mean free path.

Impurity retention in the divertor depends therefore on the interplay between the impurity stagnation surface and the location of the impurity ionization front. The most favourable situation is the one in which recycled impurity atoms are ionized close to the target plates, i.e. in the region of strongest friction below the impurity ion stagnation surface (case (1) in Fig. 2.13). In this case they are promptly returned to the target plates, increasing the probability to be scattered towards the pumps. If, instead, the ionization front of the impurities is above the stagnation surface, where thermal forces dominate, the re-ionized impurities will be transported back towards the periphery of the core plasma (case (2) in Fig. 2.13), causing an effective impurity leakage from the divertor and a reduced retention. The situation is even worse if the divertor plasma is so cold that the recycled impurity atoms can penetrate directly to the confined region (case (3) in Fig. 2.13), strongly increasing the time before they can return to the divertor and reducing the divertor retention even more. Decreasing the divertor temperature, both stagnation surface and location of the ionization front move upstream. Therefore, these two mechanisms are generally in competition. Two-dimensional plasma edge modelling is necessary to assess the behavior of divertor retention of recycled impurities under different divertor plasma conditions [42, 43, 44].

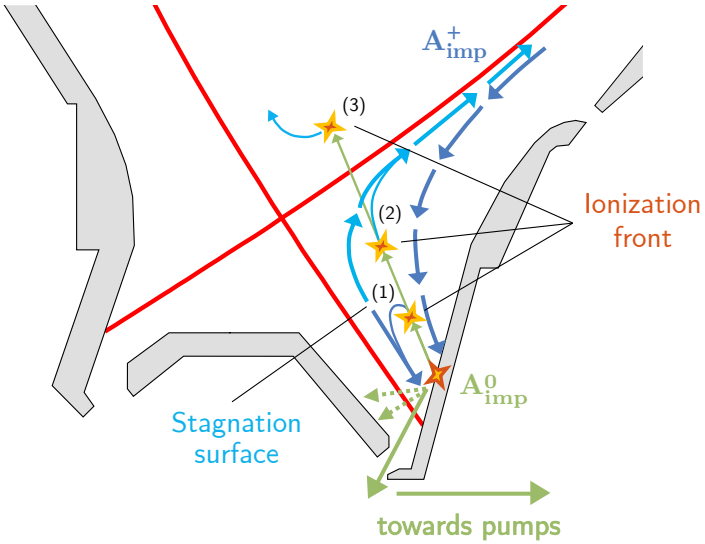

Figure 2.13: Impurity recycling mechanisms governing divertor retention. (1): if recycled impurity atoms are mostly ionized below the stagnation surface of the impurity ion flow, they promptly return to the divertor. (2): if recycled impurity atoms are mostly ionized above the stagnation surface, they leak towards upstream following the impurity ion flow reversal. (3): in case of very cold divertor plasma, recycled impurity atoms fully penetrate it and re-enter the confined region.

2.3 Neutral gas transport and pumping

After being recycled at the divertor targets, impurity atoms travel along straight lines, unless they suffer collisions. If they are not re-ionized along their trajectory, they are ballistically reflected by the surrounding material surfaces, re-entering the plasma or being scattered towards the sub-divertor region. From there, they can travel towards the pumps.
In this Section, a brief overview of the behavior of rarefied gases is given, as well as some general definitions which will be used in the next Chapters.

2.3.1 Fundamental gas properties

Transport of impurity atoms in the neutral exhaust gas towards the pumping duct can be described from the point of view of the *kinetic theory of gases* [2, 73]. The gas is modelled as an ensemble of many particles separated by distances which are large in comparison with their own dimensions. They are assumed to behave as perfect elastic spheres and are in constant state of random motion. The motion is related to the temperature of the gas. The particles are assumed to exert no force on each other, except when they collide.
The behavior of neutral particles obeys the *Boltzmann equation*

$$\frac{\partial f}{\partial t} + \boldsymbol{v} \cdot \frac{\partial f}{\partial \boldsymbol{x}} = C \tag{2.39}$$

for the neutral's distribution function f. C is a collision term. The information about the dependence of the particle velocities on the temperature is contained in the distribution function. The assumed form of the velocity distribution is a maxwellian, i.e.

$$f(\boldsymbol{v}) = n \left(\frac{m}{2\pi T} \right)^{3/2} \exp \left[-\frac{m v^2}{2T} \right] \ , \tag{2.40}$$

where m is the particle mass, n the particle density and T the temperature.
From Eq. (2.40) several quantitative relationships can be derived. Among these, the *average velocity*

$$\overline{v} = \sqrt{\frac{8T}{\pi m}} \tag{2.41}$$

and the *mean energy*

$$\overline{E} = \frac{3}{2} T \tag{2.42}$$

of the particles. Another important quantity which describes the bulk behavior of a gas is the *kinetic pressure*

$$p = nT \ , \tag{2.43}$$

which quantifies the force it exerts on the walls of its container as a result of atomic impacts.
The rate of gas particles striking a unit surface per unit time is also a quantity of practical interest. This can be calculated as

$$\Gamma = \frac{1}{4} n \overline{v} = \frac{1}{4} n \sqrt{\frac{8T}{\pi m}} \ . \tag{2.44}$$

The average distance which a particle moves before colliding with another one (collisions with chamber walls being excluded) is called *mean free path*. Calling d_0 the diameter of the gas particles, considered as hard spheres (which is usually of the order of 10^{-10} m), this can be estimated as

$$\lambda = \frac{1}{\sqrt{2} \pi n d_0^2} \ . \tag{2.45}$$

2.3.2 Gas flow regimes

The global behavior of the gas is mainly determined by the surface and geometrical properties of its container, and by gas pressure and flow rate. The nature of the gas flow is determined by the value of a dimensionless parameter, namely the *Knudsen number*. This is defined as

$$\mathrm{Kn} \equiv \frac{\lambda}{D} \ , \tag{2.46}$$

i.e. as the ratio between the particle's mean free path λ and a characteristic geometrical dimension D of the container.
At high pressures, so that $\mathrm{Kn} \lesssim 10^{-1}$, the mean free path of the particles is very short compared with the dimensions of the container, so that the flow of the gas is limited by the viscosity of the gas itself. Under this condition we have a *viscous flow*. Pressures large enough to have a fully viscous flow are usually not encountered in fusion applications.
As the pressure is reduced, so that $10^{-1} \lesssim \mathrm{Kn} \lesssim 10$, the mean free path of the particles becomes similar to the dimensions of the container, and the flow is governed by a combination of the gas viscosity and collisions with the walls. These conditions give rise to a type of flow known as *transition flow*. At these pressures the particles move in random directions, and are affected by collisions both with the walls and with each other. The flow rates are proportional to the difference in pressures across the component and the reciprocal of the square root of the molecular weight of the gas.
As the pressure continues to decrease, so that $\mathrm{Kn} \gtrsim 10$, the mean free path becomes longer than the dimensions of the container, the particles migrate through the system freely and totally independently of each other, and the flow depends only on the collisions with the walls. The flow under these conditions is referred to as *molecular flow*.
Transition and molecular flow are to be expected in fusion applications. Whether the effect of the collision of gas particles with each other can be neglected or plays a role in determining the gas flow depends on the neutral pressure achieved in a particular plasma experiment.

2.3.3 Flow conductance and gas throughput

Simple relations may be used to relate the gas flow to the device characteristics (e.g. geometry and installed pumping capability), using engineering parameters. The gas flow rate Q is usually expressed in pressure-volume units, as

$$Q = \frac{d(pV)}{dt} \ . \tag{2.47}$$

If the volumetric flow rate is caused by the presence of a pump, then

$$Q \equiv pS \ , \tag{2.48}$$

where S, defined as the *pumping speed* of the pump at the pressure p, in m^3/s, defines the capability of the pump to evacuate the container from gas particles. The pumping speed varies according to pressure, gas flow regime and type of gas.
The effective pumping speed which is applied to a gas volume can, however, be affected by the resistance to the gas flow offered by a duct connecting the volume to the pumping surface. This resistance causes a pressure drop along the duct. This is quantified by the concept of *flow conductance* L, which is defined as

$$L \equiv \frac{Q}{p_u - p_d} \ , \tag{2.49}$$

where p_u is the upstream pressure and p_d is the downstream pressure. So, L is a measure of the throughput of gas for a given pressure drop along or across a duct, and is therefore also expressed in m^3/s. The flow conductance also varies with pressure, gas flow regime and nature of the gas.

2.4 Global exhaust parameters

The experimental and numerical investigation performed in the framework of this thesis concerns the behavior of helium, with focus on the physics mechanisms determining its exhaust from tokamak plasmas. In the course of the investigation, several parameters, based on the physics described in this Chapter, were employed to quantify the various mechanisms defining helium exhaust.
Generally, helium exhaust is maximized at high neutral He pressures in the subdivertor region, from which the gas can be permanently pumped. Normalizing this to the He ion density in the confined plasma we achieve a device-independent parameter which describes how efficiently helium (1) is transported in the SOL towards the divertor, and (2) is retained in the subdivertor region rather than leaking again towards the main plasma. This defines the so-called *helium compression*

$$C_{\mathrm{He}} \equiv \frac{n_{\mathrm{He}^0}^{\mathrm{div}}}{\overline{n}_{\mathrm{He}^{2+}}^{\mathrm{plasma}}} \ . \tag{2.50}$$

With $n_{\mathrm{He}^0}^{\mathrm{div}}$ we refer to the neutral He atom density measured in the subdivertor region, where the pumps are located. Instead, with $\overline{n}_{\mathrm{He}^{2+}}^{\mathrm{plasma}}$ we refer to an average He ion density in the confined plasma. We obtain this by radially integrating the measured He ion density profile at the plasma midplane along the normalized poloidal flux coordinate ρ_p[1] as

$$\overline{n}_{\mathrm{He}^{2+}}^{\mathrm{plasma}} \equiv \frac{\int_{\mathrm{core}} n_{\mathrm{He}^{2+}}(\boldsymbol{x})\,\mathrm{d}^3\boldsymbol{x}}{\int_{\mathrm{core}} \mathrm{d}^3\boldsymbol{x}} \approx \frac{\int_0^1 n_{\mathrm{He}^{2+}}(\rho_p)\,\rho_p\,\mathrm{d}\rho_p}{\int_0^1 \rho_p\,\mathrm{d}\rho_p} \approx 2\int_0^1 n_{\mathrm{He}^{2+}}(\rho_p)\,\rho_p\,\mathrm{d}\rho_p \ . \tag{2.51}$$

The knowledge of He compression is, however, still not sufficient for a reactor-relevant extrapolation. Whereas helium should be removed from a burning plasma as efficiently as possible, at the same time fuel pumping should be minimized. This is motivated by the requirement to reduce as much as possible the pumping of tritium, mostly for the optimization of its fuel cycle [74]. This would be achieved with a large He compression but a poor compression for the main fuel, namely maximizing the parameter

$$\eta_{\mathrm{He}} \equiv \frac{C_{\mathrm{He}}}{C_{\mathrm{fuel}}} = \frac{n_{\mathrm{He}^0}^{\mathrm{div}}\,\overline{n}_{\mathrm{fuel}^+}^{\mathrm{plasma}}}{2\,\overline{n}_{\mathrm{He}^{2+}}^{\mathrm{plasma}}\,n_{\mathrm{fuel}}^{\mathrm{div}}} \ , \tag{2.52}$$

usually referred to as *helium enrichment*. The factor of 2 derives from the fact that hydrogenic fuel species (deuterium and tritium) mainly exist in form of biatomic molecules in the neutral gas. According to the most recent ITER design studies, η_{He} must not be lower than 0.1−0.2 [9].

[1] Given the magnetic flux function ψ, found as equilibrium solution of the Grad-Shafranov equation for a given magnetic configuration, the normalized poloidal flux coordinate ρ_p is defined as $\rho_p \equiv \sqrt{\frac{\psi-\psi_{\mathrm{axis}}}{\psi_{\mathrm{LCFS}}-\psi_{\mathrm{axis}}}}$.

Chapter 3

Experimental setup and results

The foundations for a prediction of helium exhaust in future fusion devices may be laid through experimental investigations of He-seeded discharges, i.e. featuring external He injection, in current devices. Such a predictive knowledge is the indispensable basis for the development of plasma scenarios compatible with the requirements of helium exhaust, and for an optimum design of plasma-facing components (PFCs) and pumping systems in future reactors.
Experiments have been already performed in several diverted tokamaks, including JET [75, 76, 77], ASDEX Upgrade [78, 79, 80], JT-60U [81] and DIII-D [82, 83, 84]. These studies have generally shown that helium exhaust is not constrained by core transport phenomena, but limited by edge phenomena, namely divertor retention and external pumping. These investigations were supported by interpretative numerical modelling [85, 86] and taken into account in the design of the ITER divertor [87, 88, 89, 90].
The experimental investigation performed for this thesis is presented in this Chapter. It consists in the revision of experiments already performed in the past at the ASDEX Upgrade tokamak. Shape and inclination of the divertor target plates have been modified [91] and the full-carbon wall has been replaced by a full-tungsten wall [92, 93]. This is a fusion-relevant material [38], and is expected to be the plasma-facing material for the divertor wall in ITER [94] and, likely, also for the main wall. One of the differences of tungsten w.r.t. carbon is a higher storage capability for He atoms [37]. Consequent wall retention effects are then expected to have a greater impact on helium exhaust than the one observed in the full-carbon ASDEX Upgrade.
In the Section 3.1 some basic features of the ASDEX Upgrade tokamak will be introduced. After that, in the Section 3.2 several diagnostics systems installed on ASDEX Upgrade, with which relevant measurements were taken, will be introduced. In the Section 3.3 emphasis on the diagnostics capable of performing He partial pressure measurements will be given. Finally, in the Section 3.4, the performed experiments, focused on measuring and characterizing the helium exhaust dynamics as well as some global exhaust parameters in different plasma scenarios, will be presented. The contents of the Section 3.4 have been already partially published in [95].

3.1 The ASDEX Upgrade tokamak

ASDEX Upgrade (AUG) (Figure 3.1) is a tokamak experiment located at the Max-Planck-Institut für Plasmaphysik in Garching (Germany), whose operation started in 1990 [96]. It is the follow-up experiment of the former tokamak *ASDEX (Axial Symmetric Divertor EXperiment)*, which was in operation from 1980 till 1990. AUG features a divertor and a device geometry which were optimized to meet the requirements of a future fusion reactor. Overall, it is one of the leading fusion experiments worldwide. The AUG operation is especially focused on the physics of the plasma edge, particle and power exhaust and plasma-material interaction issues under conditions similar to those expected in a future reactor [97, 98].

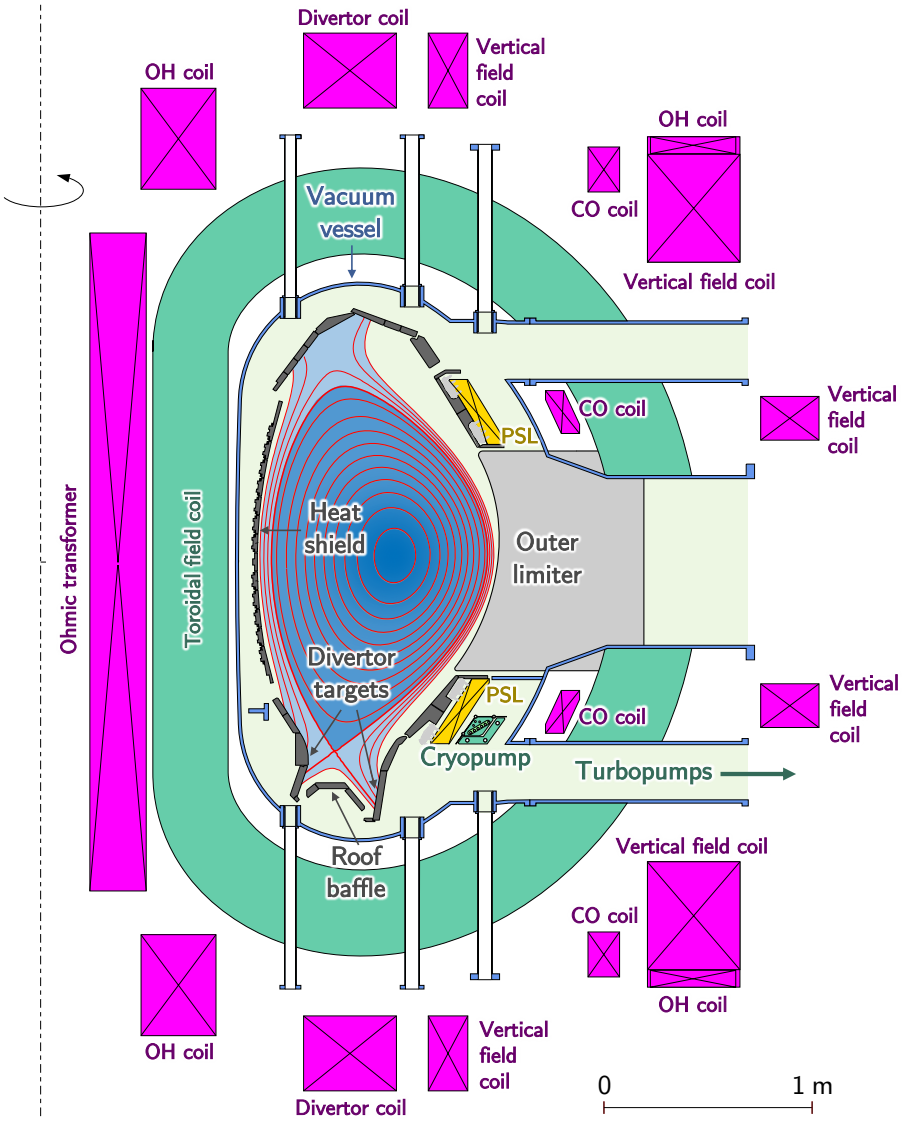

Figure 3.1: Poloidal cross section of ASDEX Upgrade showing a typical magnetic configuration, PFCs, vacuum vessel, pumping systems and coil systems.

AUG is characterized by a major plasma radius of $R = 1.65$ m, a minor horizontal plasma radius of $a = 0.5$ m and a minor vertical plasma radius of $b = 0.8$ m, which makes it a midsize device. A variety of of plasma configurations can be generated with elongation of up to $b/a = 1.6$ and an average triangularity up to $\langle\delta\rangle = 0.5$. The plasma volume is around 13 m^3. The toroidal magnetic field may be ramped up to 3.9 T, with a plasma current of up to 1.6 MA [99]. The fueling gas is provided either via *gas valves* [100], spread between main chamber and divertor, or via *cryogenic pellet injection* [99].

The *vacuum vessel* is made of austenitic steel, in a rigid self-supporting structure composed of several poloidal wedge-shaped sectors, in which the fuel gas is injected [99]. Within the vessel various PFCs are installed: the *heat shield*, located at the inner side of the torus, which is the surface covering the inner column; a *limiter*, located at the outer side of the torus, which reduce the interaction between the plasma and the vessel wall; and the *divertor targets*, located at the bottom of the vessel. All the PFCs are currently either tungsten-coated or made of bulk tungsten, making AUG a full-tungsten experiment [92, 93].

The toroidal field is generated by means of 16 D-shaped *toroidal field coils* [99]. The poloidal field is generated and controlled by means of a system of *poloidal field coils*, which create multipole components for shaping the plasma, defining the radial and vertical plasma positions and the

nulls for diverting it. In particular, there are: five Ohmic heating coils drive the plasma current; six vertical field coils inducing a vertical field used to keep the plasma in an elliptical shape; six correction coils allowing to control continuously the plasma position; two divertor coils creating the diverted magnetic configuration [99]. All these are located outside the vessel. The coil systems limit the discharge duration to a maximum of 10 s.
Particle control is ensured by 11 *turbomolecular pumps*, providing a total pumping speed of about 7 m^3/s [101], and a toroidally symmetrical *cryopump*, providing a total pumping speed of about 120 m^3/s [102, 101]. The ducts leading to the turbomolecular pumps are located at the bottom ports, while the cryopump is installed directly within the vessel, behind the outer divertor target.
Several external heating systems can provide to AUG plasmas up to several tens of MW of auxiliary power. Available systems are:

- *Electron cyclotron resonance heating (ECRH)*: it consists in injecting microwaves into the plasma at appropriate resonance frequencies (multiple of the electron gyrofrequency) through a system of gyrotrons. The waves are absorbed, heating then the electrons which thermalize with the colder ones via collisions. The employed frequencies are 140 GHz or 105 GHz, and it provides up to 8 MW of power [103].
- *Ion cyclotron resonance heating (ICRH)*: it consists in injecting radiofrequency waves into the plasma at appropriate resonance frequencies (multiple of the ion gyrofrequency) through a system of antennas. The employed frequencies are in the range of $30 - 40$ MHz, and it provides up to 6 MW of power [104].
- *Neutral beam injection (NBI)*: it consists in the injection of highly energetic beams of neutral atoms in the plasma. As these are not deflected by the magnetic field, they are able to penetrate into it, where they are ionized and then thermalized via collisions. AUG is equipped with two NBI sources providing beam energies up to 100 keV, using acceleration voltages up to 60 kV and 93 kV, respectively, each providing up to 10 MW of power [105].

3.2 Diagnostics systems

The scientific program of AUG benefits of more than 100 different raw data diagnostics measuring different core and edge plasma parameters, while further information is stored in about 200 high-level diagnostics after post-processing of the raw data [96].
In this Section, the most important diagnostics systems used to measure the experimental data on which this thesis relies will be introduced. Figure 3.2 shows the relative locations and/or lines of sight in a poloidal cross section of the device.

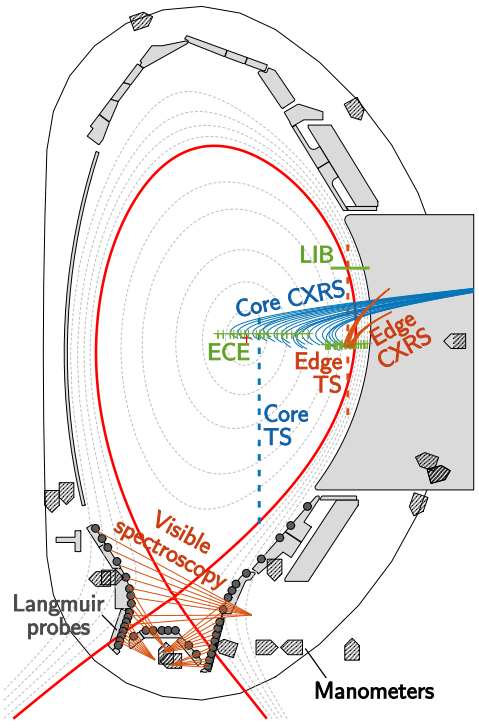

Figure 3.2: Poloidal cross section of AUG showing location and lines of sight of several relevant diagnostics.

3.2.1 Magnetic equilibrium reconstruction

Equilibrium-relevant magnetic measurements are made through a set of *Mirnov coils* poloidally distributed around the plasma vessel, which measure the radial and poloidal components of the magnetic flux [106]. These measurements are used as boundary conditions in the code CLISTE [107],

which reconstructs the full magnetic equilibrium in the plasma region numerically solving the Grad-Shafranov equation [108]. Within this framework, an uncertainty of 5−10 mm is expected in the determination of the radial position of the separatrix. This is a source of large uncertainty in the determination of the separatrix plasma conditions at the midplane, which should be carefully taken into account in transport analyses for the plasma edge.

3.2.2 Thomson scattering

The *Thomson scattering (TS)* system is suitable for the measurement of radial profiles of both electron density and temperature with good spatial resolution both in the core and in the plasma edge [109].
The physical principle on which it is based is the spectral broadening of a laser light injected in the plasma after the interaction with the hot electrons due to the Doppler effect. The broadening characteristics depend on the velocity distribution of the electrons with which the radiation interacts [110]. Therefore, by measuring the broadening it is possible to estimate the electron temperature. The intensity of the scattered radiation is also proportional to the total number of electrons contained in the scattering volume. Therefore, measuring the intensity allows to estimate the electron density as well. The radial plasma profiles are then determined by a least-square fit to the achieved scattering signals [111].
In order to obtain radial plasma profiles, the laser beams pass the flux surfaces in vertical direction. In this way plasma parameters vary slowly along the laser chord, and a spatial resolution of the order of mm is achieved. At AUG, lasers follows two lines of sight, one for the core and one for the edge (shown respectively in blue and in red in Fig. 3.2). Nd:YAG (neodymium-doped yttrium aluminium garnet) and CO_2 lasers with 1064 nm wavelength are employed for this. They have a pulse energy of about 1 J and pulse durations about 10 ns, at 80 Hz repetition rate for the core laser and 120 Hz for the edge laser [111]. The scattered light is observed with filtered photodiodes placed outside the torus.

3.2.3 Lithium beam emission spectroscopy

Lithium beam emission spectroscopy (LIB) is a major system for the plasma edge, measuring density profiles and fluctuations at the outer midplane from the limiter shadow up to the pedestal top, with a spatial and temporal resolution of around 5 mm and 1 ms respectively. [112].
Neutral lithium atoms are injected into the plasma. Collisions with the hot plasma electrons excite the lithium atoms to higher electronic states. The characteristic line intensity following their radiative de-excitation is measured along the path of the lithium beam within the plasma. In this way, the electron density profile is reconstructed via a forward model of the beam-plasma interaction, which calculates attenuation and composition of the injected neutral beam along its way through the plasma [113]. For this aim, advanced algorithms based on probabilistic approaches have been developed [114].
The lithium beam injection system at AUG produces a beam which is horizontally injected at the outer side of the torus, about 0.326 m above its equatorial midplane (shown in green in Fig. 3.2), employing atoms in the energy range of $35 - 60$ keV [115].

3.2.4 Electron cyclotron emission radiometry

The *electron cyclotron emission radiometry (ECE)* system is used to determine the electron temperature both in the core and in the plasma edge. It is based on the measurement of the radiation emitted at the second harmonic of the electron cyclotron frequency. Since such frequency depends on the magnetic field, whose radial profile is known, the analysis of the

measured spectra allows the reconstruction of the radial electron temperature profile. As long as the plasma can be considered optically thick, the intensity of the radiation is indeed related to the electron temperature [116]. The measurement points of the ECE radiometer are shown in green in Fig. 3.2.

3.2.5 Charge-exchange recombination spectroscopy

Charge-exchange recombination spectroscopy (CXRS) is an active spectroscopy technique used to measure the light emission from hydrogen-like impurity ions [117]. Such ions are generated through CX collisions of the corresponding fully stripped impurity ions with the energetic neutral atoms injected into the plasma by the NBI systems. As the impurity ions are left in an excited state after the reaction, prompt light emission follows and the emission spectrum can be analyzed. The measured radiance of the impurity emission line is proportional to the impurity density. Additionally, the Doppler broadening of the spectral lines is proportional to the impurity ion temperature, and the shift to the bulk rotation of the plasma. The application of such technique to measure impurity densities, ion temperatures and plasma rotation needs an accurate wavelength calibration of the spectrometers and accounting for the passive emission components. The assumption of thermalized impurity ions is generally employed.
Several spectrometers are installed at AUG, which observe the plasma midplane both in the core and in the edge, with lines of sight intercepting the path of the injected beam neutrals [118, 119]. The lines of sight of the toroidal core system are shown in blue in Fig. 3.2, while the lines of sight of the toroidal edge system are shown in red. The first one has a radial resolution of 2.5 cm and an integration time of 5−20 ms. The second one has a radial resolution of 0.5 cm and an integration time of 2 ms [120].
Absolute impurity density profiles are calculated using the CHarge-exchange Impurity Concentration Analysis code (CHICA) [121]. The automated analysis of the impurity line emission profile is based on ADAS data [54], assuming poloidal symmetry and based on the experimental electron density and temperature profiles. The density profile of the injected beam neutrals is calculated with a dedicated attenuation code. Spectral lines from a wide set of impurities (He, Li, B, C, N, O and Ne) are routinely analyzed. For the case of helium, the spectral analysis is made more complicate by the presence of an additional emission contribution to the spectra, namely the He plume emission [122]. This is due to the radiation following electron-impact excitation of the CX-generated He^+ ions taking place before they are re-ionized to He^{2+}, which has the same wavelength as the active CX signal. At AUG, a sophisticated kinetic model for the He plume emission is used, which allows accurate measurements of the He^{2+} density [123], which is a key measurement for the investigation performed in this thesis.

3.2.6 Visible spectroscopy

The divertor region at AUG is observed by several *spectrometers* measuring visible light, with lines of sight which cover the entire divertor plasma (orange lines in Fig. 3.2). For this, CCD cameras with integration times of 2.45 ms are used. It is possible to observe a spectral range of either 15 nm or 150 nm, at 512 pixels per spectrum, in the visible range of 395−720 nm. Each spectrometer can observe up to 25 lines of sight. Applying an absolute calibration to the observed spectra, it is possible to fit the resolved peaks and to achieve an integrated line emission along the lines of sight, at any desired wavelength, in terms of emitted photons per unit of time. Multiple line intensities associated with radiation emission following atomic de-excitation and recombination from neutrals and ionized states of main plasma species and impurities can be resolved. Line-integrated electron densities can be also determined through Stark broadening analysis [124] or line ratio measurements [125].

The interpretation of the measured line intensities requires the application of a collisional radiative model [54]. Such a model describes the charge state distribution and the excited population densities in a plasma at given parameters (mainly electron density and temperature). From this model, photon emission coefficients (PEC) can be derived, which give the photon emission rates for specific excited state transitions (i.e. at given wavelengths) at given plasma parameters. These coefficients are collected in the ADAS ADF15 database [55].
After the knowledge of the functional dependence of the measured line intensities on electron density and temperature, a correlation between the line intensities and the density of the corresponding plasma species along the observed line of sight can be established.

3.2.7 Langmuir probes

A wide set of *Langmuir probes* is employed to measure the plasma parameters at the interface with material surfaces, especially the divertor targets. They consist of one or multiple electrodes protruding into the plasma, hence collecting a current. The current-voltage (I-V) characteristic of the sheath is measured and fitted by a theoretical I-V curve [110]. The measured ion saturation current is related to the particle flux at the probe surface. From the shape and the slope of the measured I-V curve it is also possible to deduce the electron density and temperature. Finally, after assuming a total sheath heat transmission coefficient, the total heat flux can be calculated as well [126].
At AUG several systems of Langmuir probes are installed. These are flush-mounted probes in the material surfaces [127, 128]. The impinging fluxes can so be sustained also in steady state avoiding any risks of erosion or melting. The data analysis is performed taking into account the effects of the grazing incidence of magnetic field lines onto the probe surface. Such probes cover the whole poloidal range of the divertor region (grey dots in Fig. 3.2), with a spatial resolution of 3.0 and 2.5 cm for the inner and outer target surfaces respectively. These are mostly triple probes with a data acquisition rate of 25 kHz.

3.2.8 Manometers

A set of *manometers* installed at several locations within the vacuum vessel provides neutral pressure measurements (shaded polygons in Fig. 3.2). Neutral particles entering the gauge chamber are ionized via electron impact, and the resulting ion current is measured [129, 130]. The ion current can be directly related to the neutral flux density of atoms and molecules entering the gauge chamber. Assuming the flux to be thermal and following a maxwellian velocity distribution, the measured neutral flux density can be converted to a neutral density. Furthermore, assuming the gas temperature, this can be also converted to a neutral pressure. The operating range of the AUG manometers goes up to about $10-15$ Pa.
The employed gauges are not spectroscopic, therefore no species discrimination can be performed. Since the ion current generated in the gauge chamber depends on the gas species, because of different sensitivities to electron-impact ionization, absolute neutral density/pressure measurements are reliable only when the gas is constituted by a single species. For this reason, the gauges at AUG are usually absolutely calibrated only against a deuterium gas.

3.3 Helium partial pressure measurements

A key measurement for this thesis is the He partial pressure in the exhaust gas. A knowledge of the He partial pressure in front of the pumping surfaces allows indeed to calculate the pumped He fluxes, which is a necessary ingredient of the performed analyses.

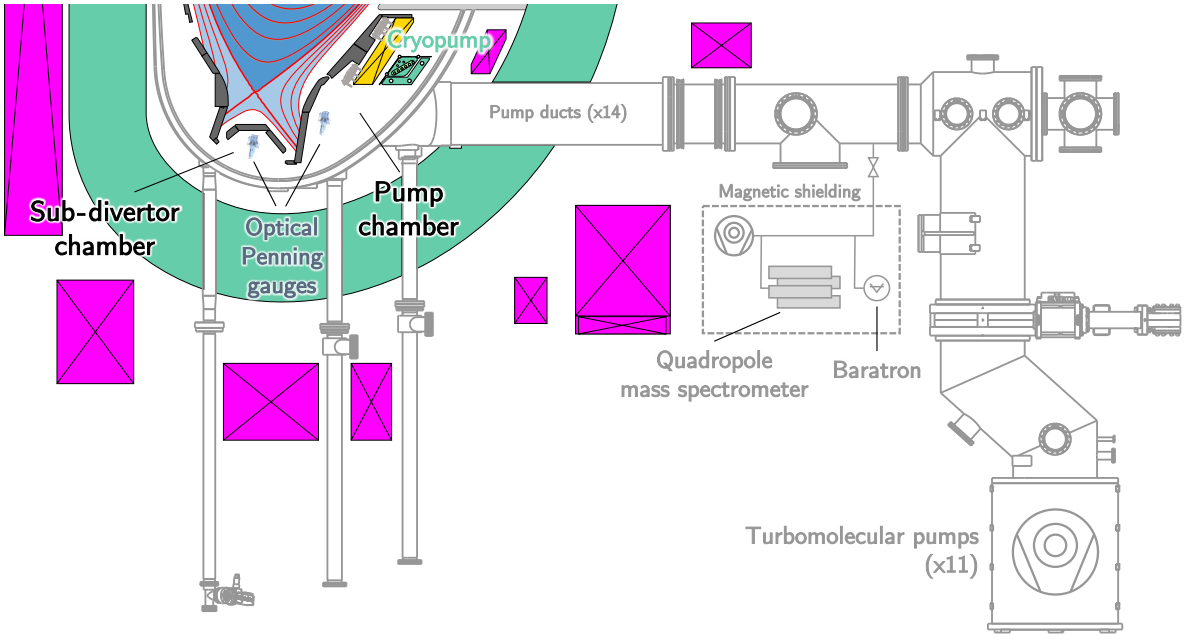

Figure 3.3: Poloidal cross section of subdivertor region and pump ducts at AUG, showing the locations of the pumps and several pressure-measuring instruments.

3.3.1 Residual gas analysis

Partial pressures of impurity species are routinely measured at AUG through residual gas analyzers [131], employing conventional *quadrupole mass spectrometers (QMS)*. Here the diagnosed neutral gas is ionized by means of electron impact, and mass separation of the generated ions is achieved via a quadrupole magnetic field. The output is a mass-resolved spectrum. This is, however, not trivially achievable for the case of helium in a deuterium environment, as conventional QMS struggle to resolve the small mass difference between He atoms (4.003 AMU) and D_2 molecules (4.028 AMU).
In this work, attempts were made using the commercial high-resolution quadrupole mass spectrometer EXTREL Max-50 [132], which is in principle capable to resolve up to 5000 data points per AMU. This was installed in a magnetically shielded box located along one of the 14 pump ducts, along the path of the exhaust gas flow towards the turbomolecular pumps (see Fig. 3.3). The total pressure at the same location was measured through the absolute capacitance manometer MKS 690 ("baratron").
Tests performed in conditions of controlled gas flow without plasma confirmed the capability of such an instrument to discriminate the He and D_2 mass peaks. The left plot in Fig. 3.4 shows the recorded spectra in scenarios of constant D_2 partial pressure and increasing He partial pressure. They were achieved by first injecting some amount of deuterium in the unpumped vessel, ensuring a constant D_2 partial pressure, and then injecting small amounts of helium in series. The increasing He partial pressure values were estimated by subtracting the known D_2 partial pressure from the increasing total pressure measured by the baratron, with the He concentration defined as $f_{He} \equiv p_{He}/(p_{D_2} + p_{He})$. All individual spectra shown in the left plot in Fig. 3.4 result from an average of all the individual measurements made over 10 s with a time resolution of 0.1 s, i.e. averaging out 100 individual measurements, to remove the statistical noise. As the shape of the D_2 peak is not affected by the relative amount of helium, the two signals can be ideally treated as independent quantities.
However, multiple issues arised when performing the same measurements during plasma discharges. The right plot in Fig. 3.4 shows several mass spetra recorded during the flat top phase

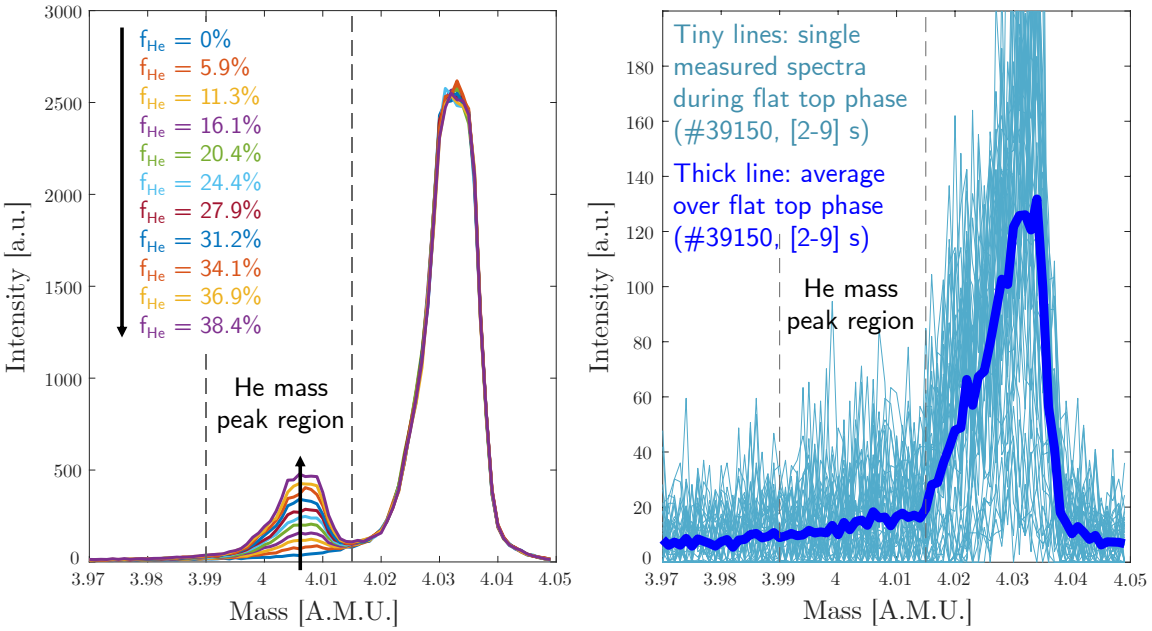

Figure 3.4: Left: mass spectra recorded by the high-resolution QMS at AUG for controlled gas flow without plasma, at different He concentrations in a deuterium environment. Right: mass spectra recorded during the flat top phase of the AUG discharge #39150, with constant deuterium pressure at the pump ducts of $5 \cdot 10^{-2}$ Pa.

of the discharge #39150 (described later in Section 3.4.3). Requesting a discharge-relevant time resolution (of the order of 0.1 s) makes the statistical noise of individual spectra very large. A shape distortion of the deuterium mass peak, w.r.t. a symmetrical shape observed without plasma, was observed. This was attributed to the presence of a residual field (of the order of mT) existing in the quadrupole chamber, induced by the current flowing in the poloidal field coils placed in the neighborhood of the instrument (see Fig. 3.3). It was concluded that the magnetically shielded boxes used at AUG were sufficient for the operation of conventional QMS during plasma operation, but not for the employed high resolution one, because of its larger sensitivity. Additionally, a constant background signal was also observed, which is likely caused by free electrons released in the multiplier chamber of the instrument during plasma operation. By comparing the intensity of such background with the ideal He mass peaks (left plot in Fig. 3.4), it is shown that this completely covers the expected He mass peak at any He concentrations relevant for the performed investigation (i.e. up to 20%).
Due to these multiple issues, it was concluded that such instrument was not capable to perform He partial pressure measurements at AUG, at least during plasma operations.

3.3.2 Optical Penning gauges

As an alternative to residual gas analysis, He partial pressure measurements were attempted by means of recently installed *optical Penning gauges* [133], similar to the one described in [134] and installed in the Wendelstein 7-X stellarator. Their operation consists in exciting the neutral gas in the probe head of the gauge, observing spectroscopically the generated Penning discharge and using the line intensities for partial pressure measurements. Whereas, in the past and in other devices, He partial pressures have been successfully measured by similar gauges, these were typically mounted at the outer periphery of the device [135, 136]. At AUG, instead, the gauges were mounted inside the vessel (see Fig. 3.3): one in the region below the roof baffle (which here and in the following we denote as *sub-divertor chamber*) and one behind the outer divertor target, in front of pumping surfaces (which here and in the following we denote as *pump chamber*). This allows response times of the measurement compatible with the characteristic

impurity residence times in the plasma and in the divertor region.
For a correct and predictable behavior, the probe head of such gauges must be aligned with the magnetic field lines. Applying a high voltage between anode and cathode, a Penning discharge is initiated, and an electron current is created. Following the electron-impact excitation of the neutral atoms and molecules present in the gauge chamber, the measured spectra can be fitted and the resulting line intensities analyzed. The emitted light is observed by a spectrometer similar to the ones employed for the visible plasma spectroscopy system (cf. Section 3.2.6). During typical AUG operation, a voltage of 2 kV or 3 kV is applied, and the generated current is of the order of several mA. The gauge operation was successful in a pressure range of up to a few Pa (typical of H-modes), but was difficult at pressures below about 10^{-2} Pa (typical of low density L-modes), mainly because the generated current was not sufficiently high.
The gauge behavior was characterized in technical shots without plasma but with magnetic field, in scenarios at constant D_2 pressure and increasing He partial pressure, similarly as it was done for the QMS. Figure 3.5 shows the line intensities measured in the shot #40717, featuring a magnetic field of 2.5 T, with the gauge voltage set at 3 kV. In this case, the D_α Balmer line at 656.2 nm and the HeI line for the 1s3d→1s2p singlet transition at 667.8 nm were observed.

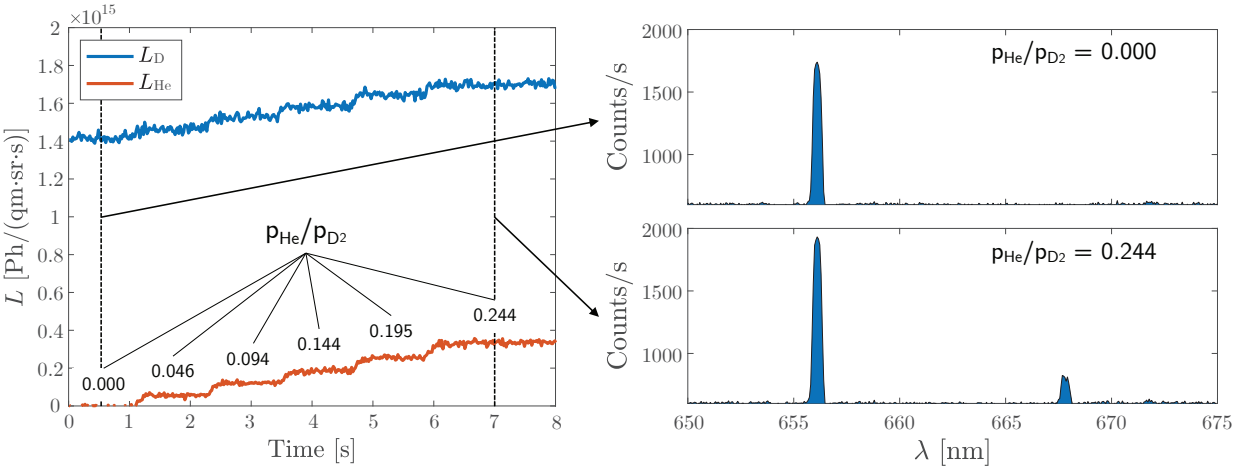

Figure 3.5: Left: spectroscopically observed line intensities from the Penning gauge in the pump chamber during the AUG technical shot #40717, with constant D_2 pressure in the pump chamber of $8 \cdot 10^{-2}$ Pa and increasing He partial pressure levels. Right: corresponding spectra for two different He partial pressure levels.

The two signals were found to be mutually dependent. The D line intensity increased with increasing He partial pressure, although the D_2 partial pressure was constant. Such behavior was also documented in [134]. This is explained by the larger number of electrons released in the gauge chamber with increasing total pressure, which excite a larger fraction of D_2 molecules, although these remain constant in number density. This makes a direct correlation between the measured line intensities with the corresponding partial pressures challenging. Since the increased amount of electrons with increasing total pressure affects in the same way the excitation of the populations of D_2 molecules and He atoms, a correlation between line intensity ratios and partial pressure ratios should be instead drafted.

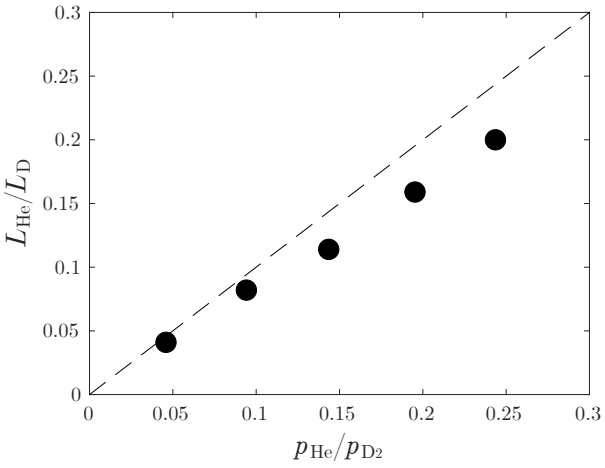

Figure 3.6: Measured correlation between line intensity ratios and partial pressure ratios of deuterium and helium during the AUG technical shot #40717.

Figure 3.6 shows indeed a nearly linear correlation between the two quantities.
Given this behavior, the strategy applied to interpret the Penning gauge measurements during the performed plasma discharges was the following. First, the measured line intensity ratios are converted to partial pressure ratios. Considering that the He concentration in the investigated discharges was typically less than 20 %, the correlation $p_{\mathrm{He}}/p_{\mathrm{D}_2} \simeq L_{\mathrm{He}}/L_{\mathrm{D}}$ was assumed. The D_2 partial pressure was estimated through the measurements of the manometers located in the same region of the vacuum vessel in phases of the discharge in which only D_2 is fueled (i.e. prior to the He gas injection). In this way, the combination of measurements of D_2 partial pressure and He/D_2 pressure ratios was sufficient to determine the resulting He partial pressure during and after the He gas injection. Such approach can be applied only in scenarios in which only the evolution of the He partial pressure is followed, while the background D_2 partial pressure may be assumed to remain constant. However, all the discharges presented in the Section 3.4 were designed in this way, so that such approach was acceptable.

3.4 Experimental results at the full-W ASDEX Upgrade

This Section documents the experiments performed at AUG aimed to investigate properties and dynamics of helium exhaust.
AUG does not operate with a D-T fuel mixture, but mostly with externally heated pure H or D plasmas. Therefore, the dynamic behavior of helium as an impurity was investigated after short external He gas injection phases performed during otherwise steady-state discharges. This was the strategy employed for the performed experiments.
All discharges documented here are lower single-null type-I ELMy H-modes with deuterium as main gas and with toroidal magnetic field $B_t = -2.5$ T, edge safety factor $q_{95} = 5.1-5.3$ and plasma current $I_p = 0.8$ MA. We applied about 2 MW of ECRH power (mainly to avoid W accumulation in the core) and 7.5−10 MW of NBI power. The goal of all discharges was to measure the time evolution of the He concentration both in the plasma and in the exhaust gas in different exhaust-relevant scenarios, namely at different levels of divertor pressure and divertor temperature.

3.4.1 Helium pumping efficiency

Historically, the vacuum systems at AUG have not been optimized for helium pumping. The cryopump installed in the pump chamber is not effective in removing He atoms, as they do not condense on the cryopanel surface [102]. In principle, adsorption of He atoms may be obtained by employing argon to form a frosted cryotrapping surface [47]. However, attempts of Ar-frost on the AUG cryopump were, so far, unsuccessful, mostly leading to a strong contamination of the plasma. The only active removal effect for helium is therefore given by the turbomolecular pumping system. This has an effective pumping speed (applied to the pump chamber) of 7 m^3/s measured for a D_2 gas [101]. As D_2 molecules and He atoms have a very similar mass, such pumping speed may be reasonably assumed to hold also for helium as the effect of a purely mechanical pump should be identical.

3.4.2 Subdivertor gas transport

As already mentioned, a distinction may be done between the region of the vacuum vessel which is directly filled by the recycled flux from the targets and the region which is exposed to the pumping surfaces. Because of the closed geometry of the subdivertor region at AUG and the physical obstacles encountered by the exhaust gas in its flow towards the pumps (e.g. support structures, cables and diagnostic gauges), a pressure drop is typically seen between

sub-divertor and pump chamber. Therefore, a knowledge of the He partial pressure in both regions is indispensable for a full interpretation of the experimental findings.
Unfortunately, technical difficulties prevented the exploitation of the Penning gauge installed in the sub-divertor chamber. The one installed in the pump chamber instead operated flawlessly. Therefore, for the analysis and the interpretation of the experiments, an a priori assumption of the expected pressure drop for the He gas between the two regions was needed.
In order to do this, the measurements from two different manometers installed in the sub-divertor chamber and in the pump chamber were used. Whereas these are calibrated against a D_2 gas, the measured pressure drop in discharges where the cryopump is switched off should be a reasonable approximation of the behavior of a He gas. A neutral gas conductance, applied to the same vessel geometry, would indeed scale only with the square root of the mass of the particles.

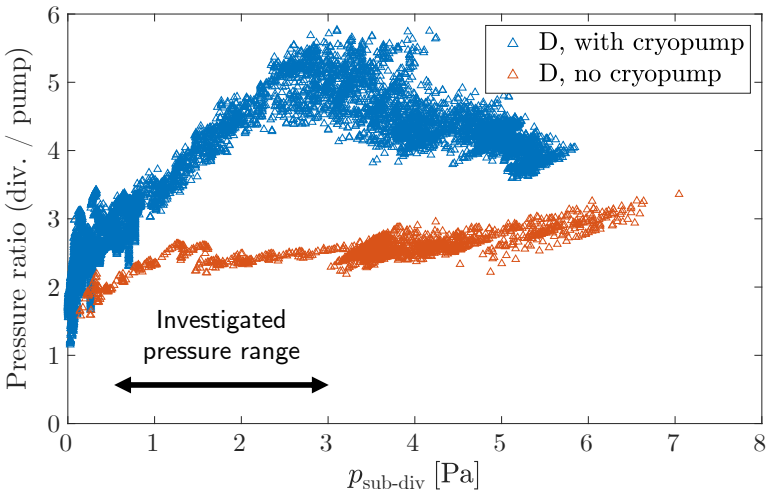

Figure 3.7: Database of pressure drops measured for a pure D_2 gas, during several AUG plasma discharges, between sub-divertor chamber (manometer 03) and pump chamber (manometer 12), with and without operating cryopump, as function of the pressure in the sub-divertor chamber. The ratio measured with cryopump switched off should approximate the behavior of a He gas.

Figure 3.7 shows the measured ratio between total pressures between sub-divertor chamber and pump chamber from a database of several AUG discharges with pure D_2 fueling, with and without operating cryopump, as function of the pressure in the sub-divertor chamber. The pressure dependence derives from a complex interplay between physical geometry and viscosity. However, it is generally seen that the pressure drop is smaller in cases with no cryopump operating. This is not surprising since, assuming the pressure in the sub-divertor chamber as fixed and dependent on the recycled flux, without cryopump the sink effect in the pump chamber would be much reduced.
Because D_2 molecules and He atoms are of similar mass, it may be safely assumed that the behavior of a pure D_2 gas in situation without cryopump would emulate that of a He gas. According to Fig. 3.7 and given the generally low measured He partial pressures (see next Sections), for all performed experiments a pressure drop of 2 was assumed for the neutral He gas between sub-divertor and pump chambers.

3.4.3 Experimental divertor pressure scan

A first series of experiments aimed to investigate the impact of *divertor neutral pressure* on the helium exhaust efficiency. A higher pumping efficiency is trivially expected with increasing pressure, because of a resulting larger throughput (cf. Section 2.3.3). Additionally, also divertor retention for impurities, which only depends on the divertor plasma characteristics and not on the pumping systems, is generally seen to scale with divertor pressure [137, 138].
We performed three H-mode discharges with constant feedback-controlled divertor neutral gas pressure, at otherwise constant parameters, including equilibrium and heating. Figure 3.8 shows the main time traces. The He CXRS measurements rely on the energetic neutrals from the NBI source Q3. The modulation scheme employed for the NBI beams was used to remove the passive emission signals and facilitate the evaluation of the CXRS spectra.

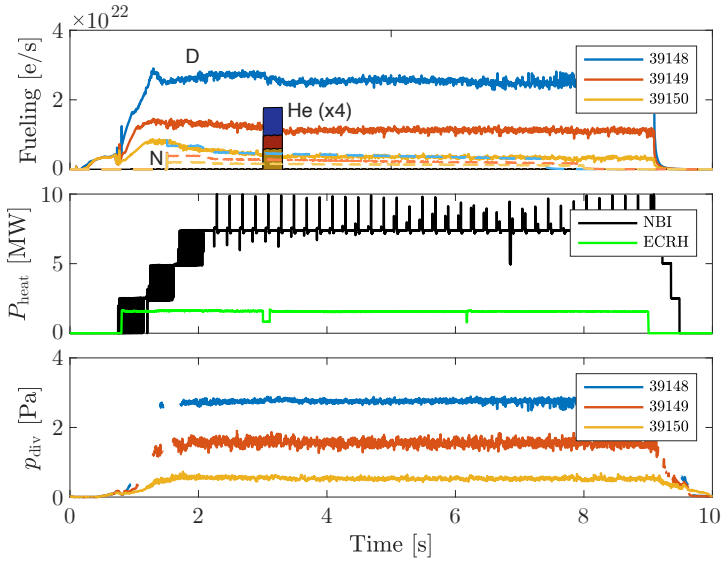

Figure 3.8: Time traces from the divertor pressure scan. From top to bottom: fueling (D as solid lines, N as dashed lines, He as filled areas, the last ones magnified 4 times w.r.t. the actual value), heating power (common for all the discharges), divertor pressure.

The different feedback-requested divertor pressure levels resulted in different D_2 fueling levels. In all discharges we applied a 300 ms long He puff performed from a midplane fueling valve. The He fueling rate was scaled with the expected D_2 gas puff in order to achieve a similar peak He concentration in the core (defined as $\overline{n}_{He^{2+}}/\overline{n}_e$) of roughly 20−25 %. Moderate N seeding was also employed for diagnostic purposes (T_i and v_{rot} measurements through CXRS). The divertor pressure traces shown in Fig. 3.8, in the range of 0.5−3 Pa, measured with a manometer, refer to the sub-divertor chamber, i.e. to the region directly coupled with recycling from the divertor targets. All discharges were with a high-recycling, moderately attached divertor.

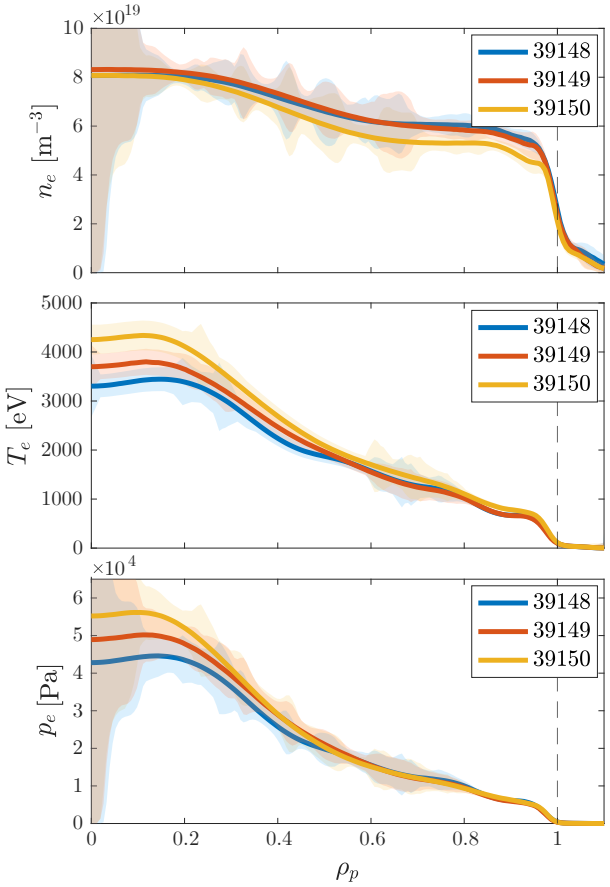

Figure 3.9: Kinetic profiles measured during the plasma flat top phase immediately before the external He puff (i.e. within the time window [2.5-3.0] s), achieved through integrated data analysis of the experimental data.

Figure 3.9 shows the kinetic profiles (namely electron density, temperature and pressure) measured prior to the external He puff. The profiles were obtained combining measurements of different diagnostics through integrated data analysis (IDA) [139, 140]. The application of ECRH produces a slightly peaked electron density profile which is similar in all discharges. The pressure profile in the edge transport barrier (ETB) is also seen to be very similar in all discharges. No strong sawtooth crashes were observed.

Helium transport in the confined plasma

Core transport, and the plasma parameters which determine it (e.g. collisionality) is known to not heavily impact the exhaust properties for light impurities [78]. Therefore we did not focus on the properties of core He transport, which was already documented in [141], and we made no attempts to vary the core collisionality. The absolute He ion density profiles measured by CXRS (Figure 3.10) are indeed similar in all discharges, being consistently slightly less peaked than the electron density profiles.

This is in agreement with the findings of [141], considering that the external heating in these discharges features a high NBI fraction, and indicates a turbulent radial transport of He ions in the inner core being mainly driven by ITG modes.
Measurements of the absolute He ion density in the edge were not available for the performed experiments. In discharges similar to the ones documented here, a pedestal peaking factor (i.e. ratio of absolute He ion density between pedestal top and separatrix) of about 4−6 was measured during inter-ELM phases [142]. This is in agreement with the inter-ELM transport for He ions in the ETB being purely neoclassical and mostly in the Pfirsch-Schlüter regime [35].

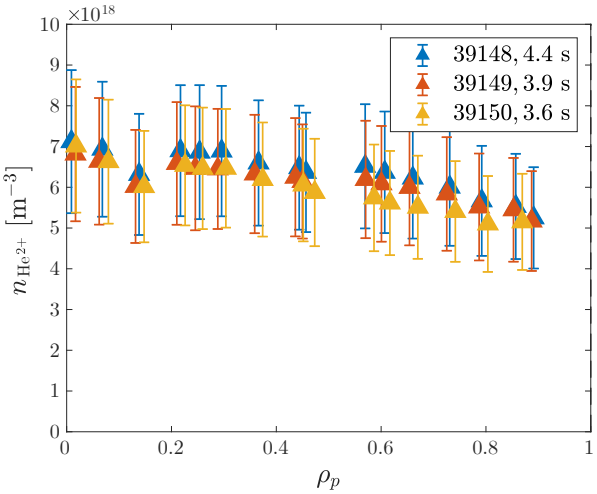

Figure 3.10: He^{2+} ion density profiles measured by the core CXRS system. Different times were selected for the various discharges to highlight the similarity of the radial gradients.

Dynamics of helium exhaust

Figure 3.11 shows the measured average He^{2+} ion density in the core plasma (Eq. (2.51)) and the neutral He atom density in front of the pumping surfaces for the three performed discharges (cf. Fig. 3.8). The entire duration of the shown diagnosed phase ([2.2,8.2] s) is within the plasma current flat-top, with constant background plasma parameters.

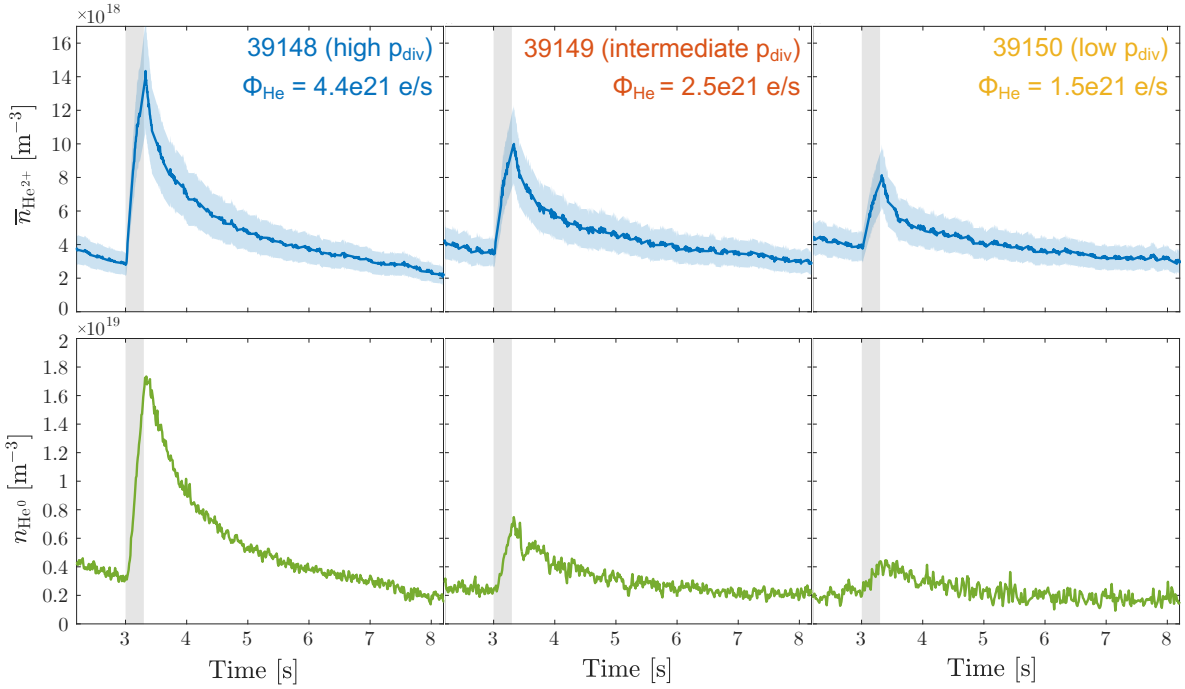

Figure 3.11: Time traces of the measured average He^{2+} ion density in the core plasma measured by CXRS (top) and neutral He atom density in front of the pumps measured by the Penning gauge (bottom) in the performed discharges at different divertor neutral pressures. Error bars of CXRS data are given as shaded areas. Uncertainties on the Penning gauge measurements could not be straightforwardly quantified, so they are not considered here. The time windows during which He is actively injected are highlighted by grey bands. The applied He fueling rates are also indicated.

At the beginning of the analyzed phase, before the active injection starts, a relevant amount of He ions is already present in the plasma. Without any external injection the only remaining possible

source is the release of He atoms previously implanted in the plasma-wetted surfaces of the tungsten PFCs. This behavior is qualitatively common for all impurities, but is quantitatively much more relevant for the case of helium. The reason is an efficient retention capability of He atoms in the surface layers of tungsten, which has been widely assessed experimentally [37, 39, 143, 144]. Implanted He atoms may be considered as permanently stuck into the tungsten lattice outside plasma operations, but can be released again during plasma exposure due to energetic-ion-bombardment driven erosion and thermally-driven effusion.
He atoms are mainly implanted in the wall surfaces during boronizations. These are He glow discharges, having a duration of several hours, which include an additional inlet of 10 % of B_2D_6. They are routinely performed during AUG operational campaigns, and their goal is to coat the wall surfaces with a layer of boron for optimal plasma conditions [145, 146]. Larger He concentrations in the plasma are indeed observed immediately after boronizations. The implantation source may also derive from previous He-seeded plasma discharges.
After the He injection phase, the relatively poor pumping performed by the turbomolecular pumps makes the He ion content in the plasma decay to its initial value only by the end of the entire discharge. For comparison, the concentration of other actively injected impurities at AUG (e.g. N, Ne and Ar, for which the cryopump is effective) after a short puff decays to their initial value in typically 0.5−1 s [138]. However, the He concentraation never falls to zero, but rather tends to become constant while reaching roughly its initial value. This indicates that, sufficiently far away from the active puff, the throughput is balanced by a constant source. Assuming a wall source remaining roughly constant while more He atoms are eroded implies that the dynamic wall inventory for He atoms must be comparatively larger than the plasma inventory.
These observations, which at this point are merely speculative, motivate the need to quantitatively assess the impact of wall retention on the exhaust dynamics, against that of active pumping. This led to the development of the interpretative model in the Chapter 4.
Figure 3.12 shows that the dynamics of the He decay in the plasma and in the exhaust gas is the same. Namely, when normalized, the signals from CXRS, divertor spectroscopy and Penning gauges overlap within the CXRS error bars, and no temporal delays are visible. This means that equilibration between plasma and neutral gas (seen as separate He particle reservoirs) is faster than any other characteristic time describing the exhaust (i.e. related to core confinement, divertor retention and pumping, cf. Section 4.3.5). Additionally, the fact that the ratios of these signals is constant during the entire discharge indicates that the exhaust is also independent from the He concentration itself. The amount of He ions present in the system does not affect the background plasma (at least in terms of core/SOL helium transport). This means that helium may be considered as a trace impurity even at concentrations of $\overline{n}_{He^{2+}}/\overline{n}_e$ up to 20−25 %.

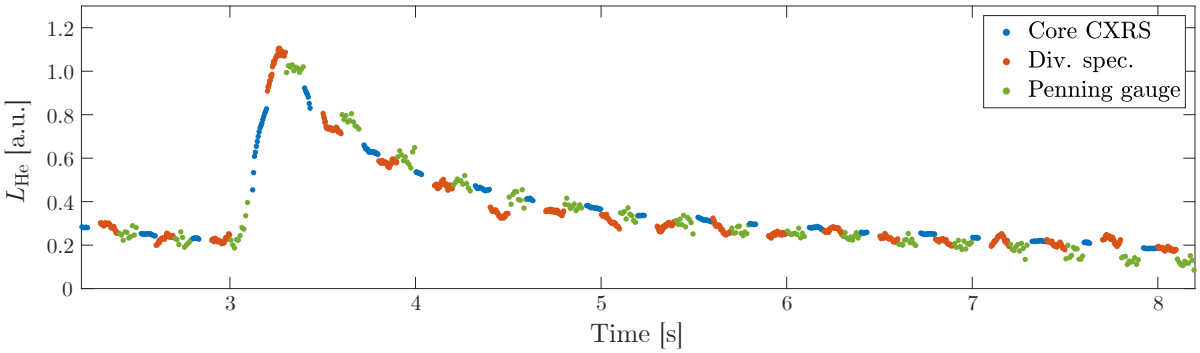

Figure 3.12: Normalized He signals from core CXRS, divertor visible spectroscopy and Penning gauge for the discharge #39149. Whereas the CXRS and Penning gauge signals are absolute He densities, the divertor spectroscopy signals refers to the line-integrated HeI line intensity from the 1s4p→1s2s singlet transition at 396.5 nm along the ROV-8 line of sight (looking through the outer divertor plasma). Since the background plasma (and hence also the PECs) is constant, such signal is also directly proportional to the neutral He atom density in the divertor plasma.

Compression and enrichment measurements

Since the exhaust dynamics is independent from the He concentration, the resulting He compression is constant during the discharges, and also independent from the He content itself. The measured compression values are shown at the top of Fig. 3.13. For the numerator of Eq. (2.50) we refer to the neutral He atom density in the sub-divertor chamber, rather than strictly in the pump chamber (see Fig. 3.3). In this way a machine-independent description is achieved. The sub-divertor chamber is indeed directly filled with the neutral flux recycled from the divertor target plates, while gas transport from this to the pump chamber does depend on the device characteristics. The denominator of Eq. (2.50) is calculated by radially integrating the He^{2+} ion density profile, measured at the midplane by CXRS, according to Eq. (2.51). Since the only available neutral He measurements are made from the Penning gauge installed in the pump chamber, the data plotted in Fig. 3.13 are produced employing the assumption of n_{He^0} in the sub-divertor chamber being two times larger than that in the pump chamber (cf. Section 3.4.2).

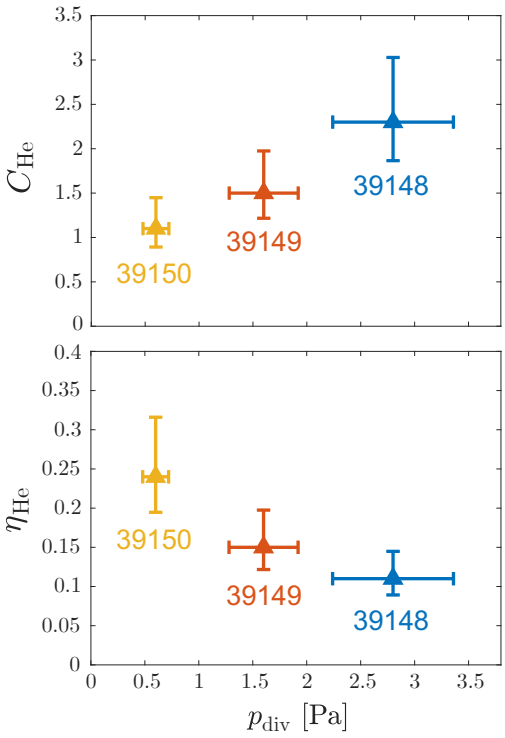

Figure 3.13: Measured values for He compression (top, Eq. (2.50)) and He enrichment (bottom, Eq. (2.52)) for the discharges #39148, #39149 and #39150, as function of the divertor pressure.

Figure 3.13 readily shows that He compression increases roughly linearly with increasing divertor neutral pressure in the investigated range. Vertical error bars are evaluated from the uncertainty of the CXRS data, as no error analysis for the Penning gauge measurements was performed. Horizontal error bars are evaluated from the uncertainty of the manometer measurements. With similar core confinement/transport properties and equal pump settings between the three discharges, the observed trend indicates a divertor retention of helium improving at larger divertor neutral pressures.

On the other hand, the measured He enrichment, shown at the bottom of Fig. 3.13, decreases, which indicates that the improvement of divertor retention of the main fuel with increasing divertor neutral pressure is faster than that of helium. Additionally, the fact that the measured enrichment is lower than unity in all discharges indicates that, at any level of divertor neutral pressure, He is compressed in the divertor worse than the main fuel is. Theoretical considerations (cf. Section 2.2.3) and experiments [147] are in agreement with the observed behavior, and relate this to the first ionization energy of He (24.6 eV) being larger than that of D (13.6 eV). This will be also further discussed later in this thesis (cf. Section 5.3.1).

Transport processes vs. exhaust dynamics

The invariance of the measured He compression w.r.t. the particular dynamic phase of a discharge has one important implication. Namely, helium transport and recycling in the divertor plasma (which determine He compression) does not depend on the dynamics of helium exhaust. The same transport and recycling takes indeed place at different He concentration levels (and, presumably, at different wall conditions w.r.t. implanted He inventory). Helium transport and recycling may be assumed as only related to the divertor plasma characteristics, while the exhaust dynamics is mostly determined by the current configuration of the device.

This allows to treat the physics defining (1) the exhaust dynamics and (2) the transport of He ions/neutrals separately. For this reason the interpretation of such two aspects was performed in separate ways, in the Chapters 4 and 5, respectively.

3.4.4 Helium exhaust with detached divertor

A second series of experiments aimed to investigate the impact of *divertor detachment* on the helium exhaust efficiency. Previous studies reported a general detrimental effect on the exhaust efficiency of the divertor entering a detached regime, manifested in a decrease of He compression [80]. We performed two H-mode discharges with constant deuterium fueling, one without N seeding and one with strong N seeding to actively cool the divertor plasma through enhanced radiation [148, 149]. Figure 3.14 shows the main time traces.

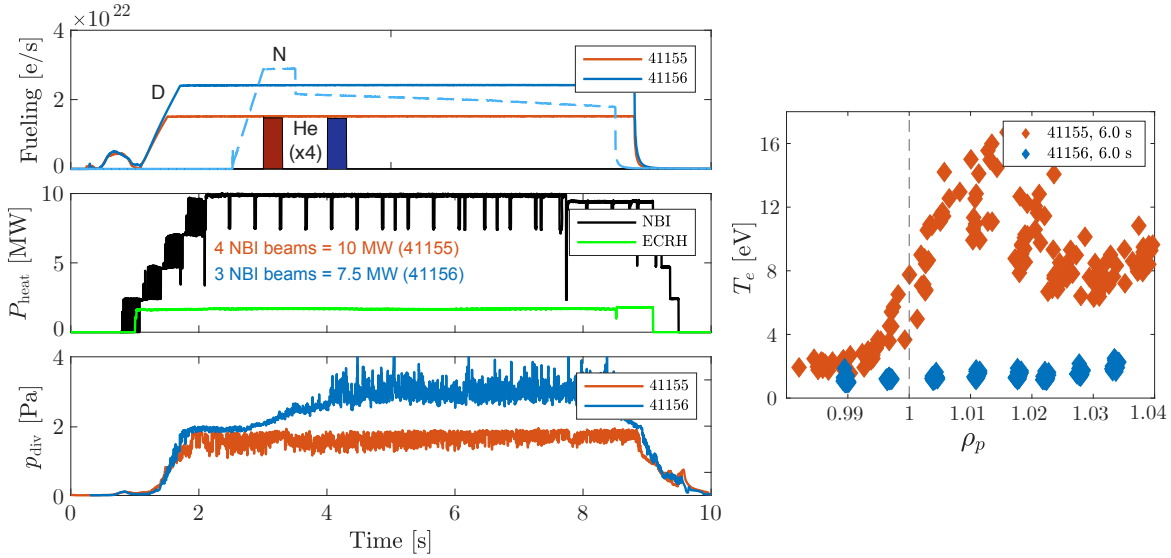

Figure 3.14: Left: time traces from the divertor detachment scan. From top to bottom: fueling (D as solid lines, N as dashed line (only for #41156), He as filled areas, the last ones magnified 4 times w.r.t. the actual value), heating power (ECRH common for all the discharges, NBI with different number of beams), divertor pressure (the latter is overestimated in the phase with active N seeding in #41156). Right: electron temperature profiles at the outer target surface measured by Langmuir probes.

The strong N seeding in the second discharge resulted in a pronounced detachment characterized by a cold divertor, with electron temperatures in front of the outer divertor target being less than 2 eV as measured by the Langmuir probe (left plot in Fig. 3.14). In both discharges we applied a 300 ms long He puff performed from a midplane fueling valve.
A full analysis of helium exhaust in these discharges was prevented by the impossibility to reliably measure the He partial pressure with the Penning gauge in the discharge with detached divertor. The strong presence of nitrogen generates additional emission lines in the neighborhood of the spectroscopically observed HeI line. This made the interpretation of the measured spectra problematic and, hence, any estimate of the He partial pressure unreliable. The N seeding in the discharges presented in the previous Section was instead moderate enough to not dramatically affect the spectra.
A qualitative interpretation of the exhaust dynamics could still be performed by observing the measured average He ion density in the core plasma for both discharges (Figure 3.15). After the active injection phase, the He content in the plasma decays visibly slower when the divertor is cold/detached. Since the pumping speeds are identical in both discharges, a slower decay implies a smaller He partial pressure in front of the pump surface, i.e. a degradation of He compression. This is, however, only a speculation at this point, because of the unavailable

experimental measurements of the He partial pressure in front of the pumps. For this reason, the dependence of divertor retention of helium as function of the divertor temperature was studied numerically, and the results will be discussed in the Chapter 5.

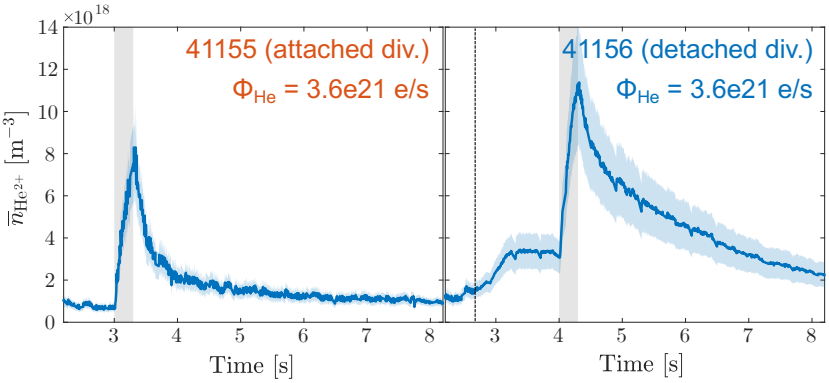

Figure 3.15: Time traces of the measured average He^{2+} ion density in the core plasma measured by CXRS in the performed discharges at different divertor detachment states. Error bars of CXRS data are given as shaded areas. The time windows during which He is actively injected are highlighted by grey bands. The applied He fueling rates are also indicated. The time at which N seeding starts in #41156 is indicated by a vertical dashed line.

It can be also noted that, in the second discharge, as soon as N seeding starts (dashed vertical line in the right plot in Fig. 3.15), the He density in the plasma increases although no active injection is performed yet. An increase of the total He partial pressure in the exhaust gas was observed as well, although not quantifiable for the above-mentioned reasons. Whereas any change of He compression indicates a redistribution of He particles between plasma and exhaust gas, this observation indicates a net increase of the He content in the entire system. The transition of the divertor plasma characteristics from an attached to a detached state [80], or the changes in the confinement properties due to the presence of N (e.g. increasing the ELM frequency [150, 151]), are expected to affect how efficiently the already present helium is flushed away from the core. However, this does not justify alone a net increase of the total amount of helium in the system. Therefore it can be assumed that the presence of more N ions contributes to an enhanced erosion of He atoms which are implanted in the wall surface, leading to an increased wall source. This is not surprising as N projectiles have a larger sputtering yield for He atoms implanted in W at high energies than, e.g., D projectiles (cf. Section 2.2.2 and Fig. 2.10). Quantifying the impact of different ion projectiles in contributing to the wall source for helium motivates further the application of the model which will be presented and discussed in Chapter 4.

3.4.5 Extrapolation towards burning plasmas

The measured trends of He compression and He enrichment, i.e. the first one increasing and the second one decreasing with divertor neutral pressure, are in qualitative agreement with past studies. Figure 3.16 shows such measurements for a database of discharges at different heating levels performed at AUG with full-C wall and the LYRA divertor geometry [80]. Here the x-axis is the neutral flux density (for which 10^{22} m^{-2}s^{-1} corresponds to 0.13 Pa, assuming an ideal maxwellian gas with mostly D_2 molecules at a temperature of 300 K). A one-by-one comparison between past and current absolute numbers is not meaningful, since divertor recycling is strongly dependent on geometric aspects such as e.g. target inclination and separatrix strikepoint position [152]. Nevertheless, both past and current measurements show similar qualitative trends, although wall materials and divertor geometry of AUG have changes since then. This strengthens the extrapolation of such behavior towards burning plasmas, at least at a qualitative level.

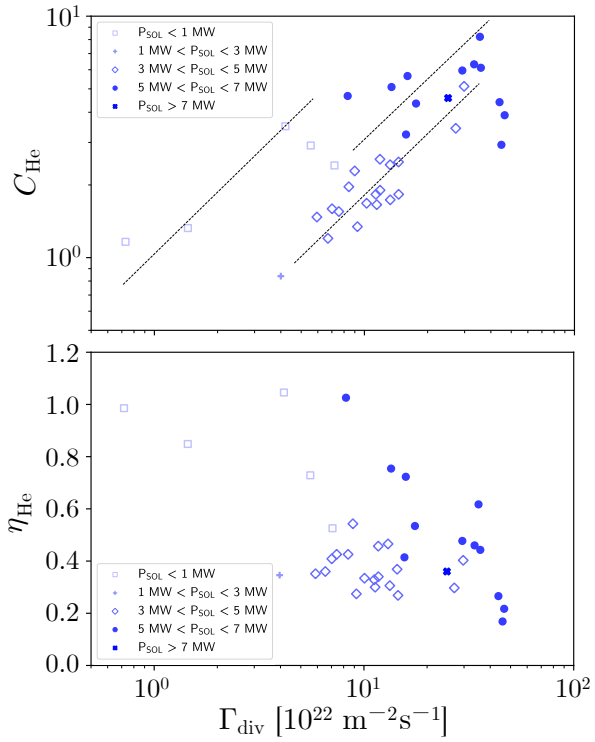

Figure 3.16: Measured values for He compression (top, Eq. (2.50)) and He enrichment (bottom, Eq. (2.52)) for a database of discharges at different heating levels, as function of the divertor neutral flux density, from AUG with full-C wall and LYRA divertor. Adapted from [80].

A large He compression favours pumping of He atoms. Operational scenarios with high divertor neutral pressures are therefore favourable in terms of helium pumping only. The observed trend for He enrichment with divertor neutral pressure is, however, negative in terms of extrapolation towards a reactor. The lowest limit for the enrichment quoted for ITER is 0.2 [9].
Whereas helium pumping needs to be maximized, the pumping of the main fuel is subject to other constraints. A highly compressed main fuel implies a large tritium throughput, which is undesired for safe operations of the fuel reprocessing plants [74]. Maximizing helium pumping and minimizing tritium pumping at the same time requires both C_{He} and η_{He} being as large as possible. Because of the opposite trends of the two parameters, an optimum point in divertor neutral pressure may be therefore found for future reactors.
Extrapolating the degradation of the exhaust efficiency with divertor detachment towards a reactor is less trivial. The mechanism through which divertor temperature affects impurity retention is the alteration of the penetration depth of recycled impurity neutrals (cf. Section 2.2.3). Having the same plasma in a geometrically larger divertor would imply an ionization front being closer to the target and more far away from upstream. Therefore, the observed degradation of helium exhaust may not take place e.g. in ITER with a comparatively similar divertor plasma, or it may take place only at a more pronounced level of detachment. Predicting such behavior for a future reactor must therefore rely on advanced modelling.

Chapter 4

Modelling and interpretation of helium exhaust dynamics

The experimental results documented in the previous Chapter indicate that the tokamak wall plays a key role in helium exhaust. It was shown that, on the other hand, helium transport/recycling and exhaust dynamics are conceptually distinct aspects. Whereas the former is mostly dependent on the divertor plasma characteristics (e.g. pressure and temperature), the latter is mainly determined by the technical aspects of the particular device (i.e. pumping systems and wall materials). This Chapter focuses on the latter aspect, namely the interpretation of the experimentally observed helium exhaust dynamics at AUG.
Simple analytic models have been developed in the past to interpret the dynamic behavior of impurities in terms of physics-based time constants [153]. However, in such models the assumption of fully recycling impurities has been always employed, neglecting wall retention effects. As discussed in the previous Chapter, at least for the case of helium in a full-W tokamak, this assumption may be invalid. For this reason a novel numerical model was developed and applied to the present AUG experiments. The novelty of this work is the possibility to disentangle and quantify the physics mechanisms determining the exhaust dynamics (namely active pumping and wall retention) taking the transport as a purely experiment-based input.
In the Section 4.1 the model will be introduced. In the Section 4.2 the modelling setup will be presented, with focus on the employed physics-based input parameters. Finally, in the Section 4.3 the results of the application of the model to the investigated AUG discharges will be presented and discussed. The contents of this Chapter have been already partially published in [95].

4.1 Development of a multi-reservoir dynamic particle balance model

Since the transition of AUG from a full-C wall to a full-W wall, helium exhaust is thought to be strongly affected by *wall phenomena*. This is explained by He atoms being efficiently retained in W surfaces [37, 143, 144], resulting in a high storage capacity of the main and divertor wall surfaces. Implantation of He atoms was observed to take place into vacancies in the W lattice caused e.g. by displacement damage [39]. The experimental findings documented in the Chapter 3 underlined the importance of the wall surfaces for the total particle inventory. The role of the walls as a continuous source and sink for He particles for the plasma is supported noting that:

- Even with no external He fueling and with active pumping, the He content in the plasma is seen to never fall to zero because of a continuous wall source, making D plasmas being polluted with a He concentration typically not less than $0.5-1\,\%$. This is different from what happens with other noble gases such as Ne and Ar, whose concentration in the plasma falls to zero in few seconds after active seeding [138]. N, instead, is seen to behave in a

similar way as He [148], due to chemical bonding of N molecules within the W lattice [154, 155].

- A continuous He fueling would produce He accumulation in the plasma, as the time of a discharge, limited to 10 seconds, is not sufficient for saturating the wall with He atoms and ensuring a puff-pump balance. This is different from what happens e.g. with D, for which a puff-pump balance is usually reached within one second in typical H-mode plasmas [40].

Quantitatively understanding the impact of the wall on the transient behavior of helium is necessary for a proper understanding of its global lifecycle in the plasma and to predict its exhaust in future tokamaks. Since accurate measurements of implantation and outflux of particles into/from the material walls during plasma discharges are not possible, such understanding must rely on the application of numerical models which take into account the underlying plasma-wall interaction mechanisms.

4.1.1 Extension of the impurity transport code Aurora

Several transport codes (e.g. STRAHL [156], DIVIMP [157]) have been developed for simulating the time-dependent impurity behavior in tokamak plasmas. Other than for transport studies, such codes have also been used in plasma-wall interaction studies. For example, the dynamic wall composition is studied using the simulated impurity fluxes towards the PFCs *as fixed inputs*, in combination with a model for implantation/erosion processes [158, 159, 160]. However, how the dynamic absorption/release rates into/from the wall act as a dynamic sink/source for the impurity population in the plasma itself, affecting again the impurity fluxes towards the PFCs, has never been taken into account. Modelling such mechanisms is essential for quantifying the impact of the wall on the exhaust of impurities from the plasma.
For the first time we developed a framework which accounts for time-dependent impurity transport in the plasma and wall retention *in a self-consistent way*. This is in form of a particle balance model which simulates a series of interconnected particle reservoirs for ions, neutrals and particles dynamically retained in the wall surfaces. The present model is specifically adapted to the AUG geometry, but can be easily generalized to any divertor tokamaks. We developed this as an extension of the 1.5D impurity transport code *Aurora* [50], which is a recent open-source code, widely based on STRAHL. Aurora simulations are run with a Python interface, while the transport equations and the wall retention calculations are efficiently solved in Fortran routines. Whereas, in this thesis, only the case of helium in a device with full-W wall was considered, this model can be easily generalized for any combination of impurity and wall material.
Figure 4.1 visually shows reservoirs, particle flows and physical processes included in the model. In the plasma transport model, continuity equations for each ion charge state are solved over time onto a 1D radial coordinate, assuming flux-surface-averaged quantities in a cylindrical geometry. Particle fluxes reaching main and divertor walls can either become stored in the wall surfaces, which constitute 0D dynamic particle reservoirs, or be recycled. Particles leaving the main wall become a source for the plasma, while particles leaving the divertor wall fill further 0D dynamic neutral particle reservoirs representing the sub-divertor/pump chambers. From here, particles can flow back towards the plasma or be permanently removed from the system through pumping.

4.1.2 Plasma particle transport equations

The *radial grid* onto which the ion transport equations are solved is based upon the experimental magnetic equilibrium. The employed radial flux coordinate r is defined through the enclosed volume V into the relative flux surface according to $r \equiv \sqrt{V/(2\pi^2 R_0)}$. Outside the LCFS this coordinate is extrapolated towards the radial grid boundary.

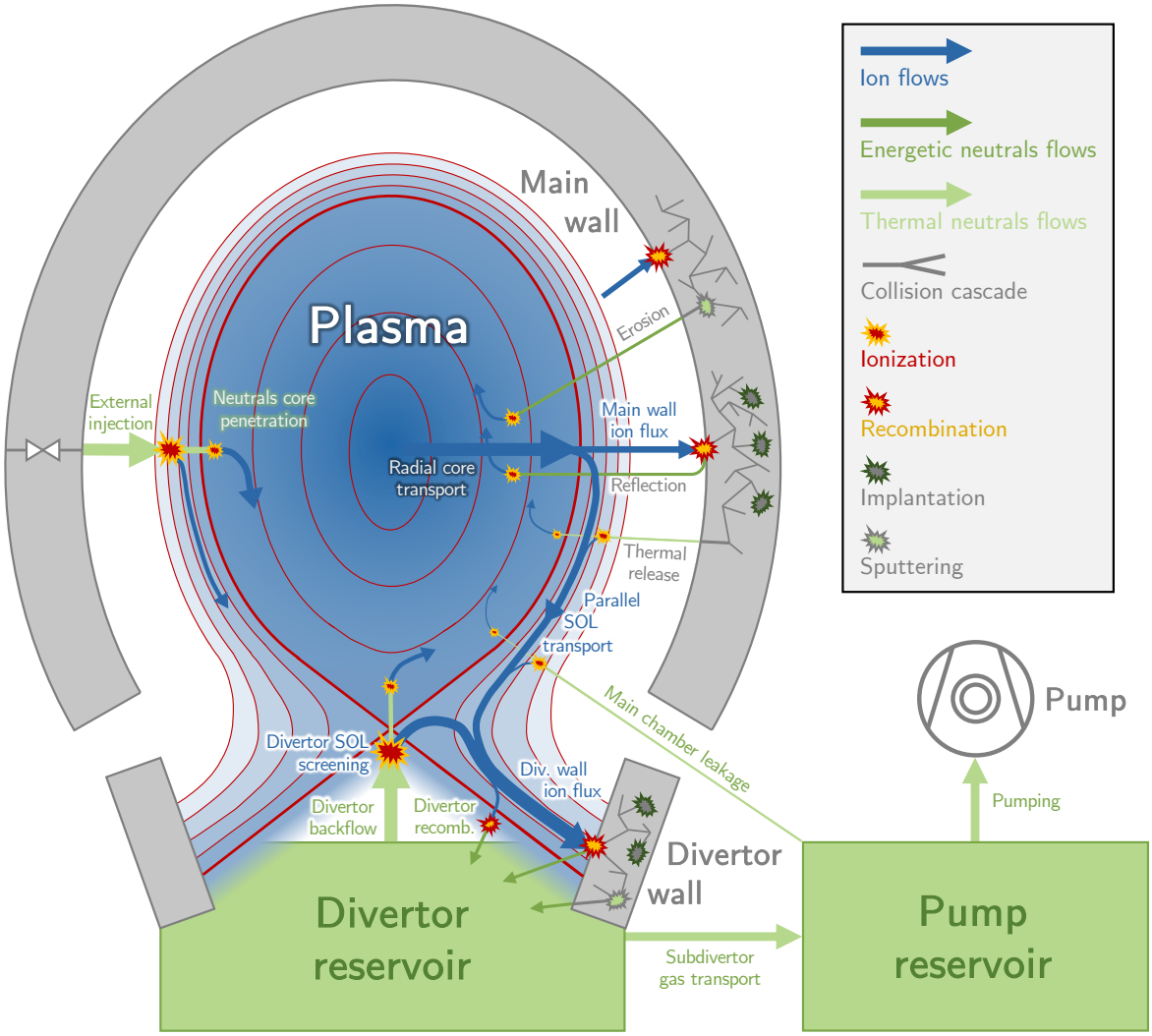

Figure 4.1: Sketch of the multi-reservoir particle balance model employed for the dynamic modelling presented in this Chapter. The *plasma* is a region filled with He ions and neutrals where the radial impurity transport equations are solved. The *divertor reservoir* and the *pump reservoir* are 0-dimensional regions filled only with He neutrals. *Main wall* and *divertor wall* constitute further 0-dimensional reservoirs for long-term (but temporary) storage of He atoms. The modelled interconnections reflect the actual AUG geometry.

The treatment of radial ion transport in the plasma is the same as presented in the Section 2.1.1. For each ion charge state z, the *continuity equation*

$$\frac{\partial n_{\mathrm{He},z}}{\partial t} = -\frac{1}{r}\frac{\partial}{\partial r}\left(r\Gamma_{\mathrm{He},z}\right) + Q_{\mathrm{He},z} \tag{4.1}$$

is solved (cf. Section 2.1.1). The radial (cross-field) particle flux in Eq. (4.1) is computed assuming separate diffusive and convective components, i.e.

$$\Gamma_{\mathrm{He},z} = -D_{\mathrm{He}}\frac{\partial n_{\mathrm{He},z}}{\partial r} + v_{\mathrm{He}} n_{\mathrm{He},z} \ , \tag{4.2}$$

where D_{He} is the *diffusion coefficient* and v_{He} is the *convective velocity*. These coefficients are an input for the model, therefore they must be empirically assumed or experimentally inferred [161, 162]. These coefficients are dependent on the radial coordinate r, and optionally a dependence on the charge state z can be also specified (although this possibility has not been exploited in the presented results).
Transitions between charge states are computed assuming *ionization equilibrium* (cf. Section 2.1.1). Therefore, for each charge state z, the ion sources/sinks are given by

$$
\begin{aligned}
Q_{\mathrm{He},z} = & -\left(n_e\langle\sigma v\rangle^{\mathrm{ion}}_{\mathrm{He},z} + n_e\langle\sigma v\rangle^{\mathrm{rec,RDR}}_{\mathrm{He},z} + n_n\langle\sigma v\rangle^{\mathrm{rec,CX}}_{\mathrm{He},z}\right) n_{\mathrm{He},z} \\
& + \left(n_e\langle\sigma v\rangle^{\mathrm{ion}}_{\mathrm{He},z-1}\right) n_{\mathrm{He},z-1} \\
& + \left(n_e\langle\sigma v\rangle^{\mathrm{rec,RDR}}_{\mathrm{He},z+1} + n_n\langle\sigma v\rangle^{\mathrm{rec,CX}}_{\mathrm{He},z+1}\right) n_{\mathrm{He},z+1} \ .
\end{aligned} \tag{4.3}
$$

The background kinetic plasma profiles, namely electron density n_e, electron temperature T_e, ion temperature T_i and main species neutral density n_n are also an input for the model. These allow to calculate the atomic rates (cf. Fig. 2.4) and computing the total source/sink for each charge state z, in Eq. (4.3), at each point of the radial grid.

4.1.3 Particle fluxes towards the walls

Outside the LCFS the grid is divided into a *divertor SOL* and a *limiter SOL*, and the transport equations are solved adding an additional loss term in Eq. (4.3), which accounts for the number of particles lost per unit of time due to parallel transport. This is approximated by dividing the parallel ion velocity in the SOL by a characteristic parallel length, i.e.

$$
Q^{\mathrm{SOL}}_{\mathrm{He},z} = \frac{v_{\parallel,\mathrm{He}}}{L_\parallel} \ . \tag{4.4}
$$

The distinction between divertor SOL and limiter SOL determines the destination of the particles accounted in the parallel loss term $Q^{\mathrm{SOL}}_{\mathrm{He},z}$. The first region lies between the LCFS and the limiter shadow. The parallel losses calculated here constitute the flux $\Gamma_{\mathrm{He,div}}$ directed onto the divertor wall. The second region lies between the limiter shadow and the outermost grid boundary. The particles lost here will intercept the limiter. Therefore the sum of such losses plus the radial particle flux calculated at the outermost grid boundary constitutes the flux $\Gamma_{\mathrm{He,main}}$ directed onto the main wall.
This model is rather crude, and is not aimed to provide an accurate description of parallel SOL transport, which is not constant neither radially across the SOL nor in parallel direction. Nonetheless, a proper empirical assumption for $v_{\parallel,\mathrm{He}}$ allows to estimate the parallel transport.

4.1.4 Neutral sources in the plasma

Eq. (4.1) is not solved for neutrals ($z = 0$), which only act as a source for the first ionization stage. The neutral He density profile on the radial grid is estimated assuming the fueled/recycled neutrals to enter the plasma with a given speed $v_{\mathrm{He},0} = \sqrt{2E_{\mathrm{He},0}/m_{\mathrm{He}}}$, calculated from the energy $E_{\mathrm{He},0}$ at which they are emitted. The resulting profile is

$$
n_{\mathrm{He},0}(r) \propto \frac{r_{\mathrm{edge}}}{r} \exp\left(-\int_{r_{\mathrm{edge}}}^{r} \frac{n_e\langle\sigma v\rangle^{\mathrm{ion}}_{\mathrm{He},0}}{v_{\mathrm{He},0}}\,\mathrm{d}r\right) , \tag{4.5}
$$

with r_{edge} being the outermost boundary of the grid, from which the neutrals are injected. The resulting profile will decay with decreasing radial coordinate due to ionization. The injection energy defines how far the neutrals can penetrate into the plasma before being ionized.

4.1.5 Plasma-wall interaction

He particle fluxes reaching the main and divertor walls fill up dynamic particles reservoirs. Their content is expressed in terms of He particle surface densities $\sigma_{\mathrm{He,wall}}$ (in m^{-2}), evaluated dividing the total number of stored He particles by the user-defined wall surfaces.
A fraction of all He particles reaching a wall surface is reflected, according to a *particle reflection coefficient* $R_{N,\mathrm{He}}$. In this case, they are immediately re-emitted as fast particles, carrying a relevant fraction of the original energy of the ion projectiles.
The fraction of the He flux which is not reflected penetrates the wall surface. A saturation

effect is included, employing a *saturation density* $\sigma^{\text{sat}}_{\text{He,wall}}$ which defines the theoretical maximum amount of dynamically stored particles. The fraction $\frac{\sigma_{\text{He,wall}}}{\sigma^{\text{sat}}_{\text{He,wall}}}$ of the non-reflected flux will be promptly released as thermal neutrals. Only the remaining fraction $\left(1 - \frac{\sigma_{\text{He,wall}}}{\sigma^{\text{sat}}_{\text{He,wall}}}\right)$ will fill the wall reservoir, defining an *implanted flux*

$$\Gamma^{\text{impl}}_{\text{He,wall}} = \Gamma_{\text{He,wall}} \left(1 - R_{N,\text{He}}\right) \left(1 - \frac{\sigma_{\text{He,wall}}}{\sigma^{\text{sat}}_{\text{He,wall}}}\right) . \tag{4.6}$$

Particles implanted in the wall reservoirs can be released again, at a later time, due to sputtering through ion bombardment of the wall surfaces. Projectiles are the simulated impurity itself and all other species in the plasma, including main ions and possibly other impurities. Therefore, the wall fluxes of the species not included in the current simulation need to be defined by the user. In this way, the *sputtered flux* released from the wall surface will be

$$\Gamma^{\text{sput}}_{\text{He,wall}} = \sum_{s \in [\text{species}]} Y_{s\rightarrow\text{He}} \Gamma_{s,\text{wall}} \tag{4.7}$$

$Y_{s\rightarrow\text{He}}$ is a *sputtering yield* for the He atoms implanted in the wall surface caused by bombardment of the projectile s. These neutrals are also fast, carrying some fraction of the original energy of the ion projectiles.
The total recycled flux from the main wall and the energy at which the recycled He atoms are emitted allow to compute a neutral He density profile on the radial grid through Eq. (4.5). In this way, how far each population of recycled neutrals (reflected, thermally released and sputtered) can penetrate into the confined plasma before being ionized is roughly estimated.
All surface coefficients are calculated from the theoretical curves (cf. Figs. 2.9, 2.10) after the specification of user-defined electron temperatures at the plasma-wall interfaces and impact angle of the ion projectiles.

4.1.6 Neutrals recycling and pumping

Whereas He particles recycled from the main wall (reflected, thermally released and sputtered) constitute a source for the plasma, those recycled from the divertor wall fill a dynamic particle reservoir of neutral particles, the divertor reservoir. The content of this reservoir is expressed in terms of volume density $n_{0,\text{He}}$ (in m^{-3}), evaluated dividing the total number of contained He particles by the user-defined reservoir volume V_{div}.
Divertor retention (to be considered as an input for such a model) is emulated through a loss term for particles from the divertor reservoir, over a time scale given by an empirical *divertor retention time* τ_{ret}. This defines a backflow of particles towards the plasma as

$$\Gamma^{\text{back}}_{\text{He}} = \frac{N^{\text{div}}_{0,\text{He}}}{\tau_{\text{ret}}} , \tag{4.8}$$

where $N_{0,\text{He}} = n^{\text{div}}_{0,\text{He}} V_{\text{div}}$. A screening effect for the divertor may be optionally included, empirically defining the fraction of the total backflow which gets to penetrate the divertor and to become a new source for the plasma.
The divertor reservoir is connected with a pump reservoir, with volume V_{pump}. Neutral particle transport is defined through a *neutral transport conductance* $L_{\text{div-pump}}$ in m^3/s, such that the neutral flow from the divertor reservoir towards the pump reservoir is given by

$$\Gamma^{\text{div-pump}}_{\text{He}} = L_{\text{div-pump}} \left(n^{\text{div}}_{0,\text{He}} - n^{\text{pump}}_{0,\text{He}}\right) . \tag{4.9}$$

$L_{\text{div-pump}}$ can be empirically imposed in order to reproduce the experimental pressure/density drop between divertor and pump reservoirs.

Finally, particles in the pump reservoir can leak again towards the plasma, with a user-imposed *leak conductance* L_{leak} (although this possibility has not been exploited in the presented results), or can be permanently removed from the system through active pumping. The pumped flux is

$$\Gamma_{\text{He}}^{\text{out}} = S_{\text{pump}} n_{0,\text{He}}^{\text{pump}} \ , \tag{4.10}$$

with S_{pump} being the engineering *pumping speed* in m^3/s.

4.1.7 Numerical algorithms

The algorithm employed for solving the radial transport equations in the plasma (Eq. (4.1)) is a variation of the original central finite-difference scheme used in STRAHL [163]. The equations are solved through a *vertex-centered, finite-volume discretization scheme* using adaptive upwinding for the spatial discretization of the convective terms. The level of upwinding depends on the value of the local *Péclet number* $\mu_i \equiv |v(r_i)|\Delta r_i / D(r_i)$ at any given point i of the radial grid with radial coordinate r_i.
The conservative form of the transport equation for the density

$$\overline{n}_i(r_i, t) = \frac{\int_{\Omega_i} r n(r,t)\,\mathrm{d}r}{\int_{\Omega_i} r\,\mathrm{d}r} \tag{4.11}$$

averaged over the cell $\Omega_i = \left[r_{i-1/2}, r_{i+1/2}\right]$ is

$$\frac{\partial \overline{n}_i}{\partial t} = \frac{2}{r_{i+1/2}^2 - r_{i-1/2}^2}\left[rD\frac{dn}{dr} - rvn\right]_{r_{i-1/2}}^{r_{i+1/2}} + \overline{Q}_i \ . \tag{4.12}$$

The following replacements for the transport coefficients are applied:

$$\tilde{D}_{i\pm} = \frac{r_{i\pm1/2}}{\mp(r_{i+1/2}^2 - r_{i-1/2}^2)(r_i - r_{i\pm1})} D_{i\pm1/2} \ , \tag{4.13}$$

$$\tilde{v}_{i\pm} = \frac{r_{\pm1/2}}{2(r_{i+1/2}^2 - r_{i-1/2}^2)} v_{i\pm1/2} \ . \tag{4.14}$$

The time discretization is performed by equally weighting the density contributions from previous and future time steps, i.e. $\frac{\partial \overline{n}_i}{\partial t} = \frac{1}{2}F\left(\overline{n}_i^{j+1}\right) + \frac{1}{2}F\left(\overline{n}_i^{j}\right)$. In this way, for a time step Δt such that $t^{j+1} = t^j + \Delta t$, the complete discretization is

$$\begin{aligned}
\overline{n}_i^{j+1} + \overline{n}_i^{j} = {} & \Delta t\, \overline{Q}_i \\
& + \Delta t \left[\tilde{D}_{i-} + \left[1 + K_{i-1/2}\right]\tilde{v}_{i-}\right]\left(\tilde{n}_{i-1}^{j+1} + \tilde{n}_{i-1}^{j}\right) \\
& - \Delta t \left[\tilde{D}_{i-} - \left[1 - K_{i-1/2}\right]\tilde{v}_{i-}\right]\left(\tilde{n}_{i}^{j+1} + \tilde{n}_{i}^{j}\right) \\
& + \Delta t \left[\tilde{D}_{i+} - \left[1 + K_{i+1/2}\right]\tilde{v}_{i+}\right]\left(\tilde{n}_{i}^{j+1} + \tilde{n}_{i}^{j}\right) \\
& + \Delta t \left[\tilde{D}_{i+} - \left[1 - K_{i+1/2}\right]\tilde{v}_{i+}\right]\left(\tilde{n}_{i+1}^{j+1} + \tilde{n}_{i+1}^{j}\right) \ .
\end{aligned} \tag{4.15}$$

Here we have $K_i \equiv \max(0\,, 1 - 2/|\mu_i|) \cdot \text{sgn}(\mu_i)$. In this way, in the limit $\mu_i \to 0$ (diffusion-dominated transport) a purely central scheme ($K_i = 0$) is adopted, while in the limit $\mu_i \to \infty$ (convection-dominated transport) pure upwinding ($K_i = 1$) applies.
While calculating the source term $\overline{Q}_i$ at each time step, atomic rates act on each charge state considering ionization and recombination terms in two half steps. In the first half step, the ionization term is computed using the density at the new time step $j+1$ and recombination with the density at the previous time step j. In the second half step, ionization is computed at

the previous time step j and recombination at the new time step $j+1$.
Finally, the time discretization of the temporal evolution of the particle content N in the 0D reservoirs is done through a standard *finite-differences forward Euler scheme*, namely

$$N^{j+1} = N^j \left(1 - \frac{\Delta t}{\tau_{\text{depl}}}\right) + \Gamma_{\text{in}}^j \Delta t - \Gamma_{\text{out}}^j \Delta t \ . \tag{4.16}$$

Here τ_{depl} is a characteristic time scale for depletion of the particle content in the reservoir, in case of definition of a loss term proportional to the current particle content, and Γ_{in} and Γ_{out} are the particle fluxes entering/leaving the reservoirs respectively.

4.2 Modelling setup

The model described in Section 4.1 contains a large number of physics-based *input parameters*, to be imposed in agreement with the experiment. In this Section, the most important ones are described, and the underlying assumptions are discussed.

4.2.1 Geometry

The *magnetic equilibrium* is read in the EFIT format [164]. For all performed simulations it is based upon the discharge #39149 at 2.7 s. The 1D radial grid onto which the radial transport equations (Eq. (4.1)) are solved is a list of values of the flux-surface-volume normalized coordinate r constituting the centers of the radial locations of the grid cells. By default, the radial steps are smaller towards the edge, where larger gradients occur (Figure 4.2). Outside the LCFS the division of the grid into a divertor SOL and a limiter SOL is based upon user-defined distances. According to the real AUG equilibrium and wall geometry, we set the distance between LCFS and limiter shadow as 6 cm, and the distance between LCFS and grid boundary as 10 cm. The parallel connection lengths in the SOL, used to calculate the loss terms (Eq. (4.4)) are also user-defined. For these, we choose 50 m for the divertor SOL and 1 m for the limiter SOL [165].

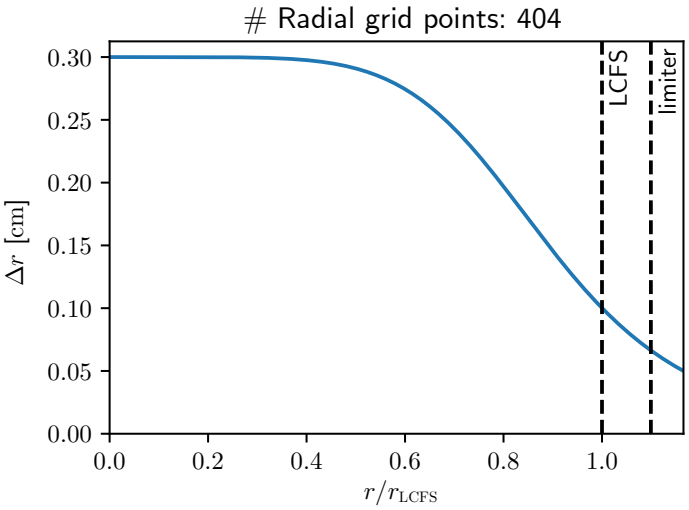

Figure 4.2: Radial step widths of the grid onto which the plasma transport equation are solved, as function of the normalized radius.

For calculating the temporary particle retention in the wall reservoirs, surface areas for main and divertor walls must also be defined. We set such areas to 5 m^2 and 0.5 m^2 respectively, as estimates of the geometrically measured plasma-wetted areas. Both areas can be multiplied by a parameter to arbitrarily increase the surfaces for the particle retention calculation, w.r.t. the "geometrical" plasma-wetted surfaces, in order to account for the surface roughness. The choice of such a factor, which substantially affects the modelled dynamics, is discussed in detail in the Section 4.3.1.
Finally, we set the volumes for the divertor and pump reservoirs, used in the neutral transport calculations, to 0.8 m^3 and 1.7 m^3, respectively, as estimates of the geometrically measured dimensions of the relative chambers within the AUG vacuum vessel.

4.2.2 Transport coefficients

The cross-field *transport coefficients* D_{He} and v_{He} (Eq. (4.2)) and the parallel SOL flow velocity $v_{\parallel,\mathrm{He}}$ (Eq. (4.4)) are the main input parameters for the ion transport modelling.
In H-mode plasmas at AUG it has been observed that transport of He ions in the core plasma is dominated by turbulence [141], not considering the presence of possible internal transport barriers (ITBs) [52]. Within the edge transport barrier (ETB), however, transport of He ions between ELMs is mostly collisional and well described by the neoclassical theory [35].

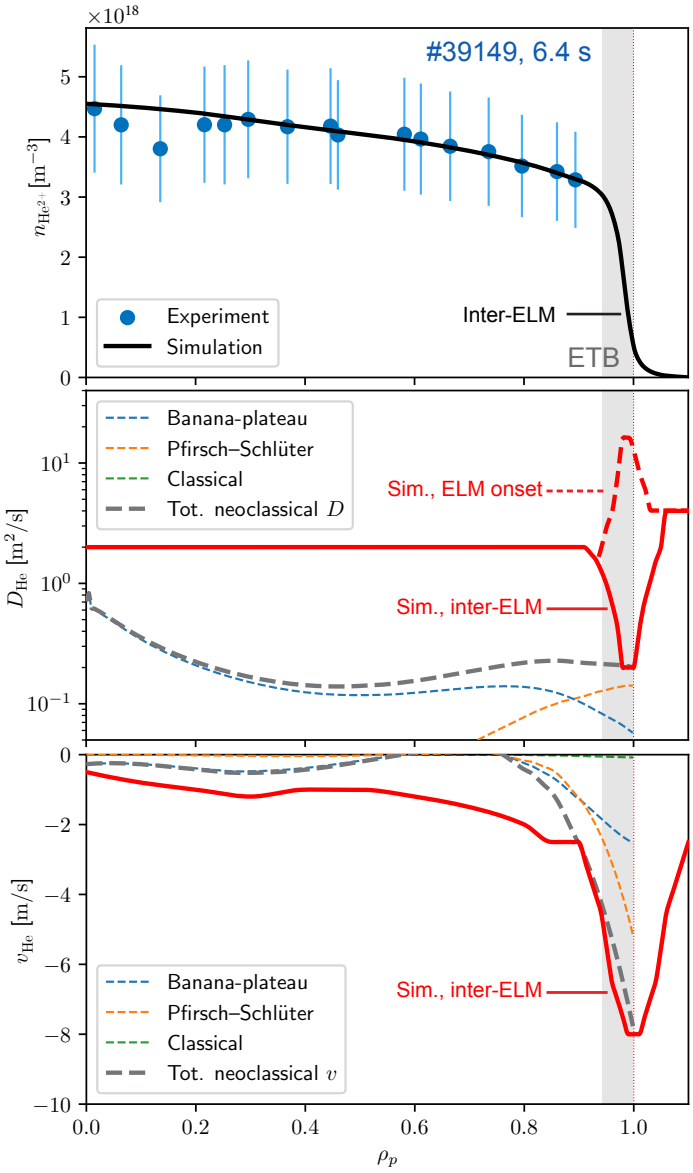

Figure 4.3: Radial profiles for the modelled He^{2+} density profile (inter-ELM) vs experimental CXRS data as blue points (top plot), used particle diffusivity D_{He} (middle plot) and convective velocity v_{He} (bottom plot). The solid red lines depict the coefficients used in the inter-ELM phases. The dashed red line shows the periodically imposed step increase of D_{He} at the ELM onsets. The dashed grey lines depict the neoclassical prediction, calculated with the FACIT program [58], while the decomposition in individual terms is given by the thin dashed colored lines.

Figure 4.3 shows the employed particle diffusivity and convective velocity profiles for the modelled discharge #39149 as red lines, the neoclassical predictions as dashed colored lines (cf. Fig. 2.7), and the resulting modelled He^{2+} density profile in the plasma. For our purpose, the choice of specific values for D_{He} and v_{He} is arbitrary, as only the ratio $v_{\mathrm{He}}/D_{\mathrm{He}}$ determines the density gradient.
Inside the ETB, we empirically set the values of D_{He} and v_{He} to reproduce the radial gradient as measured by core CXRS. As expected, the values of D_{He} and v_{He} required for this are much larger than the neoclassical ones.
Within the ETB, instead, we set the values for D_{He} and v_{He} to the neoclassical ones. Here He ions are mostly in the Pfirsch-Schlüter regime, with a strong inward-directed convective velocity around the separatrix. No edge CXRS data for the He^{2+} density were available for comparison with the modelling. However, the simulated ratio of He ion densities between pedestal top and pedestal bottom of about 4–6 is compatible with already published results from similar plasma scenarios at AUG [142].
Outside the LCFS D_{He} is raised to a second plateau while v_{He} is reduced again. In absence of solid information about transport of He ions outside the LCFS, we chose the value for D_{He} here to achieve a decay length of the He ion density profile in the SOL comparable to that of the electron density.
We also implemented a time-dependent parametrization of the transport coefficients to emulate the *ELM events*.

ELMs eject particles and energy from the edge plasma [35]. Therefore, during ELMs both the particle fluxes towards the walls and the energies of the ions increase. An estimate of the ELM-related fluxes towards the walls is necessary for a realistic modelling of the plasma-wall interaction. A periodic increase of the transport coefficients in the edge can mimic ELM crashes, and help achieving a correct time-dependent modelling.

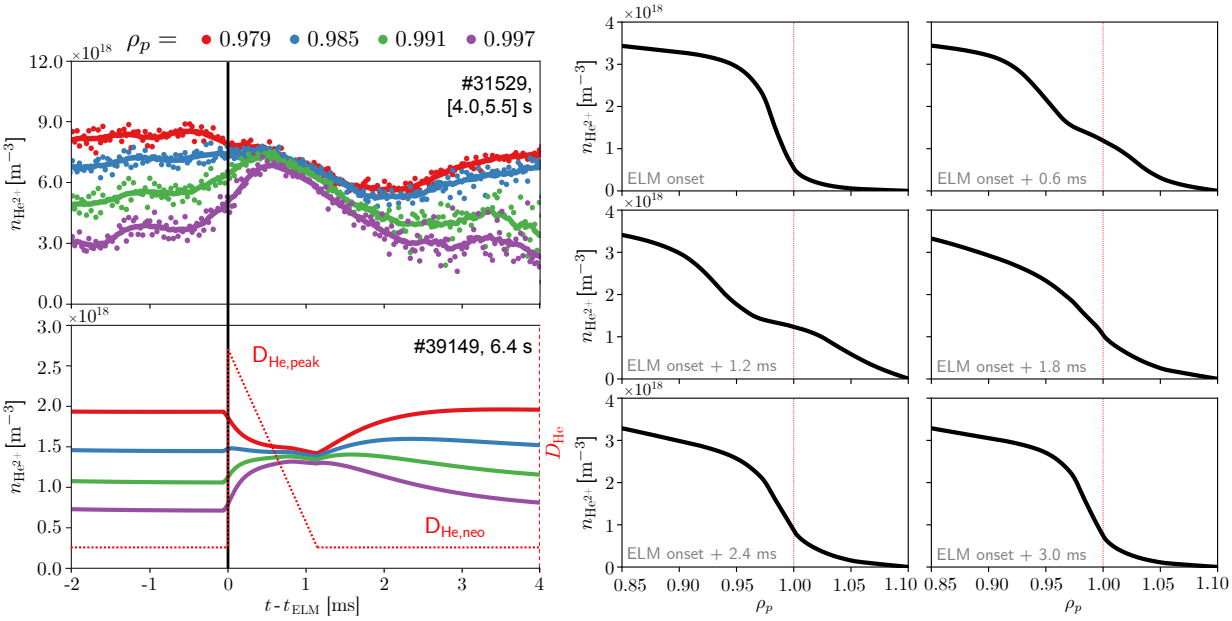

Figure 4.4: Left panel: Modelled time traces of the He^{2+} density at some radial locations in the edge as colored solid lines, and evolution of the edge particle diffusivity as dashed red line, during an ELM cycle (bottom) vs experimental data at the same radial locations from the AUG discharge #31529 (top, adapted from [142]), with pedestal characteristics and ELM sizes similar to those in #39149. Right panel: corresponding evolution of the modelled He^{2+} density profile in the edge/SOL during an ELM cycle.

The phenomenological model employed to emulate ELMs is inspired by [165] and [166]. To mimic an ELM crash, a step increase of D_{He} at the edge, up to values of the order of $10-20$ m^2/s, is used (see middle plot of Fig. 4.3) [167]. After the ELM onset, D_{He} decays linearly within 1.2 ms back to the neoclassical value and remains constant until the successive ELM event. This is done with a frequency consistent with the experimental one (which is 125 Hz for discharge #39149). In this way, the modelled evolution of the He ion density profile at the edge during an ELM cycle (Figure 4.4) is also compatible with the previously measured experimental intra-ELM profiles [142]. In such previous measurements, an increase of the He ion density at the separatrix by a factor of $2-2.5$ after the crash, a maximum relaxation of the profile region about 1 ms after the crash and a full recovery of the pedestal about $2.5-3$ ms after the crash were observed. All these features were qualitatively reproduced by our model.
Finally, for modelling the parallel losses outside the LCFS, we assumed a He ion flow fully entrained into the D ion flow, resulting in a similar parallel ion flow velocity. This is reasonable as the collisional mean free path between D and He ions is in the range $0.1-1$ m at usual AUG SOL plasma conditions ($n_e \approx 2-3\cdot 10^{19}$ m^{-3}, $T_e \approx 50-100$ eV), assuming $n_{He^{2+}} \approx 0.1\, n_{D^+}$, i.e. much shorter than the parallel connection length. We specified then the He ion flow velocity as $v_{\parallel,\mathrm{He}} \approx v_{\parallel,\mathrm{D}} = M\sqrt{(3T_i + T_e)/m_{\mathrm{D}}}$. The Mach number M was within the range $0.1-0.3$.

4.2.3 Kinetic profiles and atomic rates

We took the *kinetic profiles* of the background plasma from the experiment. Under the assumption of coronal equilibrium, this allows the specification of the *atomic rates* used for the calculation of the ion sources/sinks for every charge stage (Eq. (4.3)).

Figure 4.5 shows the kinetic profiles for discharge #39149, and the resulting He atomic rates for the charge transitions $z = 0 \leftrightarrow z = 1$ and $z = 1 \leftrightarrow z = 2$ used in the transport calculations, obtained from ADAS data (cf. Fig. 2.4) [54]. For the electron density and temperature, we used a fit achieved via integrated data analysis (IDA) [139] combining measurements of vertical Thomson scattering (TS) (cf. Section 3.2.2), lithium-beam emission spectroscopy (LIB) (cf. Section 3.2.3) and electron cyclotron emission radiometry (ECE) (cf. Section 3.2.4). For the ion temperature, we used a spline fit to core and edge CXRS data (cf. Section 3.2.5). For the calculation of the CX-assisted recombination rates, the neutral D density in the edge was estimated based on results from SOLPS-ITER simulations (cf. Chapter 5).

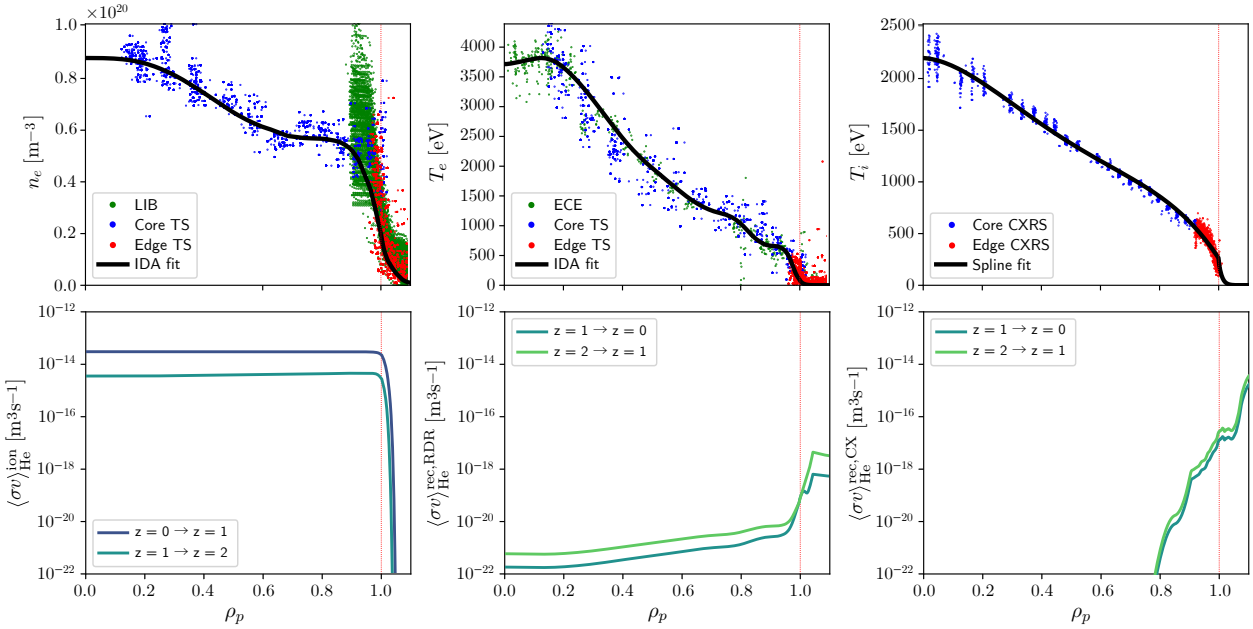

Figure 4.5: Top row: experimental data of electron density, electron temperature and ion temperature at the plasma midplane, taken from different diagnostics, as colored points, for discharge #39149 within the time window [2.5,3.0] s. The fits used as input for the simulations and for calculating the He atomic rates are given by black lines. Bottom row: calculated He atomic rates for all charge transitions, namely ionization rates, radiative+dieletric recombination rates, CX-assisted recombination rates, extracted from the ADAS ADF11 database [55].

4.2.4 Wall loads and surface coefficients

Modelling the plasma-wall interaction, which is necessary for simulating wall retention, requires the knowledge of reflection coefficients and sputtering yields for the considered combination of ion projectile and material species. Both types of data were calculated using the binary-collision-approximation-based Monte Carlo code TRIM.SP [68, 69, 168].
The reflection coefficients for He ions on W (cf. Fig. 2.9), used in Eq. (4.6), are widely available in the literature, and were extracted from an already existing database [169]. The sputtering yields for He atoms implanted in W due to ion bombardment (cf. Fig. 2.10), used in Eq. (4.7), were instead calculated for this work. For such calculations, the ansatz of a flat surface was used, and He atoms were assumed to be uniformly implanted into a layer of surface material to a given depth, with no surface binding energy to the bulk lattice atoms. The depth of the implantation profile was assumed to be equal to the mean penetration depth of He atoms into a W lattice, also calculated by TRIM.SP. In the model calculation, such depths were taken as 3 nm for the main wall and 6 nm for the divertor wall. The different depths come from the different average impact energies for He ions on W during plasma operations.
All surface coefficients depend on the impact angle of the ion projectiles onto the surface and

on their impact energy. We assumed an impact angle of 65° for all considered species (cf. Figs. 2.9 and 2.10). This is a good assumption for light projectiles (for which long-range transport prevails over prompt redeposition) derived from gyro-orbits calculations, considering AUG-typical magnetic field intensity and inclination angle, sheath characteristics and wall roughness [67]. The energy dependence is resolved by employing adequate models which relate the plasma temperature to an average energy of the ion projectiles in both inter- and intra-ELM phases. Figures 4.6 and 4.7 show the values of the input parameters for the plasma-wall interaction model for the main and divertor walls, respectively, during an ELM cycle. This time-dependent pattern is repeated for the entire modelled duration of the discharge with a frequency equal to the experimental ELM frequency (125 Hz for discharge #39149). The various entries in these plots are discussed in the subsequent paragraphs.

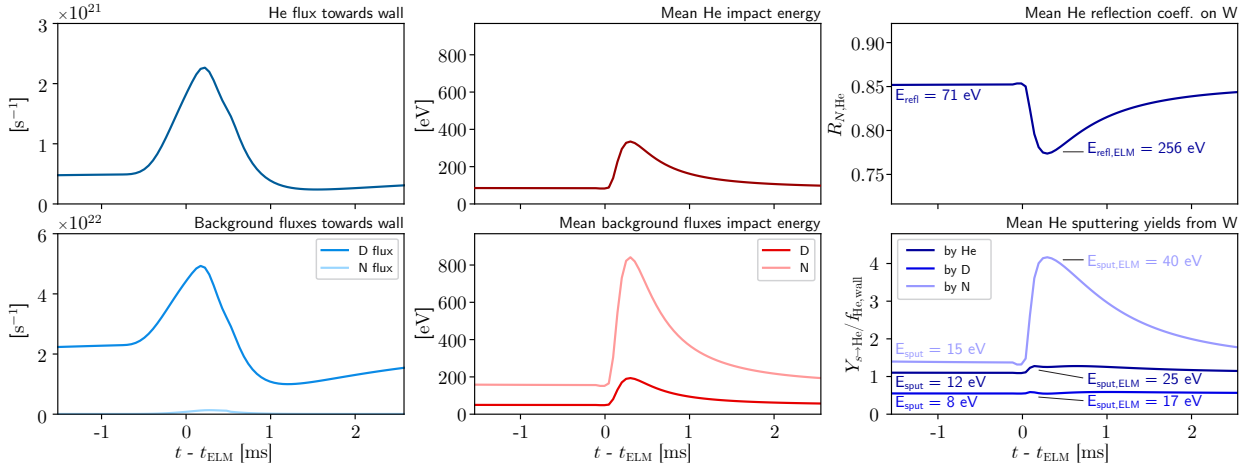

Figure 4.6: Values of the input parameters for the plasma-wall interaction model for the main wall during an ELM cycle. Left plots: simulated particle fluxes for He and background plasma species towards the wall. Middle plots: assumed impact energy for the ion projectiles of He and background species. Right plots: reflection coefficient of He ions on W and sputtering yields of He atoms implanted in W due to bombardment of He itself and background plasma species, calculated using the TRIM.SP program. The corresponding calculated energies at which reflected and sputtered He atoms are emitted towards the plasma (both in inter-ELM phases and at the ELM peak) are also indicated.

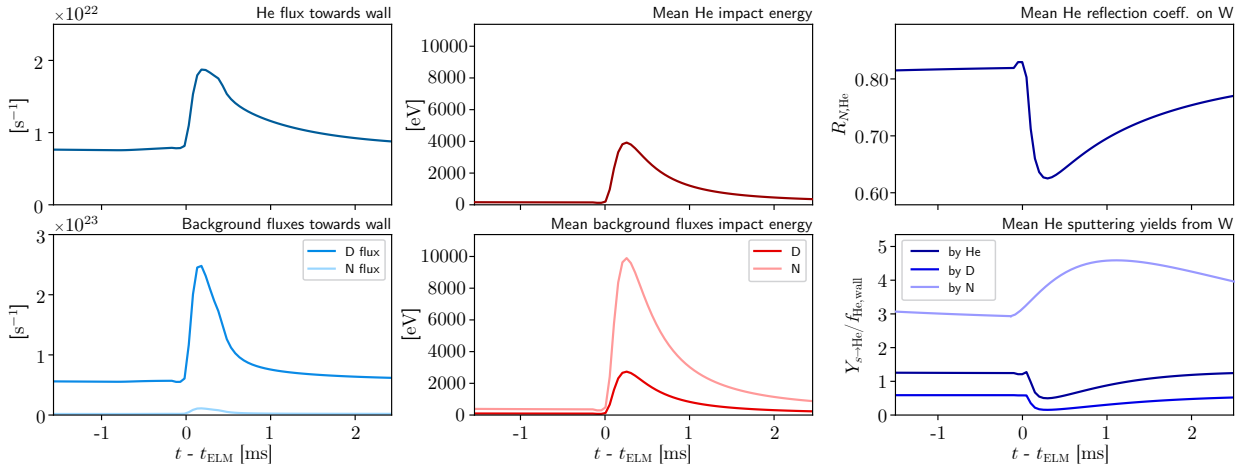

Figure 4.7: Same as Fig. 4.6, but for the divertor wall.

Particle fluxes

The left plots in Figs. 4.6 and 4.7 show the total *fluxes of ion projectiles* to the main and divertor walls, which directly enter Eqs. (4.6) and (4.7). The fluxes are expected to increase during ELM

events w.r.t. the inter-ELM phases, enhancing any types of plasma-wall interaction. The increase of the wall fluxes in our model results from the periodic step increase of transport in the edge (cf. Section 4.2.2), which produces an abrupt ejection of particles from the core plasma.
The He flux (at the top) is self-consistently modelled, therefore it does not require an a priori assumption. The fluxes of main species and other impurities (D and N in this case, at the bottom) must be instead assumed. They were obtained running Aurora simulations for the background plasma, i.e. for D and N separately, consistently with the available measurements from the experiment, e.g. from the divertor Langmuir probes. These, found as outputs from the D/N simulations, are then used as input for the He simulation. The background solutions are constant (apart from ELM events), relying on the assumption of constant D and N densities while the evolution of He is considered. The estimated values of the D fluxes of about $0.5 \cdot 10^{23}$ ions/s for the inter-ELM phases and about $2.5 \cdot 10^{23}$ at the ELM peak for the divertor wall load are consistent with the measurements of the Langmuir probes for discharge #39149. The relative increase of the modelled D flux towards the divertor between inter- and intra-ELM phases is, also, consistent with past experimental observations [170, 171, 172].
The estimates of the N fluxes are instead based on the assumption that the N partial pressure depends linearly on the external N gas puff rather than on the core N concentration [173]. In other words, as in the discharge #39149 N fueling is 3 % of the D fueling (if expressed in ions/s), then the N partial pressure is also 3 % of the D partial pressure. Therefore, as the partial pressure is strongly coupled to the recycling fluxes from the wall, the assumed N fluxes onto the walls are also 3 % of the assumed D fluxes.

Impact energies

The middle plots in Figs. 4.6 and 4.7 show the average *impact energy* of the different ion projectiles, which are needed to estimate realistic values for both reflection coefficients and sputtering yields, starting from their calculated energy dependence (cf. Figs. 2.9 and 2.10).
Generally, the ion impact energy onto a material surface is given by the sum of kinetic energy of the ions plus a contribution caused by sheath acceleration, i.e. as $E_{0,s} = 3T_e\overline{Z}_s + 2T_i$ [174]. Therefore, one only needs to know the plasma temperature at the plasma-material interfaces, and the mean charge state of the ions. An exception is the peak energy value during ELMs at the divertor. For estimating this the free-streaming model [175, 176] was employed. This relies on the assumption that the parallel energy flux from the pedestal is not limited by the sheath during ELMs. Therefore, the peak impact energy during ELMs is assumed to be simply proportional to the plasma temperature at the pedestal top, i.e. $E_{0,s} = \alpha_s T_{e,\mathrm{ped}}$.
Therefore, for the calculation of the impact energies at the main wall we used $E_{0,s} = 3T_e\overline{Z}_s + 2T_i$ with $T_{i,\mathrm{main}} = T_{e,\mathrm{main}} = 10$ eV for the inter-ELM phases and $T_{i,\mathrm{main}} = T_{e,\mathrm{main}} = 30$ eV at the ELM peak. The mean charge states $\overline{Z}_s$ for the different projectiles were calculated from the electron temperature at the plasma-material interface assuming coronal equilibrium. For the calculation of the impact energies at the divertor, for inter-ELM phases we used $E_{0,s} = 3T_e\overline{Z}_s + 2T_i$ with $T_{i,\mathrm{div}} = T_{e,\mathrm{div}} = 15$ eV, and at the ELM peak we used $E_{0,s} = \alpha_s T_{e,\mathrm{ped}}$) with $T_{e,\mathrm{ped}} = 600$ eV. The proportionality coefficients α_s for the different projectiles were calculated analytically according to [176]. All the chosen temperatures are consistent with what was observed in the discharge #39149. The values up to several thousands of eV which are estimated for the impact energies for the divertor wall at the ELM peaks are supported by experimental observations [177].
Given the inter- and intra-ELM values for the impact energies, the time-dependent shape used as input for the simulations has the inter-ELM value as baseline and the peak ELM value as cyclically recurring maximum. It follows the theoretical intensity of the ELM-driven parallel transport as [178]

$$I_{\mathrm{ELM}}(t - t_{\mathrm{ELM}}) \propto \frac{1}{(t - t_{\mathrm{ELM}})^2} \exp\left[-\frac{\tau^2_{\mathrm{ELM,decay}}}{2(t - t_{\mathrm{ELM}})^2}\right] . \tag{4.17}$$

The input parameter $\tau_{\mathrm{ELM,decay}}$, which controls the decay time of the shape function I_{ELM}, was chosen as $0.6 \cdot 10^{-3}$ s, in order to match the experimentally observed decay time of the ELM-driven fluxes in the discharge #39149 as seen by different diagnostics.

Reflection coefficients and sputtering yields

The right plots in Figs. 4.6 and 4.7 show the *surface coefficients*, namely reflection coefficient and sputtering yields, which are calculated from the energy-dependent curves (cf. Figs. 2.9 and 2.10 respectively) after the assumed impact energies, and directly enter Eqs. (4.6) and (4.7).
The value of the reflection coefficients determines the fraction of He ions which is reflected from the wall, rather than penetrating it, at each time step (Eq. (4.6)). The value of the simulated implanted flux, however, will also depend on how much the wall is already saturated with He atoms at that specific time step (see Section 4.3.1). Both in inter-ELM phases and during ELM events, most of the He ions impacting main and divertor wall are reflected. During ELMs, a slight decrease of the reflected flux is derived from the decreasing trend of the reflection coefficient as function of the impact energy.
The values of the sputtering yield determine the efficiency with which the ion fluxes towards the wall of both He and background species erode the He atoms which are implanted at the wall at each time step (Eq. (4.7)). They are expressed in terms of yields normalized to the concentration of implanted He atoms within the W lattice (i.e. as $Y_{s\to\mathrm{He}}/f_{\mathrm{He,wall}}$, with $f_{\mathrm{He,wall}} \equiv N_{\mathrm{He}}/(N_{\mathrm{W}} + N_{\mathrm{He}})$). At each time step, the absolute yields are calculated as $Y_{s\to\mathrm{He}} = (Y_{s\to\mathrm{He}}/f_{\mathrm{He,wall}}) \cdot f_{\mathrm{He,wall}}$ and used in Eq. (4.7) to calculate the total sputtered He flux.
Different projectiles species behave differently in this regard. The energy-dependent curves of the sputtering yields (2.10) show that a strong dependence on the eroding species exists, scaling with the mass of the projectiles. This dependence is more relevant at large impact energies, i.e. from few hundreds of eV up to several thousands of eV. In this range, a given impinging flux of N ions is e.g. up to 40 times more efficient than the same impinging flux of D ions in eroding He atoms implanted in W. This supports the observation reported in the Section 3.4.4 of a higher He content in the plasmas as a consequence of increased N seeding, which was speculated to be due to an increased erosion of He atoms implanted in the walls.
Because of this, a different behavior of the sputtering yields for different projectiles due to ELMs is estimated as well. At the main wall, in which the energy peak of the ion projectiles during ELMs is of the order of hundreds of eV, a relevant increase of the sputtering yield from N ions is calculated, while the sputtering yields from D ions and He ions are roughly constant. At the divertor wall, in which the energy peak of the ion projectiles during ELMs is of the order of thousands of eV, the sputtering yields from N ions still increases. Conversely, the sputtering yields from D ions and He ions decrease.
The energies at which reflected and sputtered He atoms (from different projectiles) are released from the wall are calculated as well. In our model, the energy at which the recycled He atoms are released plays a role only for those recycled from the main wall. That is because these are released towards the plasma. Employing the assumption of a 1-dimensional geometry, such energy is used to estimate their penetration into the plasma, determining in turn the neutral He source for the transport calculations (cf. Section 4.1.4). The He atoms recycled from the divertor wall, instead, directly enter the divertor neutral reservoir. Therefore, the energy at which these are released is irrelevant in this regard.

4.3 Multi-reservoir modelling results

This Section presents the results of applying the multi-reservoir model described in the Section 4.1 achieved with the input parameters described in the Section 4.2. Focus is put on the discharge #39149, described in the Section 3.4.3. Whereas the input parameters come from the experiment, the model features a number of inputs which should be considered free parameters, whose choice will be justified later in this Section.

4.3.1 Time-dependent results overview

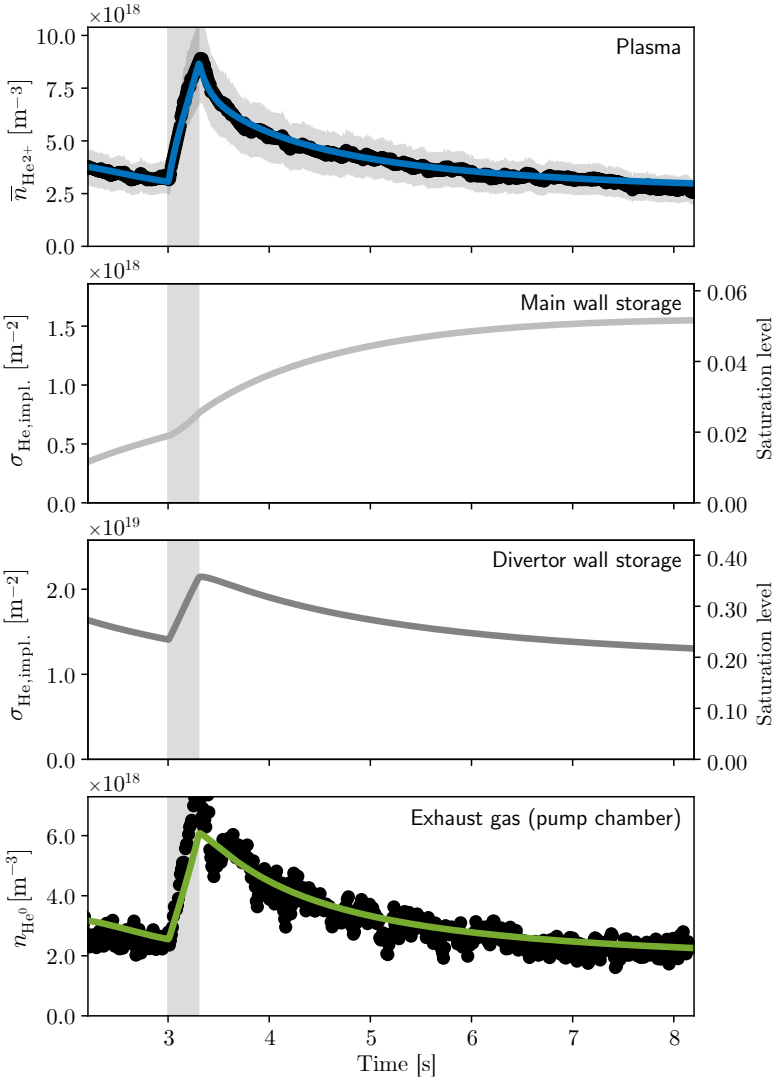

Figure 4.8: Modelled time traces of the He particle content in the reservoirs described by Fig. 4.1 for discharge #39149. Top plot: average He ion density in the core plasma and comparison with CXRS measurements (black points). Middle plots: surface densities of He atoms dynamically retained at the main and divertor walls; these are also expressed in terms of saturation level, i.e. fraction between dynamically implanted He atoms and maximum amount of He atoms which the walls can accommodate ($\sigma_{\mathrm{He,wall}}/\sigma^{\mathrm{sat}}_{\mathrm{He,wall}}$), at the right axes. Bottom plot: neutral He density in the pump reservoir and comparison with the Penning gauge measurements (black points).

The time-dependent simulation covers the stationary phase of the investigated discharge. The amount of He ions and atoms already present in the system at the initial time of the simulation is an initial condition. The simulation was performed with a constant time step of $5 \cdot 10^{-5}$ s.
The plasma background (in terms of kinetic profiles) is kept constant during the time window. In the discharge #39149, the He concentration in the core raises up to roughly 20 % following the external puff. Inside the LCFS only fully stripped He ions exist, as at any radial location the ionization rates for both charge transitions dominate over the recombination rates (cf. Fig. 4.5). Therefore any possible variation of the kinetic profiles due to the time variation of the He concentration is not expected to qualitatively affect the results.
Figure 4.8 shows the modelled He time traces in the various particle reservoirs for discharge #39149. The effective pumping speed on He atoms applied to the pump reservoir (Eq. (4.10)) was set to 7 m^3/s (cf. Section 3.4.1), while the conductance between divertor and pump neutral reservoirs (Eq. (4.9)) was set to obtain a pressure drop of 2 (cf. Section 3.4.2).
With the input parameters imposed by experiment and a proper choice of the free input parameters, the model successfully reproduced

the experimentally observed exhaust dynamics. The measured average He ion content in the confined plasma measured by CXRS (top plot in Fig. 4.8) and the neutral He density in the exhaust gas at the pump reservoir measured by the Penning gauge (bottom plot in Fig. 4.8) are matched before, during and after the external He injection phase. The proper choice of the transport coefficients also allowed the modelled He ion density profile in the core plasma to match the radially-resolved CXRS measurements at each time (see e.g. Fig. 4.3). The external source was imposed consistently with the experimental He puff, i.e. in the time window [3.0,3.3] s with an intensity of $1.25 \cdot 10^{21}$ injected He ions/s (aside possible uncertainties). The middle plots in Fig. 4.8 show the modelled amount of He atoms dynamically retained by the main and divertor wall surfaces in terms of surface densities. Whereas the dynamic content of He atoms implanted in the divertor wall closely follows that of the plasma and neutrals reservoirs, the main wall content constantly increases starting from its initial condition. This identifies the main wall as a net particle absorber throughout the time of a discharge, and the divertor wall as a more efficient recycling surface.
The model shows a very satisfactory balance between the numbers of integrated injected particles, permanently removed particles and dynamic particle content in the various reservoirs. As shown in the Fig. 4.9, the error in the numerical particle conservation at the end of the simulated time is less than 1 %. This corresponds to a residual of about 10^{19} particles, which is less than estimated error in the experimentally measured total number of He ions in the core plasma by CXRS (blue curve).

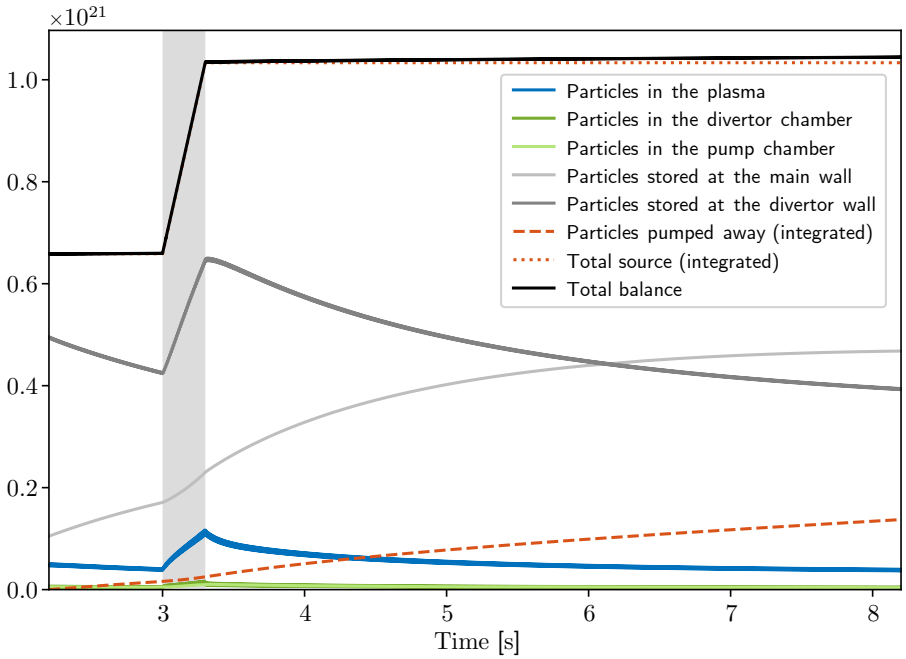

Figure 4.9: Global particle balance for discharge #39149. The dynamic value of the absolute number of particles in each reservoir is shown, as well as the integrated external source (through gas puff) and the integrated permanent sink (by active pumping). The numerical error is given by the difference between the black line (i.e. sum of total number of particles in the system and time-integrated sink by active pumping) and the dotted red line (i.e. the sum of total number of particles in the system at the beginning of the simulation and time-integrated source by external fueling).

Unless otherwise specified, the plots of the reservoir contents presented in this Section show temporal averages of the modelled time traces over ELM cycles, in the form

$$\langle n_{\mathrm{He}} \rangle (t) = \frac{1}{\Delta t_{\mathrm{ELM}}} \int_{t}^{t+\Delta t_{\mathrm{ELM}}} n_{\mathrm{He}}(t')\, \mathrm{d}t' \ , \tag{4.18}$$

where Δt_{ELM} is the duration of an ELM cycle.

Initial conditions of wall inventories

A successful application of the model requires an appropriate choice of the *initial conditions* for all the particle reservoirs. For the discharge #39149, these are referred to $t = 2.2$ s (Figure 4.8). The initial conditions for plasma and neutrals reservoirs (in terms of volume densities) are simply given by the experiment. The initial conditions for the wall reservoirs (in terms of surface densities), instead, are unknown and should be considered as free parameters of the model. We found that such initial conditions can be self-consistently chosen studying the behavior of the model itself. Figure 4.10 shows the impact of imposing different initial conditions for main and divertor wall reservoirs separately on the simulation results, with all other input parameters remaining unchanged.

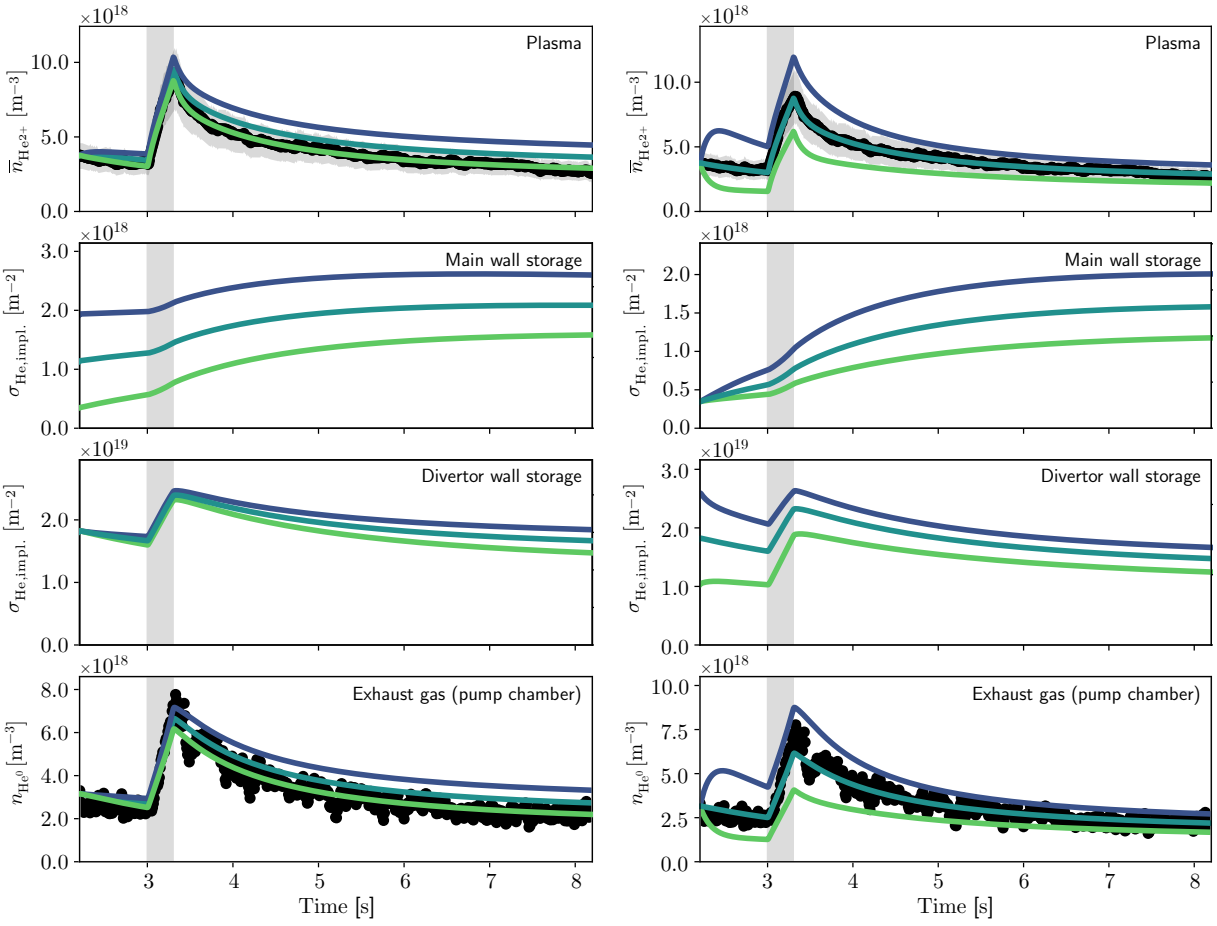

Figure 4.10: Sensitivity analysis of the modelling results on different initial conditions. Left: different colors indicate simulations performed with three different values for the initial conditions of the main wall reservoir (see second plot from top). Right: indicate simulations performed with three different values for the initial conditions of the divertor wall reservoir (see third plot from top). All other input parameters are kept the same.

Imposing different initial conditions for the main wall implies modelling a faster or slower decay of the He content in the plasma after the active injection phase, with the relevant recycling/pumping parameters (e.g. divertor retention time, pumping speed) remaining unchanged. This is consistent with the main wall being a net absorber of He atoms throughout plasma discharges: how many He atoms are already implanted into it at the beginning of a discharge will indicate how many more He atoms it can accommodate before reaching equilibrium, and how quickly it absorbs them.

Imposing different initial conditions for the divertor wall implies different responses, to such initial conditions, for the plasma and the neutrals reservoirs. If the initial divertor wall He

content is too high, then the modelled time traces for He ions in the plasma and He neutrals in the exhaust gas jump to larger values than the experimental ones. Indeed, if the modelled He content in the wall is higher than in reality, then also the modelled dynamic He particle release is too large to be compatible with the initial conditions for plasma and exhaust gas observed experimentally. This even though although the relevant plasma-wall interaction parameters (e.g. background fluxes towards walls, surface coefficients) are unchanged. Conversely, if the initial divertor wall content is too low, then the dynamic He particle release is too low as well and the modelled time traces for He ions in the plasma and He neutrals in the exhaust gas drop to smaller values than the experimental ones.
From this we conclude that there is only one initial value for both wall reservoirs compatible with the experiment. Therefore, such initial conditions for the wall reservoirs may be identified to reproduce the experimental observations. Their values can be obtained through the application of the model in a self-consistent way in order to fit the experimental behavior of the plasma and neutrals reservoirs.
The fact that a higher value of initially implanted He atoms in the walls translates into a higher simulated He content in the plasma and in the exhaust gas, even with otherwise identical input parameters, is also consistent with the experimentally observed impact of boronizations on AUG plasmas (cf. Section 3.4.3) [145, 146]: the measured core He concentration in discharges without He seeding decreases with the time distance from a boronization. The He concentration is indeed higher in discharges performed soon after a boronization than later.

Sensitivity analyses on free input parameters

In order to identify the impact of the free input parameters present in the model and set appropriate values for these, *sensitivity studies* were performed. Namely, simulations were run varying one free parameter individually, with all other input parameters kept fixed. The results were contrasted against the experimental data on He ion density in the plasma and He neutral atom density in the exhaust gas. The free parameters were chosen from the best fit to the experimental data. The results of the sensitivity analysis on few of such parameters, applied to the discharge #39149, are presented here.
First of all, the divertor retention time τ_{ret} is the parameter describing the backflow of He particles from the divertor reservoir towards the plasma (Eq. (4.8)). Assuming fixed transport coefficients in the plasma (hence a fixed core confinement time τ_{main}, which describes the flow of He particles leaving the plasma), such time is directly coupled with the He compression, as it can be shown that

$$C_{\text{He}} \propto \frac{V_{\text{plasma}}}{V_{\text{div}}} \frac{\tau_{\text{ret}}}{\tau_{\text{main}}} \,. \qquad (4.19)$$

Therefore, different imposed divertor retention times produce different ratios between He content in the plasma and in the divertor (Figure 4.11). The most appropriate value was 4 ms, as it reproduced the experimental ratio between the experimental He densities in the plasma and in the exhaust gas.

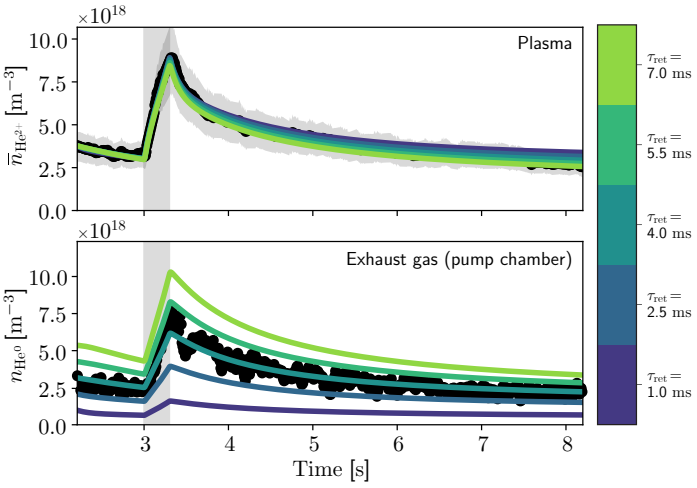

Figure 4.11: Results of a sensitivity analysis of the divertor retention time, based on the discharge #39149, with otherwise identical other input parameters. Only plasma reservoir and pump reservoir are shown.

This highlights that He compression must be considered as a purely experimental input. Without the knowledge of the He partial pressure in the exhaust gas, the time traces of the He ion density in the plasma can be fitted with a wide range of divertor retention times. This could lead to a misinterpretation of the role of the wall retention in the exhaust dynamics.

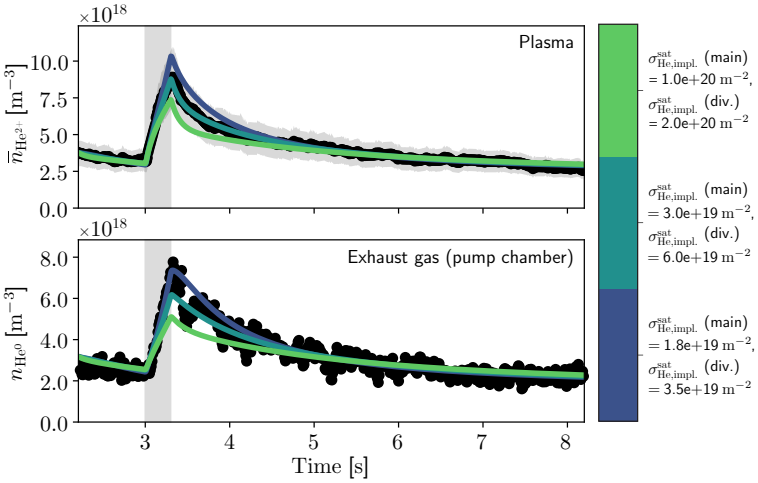

Figure 4.12: Results of a sensitivity analysis of the wall saturation densities for He, based on the discharge #39149, with otherwise identical other input parameters. Only plasma reservoir and pump reservoir are shown.

Further free parameters are the saturation densities $\sigma^{sat}_{He,wall}$ of He atoms implanted in the main and divertor walls, which limit the amount of He atoms which can be dynamically stored in the wall reservoirs (Eq. (4.6)). The sensitivity analysis (Figure 4.12) shows that, increasing the saturation densities, the wall pumping effect becomes more relevant and the same He gas puff results in a smaller increase of the He content in the plasma and in the neutral gas. The reason is a larger fraction of the injected He particles being promptly absorbed by the walls. For the present case, the most appropriate values were $3 \cdot 10^{19}$ He atoms per m^2 for the main wall and $6 \cdot 10^{19}$ He atoms per m^2 for the divertor wall. A higher value for the divertor wall is to be expected because of the higher average impact energy.

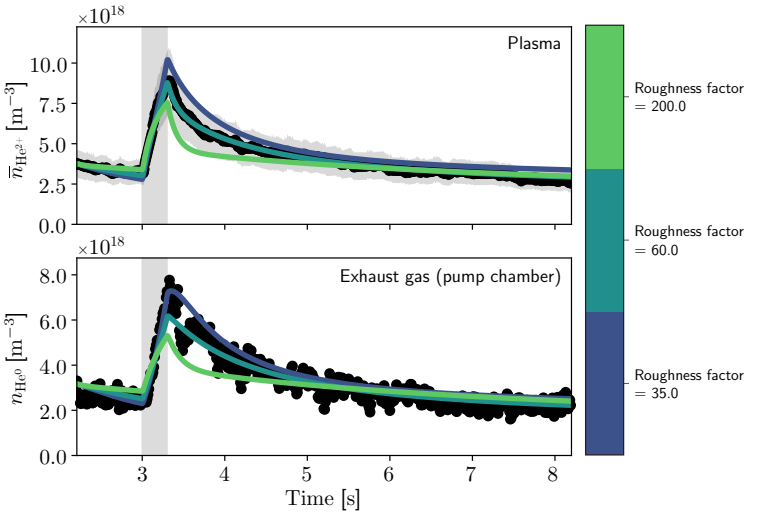

Figure 4.13: Results of a sensitivity analysis of the wall roughness factor, based on the discharge #39149, with otherwise identical other input parameters. Only plasma reservoir and pump reservoir are shown.

A final relevant free parameter is the roughness factor, which multiplies the geometric main and divertor wall surface areas (which are defined as 5 m^2 and 0.5 m^2, respectively) when converting He implantation densities into absolute numbers of implanted He atoms in the walls. The sensitivity analysis (Figure 4.13) shows that the effect of wall roughness is similar to that of the wall saturation densities. In both cases, the maximum absolute numbers of He atoms that the walls can dynamically accommodate increase. Multiplying the geometric areas by a factor of 60 is required to correctly reproduce the experimentally observed dynamics. If it were smaller, the walls would not be able to accommodate a sufficient number of He atoms to reproduce the experimental measurements in the plasma and in the exhaust gas.

4.3.2 Characterization of the behavior of the wall reservoirs

The results presented above have already highlighted the role of the wall reservoirs for the global He particle balance. Figure 4.9 readily shows that the total He content in the walls is up to one order of magnitude larger than that in the plasma.
This is consistent with the experimental observation of a He particle content in the plasma in AUG discharges without any active He seeding being roughly constant over the timescale of a discharge. This indicates the presence of a wall source which is also constant. In turn, the presence of a constant wall source while more He atoms are eroded indicates that the dynamic wall inventory must be comparatively larger than the amount of He particles which are released during an entire discharge.

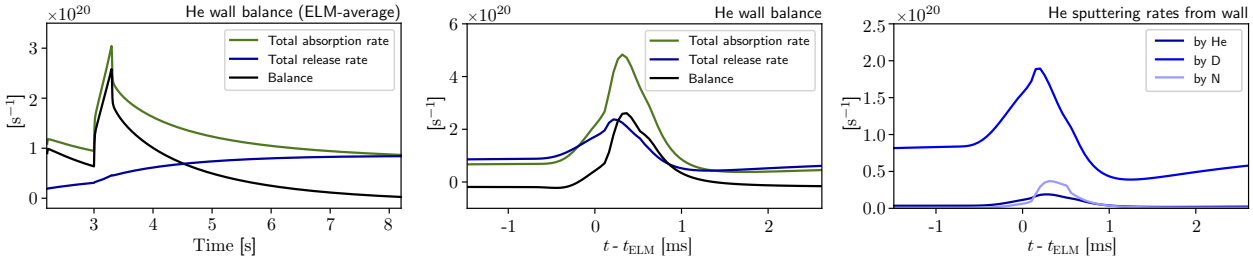

Figure 4.14: Modelled particle balance for the main wall for the discharge #39149. From left to right: individual ELM-averaged absorption and release rates, determining the dynamic wall behavior; zoom-in in time of the absorption and release rates during an ELM event (at t = 8.0 s); decomposition of the release rate during an ELM event in terms of the eroding species.

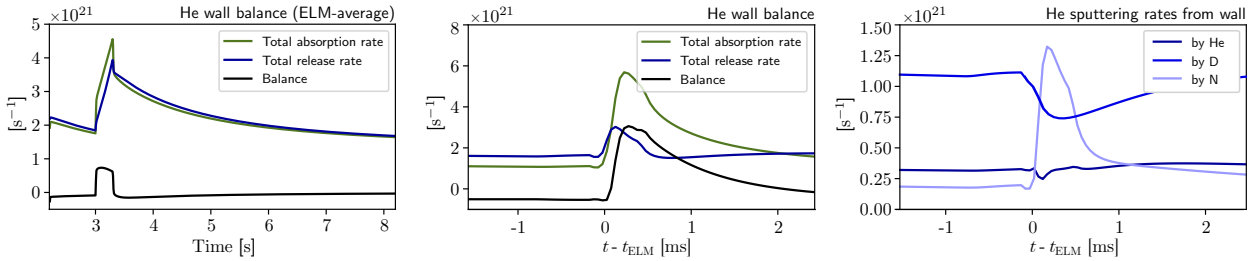

Figure 4.15: Same as Fig. 4.14, but for the divertor wall.

Global wall inventory balances

The balance between absorption and release rates into/from the wall reservoirs is crucial for matching the experimental measurements in the plasma and neutrals reservoirs. The main wall reservoir constantly acts as a net sink for He ions from the plasma, as the modelled amount of implanted He atoms always increases throughout the discharge. The divertor wall reservoir instead acts as a net source of He atoms, as the modelled amount of implanted He atoms decreases after the external puff. This was shown in Fig. 4.9 and is further addressed in the left plots of Figs. 4.14 and 4.15, which show the individual ELM-averaged absorption and release rates for main and divertor walls, respectively. For the main wall, the absorption rate is always higher than the release rate. For the divertor wall, the release rate is slightly higher than the absorption rate, apart from the time window of the external puff.
Table 4.1 contains the modelled global particle balance for main and divertor wall reservoirs integrated over the decay phase of the He content of the discharge #39149, i.e. in the time window [3.3,8.2] s.
The main wall has absorbed $2.46 \cdot 10^{20}$ He atoms, while the divertor wall has released $2.69 \cdot 10^{20}$ He atoms. We note that many more He atoms are exchanged (absorbed and released) with the divertor wall than with the main wall, although the divertor wall surface area is smaller

Table 4.1: Particle balance for the main and divertor wall reservoirs for discharge #39149 during the decay phase (i.e. time window [3.3,8.2] s). The balance is given by the difference between absorbed and released He atoms within the considered time window. The decomposition of the total number of released He atoms in terms of eroding species is also shown.

	Main wall reservoir	Divertor wall reservoir
Initial content ($t = 3.3$ s)	$2.39 \cdot 10^{20}$	$6.74 \cdot 10^{20}$
Final content ($t = 8.2$ s)	$4.85 \cdot 10^{20}$	$4.05 \cdot 10^{20}$
Wall balance	$\mathbf{+2.46 \cdot 10^{20}}$	$\mathbf{-2.69 \cdot 10^{20}}$
Total absorbed He atoms	$6.01 \cdot 10^{20}$	$10.35 \cdot 10^{21}$
Total released He atoms	$3.55 \cdot 10^{20}$	$10.62 \cdot 10^{21}$
(released by He sputtering)	$0.23 \cdot 10^{20}$ (6.5 %)	$2.81 \cdot 10^{21}$ (26.5 %)
(released by D sputtering)	$3.18 \cdot 10^{20}$ (89.6 %)	$6.11 \cdot 10^{21}$ (57.5 %)
(released by N sputtering)	$0.14 \cdot 10^{20}$ (3.9 %)	$1.70 \cdot 10^{21}$ (16.0 %)

than that of the main wall. This is not surprising given the much higher ion fluxes reaching the divertor. It is also worthwhile to note that the effect of the two walls combined (i.e. the net sum of the two wall balances) is only a moderate net release of He atoms towards the plasma when integrated over the decay phase ([3.3,8.2] s). What mostly affects the decay of the He content in the plasma is the fact that He particles might undergo several absorption/release cycles into/from the walls before being permanently removed by active pumping.

Saturation behavior of wall reservoirs

The modelled saturation levels ($\sigma_{\mathrm{He,wall}}/\sigma^{\mathrm{sat}}_{\mathrm{He,wall}}$) are far below unity, especially for the main wall, in which it stays below 10 % (see Fig. 4.8). Since the main wall is further away from saturation than the divertor wall, it constantly acts as a particle absorber. The elevated absorbing capability of the two walls implies that, even with constant external He gas puff, wall saturation with He is hardly reachable within the time of a discharge (see also Section 4.3.3). This is consistent with the experimental observation that the He content in AUG plasmas increases, when a constant puff is applied, without reaching a constant equilibrium value.
The values for the saturation density chosen after performing a sensitivity analysis (cf. Section 4.3.1) are $3 \cdot 10^{19}$ m^{-2} for the main wall and $6 \cdot 10^{19}$ m^{-2} for the divertor wall. The larger value for the divertor wall comes from the higher average impact energy of He ion projectiles striking this, which may then penetrate deeper into the material lattice. The chosen values are roughly consistent with past experimental observations. It was observed that W surfaces can accommodate up to $5 \cdot 10^{19}$ He atoms per m^2 when bombarded with 200 eV He beams, or up to $10 \cdot 10^{19}$ He atoms per m^2 when bombarded with 600 eV He beams [37]. Values of the same order were found in more recent studies [39, 143, 144].
In particular, the measured retention of He atoms in tungsten is about one order of magnitude larger than what is observed in carbon [37]. The more efficient retention of He atoms in tungsten is a major player in explaining the well detectable He content in AUG plasmas even in discharges without active He seeding w.r.t. that observed in the full-C AUG. This highlights the key role of the walls as particle reservoirs in this modelling.

Inter- and intra-ELM plasma-wall interaction

The middle plots of Figs. 4.14 and 4.15 show a zoomed-in excerpt of the same modelled absorption/release rates of the left plots, for main and divertor walls respectively, but without temporal averaging over ELMs. This allows to observe the modelled wall behavior over an ELM cycle.

During ELMs, the sudden increase of wall fluxes results in an increase of both implantation and sputtering rates. However, the increase of the implantation rates prevails over the increase of the sputtering rates for both main and divertor walls. This means that the net effect of ELMs is a transient amplification of wall absorption of He particles. This is different from the impact of ELMs to the wall materials, whose global release rate was seen to be amplified during ELMs in tungsten erosion studies [165].
The right plots of Figs. 4.14 and 4.15 show the decomposition of the sputtering rates in terms of eroding species, for main and divertor walls, respectively. For the main wall, He release is dominated by D sputtering both between and within ELMs. For the divertor wall, the sputtering by impurities (He itself and N) is proportionally higher than for the main wall, but still less relevant than D sputtering in inter-ELM phases. During ELMs we note a decrease of D sputtering and a strong increase of N sputtering. The latter component temporarily becomes the dominant one, although the N flux towards the wall surface is much less than the D flux. This is explained by the sputtering yield for He atoms released by D decreasing at the impact energies of thousands of eV assumed at the ELM peak (see Fig. 4.7). At the same energy, instead, the sputtering yield for He atoms released by N is much larger than at inter-ELM energies.

Global He erosion sources by different sputtering species

The contribution to the erosion of He atoms implanted in the walls by the various species is now assessed. Globally (see Table 4.1), the release of He atoms from the main wall is dominated by D sputtering. Instead, for the divertor wall, which is the most relevant source of He atoms, almost half of the released He atoms are due to impurity sputtering (He self-bombardment and N bombardment). N sputtering causes about 16 % of the He release from the divertor wall although the N content in the modelled discharge is very moderate (the N fueling (in ions/s) is only 3 % of the D fueling).
It may then be expected that, in discharges with strong N fueling, N becomes the main eroding species for He atoms implanted in the walls. This is consistent with the observation in the discharge #41156 (cf. Section 3.4.4) in which, when the N fueling is ramped from 0 to 13 % of D fueling (in ions/s), the amount of He in the plasma roughly doubles (see Fig. 3.15). According to these numbers, the additional amount of N ions provides a new source of He particles for the plasma, as a result of additional wall erosion, of the same amount as already caused by erosion by D ions.

Validity of the plasma-wall interaction calculations

The presented results regarding implantation and erosion of He atoms into/from the W surfaces were achieved through simplified calculations and by means of several ad hoc assumptions.
Whereas in our model erosion due to ion bombardment is the sole mechanism allowing implanted impurity atoms to be released from the wall, in principle also outgassing due to thermal effusion may play a role, because of the PFCs temperatures reaching up to 1000 K during plasma discharges. He outgassing could be estimated by measuring the He partial pressure in the exhaust gas immediately after the end of plasma discharges, when the wall surfaces are still hot and thermal release is still comparable to that during the plasma phase. However, such measurements are difficult: the Penning gauges do not operate anymore as soon as the magnetic field is shut off (cf. Section 3.3.2), and attempts to use conventional and high-resolution mass spectrometers for measuring the He partial pressure at AUG have been, so far, unsuccessful (cf. Section 3.3.1). It is expected, however, that, during plasma discharges, outgassing is much less relevant than erosion. This is supported by the dynamic behavior of He in the discharge #41156 after the start of N seeding (see Fig. 3.15): a more than doubled He density in the plasma only after the start

of N seeding points in the direction that any release due to erosion dominates over the release due to outgassing.
A further issue is the very large value of the roughness factors found to fit the experimental data (cf. Section 4.3.1). If using the mere geometric plasma-wetted areas for the plasma-wall interaction calculations (i.e. 5 m^2 and 0.5 m^2 for main and divertor walls, respectively), the resulting particle exchange between plasma and wall surfaces would not be sufficient to reproduce the observed dynamics, and a roughness factor of 60 is seen to be required in the presented modelling. This implies a much higher number of He atoms which the wall can accommodate before saturating, still using the same values for the saturation densities as suggested by experimental evidence [37].
The need for a roughness factor larger than 1 is reasonable, as the employed reflection coefficients and sputtering yields were calculated by assuming polished W surfaces. Effective surface coefficients of rough surfaces might be much different than the ones of polished surfaces [179, 180]. Plasma-exposed W PFCs at AUG show a roughness of the order of several µm [181]. The implantation profile of He atoms retained in W surfaces only extends to a depth of few nm [39]. It is therefore not surprising that accounting for wall roughness would imply increased effective surface areas in which He atoms can be implanted, when using surface coefficients calculated for polished surfaces. However, how roughness relates to an effective surface area to be used for plasma-wall interaction calculation is difficult to quantify. Roughness is indeed usually defined just as the vertical deviation of a surface topography from the mean height.
Such a multiplication factor, which we qualitatively consider by accounting for wall roughness, is not intended to have any precise physical meaning. We do not claim that roughness does increase the effective surface area exposed to the plasma fluxes by a factor of 60. Rather, this factor should be regarded as an arbitrary parameter whose specification is required to fit the experimental measurements and model the global picture of how many He particles are dynamically contained in the various particle reservoirs and of the particle exchange rates between plasma and walls. Any other statement about the wall morphology is beyond the scope of this work.

4.3.3 Impact of active pumping and wall retention on the exhaust dynamics

The most relevant feature of the present multi-reservoir particle balance model is the possibility to disentangle the impacts of the *inefficient pumping system* and the *long-term wall storage* in determining the helium exhaust dynamics at AUG.
For this we performed a series of simulations employing the same physics-based input parameters as described in the Section 4.2 and changing the input parameters related to active pumping and wall retention one at a time. The following simulations are compared:

1. The full simulation (i.e. the one of Fig. 4.8) with realistic pumping speed ($S_{\mathrm{pump}} = 7$ m^3/s, i.e. considering only the effect of the AUG turbomolecular pumps) and activated wall retention model.
2. A simulation with realistic pumping speed ($S_{\mathrm{pump}} = 7$ m^3/s) and with deactivated wall retention model (i.e. the wall is fully recycling).
3. A simulation with enhanced pumping speed ($S_{\mathrm{pump}} = 127$ m^3/s, which simulates a case where He atoms are removed also by the AUG cryopump), and activated wall retention model.
4. A simulation with enhanced pumping speed ($S_{\mathrm{pump}} = 127$ m^3/s) and fully recycling wall.

Removal rate

In a first test, the *helium removal rate* is investigated following the decay phase without any active external fueling. The simulations were started at t = 3.3 s, i.e. at the end of the active injection phase when the He content is maximum. In the simulations (1) and (3), with activated wall retention model, the initial wall particle content is the one modelled in the main simulation (Figure 4.8) at the time t = 3.3 s. In the simulations (2) and (4), with deactivated wall retention model, there is no need to impose an initial particle content in the wall reservoirs as these are not filled. Figure 4.16 shows the modelled decay curves. Table 4.2 gives the global particle balance for the modelled time window.

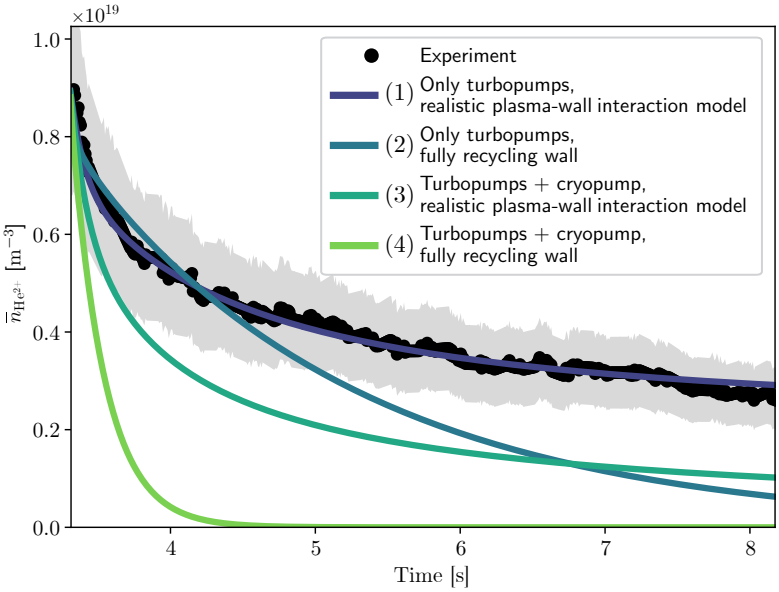

Figure 4.16: Modelled decay of the He content in the plasma, starting at the experimental conditions of the discharge #39149 at t = 3.3 s, for the four test simulations described in this paragraph. No external He fueling is applied during the simulation time, and the same input parameters (apart from wall and pump settings) are used.

Table 4.2: Global particle balance for the four simulations shown in Fig. 4.16. The columns contain (from left to right): initial and final total number of He particles within plasma + neutrals reservoirs; initial and final total number of He atoms implanted into the walls; total source (+) or sink (-) effect given by the walls and by the pump, respectively, for plasma + neutrals reservoirs; total He particles removed from plasma + neutrals reservoirs.

	Plasma + neut. (init.)	Plasma + neut. (fin.)	Walls (init.)	Walls (fin.)
Simulation (1)	$1.38 \cdot 10^{20}$	$0.42 \cdot 10^{20}$	$9.13 \cdot 10^{20}$	$8.90 \cdot 10^{20}$
Simulation (2)	$1.38 \cdot 10^{20}$	$0.10 \cdot 10^{20}$	-	-
Simulation (3)	$1.38 \cdot 10^{20}$	$0.15 \cdot 10^{20}$	$9.13 \cdot 10^{20}$	$4.47 \cdot 10^{20}$
Simulation (4)	$1.38 \cdot 10^{20}$	$0.00 \cdot 10^{20}$	-	-

	Wall source/sink	Pump sink	Net balance for plasma + neut. reservoirs
Simulation (1)	$+0.23 \cdot 10^{20}$	$-1.19 \cdot 10^{20}$	$-0.96 \cdot 10^{20}$ **(70 % removed)**
Simulation (2)	-	$-1.28 \cdot 10^{20}$	$-1.28 \cdot 10^{20}$ **(93 % removed)**
Simulation (3)	$+4.66 \cdot 10^{20}$	$-5.89 \cdot 10^{20}$	$-1.23 \cdot 10^{20}$ **(89 % removed)**
Simulation (4)	-	$-1.38 \cdot 10^{20}$	$-1.38 \cdot 10^{20}$ **(100 % removed)**

In the simulations (1) and (3), in which the wall retention model is employed, the dynamics of the He decay in the plasma is characterized by two phases: a relatively quick decay in the first 1−1.5 seconds of the simulations is followed by a slower decay. This is caused by the presence of a source of particles from the wall, which tends to compensate pumping effect towards the end of the simulation. In the simulations (2) and (4), in which the wall retention model is deactivated, the decay has a nearly exponential trend, which is dominated by the slowest time scale of the system, set by the pumping speed (cf. Section 4.3.5).
Removal of He particles becomes more efficient without wall retention (simulation (2)) w.r.t. the full model (simulation (1)), albeit keeping the same pumping speed. This is explained noting

that He particles absorbed by the walls in simulation (1) are not permanently removed from the system, as they can re-enter in the plasma. In simulation (2) we exclude the possibility for He particles to be temporarily retained in the wall reservoirs. Wall retention, in this sense, delays a permanent removal of He particles from the system as they spend some amount of time stuck in the walls. Indeed, in the first second of the decay, simulation (2) starts with a slower decay than in simulation (1), because there is no wall absorption effect in the former. After few seconds, however, the decay in the simulation (1) becomes slower because, in this case, the He particles previously absorbed from the wall are re-injected in the plasma.
Enhancing only the pumping speed (simulation (3)), maintaining the wall retention model activated, we also note an expected enhancement of the removal efficiency w.r.t. the full model (simulation (1)). Since the active removal is faster, He particles have indeed less time to interact with the wall (and hence be absorbed). In this case the removal is, however, still hindered by the possibility for He particles to spend time within the walls. After the first quickly decaying phase, the decay of the He content slows down because of the wall still acting as a source of particles for the plasma.
In simulations (2) and (3), the He content at the end of the modelled time window is similar, although the underlying exhaust dynamics is very different. Therefore, we conclude that wall retention and inefficient pumping individually play a similar quantitative role in hindering the global helium removal over a time scale comparable with AUG discharges (5−10 seconds). In both cases the usual duration of an AUG discharge would be not enough to remove all the He particles, if starting with an initial He concentration of 20 % in the plasma. Only with both wall retention deactivated and enhanced pumping (simulation (4)) the He content decays to roughly zero within the time of a discharge.

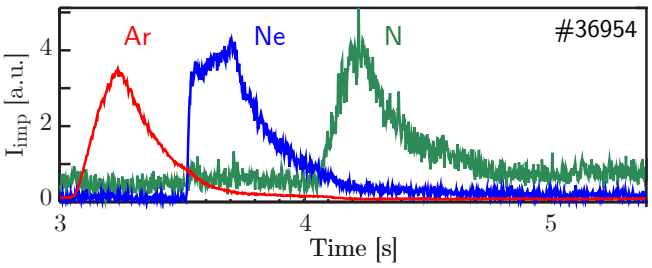

Figure 4.17: Time traces of the line intensity signals from main chamber UV spectroscopy for radiating impurities (argon, neon and nitrogen) showing the decays after short injection phases. As the main chamber plasma is less affected by the concentration of radiating impurities than the divertor plasma, such signals are a good proxy for the time evolution of the relative impurity densities. Adapted from [138].

The modelling results also reflect the experimentally measured decay of the concentration of radiating impurities after external active injection at AUG (Figure 4.17). Nitrogen (green line) is efficiently removed by the cryopump, and shows a high retention in tungsten due to chemical bonding [154, 155]. After active injection, there is a quick decay phase of roughly 1 second, after which its removal rate slows down and its concentration in the plasma approaches a nearly constant value because of a constant wall source. This behavior is qualitatively similar to the simulation (3) in the Fig. 4.16. Argon and neon (red and blue lines respectively) are also efficiently removed by the cryopump, but their retention capability in tungsten is negligible. After active injection the concentration of both decays to nearly zero in less than 1 second, being the effect of a wall source less relevant. This behavior is qualitatively similar to the simulation (4) in the Fig. 4.16. Although the pumping rate also depends on the various compression values in the divertor, which strongly differs for different species [147], such qualitative comparison supports the impact of wall retention on the exhaust dynamics as captured by our model.
This result highlights that, even if the AUG cryopump were designed to efficiently remove He atoms, they can not be totally pumped within the time of a plasma discharge. The delay in the permanent removal caused by the several wall absorption/release cycles, which individual He atoms undergo before being pumped, is closely linked to the intrinsic behavior of the interaction with tungsten. Arbitrarily increasing the applied pumping speed may reduce this effect, but

never completely overrule it. Pollution of the plasma with some amount of helium is unavoidable for short-pulsed full-W tokamaks, if the wall has been somehow loaded with He atoms, because of the continuous release of these from the wall surfaces.

Equilibrium behavior

We also performed a similar test aimed to quantify the impact of the *wall saturation behavior* on the equilibrium value of the He content in the plasma. The same simulations (1–4) were performed, starting with empty reservoirs and applying a constant He fueling rate of $1.25 \cdot 10^{21}$ ions/s (i.e. the same one as applied in the discharge #39149, but therein only for 300 ms). Figure 4.18 shows the modelled increase of the He content in the plasma.

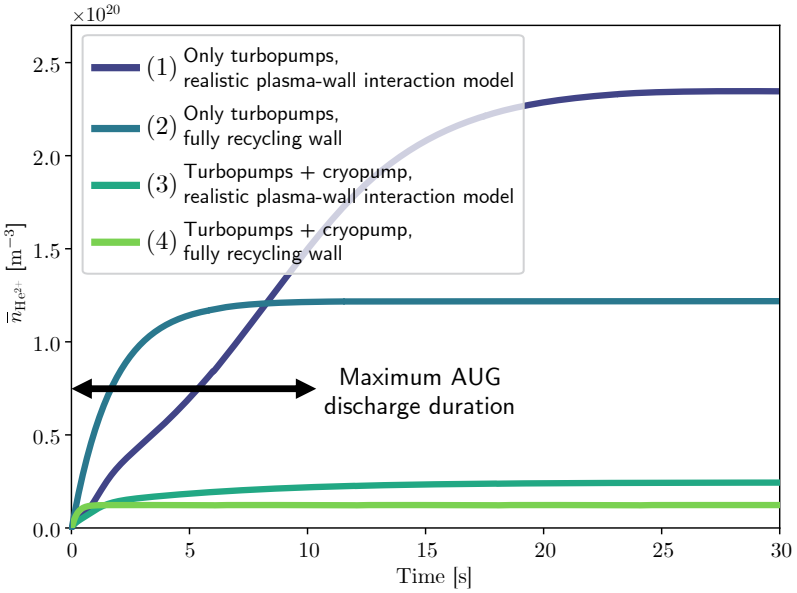

Figure 4.18: Modelled increase for the He content in the plasma, starting with empty reservoirs, at the same background plasma conditions of the discharge #39149, with a constant He fueling rate of $1.25 \cdot 10^{21}$ ions/s, assuming an indefinitely long discharge. The same input parameters (apart from wall and pump settings) are used.

Pumping plays a quantitatively major role in the modelled accumulation of helium in the plasma. In the two simulations with only turbomolecular pumps considered (simulations (1) and (2)) an equilibrium value for the He content in the plasma is reached over a time scale longer than that of a single discharge. The modelled equilibrium density values are larger than 10^{20} m^{-3}, i.e. even larger than the density of the main species, leading to an unacceptable accumulation. With an effective cryopump (simulations (3) and (4)), instead, the equilibrium density values are around $1 - 2 \cdot 10^{19}$ m^{-3}. However, also in simulation (3), equilibrium is reached over a time scale longer than a single discharge, because of the wall being continuously filled during the external injection. Therefore, even if the AUG cryopump were designed to efficiently remove He atoms, a constant concentration in the plasma may not be achieved with a constant puff. Only in the simulation (4), i.e. with effective cryopump and deactivated wall retention model, equilibrium is reached in less than 1 second.
It is also noteworthy that, in the simulations with activated wall retention, the He particle inventory in the walls at equilibrium is less than the imposed maximum value. This results from a dynamic balance between implantation and sputtering. For simulation (1), the surface densities of implanted He atoms at the main and the divertor walls are 33 % and 57 % of the respective saturation densities. For simulation (3), these are 15 % and 44 %. Different values would be achieved with different plasma backgrounds, i.e. with different sputtering rates from D ions and N ions.

4.3.4 Impact of plasma-wall interactions on edge transport

The plasma-wall interaction model also impacts the modelled He ion density profiles in the plasma. Externally injected and promptly released neutrals reach the plasma as thermal particles, with energy determined by room and main wall temperatures, respectively. Reflected and sputtered neutrals, instead, are emitted as energetic particles, at up to several tens of eV (cf.

Section 4.2.4). It is, therefore, expected that these particles penetrate and are ionized deeper in the core, with a same fixed plasma background. The neutrals profile is roughly modelled according to Eq. (4.5). The model used for the neutral penetration into the plasma is very crude. A Monte-Carlo-based approach for following the trajectories of the recycled neutrals until their ionization location, as it is done e.g. in DIVIMP [157], would be preferable. Nonetheless, a qualitative interpretation for the impact of the plasma-wall interactions on the He ion density profiles in the plasma may still be given. The impact of the energy of the recycled neutrals is highlighted by comparing the modelled He ion density profiles in simulations with and without plasma-wall interaction model activated. In the second case, all particles hitting the main wall are released towards the plasma as thermal neutrals, i.e. at 0.025 eV.

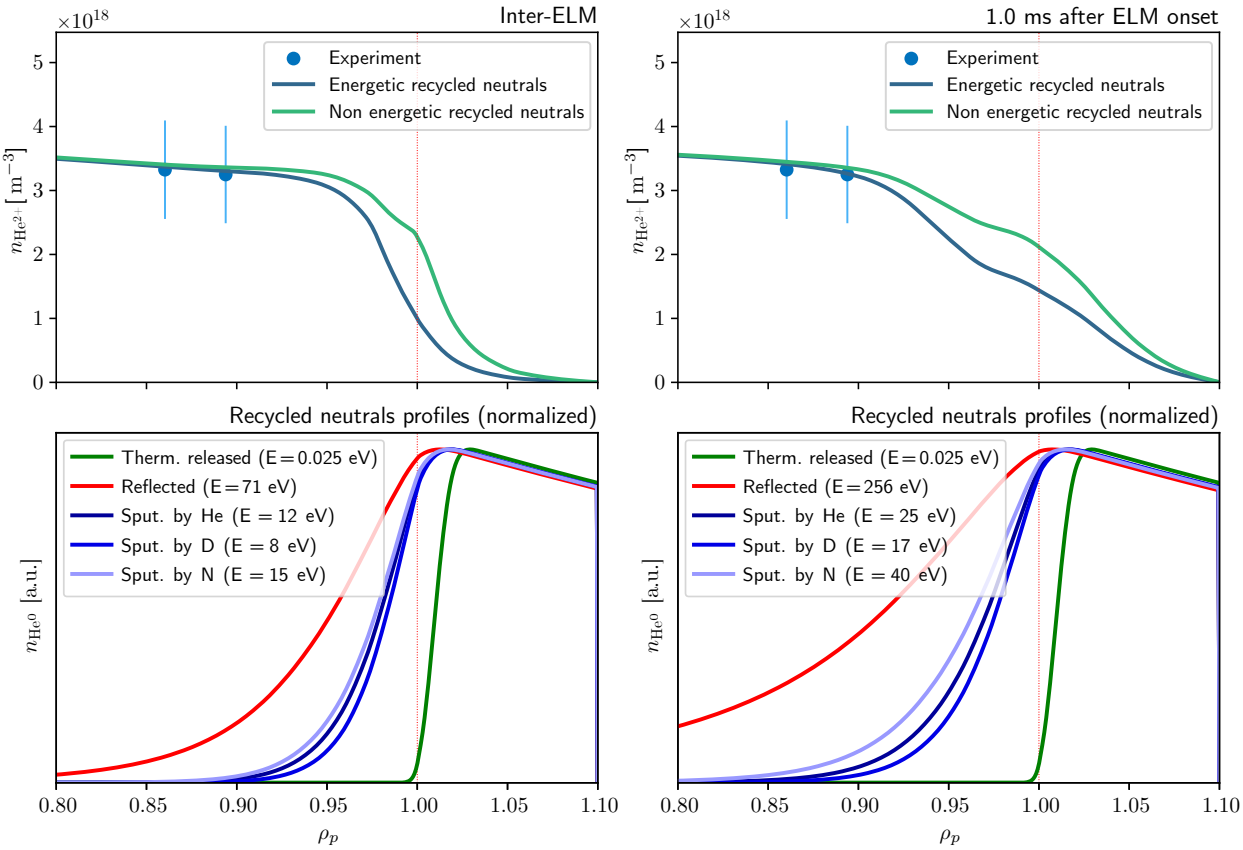

Figure 4.19: Top row: modelled He^{2+} density profiles (inter- and intra-ELM) in the edge region with and without employing the plasma-wall interaction model, with otherwise same input parameters. Bottom row: normalized neutral He density profiles employed as source terms for the plasma transport equations, at the same inter- and intra-ELM times, for different populations of He neutrals recycled from the main wall, in the simulation in which the plasma-wall interaction model is used.

The bottom plots in Fig. 4.19 show the neutral He density profiles, estimated according to Eq. (4.5), for the different populations of He neutrals recycled from the main wall. Both inter- and intra-ELM times are considered. The neutrals contribute to the source term in the transport equations (Eq. (4.3)) for the first ionized state. The profiles shown here are normalized to highlight the different shapes. The nearly exponential decay of the neutral He content is slower with increasing energy, resulting in a deeper penetration into the plasma.
The top plots in Fig. 4.19 compare the modelled He ion density profiles with and without employing the plasma-wall interaction model. If the recycled neutrals are not energetic, they are ionized at larger radii (i.e. green curves in the bottom plots of Fig. 4.19). Since the profiles are constrained by the available experimental data in the inner core, this results in a higher He ion density in the edge region. Here different radial gradients are modelled, at both inter- and

intra-ELM times, although the used transport coefficients are the same. The radial gradients of the He ion density profile in the edge, measured in [142], could only be reproduced, with neoclassical transport coefficients within the ETB, taking into account the deeper penetration of reflected and sputtered neutrals.
In order to not misinterpret the Fig. 4.19 it should be also stressed that, in the reality, a different source from wall-recycled neutrals in the plasma would affect the He ion density profile in the entire plasma, and not only in the edge. This is not readily visible in Fig. 4.19 as here the modelled profiles are constrained by the experimental data, available only in the inner core. The only conclusion we can draft is that different radial gradients of the He ion density profile in the edge are simulated, with identical transport coefficients, using different assumptions for the plasma-wall interaction.
The major contribution to the impact of plasma-wall interaction on the simulated radial He ion density gradient comes from the reflected neutrals (red curves in the bottom plots of Fig. 4.19). Not only are they more energetic, but also constitute the largest fraction of the recycled neutrals at the main wall, since the particle reflection coefficient of He ions on W is larger than 0.80 (cf. Fig. 4.6). Therefore, this effect is not much related to the high retention capability of He atoms in W, as the sputtered He neutrals are fewer than the reflected ones. It could be expected that the same effect takes place also for other impurities which are not significantly retained by the main wall surface.

4.3.5 Implications of the results

The modelling results presented in this Section have confirmed that the wall plays a major role in acting as a dynamic source and sink for impurities in the plasma, at least for the case of helium in a short-pulsed tokamak with full-tungsten wall. The absolute number of He atoms dynamically retained in the walls is about one order of magnitude larger than the sum of He particles dynamically in the plasma and neutrals reservoirs (Figure 4.9). Temporary retention of He atoms in the wall slows down the permanent removal of helium at AUG in a quantitatively similar way as the lack of an efficient pumping system (Figure 4.16). This suggests that any attempts to fit the time-dependent He concentration in short-pulsed tokamaks with models which do not make use of wall reservoirs for particle storage may result in a misleading interpretation of the underlying physics.
The model presented here is mostly interpretative. Predictive capabilities are mainly limited by the lack of information about the initial wall inventory, which is a required input for the model and can only come from experimental data (cf. Section 4.3.1). Nonetheless, several general implications for impurity transport and exhaust studies and burning plasma behavior can be formulated.

Impurity transport studies

The simulated He ion transport in the edge was shown to be strongly affected by plasma-wall interaction. This is caused by the deeper penetration up to the pedestal top of the energetic reflected and sputtered He atoms from the main wall. The particle source by ionization of such neutrals has an impact on the simulated He ion density gradient, even with fixed transport coefficients (Figure 4.19). This does not affect the simulated He ion density gradient in the inner core, where the particle source by recycled neutrals is negligible.
This implies that a correct assessment of main wall recycling does affect the experimental inference of impurity transport in the plasma edge, or, vice versa, the prediction of the pedestal profiles with prescribed transport coefficients.
It is worthwhile to note that, in ITER, the edge/SOL plasma temperatures are expected to be

considerably higher than in AUG. This would imply a shallower penetration of the neutrals recycled from the main wall, and hence a minor impact of the neutral source term inside the LCFS on the impurity density profiles at the edge.

Prediction of divertor retention

Another important implication is the impossibility to estimate divertor retention of recycling impurities from experiments through analytical models only relying on core plasma measurements, unless wall saturation is reached. In [153] impurity compression is inferred from a multi-reservoir model similar to the one that we employed, fitting time-dependent impurity density measurements from the core plasma. This is possible only as long as there are no other net particle sources or sinks for the plasma, apart from the exchange with the divertor neutrals reservoir. The presence of a fully recycling wall is one basic assumption for the analytic equations on which this model is based. The previous studies at AUG with full-C wall [78, 79, 80] also relied only on core He measurements, and estimated He compression according to the model described in [153]. We assume that the poorer retention capability of He atoms in a C surface [37] may result in a wall closer to saturation, fulfilling the basic assumptions of the model described in [153]. For the case of a full-W device, the wall is far from being saturated with He atoms, and a model neglecting wall retention should not be applied.
A necessary ingredient for the quantification of the wall effects and the interpretation of the exhaust dynamics in the full-W AUG was the possibility to consider He compression as an experimental input, thanks to the combination of measurements from CXRS and in-vessel Penning gauge. The modelling of the absorption and release rates from the walls is constrained by the experimental He compression. The opposite process, i.e. an inference of the compression without any experimental data for the impurity partial pressures, may lead to misleading results. A wide range of values of the divertor retention time, indeed, fit the core plasma measurements equally well, employing different assumptions on the initial conditions of the wall inventories (Figure 4.11). Whereas this holds for the case of helium and nitrogen, divertor compression of other recycling impurities presenting a minor retention in a W-wall (e.g. argon and neon) may be still roughly estimated only using core data [147].
This highlights the importance to have reliable partial pressure measurements of impurities in the exhaust gas. For ITER, it is planned to use residual gas analyzers for such a task, to be installed in remote areas w.r.t. to the vacuum vessel [182, 183]. This solution is not sufficient for short-pulsed devices like AUG, because of the response time and time resolution of mass spectrometers both being of the order of seconds (cf. Section 3.3.1), but may be successful for ITER-relevant discharge time scales. Optical Penning gauges are, at the moment, the only solution which allows measuring impurity partial pressures in the exhaust gas directly at the divertor in short-pulsed devices.

Helium confinement in burning plasmas

In a burning plasma, a constant core source of He ions will be present as a result of the D-T fusion reactions. The source is $3.53 \cdot 10^{11}$ He ions per watt of fusion power. Future fusion devices will have pulse duration of minutes (like ITER) or even hours (like DEMO). The modelling results show that saturation of a full-W wall with regard to He atoms is expected to be reached relatively soon after the start of the discharge (Figure 4.18). In equilibrium, influx and outflux of He particles into/from the walls will be equal.
Therefore, the model presented here may be used to infer a global *helium confinement time* τ_{He}, which describes the helium exhaust efficiency in steady-state conditions. This is possible by analyzing the modelled fluxes in the simulations shown in Fig. 4.18, which use experiment-based

input parameters, at the limit in which equilibrium between plasma and wall reservoirs is reached. In this way we extrapolate the behavior of AUG, in terms of helium exhaust, towards a fusion reactor, and we can evaluate this in view of burning plasma requirements (cf. Section 1.2.1).
In equilibrium, when influx and outflux of He particles into/from the wall are equal, the walls do not affect the dynamic balance of He particles in the system anymore. For this case, our model is reduced to an analytical multi-chamber model, as the one described in [16]. The equations describing the dynamic behavior of He particles would be

$$\frac{dN_{\mathrm{He}}^{\mathrm{plasma}}}{dt} = -\frac{N_{\mathrm{He}}^{\mathrm{plasma}}}{\tau_{\mathrm{main}}} + \frac{N_{\mathrm{He}}^{\mathrm{div}}}{\tau_{\mathrm{ret}}} + \Phi_{\mathrm{He}}^{\mathrm{ext}} \ , \tag{4.20}$$

$$\frac{dN_{\mathrm{He}}^{\mathrm{div}}}{dt} = +\frac{N_{\mathrm{He}}^{\mathrm{plasma}}}{\tau_{\mathrm{main}}} - \frac{N_{\mathrm{He}}^{\mathrm{div}}}{\tau_{\mathrm{ret}}} - \frac{N_{\mathrm{He}}^{\mathrm{div}}}{\tau_{\mathrm{pump}}} \ . \tag{4.21}$$

Here, $N_{\mathrm{He}}^{\mathrm{plasma}}$ and $N_{\mathrm{He}}^{\mathrm{div}}$ are the absolute numbers of He particles contained in the plasma reservoir and in the divertor reservoirs. Note that, in this case, the divertor reservoir combines the ones called divertor and pump reservoirs from Fig. 4.1, assuming pumping applied directly to the divertor volume. The dynamics of this system is fully described in terms of three time constants:

- A *core confinement time* τ_{main}. This is the characteristic time describing how efficiently He particles are confined in the core plasma. Therefore, the quantity $N_{\mathrm{He}}^{\mathrm{plasma}}/\tau_{\mathrm{main}}$ describes the loss of He particles from the core plasma, which enter the divertor reservoir.
- A *divertor retention time* τ_{ret}. This is the characteristic time describing how efficiently He particles are retained in the divertor reservoir. Therefore, the quantity $N_{\mathrm{He}}^{\mathrm{div}}/\tau_{\mathrm{ret}}$ describes the backflow of He particles from the divertor reservoir, which return to the core plasma.
- A *pumping time* τ_{pump}. This is the characteristic time describing the pumping from the divertor reservoir. Therefore, the quantity $N_{\mathrm{He}}^{\mathrm{div}}/\tau_{\mathrm{pump}}$ describes the pumped flux.

Considering the simulations presented in Fig. 4.18, the core confinement time may be calculated as the limit to which the quantity $N_{\mathrm{He}}^{\mathrm{plasma}}/\Phi_{\mathrm{He}}^{\mathrm{out}}$ converges when equilibrium between plasma and wall reservoirs is reached. This situation emulates a reactor-relevant steady-state scenario. $\Phi_{\mathrm{He}}^{\mathrm{out}}$ is the He ion flux leaving the core across the LCFS. The divertor retention time has the same meaning as in our full model, being defined through Eq. (4.8). Finally, an effective pumping time applied to a single neutrals reservoir may be derived, combining the behavior of the divertor and pump reservoirs in our full model as defined by Eqs. (4.9) and (4.10).

Table 4.3: Calculated time constants related to helium exhaust at the equilibrium limit for the four simulations shown in Fig. 4.18, and estimated values of the confinement ratio ρ_{He} assuming an energy confinement time $\tau_{\mathrm{E}} = 50$ ms, as in the discharge #39149.

	τ_{main} [s]	τ_{ret} [s]	τ_{pump} [s]	τ_{He} [s]	$\rho_{\mathrm{He}} \equiv \tau_{\mathrm{He}}/\tau_{\mathrm{E}}$
Only turbopumps, with wall retention model	0.048	0.004	0.230	2.990	**59.8**
Only turbopumps, without wall retention model	0.020	0.004	0.230	1.380	**27.6**
Turbopumps + cryopump, with wall retention model	0.048	0.004	0.022	0.286	**5.7**
Turbopumps + cryopump, without wall retention model	0.020	0.004	0.022	0.132	**2.6**

The values of such time constants for the four simulations with constant external He fueling (Figure 4.18), at the equilibrium limit, are given in the Table 4.3. In the simulations without wall retention model, a decrease of the core confinement time is observed. This is caused by the

He ion density in the edge being higher in the latter case, because of the reduced penetration of the neutrals recycled at the main wall (Figure 4.19). This causes a larger He flux crossing the separatrix, i.e. a lower ratio $N_{\mathrm{He}}^{\mathrm{plasma}}/\Phi_{\mathrm{He}}^{\mathrm{out}}$. In the simulations with enhanced pumping speed, i.e. considering both turbomolecular pumps ($S_{\mathrm{pump}} = 7$ m^3/s) and cryopump ($S_{\mathrm{pump}} = 120$ m^3/s) effective, the pumping time is reduced by a factor of 10. The divertor retention time is kept constant at a value compatible with the experimental He compression (cf. Section 4.3.1).
The analytical solutions of Eqs. (4.20) and (4.21) show that, at equilibrium,

$$\frac{N_{\mathrm{He}}^{\mathrm{plasma}}}{N_{\mathrm{He}}^{\mathrm{div}}} = \tau_{\mathrm{main}} \left(\frac{1}{\tau_{\mathrm{ret}}} + \frac{1}{\tau_{\mathrm{pump}}} \right) \approx \frac{\tau_{\mathrm{main}}}{\tau_{\mathrm{ret}}} \ . \tag{4.22}$$

(having assumed $\tau_{\mathrm{ret}} \ll \tau_{\mathrm{pump}}$). A global helium confinement time τ_{He}, as defined in the Section 1.2.1, is the total equilibrium inventory for a given source rate $\Phi_{\mathrm{He}}^{\mathrm{ext}}$, when $\Phi_{\mathrm{He}}^{\mathrm{ext}}$ becomes equal to the removal rate $N_{\mathrm{He}}^{\mathrm{div}}/\tau_{\mathrm{pump}}$, therefore

$$\tau_{\mathrm{He}} \equiv \frac{N_{\mathrm{He}}^{\mathrm{plasma}} + N_{\mathrm{He}}^{\mathrm{div}}}{\Phi_{\mathrm{He}}^{\mathrm{ext}}} = \tau_{\mathrm{pump}} \frac{N_{\mathrm{He}}^{\mathrm{plasma}} + N_{\mathrm{He}}^{\mathrm{div}}}{N_{\mathrm{He}}^{\mathrm{div}}} = \tau_{\mathrm{pump}} \left(1 + \frac{N_{\mathrm{He}}^{\mathrm{plasma}}}{N_{\mathrm{He}}^{\mathrm{div}}} \right) \approx \tau_{\mathrm{pump}} \left(1 + \frac{\tau_{\mathrm{main}}}{\tau_{\mathrm{ret}}} \right) \ . \tag{4.23}$$

The resulting values of τ_{He}, as well the confinement ratio $\rho_{\mathrm{He}} \equiv \tau_{\mathrm{He}}/\tau_{\mathrm{E}}$, are also listed in the Table 4.3.
In the realistic AUG simulation including only the effect of turbomolecular pumps and with activated wall retention model, a confinement ratio ρ_{He} of nearly 60 is estimated. This would be much larger than the limit of 10 foreseen for a burning plasma to keep fuel dilution within tolerable values (cf. Section 1.2.1). Implementing also the effect of the AUG cryopump, ρ_{He} decreases to a reactor-relevant value of nearly 6. This shows that ρ_{He} scales roughly linearly with the applied pumping speed. A reduction by a further factor of 2 is observed with deactivated wall retention model. This is, however, an unphysical scenario useful only for modelling purposes. For ITER, values of τ_{E} up to several seconds are expected [36]. Particle confinement is related to energy confinement, therefore, from AUG to ITER, an increase of τ_{main} could be expected as well. τ_{ret} is not easily controllable because it is mainly determined by the divertor plasma characteristics. The most promising perspectives for improvement should therefore be entrusted to an optimization of τ_{pump}. This result highlights the importance of designing adequate pumping systems in future fusion reactors, to allow reliable steady-state operations for a burning D-T plasma. Cryopumps capable of pumping He atoms are already being implemented in the ITER pumping systems [184, 185, 186]. Their application to devices with even larger fusion reaction rates, such as DEMO, appears essential to avoid levels of fuel dilution not compatible with fusion power generation.

Chapter 5

SOLPS-ITER simulations of helium transport, recycling and pumping

In the previous Chapter, the mechanisms defining the dynamic behavior of helium in tokamak plasmas were investigated. The parameters defining helium transport and recycling in the divertor, such as divertor retention time and subdivertor neutral conductance, were empirical inputs. As such, interpreting these components of helium exhaust is not possible with the model presented in the previous Chapter.
Identifying the underlying mechanisms which determine helium transport and recycling is the final missing piece for fully understanding the physics of helium exhaust in tokamaks and allowing extrapolations towards reactor plasmas. To this end, this Chapter presents SOLPS-ITER simulations of He-seeded D plasmas, based upon the performed experiments at AUG. Although the achieved plasma solutions are steady-state, such simulations allowed the characterization of the impact of the divertor plasma characteristics on transport of He ions and recycling from the divertor target plates, and the impact of the exhaust gas flow characteristics on transport and pumping of He gas in the subdivertor region.
In the Section 5.1 some details about the SOLPS-ITER code package will be given. In the Section 5.2 the basic modelling setup will be presented, with focus on the employed physics-based input parameters and the included atomic, molecular and neutrals physics. Finally, in the Section 5.3 the simulations results will be presented and discussed.

5.1 The SOLPS-ITER code package

SOLPS-ITER [187, 188] is one of the most sophisticated tools for plasma edge modelling. It consists of the self-consistent coupling of two distinct physics modules, namely the multi-species fluid plasma transport code *B2.5* and the kinetic neutral transport code *EIRENE* [51]. The first one is a fluid code which solves the conservation equations for density, momentum, energy and current for the ionized particle species in two dimensions, to cope with effects of both parallel and radial transport in the SOL and in the divertor plasma [189, 190]. The second one is a Monte Carlo code for the kinetic treatment of neutral particles, accounting for the involved atomic and molecular physics [191, 192]. SOLPS-ITER allows to achieve a full steady-state plasma solution within the edge region in a poloidal plane of the torus assuming axial symmetry. This is obtained at the end of a time-dependent convergence process in which the plasma evolution is followed by solving the conservation equations. It allows to model in a realistic way the complex and inter-related physics mechanisms determining particle and power exhaust in tokamaks.
SOLPS-ITER has been widely used for interpretative purposes on the major operating tokamaks, including JET [193, 194], AUG [195, 196, 197, 198], DIII-D [199], Alcator C-Mod [200] and

TCV [201] and for predictive purposes in view of ITER operations [202] and DEMO scenario development [203]. Previous SOLPS versions have played a key role in the design of the ITER divertor [204].

5.1.1 The B2.5 program

B2.5, the fluid module of SOLPS-ITER for plasma transport, is written in Fortran 90, and is the evolution of the program B2 originally developed by B. Braams [189] and expanded by M. Baelmans [190] by improving the handling of the geometry and implementing the fluid drifts. It solves a set of modified Braginskii equations for the electrons and an arbitrary number of ion species. The time-dependent balance equations are solved for the necessary number of time steps until convergence is reached. Steady state is achieved if no major variation of the main plasma parameters is observed.
The two-dimensional equations are solved in a curvilinear toroidal geometry mapped to a topologically rectangular mesh. The (x, y) coordinates of such a system represent the orthogonalized poloidal and radial coordinates (θ, r), respectively.
More details about the physics of B2.5, together with a deeper insight into the conservation equations which are solved, the specification of boundary conditions and some additional numerical aspects can be found in the theses [189] and [190].

5.1.2 The EIRENE program

EIRENE, the kinetic module of SOLPS-ITER for neutral transport, is also written in Fortran 90, and was originally developed by D. Reiter [191]. Several extensions were introduced during the years, including the possibility to simulate non-linear phenomena such as neutral-neutral collisions [205].
A number of test particles is launched in the simulation domain from a source location (e.g. from external fueling or recycling), with a given distribution in directions and velocities. The lengths of the travelled trajectories are pseudorandomly generated, related to the relative mean free path. The trajectories of each test particle are followed until these are removed, e.g. because of ionization. All the events which can occur along the trajectories have probabilities depending on the cross sections of the related atomic process. Such coefficients are extracted from external atomic databases. Global gas quantities in each point of the domain are finally calculated sampling all the simulated trajectories.
EIRENE computations are performed on tetrahedral volumes in a full 3D geometry, which reduce to a triangular mesh in the poloidal plane. This extends over the entire grid of B2.5 and beyond, up to the material boundaries of the vacuum vessel. Particles can be reflected on the material boundaries or may be absorbed with a probability proportional to a given absorption coefficient, to emulate a pumping effect.
More details about the physics of EIRENE, together with an insight into the employed Monte Carlo method and the kinetic equations which are solved, can be found in the thesis [191].

5.1.3 B2.5-EIRENE coupling scheme

SOLPS-ITER can be used in *standalone mode* (B2.5 only running), or in a fully *coupled mode* (B2.5 + EIRENE running). In the first case, the fluid equations are solved for both ions and neutrals. In the second case, plasma transport is solved using the fluid module, while neutral transport and plasma-neutral interactions are modelled by the kinetic module. In the latter case the coupling scheme, actuated after each time step of B2.5, is the following:

1. B2.5 calculates a plasma background solution, and sends it to EIRENE.
2. A number of neutral trajectories is simulated by EIRENE within the plasma background.
3. The neutral-plasma interaction modelled by EIRENE is transferred back to B2.5 in form of sources and sinks for particles, momentum and energy.
4. B2.5 re-calculates the plasma solution by solving the conservation equations using the EIRENE sources/sinks, and prepares a new plasma background.

5.2 Modelling setup

The goal of the modelling activity was the achievement of physically reasonable simulations, inspired by the experiments documented in the Chapter 3. All simulations were performed as coupled B2.5-EIRENE runs featuring deuterium as main species, and including nitrogen and helium as impurities. Analyzing the steady-state plasma solutions allowed to study the characteristics of helium transport and recycling, and to identify the underlying mechanisms which determine the simulated densities and fluxes. Performing input parameter scans allowed to document the dependence of helium transport and recycling in the simulated divertor plasma scenarios. The physics-based input parameters and boundary conditions are based on the plasma background from AUG discharge #39149, i.e. the same which was modelled in the previous Chapter.
The duration of one time step for a typical AUG grid and including deuterium, nitrogen and helium as plasma species is of the order of one minute, employing one single core of a modern CPU. The required time step to achieve a numerically stable run is about 10^{-4} s without drift-related fluxes in the B2.5 equations. Including drifts, the time step should be reduced to about 10^{-6} s. Bringing one single run to convergence (which may require one second of simulated physical time) would then require one week of single-core CPU-time without drifts, or two years including drifts. Since parameter scans comprising several different simulations were performed, the required CPU-times in case of drift-simulations would have been far beyond the available time for this work, even employing multi-core runs with MPI parallelization. Therefore, all drift terms were neglected in the simulations presented here.
For this reason, a quantitative match between the divertor plasma characteristics with the experimentally measured ones was not possible. This possibly impacts a quantitative comparison between simulated and experimentally measured helium transport in the divertor as well. Nonetheless, we could observe the trends of several helium-exhaust-related parameters evolving with the performed scans. This allowed to reach several qualitative conclusions.

5.2.1 Computational grid

SOLPS-ITER solves the fluid equations in a region consisting of a thin annulus of the outer core plasma, the SOL and the PFR. Figure 5.1 shows the *computational grid* which we used for all simulations. The B2.5 grid is based upon the magnetic equilibrium configuration of the AUG discharge #39149, at t = 2.7 s. A resolution of 96×36 (i.e. 96 cells in poloidal direction and 36 cells in radial direction) was chosen. For the triangular grid used by EIRENE an average triangle size of about 5 cm was used.
The *gas puff source* for D and N was set in front of the dome baffle, while for He was set at the outer midplane. This resembles the relative locations at which these species are injected in the experiment. Two *pumping surfaces*, emulating the effect of the cryopump and the turbo-molecular pumps, were defined in terms of absorption coefficients (i.e. the probability that an incident particles is absorbed). For D and N we set the values to 0.20 and 0.007 for the cryo- and the turbopumps, respectively. These values ensure that the ratio of the fluxes of pumped particles

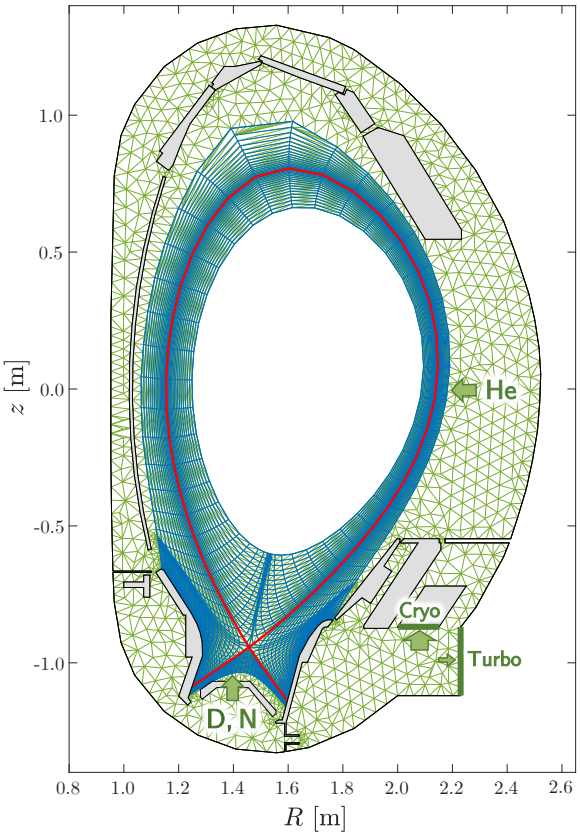

Figure 5.1: Field-aligned grid used by B2.5 (in blue) and triangular grid used by EIRENE (in green). The locations of gas puff sources and pumping surfaces are indicated by arrows.

between the two surfaces equates the ratio between the relative pumping speeds, i.e. 120 m^3/s and 7 m^3/s, respectively (cf. Section 3.1). As the cryopump is ineffective for He, for this we set an absorption coefficient of 0, while the value for the turbopumps is the same as the one employed for D and N. A fictitious duct was placed in the connection between sub-divertor chamber and pump chamber, to emulate a conductance effect generating a pressure drop between the two chambers.
All material surfaces are tungsten. Accordingly, coefficients extracted from a TRIM-generated database are employed to simulate the reflection of ions and neutrals as the surface boundaries. The surface temperatures determine the energy at which the neutrals are reflected. We used 0.1 eV ($\approx$ 1160 K) for the inner and outer targets, 0.001 eV ($\approx$ 11.6 K) for the cryopump surface, and 0.025 eV ($\approx$ 300 K, i.e. room temperature) for all other surfaces.

5.2.2 Atomic, molecular and neutrals reactions

Table 5.1: List of atomic and molecular reactions included the simulations.

$D^0 + e \rightarrow D^+ + 2e$	Ion.
$D_2^0 + e \rightarrow D_2^+ + 2e$	Ion.
$D_2^0 + e \rightarrow D^0 + D^+ + 2e$	Ion.-Diss.
$D_2^+ + e \rightarrow D^+ + D^+ + 2e$	Ion.-Diss.
$D_2^0 + e \rightarrow D^0 + D^0 + e$	Diss.
$D_2^+ + e \rightarrow D^+ + D^0 + e$	Diss.
$D^+ + e \rightarrow D^0$	Rec.
$D_2^+ + e \rightarrow D^0 + D^0$	Rec.-Diss.
$D^0 + D^+ \rightarrow D^+ + D^0$	CX
$D_2^0 + D^+ \rightarrow D_2^+ + D^0$	CX
$D^0 + D^+ \rightarrow D^0 + D^+$	El. scat.
$D_2^0 + D^+ \rightarrow D_2^0 + D^+$	El. scat.
$N^0 + e \rightarrow N^+ + 2e$	Ion.
$N^+ + e \rightarrow N^0$	Rec.
$He^0 + e \rightarrow He^+ + 2e$	Ion.
$He^+ + e \rightarrow He^0$	Rec.
$He^0 + He^+ \rightarrow He^+ + He^0$	CX
$He^0 + He^{2+} \rightarrow He^{2+} + He^0$	CX

The atomic and molecular processes determine the mutual interactions between plasma species and neutral species. Table 5.1 lists all *atomic* and *molecular reactions* modelled by EIRENE, involving the interaction between neutrals and plasma constituents. The relative cross sections and rate coefficients are extracted from the AMJUEL [206] and HYDHEL [70] databases. For D, the full standard set of reactions was used. This includes electron-impact dissociation and ionization, radiative and dissociative recombination, CX collisions and elastic scattering. For N and He, by default only electron-impact ionization and recombination are included. As the focus of the simulation activity was on helium transport, resonant CX collisions for He (i.e. collisions between He atoms and He ions) were included. The impact of such reactions is negligible for low He densities, where collisions with electrons are much more frequent than with He ions. However, as in the modelled experiments the ratio between He ion density and electron density goes up to 0.2 (cf. Sec-

tion 3.4.3), a small but visible impact on the penetration depth of recycled He atoms may be expected (cf. Section 2.2.2). Instead, we did not include non-resonant CX collisions (i.e. collisions between He atoms and D ions). In the current implementation of EIRENE, a reaction involving two different types of test particles would create issues in the statistics model, if the relative neutral densities are much different. The impact of these reactions on the penetration depth of recycled He atoms would not depend on the He density, but would be limited to plasma regions at very low temperatures (cf. Section 2.2.2).
Finally, *charge transitions* through ionization and recombination between higher charged states for N and He are modelled by B2.5 using the ADAS rate coefficients. Radiation losses from ions are also calculated by B2.5 using the ADAS cooling rates, which include line radiation after electron-impact excitation+recombination and bremsstrahlung. Neutral radiation is instead calculated by EIRENE.
Neutral-neutral collisions [205, 207] are not included by default in the EIRENE reaction set. The impact of these, in terms of neutral gas flow viscosity and inter-species friction, is thought to be limited to large neutral pressures (of the order of 10 Pa or more) [208]. For this reason, although they are routinely employed in the modelling of larger devices such as e.g. ITER [209], they have never been employed in AUG simulations, to save computation time. For the case of helium at AUG, such assumption might not be valid. The neutral He flow towards the pumps in the subdivertor region is much weaker than the D flow, because of the difference in the sink effect due to the ineffectiveness of the cryopump on He atoms. Therefore, because of the strong difference which may be expected between the average flow velocities of the D and He gases, even a relatively small D-He friction may result in some degree of entrainment of the neutral He flow in the viscous D flow [147]. This can enhance the transport of He atoms towards the pumps.

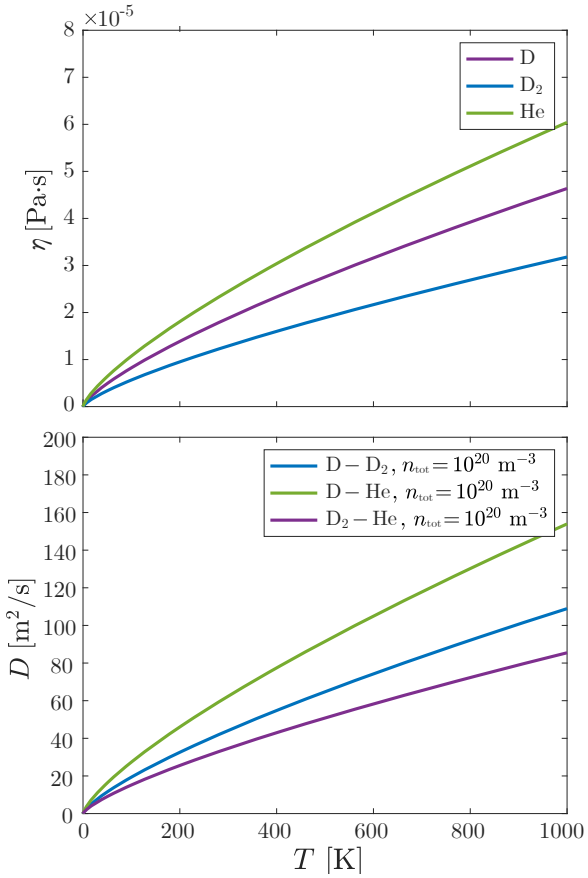

Figure 5.2: Viscosities and diffusivities describing the collisions involving D, D_2 and He, calculated using a rigid sphere model.

In order to investigate this, for the first time we run EIRENE in non-linear mode in SOLPS-ITER simulations for AUG, which allows to simulate neutral-neutral collisions employing the BGK approximation [210]. We included self-collisions for D atoms, D_2 molecules and He atoms, and cross-collisions between these species. Figure 5.2 shows the viscosities determining the viscous behavior of the various species and the diffusivities determining the inter-species friction effect. These coefficients are used to calculate the collision frequencies for the relative reactions. Unless otherwise specified, all simulations are performed with neutral-neutral collisions activated.

5.2.3 Physics input parameters

The main physics-based *input parameters* for the simulations are the fueling rates, the heating power and the anomalous transport coefficients describing radial transport.
We performed one initial simulation to model with a reasonable accuracy the plasma background

as measured in the AUG discharge #39149 in the time window [2.5,3.0] s, which here and in the following is referred to as "base case". This simulation is analyzed to draft some general observation about helium transport in the Sections 5.3.1 and 5.3.3, and used as starting point for the parameter scans described in the Sections 5.3.2 and 5.3.4.

Fueling rates

The *fueling rates* determine the number of molecules (for D) or atoms (for N and He) injected into the computational domain by EIRENE, in ions/s.
With a fixed D fueling rate of $0.65 \cdot 10^{22}$ ions/s we reproduced the experimental electron density at the midplane. The fueling rate is about a factor of 2 lower than the experimental one (cf. Fig. 3.8). This is probably caused by the pumping rate being lower than in the experiment by the same factor. However, in the framework of the performed analysis, such discrepancy is not an issue. The quantities which are relevant for exhaust analyses are the absolute D_2 densities in the subdivertor regions and the ratio of the particles pumped by the cryopump and the turbomolecular pumps. These quantities match the experiment.
For N atoms we imposed the fueling rate in such a way to roughly reproduce the experimentally measured radiation in the SOL and divertor regions. The fueling rate in the base case was $2 \cdot 10^{20}$ ions/s $= 1.4 \cdot 10^{21}$ e/s.
Finally, the plasma scenario reproduced by the simulations has a constant external He fueling and He content in the plasma and in the exhaust gas. A fueling rate of He atoms of $2.5 \cdot 10^{19}$ ions/s $= 5 \cdot 10^{19}$ e/s allowed to model a He concentration at the midplane ($n_{\mathrm{He}^{2+}}/n_e$) of roughly 20 %. Whereas for D the puff-pump balance in the simulation is perfectly satisfied, for impurities, whose fueling rates are considerably lower, some numerical error in such balance is present. As reported in other works (e.g. [44]), the pumped fluxes may be even several times smaller than the fueled ones. This does not allow to directly relate fueling rate and impurity content in the plasma within the simulations. Nonetheless, the analysis of impurity particle transport in terms of ratios between impurity densities between different regions of the domain, such as e.g. compression and subdivertor pressure drop, is not affected by this issue.

Input power

We imposed an *input power* by specifying the electron and ion energy fluxes crossing the core plasma boundary (which is around $\rho_p = 0.9$ for the employed grid).
A total input power of 5 MW was used. We calculated this from the difference between the total input power and the experimentally measured radiated power in the region at $\rho_p < 0.9$ applying a tomographic analysis on the bolometric measurements [211]. The same value of total input power was also used in the parameter scans (cf. Section 5.3).
From the current simulations, we observed that different ratios between the energy fluxes carried by electrons and ions do not have a significant impact on the plasma solution, because of the efficient energy exchange between these in the plasma edge.

Anomalous transport coefficients

Regarding the assumptions on the *anomalous transport coefficients*, we empirically defined radial profiles for the particle diffusivity D_n and electron and ion thermal diffusivities χ_e, χ_i, driving the anomalous radial transport. A fine tuning of these profiles was performed to achieve the best match between the simulated radial plasma profiles and the experimental midplane profiles.

Radial particle transport is treated as purely diffusive. A diffusive approximation can indeed effectively mimic the effect of a general diffusive-convective transport [212]. The choice of the radial profile for the particle diffusivity followed the optimization algorithm described in [196]. An empirical optimization of the radial energy transport coefficients was also performed. Following the evidence of enhanced radial transport in the divertor [149], all such coefficients were multiplied by 2 in the divertor region w.r.t. the values imposed at the outer midplane.

Figure 5.3 shows the employed anomalous transport coefficients at the outer midplane, as well as the simulated plasma profiles compared with the corresponding experimental measurements. The particle diffusivity shown here is applied for all ion species in the simulation.

Because of the absence of drift-driven fluxes, the agreement between the simulated plasma profiles at the divertor target with the experimental ones is not as good as at the midplane. The electron density in the divertor is overestimated. Instead, the match between simulated and experimental electron temperatures in the divertor, shown in Fig. 5.4, is reasonable. As discussed in Section 2.2.3, the plasma temperature is the main parameter determining the recycling behavior of impurities, which is one key aspect of the present investigation.

The transport coefficients employed in the base case are also used in the parameters scans (cf. Section 5.3).

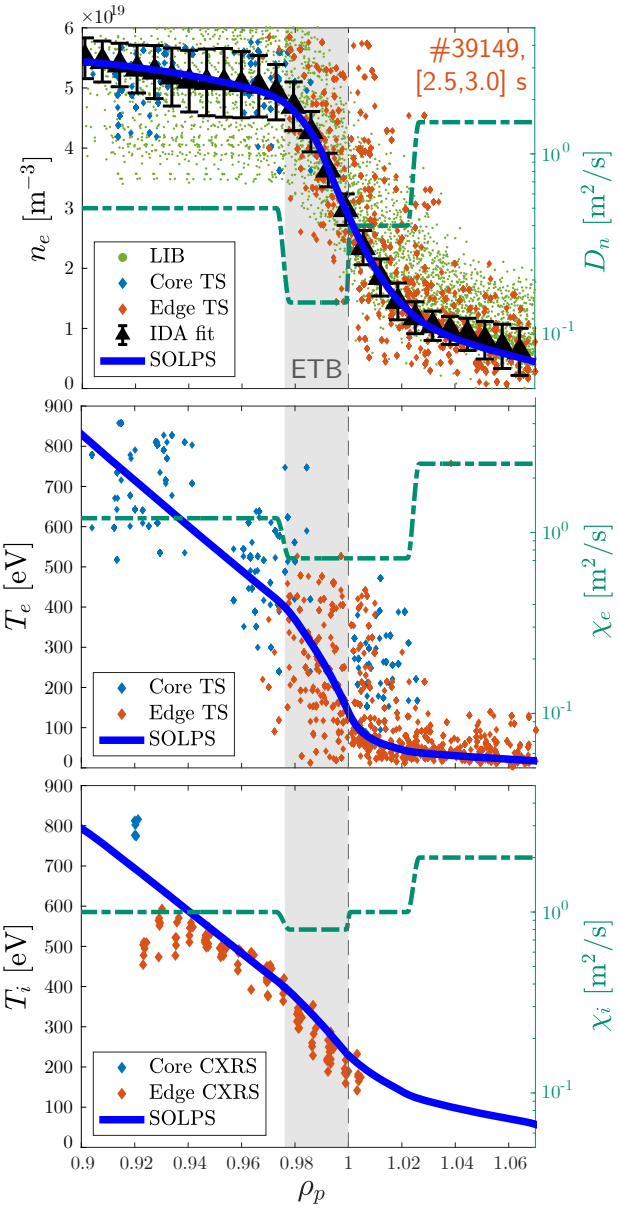

Figure 5.3: Comparison between simulated plasma profiles at the outer midplane, as blue solid lines, and experimental data from different diagnostics as colored points. The relative anomalous transport coefficients profiles are shown as dashed green lines.

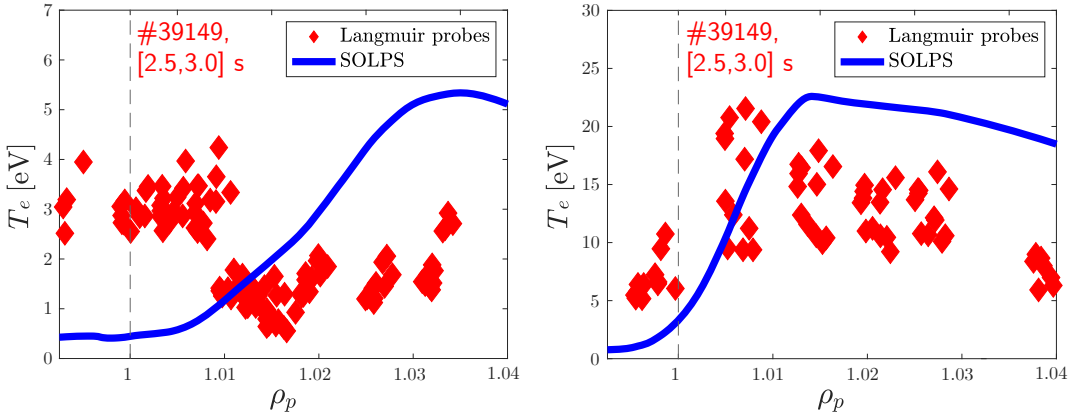

Figure 5.4: Comparison between simulated electron temperature profile at the inner target (left) and at the outer target (right), as blue solid lines, and experimental data from Langmuir probes as red points.

5.3 Modelling results

This Section presents the behavior of helium in the performed simulations, achieved employing the physics-based input parameters described in the Section 5.2, aimed to provide an interpretation of the general features of helium transport, recycling and pumping.
The performed analyses are inspired by previous modelling studies focused on the radiating impurities nitrogen and argon [42, 43, 44]. The radiating efficiency of helium is much lower than that of nitrogen and argon. For this reason, even high He concentrations are not expected to significantly alter the background plasma. This was confirmed during the setup of the base case presented in the previous Section. While ramping the He concentration up to 20 %, a increase of the electron density is observed at midplane. Electron density and temperature in the divertor, as well as main ion fluxes and global power balance, do not change. Whereas the behavior of radiating impurities is also determined by a modification of the plasma background due to radiative losses, for helium the plasma background remains unchanged. Therefore, the characteristics of helium transport and recycling is not dependent on the He concentration itself. This is consistent with the experimental observation of He compression being constant and independent on the He concentration in a given background plasma (Figure 3.12).

5.3.1 Characterization of divertor retention of recycled helium atoms

For an efficient exhaust, it is of great importance that recycled He atoms are preferentially directed towards the pumps, i.e. that *divertor retention of recycled He atoms* is maximized.
The probability that individual recycled He atoms are scattered towards the pumps depends mostly on geometric aspects, such as distance of the recycling location from the subdivertor entrance and target inclination. Therefore, the neutral He pressure in front of the pumps will be largest if those recycled He atoms which are not directly scattered towards the pumps are re-ionized close to the target plates, so that the resulting He ions are promptly returned to the targets. For this to happen, He atoms must be ionized below the stagnation surface of the He ion flow, which defines the boundary between the regions with downstream- and upstream-directed flow (cf. Section 2.2.3). Therefore, divertor retention depends on the competition between stagnation surface of the He ion flow and ionization front of the recycled He atoms.

Interpretation of helium ion transport in the divertor

The *stagnation surface* of the He ion flow is visible in the two-dimensional flow pattern of He ions. It mostly follows the flow pattern of the main ions, because of the friction exerted by them on the impurity ions. In a high recycling regime, the flow pattern of main ions typically presents a flow reversal effect in the flux tubes closest to the separatrix, because of the formation of a convective cell due to an excess of the ionization source close to the separatrix, where the temperature is higher. Therefore, a similar degree of flow reversal is expected also for impurities, and indeed such a phenomenon was modelled for nitrogen and argon [42, 43, 44].
The same is observed for helium. Figure 5.5 shows the simulated flow pattern of He ions in the divertor region in the base case. The flow direction is specified through different colors. While in the far SOL the He ions move towards the target plates, in the near SOL the flow is reversed at some distance from the targets. The flow patterns for He^+ and He^{2+} are very similar, whereas qualitative differences were observed between higher charge states for N and Ar ions [44].
Other mechanisms play a role in determining such flow pattern, additionally to the main ion friction. These may be investigated by individually quantifying the various forces acting on the He ions as computed by SOLPS-ITER. Let us consider the parallel momentum balance equation solved by B2.5 for He ions [51].

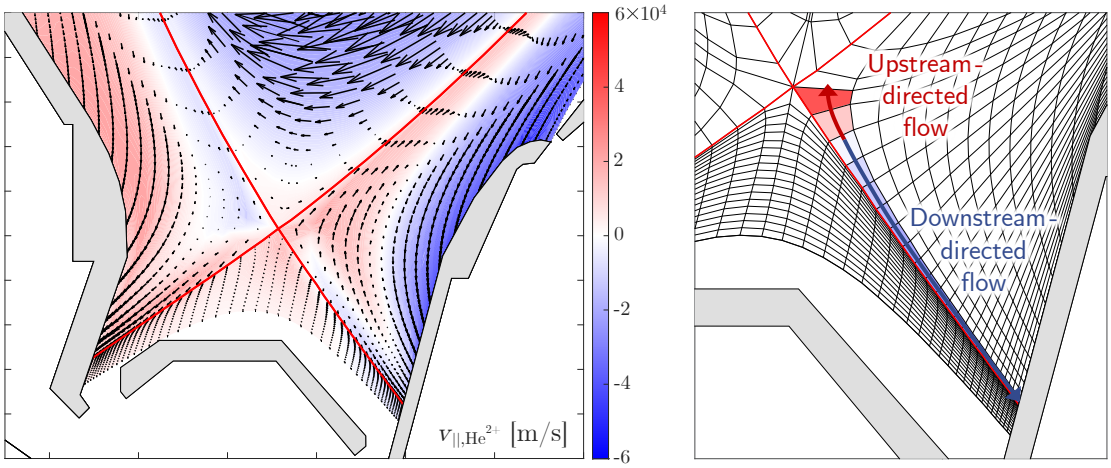

Figure 5.5: Simulated flow pattern of He^{2+} ions in the divertor. The arrows indicate intensity and direction of the total He^{2+} particle flux, while the color indicates the He^{2+} flow velocity. Red colors indicate a flow directed towards the inner target, while blue colors indicate a flow directed towards the outer target. At the right a zoom-in on the flux tube closest to the separatrix is shown.

The poloidal ion flow direction is given by the sign of poloidal gradient of the convected parallel momentum flux. This term may be isolated re-arranging the parallel momentum balance equation in such a way that

$$\frac{1}{\sqrt{g}}\frac{\partial}{\partial x}\left[\frac{\sqrt{g}}{h_x}\left(m_{\mathrm{He}} v_{\parallel,\mathrm{He}} \Gamma_{x,\mathrm{He}}\right)\right] = \sum F_{\mathrm{mom,He}} \tag{5.1}$$

Eq. (5.1) allows therefore to describe this sign as that of the net sum of several forces acting on the He ions, namely *poloidal viscosity effect*, *radial viscosity effect*, *radial momentum transport effect*, *static ion pressure gradient*, *electrostatic force*, *friction forces*, *electron+ion thermal forces* and other *volumetric sources*.

Figure 5.6 shows the results of such force balance applied to the He^{2+} ions along the flux tube closest to the separatrix in the base case. Here, all terms are normalized to the He^{2+} ion density, therefore the forces are expressed in unit of newton per He^{2+} ion. The gradient of the convected parallel momentum flux is positive until a poloidal distance of roughly 20 cm from the outer target, where the flux becomes stagnant. This is exactly how the simulated He^{2+} ion flux behaves in the considered flux tube (right panel in Fig. 5.5).

The largest terms contributing to the force balance are friction and thermal forces. The former are always positive, i.e. they drive

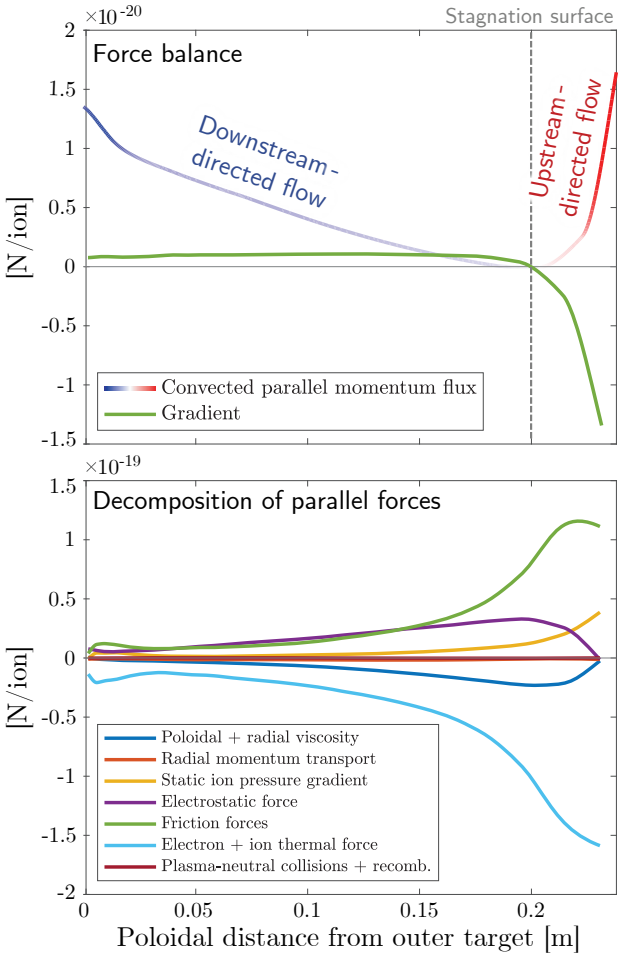

Figure 5.6: Total force applied to the He^{2+} ions in the outer divertor region, in the flux tube closest to the separatrix, from target to X-point. Top plot: poloidal projection of the convected parallel momentum flux for He^{2+} ions ($m_{\mathrm{He}} v_{\parallel,\mathrm{He}^{2+}} \Gamma_{x,\mathrm{He}^{2+}}$) and relative gradient (R.H.S. of Eq. (5.1)), whose sign determined the flow direction. Bottom plot: decomposition of the gradient in terms of the individual applied forces.

the He ions towards downstream, while the latter are always negative, i.e. they drive the He ions towards upstream, against the parallel temperature gradient. Analyzing the relative balance between these two terms allows to interpret the movement of the stagnation surface when performing divertor parameter scans as function of these parameters.

Role of the helium ionization front

The *penetration depth* of recycled He atoms in the divertor plasma is the second player determining divertor retention. It is strongly varying with the electron temperature in the divertor plasma and mainly determined by the mean free path for electron-impact ionization.

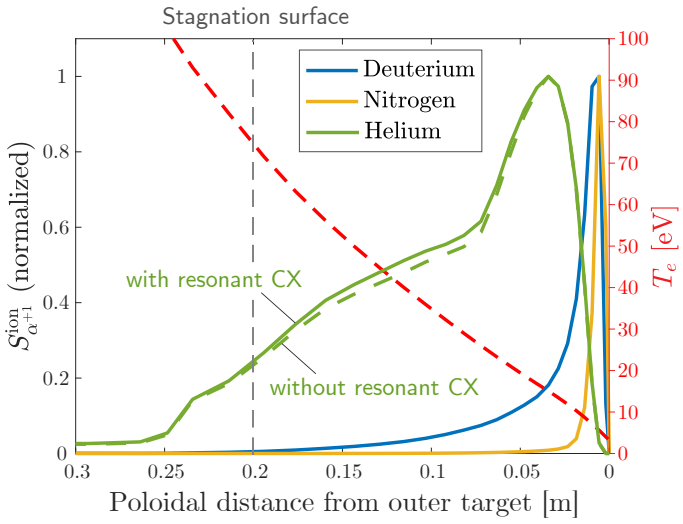

Figure 5.7: Source terms from ionization of neutral atoms for D, N and He, in different colors, in the divertor along the flux tube closest to the separatrix, normalized to their peak value. For He, the solid and dashed lines indicate the curves simulated with and without including the resonant CX collisions, respectively. The vertical dashed line indicates the location of the stagnation surface (roughly similar for the three species). The dashed red curve indicates the electron temperature.

Figure 5.7 shows the poloidal variation of the ion source from ionization of neutrals along the flux tube closest to the separatrix for He (in green) compared to those of D and N (in blue and yellow, respectively). The source curves, which are normalized for an easier comparison, are very different. He atoms penetrate much deeper into the plasma than D and N atoms. This is understood by the first ionization energy of He atoms (24.6 eV) being much larger than those of D atoms (13.6 eV) and N atoms (14.5 eV). This effect adds to that of the high thermal velocity of He atoms because of their relatively small mass. The major difference between He atoms and the other species is not, however, in the location of the peak source, which is in any case shifted few cm more upstream. Rather, the main difference is the fact that the ionization source from He atoms is spread quite farther from the peak location towards upstream, while that from D and N atoms it is more concentrated close to the peak location. Because of this, a non negligible fraction of the ionization events of recycled He atoms occurs above the stagnation surface, which is detrimental for divertor retention.
Figure 5.7 also shows that including or excluding the resonant CX collisions for He from the list of activated reactions in EIRENE has a negligible impact of the simulated penetration depth of recycled He atoms. This is consistent to the expectation that a non negligible effect of CX collisions is limited to very low plasma temperatures (cf. Section 2.2.2).
Figure 5.7 strictly refers only to a single flux tube, while divertor retention is determined by the distribution of the ionization source in the entire SOL. Nonetheless, it is indicative of the major difference in the penetration depth of recycled He atoms w.r.t. that of other species.

Simulated helium compression

As discussed throughout this thesis, *divertor compression* is the parameter which best quantifies the efficiency of divertor retention of recycled atoms. High values imply that recycled atoms from the divertor targets are retained in the subdivertor volume, rather than leaking towards the main plasma.

Since SOLPS-ITER does not simulate the inner core plasma, the experimental definition used so far (Eq. (2.50)) cannot be applied. In this Section we employ a slightly different definition which replaces the volume-averaged ion density in the confined region (starting from $\rho_p = 0$) with the volume-averaged ion density in the annulus of plasma edge modelled by SOLPS-ITER (in this case starting from roughly $\rho_p = 0.9$). As such, the simulated He compression is 0.32, while the simulated values for D and N are are 9.75 and 9.87, respectively.
The experimentally measured He compression for this simulated scenario, using the entire core-averaged He^{2+} density as denominator, was roughly 1.5 (Figure 3.13). Even accounting for the different definition, SOLPS-ITER underestimates He compression by a factor of at least 5. The agreement with the experimental D and N compressions is, instead, much better, with discrepancies of mostly a factor of 1.5. This suggests that the reason for the discrepancy is not related to the general simulation setup or to the difference between the simulated divertor plasma background w.r.t. the experimental one (e.g. due to the absence of drifts). Rather, some pieces of the physics of helium transport and recycling may be still missing, as will be discussed in the Section 5.3.5.
What is observed in the experiment and reproduced, at least qualitatively, by SOLPS-ITER, is that divertor retention of recycled He atoms is much lower than for D and N atoms. The result is a comparatively lower He partial pressure in the subdivertor region. This may be identified as a physics-related characteristic which is not beneficial for an efficient helium exhaust. It sums up to those alraedy identified in the previous Chapter (i.e. wall retention and poor pumping efficiency) and related to the technical design of AUG.
Figure 5.7 suggests that the main reason for the low He compression is the mean free path of recycled He atoms being much longer than those of D and N atoms. This leads to a much larger fraction of recycled He atoms being ionized above the stagnation surface of the corresponding ion flow. This is further supported by noting that the simulated values of divertor compression for D and N, which have a similar first ionization energy and a similar poloidal location of the ionization front, are almost identical. In high recycling regimes, the impurity stagnation surfaces tend to align to that of the main ions, becoming similar for different impurities [44]. Therefore, the first ionization energy may be invoked as the main ordering parameter for a quantification of divertor retention [147].

5.3.2 Impact of divertor temperature on helium compression

Despite the quantitative disagreement between the experimental and simulated values of He compression, performing parameter scans with SOLPS-ITER still allows to study the general qualitative behavior of this as function of the divertor plasma parameters. This is particularly useful to complement the experiments discussed in the Section 3.4.4. The much slower decay of the He content in the plasma, which is observed when transiting from an attached to a strongly detached divertor regime, suggests a degradation of divertor retention of recycled He atoms in the former case. Because of the unavailability of Penning gauge measurements for discharges with a detached divertor, an experimental confirmation of this is missing.
We performed a series of simulations with the same physics input parameters as the base case, keeping a constant D and He fueling and varying the N seeding. Because of the high radiating efficiency of N at divertor-relevant temperatures, this allowed to simulate a wide range of divertor temperatures, spanning from a high recycling but attached divertor to a completely detached divertor, as shown in Fig. 5.8. The simulated temperature in the entire divertor plasma region, therefore, also strongly drops.
The processes taking place in the divertor related to transport and plasma-neutral interactions strongly depend on the plasma temperature. Therefore, the stagnation surface of the He ion flow and the location of the ionization front of recycled He atoms are expected to change.

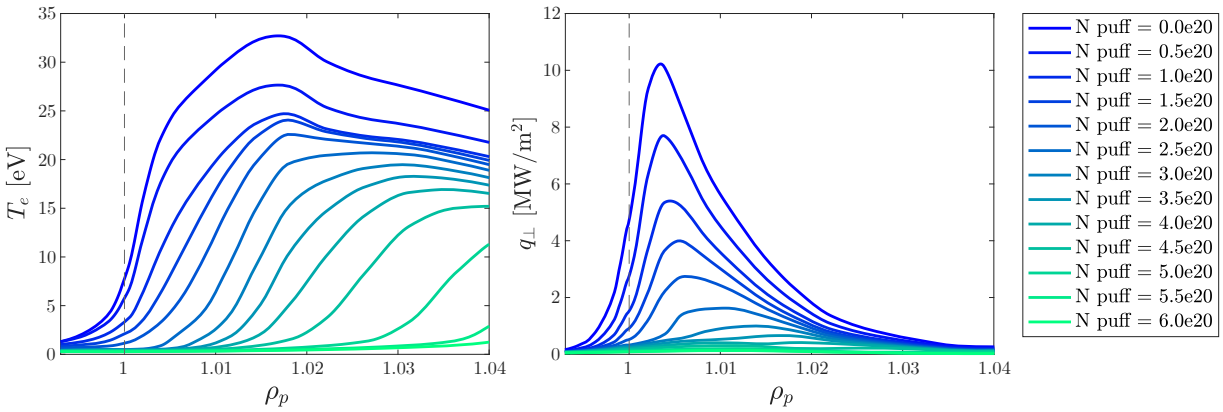

Figure 5.8: Profiles of the electron temperature and total energy flux density at the outer divertor target in the simulations at varying N seeding level.

Since, in the performed simulations, the divertor is cooled down by means of N radiation, most of the energy loss is expected to take place where the N cooling factor is largest, i.e. where the temperature is between 10 and 20 eV. This produces a flattening of the parallel electron temperature profile in front of the target with increased N seeding, because most of the energy loss takes place at a more upstream location. The friction coefficients are inversely proportional to the plasma temperature, as $C_{\text{fr}} \propto T^{-3/2}$, while the thermal forces are proportional to the parallel temperature gradient, i.e. $F_{\text{th}} \propto \nabla T$. Therefore, with decreasing temperature, the ratio between thermal and friction forces is expected to decrease. Consequently, the stagnation surface of the He ion flow is expected to shift towards that of the D ion flow, i.e. towards upstream [44]. The simulations confirm this expectation. The left panel in Fig. 5.9 shows the evolution of the contours of the stagnation surface of the He ion flow with decreasing divertor temperature. This behavior is mainly driven by the decrease of the thermal force component in Eq. (5.1), which is the main component which drives the ions in reversed direction. The net effect is an enlargement of the region characterized by a forward He ion flow, i.e. directed towards the targets.

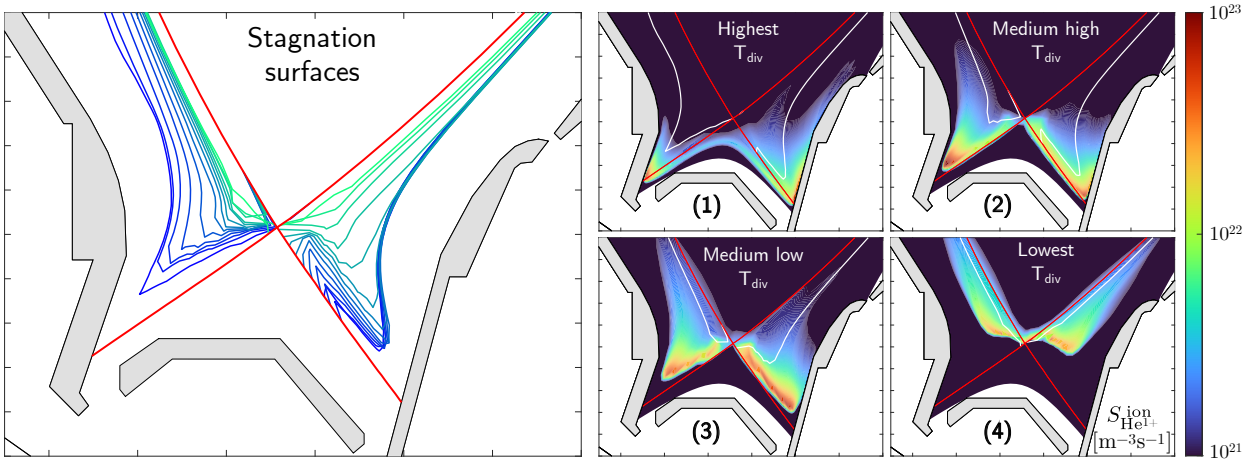

Figure 5.9: Left panel: contours representing the stagnation surface of the He ion flow for the performed simulations, as function of the divertor temperature. The color code is the same as in Fig. 5.8. Right panel: distribution of the ionization density rate of He atoms in four characteristic simulations, with relative stagnation surface of the He ion flow represented as white lines.

On the other hand, decreasing the temperature also makes the divertor plasma more and more transparent to the recycled He atoms. This is well visible in the right panel in Fig. 5.9, which shows the distribution of the ionization density rate of He atoms in four simulations. When the temperature is highest, the ionization front is well attached to the target plates and spread in both SOL and PFR. Decreasing the temperature from case (1) to case (2) implies a reduction

of the ionization in the PFR, with the ionization front being still attached to the target plates. Decreasing the temperature further, from case (2) to case (3), the ionization front detaches from the target plates. Finally, going from case (3) to case (4), where the temperature is lowest, the divertor plasma becomes completely transparent for recycled He atoms, which penetrate to the core to some extent.
The evolution of divertor retention as function of the divertor plasma temperature is studied putting in relation the stagnation surface of the He ion flow w.r.t. where the recycled He atoms are ionized. The plasma temperature at the stagnation surface of the He ion flow slightly increases with the transit from an attached to a detached divertor. This implies that the stagnation surface moves towards upstream faster than the ionization front does. This is beneficial for divertor retention, and is confirmed by plotting the simulated He compression for the performed simulations (left plot in Fig. 5.10). Initially, transiting from a hot and attached divertor to a cold and detached divertor, the simulated He compression increases by a factor of 5.
At some point, however, this trend changes, and the simulated He compression exhibits a rollover. This can be attributed to the divertor plasma becoming so cold that a relevant fraction of the He atoms penetrates to the confined region (see e.g. case (4) in Fig. 5.9). This is the worst scenario in terms of divertor retention, as these ions would be ejected from the core only over a time scale comparable to the core confinement time, hence dramatically increasing the time to the next recycling cycle.

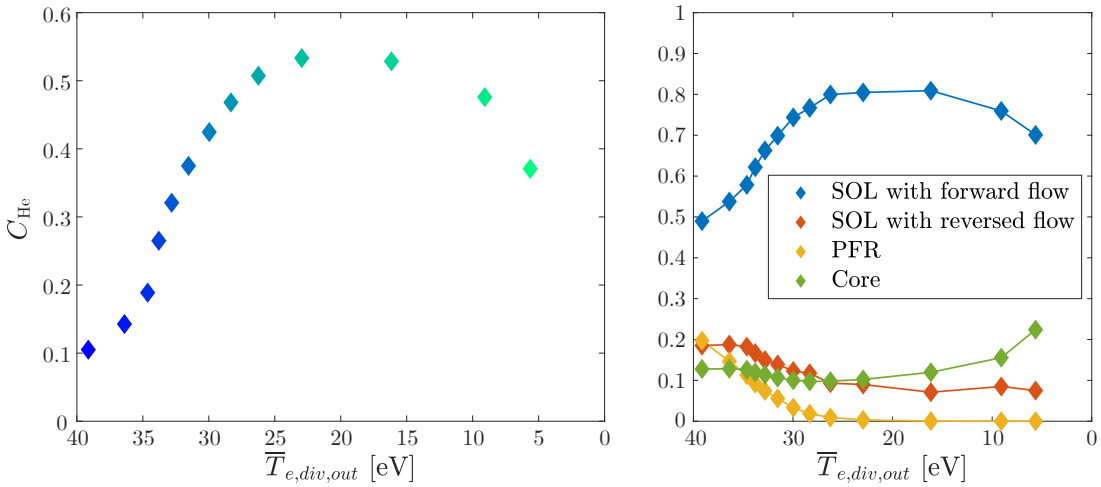

Figure 5.10: Left plot: trend of the simulated He compression in the performed scan, as function of the divertor temperature. Right plot: relative fractions of He atoms recycled from the divertor targets ionized in each of the distinct regions w.r.t. divertor retention in the same simulations. For these plots the volume-averaged electron temperature in the outer divertor region is used as ordering parameter.

Ultimately, divertor retention is proportional to the probability that every individual recycled He atom is ionized in the portion of the SOL with forward flow, rather than in the portion of the SOL with reversed flow, or in the PFR, or in the core. Only the first case would ensure a prompt return to the targets. The right plot in Fig. 5.10 shows the calculated fraction of the total recycled He atoms which are ionized in each of these distinct regions. The trend of the fraction of He atoms which are ionized in the portion of the SOL with forward flow qualitatively correlates very well with the trend of the simulated He compression. This confirms that, while decreasing the divertor temperature, the initial increase of the He compression is correlated with a decrease of the ionization in the portion of the SOL with reversed flow and in the PFR. Its rollover is instead correlated with an increase of the fraction of He atoms penetrating the entire divertor and being ionized within the confined region.
In the performed experiments (cf. Section 3.4.4) the decay of the He content in the plasma was seen to slow down in a discharge with very cold divertor. It is therefore possible that such a

case could be represented by one simulation after the rollover, i.e. with a non negligible amount of recycled He atoms penetrating to the confined region. In this sense, the simulated trend of the He compression with decreasing divertor temperature does not qualitatively contradict the experimental observations.
In the simulations, the increase of the N seeding level was stopped after a maximum value of $6 \cdot 10^{20}$ ions/s because simulations at larger seeding levels were unstable and prone to a radiation collapse. Assessing the behavior of He compression at such higher seeding levels is of practical interest. It is indeed experimentally shown that, at high N seeding levels, a so-called X-point radiator (XPR), which is a highly radiating region localized near the X-point within the confined plasma, is formed [213]. This is observed in different tokamaks, and is an attractive scenario in view of the requirements of power exhaust thanks to a strong power dissipation and mitigated ELMs. Theoretical models [214] and SOLPS-ITER simulations [197, 198] suggest that this scenario is intimately related with the formation of a cold plasma region around the X-point, allowing a very large fraction of neutrals recycled at the target plates to penetrate the confined plasma.
The simulations presented here, which only approach an XPR without actually reaching a cold X-point plasma, have shown a correlation between the degradation of He compression and the amount of He atoms penetrating the confined plasma. If this is confirmed, then an even more pronounced degradation of He compression may be expected when an XPR is fully reached. It is worth to note that a degradation of divertor retention with an XPR has not been observed for D and N. However, in view of the very different behavior in terms of penetration depth into the plasma of He atoms (cf. Fig. 5.7), a degradation of divertor retention for helium cannot be ruled out. Ultimately, this could be assessed only performing experiments and simulations of an XPR regime featuring He seeding.

5.3.3 Characterization of subdivertor helium gas transport

Subdivertor helium gas transport is the second phenomenon on which the analysis of the simulations focuses. Those He atoms which successfully escape the divertor plasma region still have a chance to be reflected multiple times by the material boundaries of the vessel and return towards the plasma. For maximizing the pumping, the He gas flow should be preferably directed towards the pumps. The characteristics of this flow strongly depend on the mass of the considered particles, on the sink effect due to active pumping, and possibly on the presence of viscous and friction effects (cf. Section 2.3.2).
A key aspect for a realistic simulation of neutral gas flows towards the pumping surfaces regards the physical obstacles encountered on the way, i.e. the shrinkage of the flow channel below the outer divertor target plate and the various support structures for the vessel, as well as cables and diagnostic gauges. Since the impact of such physical structures is the same for all neutral gas species, it is emulated by creating a fictitious duct between the sub-divertor chamber and the pump chamber. Its aperture was regulated in such a way to reproduce the experimentally observed pressure drop for the D_2 gas. The pressure drop for impurities depends additionally on the possible difference in the sink effect in the pump chamber (which exists for the case of He atoms), on the mass difference w.r.t. D_2 molecules and on the possible entrainment into the D_2 flow due to friction. These aspects are expected to be capture by EIRENE.
For a better understanding of the subdivertor neutral gas flows, we extracted the macroscopic quantities simulated by EIRENE along the flow domain. The top panel in Fig. 5.11 shows the simulated neutral He atom density in the entire subdivertor region. The employed pipe duct between sub-divertor chamber and pump chamber, which is visible in the Figure, produces a pressure drop for the D_2 gas of about $4-5$, while for the He gas the drop is about $2-2.5$. Since D_2 molecules and He atoms have nearly the same mass, this difference is explained by the less

intense sink effect in the pump chamber for He atoms, because of the ineffectiveness of the cryopump for them. These numbers are consistent with what was observed experimentally (cf. Section 3.4.2). This supports the assumption on the subdivertor conductance for the He gas which was employed in the time-dependent modelling presented in the previous Chapter. An a priori assumption on the subdivertor He partial pressure drop was indeed necessary because of the absence of He partial pressure measurements in the sub-divertor chamber.
Another important qualitative observation regarding the behavior of the He gas flow is the recirculation pattern which takes place between the divertor plasma region and the sub-divertor chamber. The bottom panel of Fig. 5.11 shows the simulated streamlines of the He atom flow. We note that, from the inner divertor, the gas flow is directed away from the plasma chamber, while it is directed towards the plasma through the outer divertor slit. This behavior is consistent with what was observed in similar simulations in the JET subdivertor [208]. It may have some impact on the simulated subdivertor pressure drop, but it is not expected to have a strong influence on the particle balances in the divertor plasma. The He neutral flux density through the slits is of the order of 10^{20} $m^{-2}s^{-1}$, which is roughly one order of magnitude less than the recycled He flux from the inner and outer divertor targets.

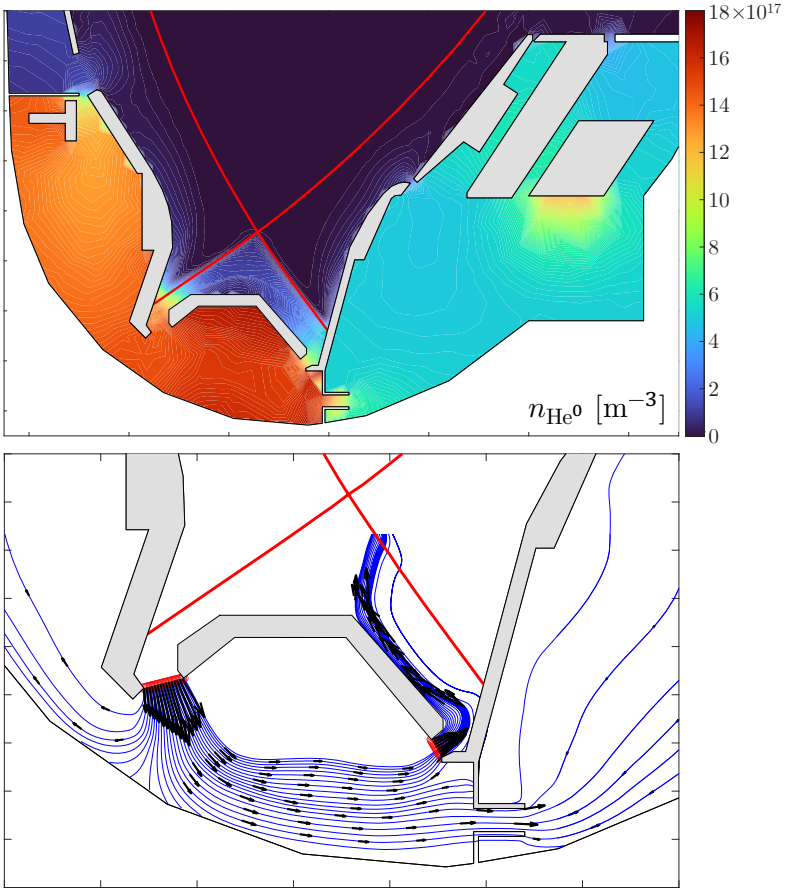

Figure 5.11: Top panel: distribution of the simulated neutral He atom density in the subdivertor region in the base case. Bottom panel: streamlines of the simulated He atom flow through the inner and outer divertor slits in the base case.

As a final remark, we note that the temperature of the wall boundaries, which was set to 300 K, has an impact on the simulated flow which is different for different species. The energetic atoms leaving the divertor plasma region undergo many collisions with the walls, leading to some degree of thermalization. For both D_2 molecules and He atoms, a temperature of 1000−1200 K is found in the sub-divertor chamber, as this is directly exposed to the energetic particles released from the plasma. In the pump chamber, instead, the thermalization of D_2 molecules is total, at a temperature of 300 K, while He atoms have still a temperature of about 800 K.

5.3.4 Impact of neutral gas friction on the helium gas flow

With the simulations we were able to quantify how much the implementation of neutral-neutral collisions contributes to the general behavior of subdivertor helium gas transport.
The neutral He atom density in the simulated scenario (cf. Figure 5.11) is relatively low, i.e. up to $2 \cdot 10^{18}$ m^{-3} in the sub-divertor chamber, corresponding to a He partial pressure of 0.03 Pa. For this reason, intrinsic viscous effects in the He gas flow can be safely ruled out. However, the friction exerted by the background deuterium gas may play a more relevant role, because

of the larger density of the latter and its more intense flow due to the action of the cryopump. This potentially induces some entrainment of He atoms within the background flow. The biggest impact is expected to come from D_2 molecules, which constitute the greater fraction of the deuterium gas in the subdivertor region.

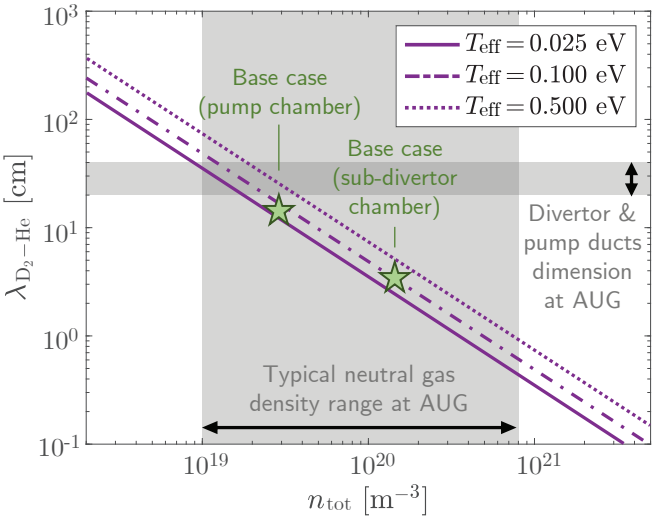

Figure 5.12: Predicted mean free path for the collisions between He atoms and D_2 molecules, as function of the total neutral gas density (i.e. $n_{\mathrm{tot}} \equiv n_{\mathrm{He}} + n_{\mathrm{D_2}}$), calculated using a rigid sphere model. Here, the effective temperature is given by $T_{\mathrm{eff}} \equiv \frac{m_{\mathrm{D_2}} T_{\mathrm{He}} + m_{\mathrm{He}} T_{\mathrm{D_2}}}{m_{\mathrm{He}} + m_{\mathrm{D_2}}}$.

This may be deduced from the mean free path for collisions of He atoms with D_2 molecules, as plotted in Fig. 5.12 as function of the D_2 density. For most of the typical density range encountered in AUG discharges, the mean free path is of the order of several cm, i.e. shorter than the typical dimensions of subdivertor region and pump ducts at AUG (which means a Kundsen number < 1). For example, in the base case, the mean free path for D_2-He collisions is around 4 cm in the sub-divertor chamber, and around 15 cm in the pump chamber. These values are only slightly smaller than the typical dimesions of the regions of interest. Therefore, it is not trivial to estimate whether the friction exerted by the D_2 flow does really enhance the transport of He atoms towards the pumping surfaces.

To assess this we performed a further series of simulations, with the same input parameters as the base case, varying the D fueling in order to achieve a wide range of neutral gas pressures in the subdivertor region, with and without including the D_2-He collisions. In this way, a range of total neutral pressures in the sub-divertor chamber of roughly 1−2 Pa (typical for H-mode plasmas in AUG) was simulated. For quantifying the neutral gas transport from the divertor towards the pumps, we considered the pressure drop between sub-divertor chamber and pump chamber as a figure of merit, as a larger pressure gradient implies a more intense flow.

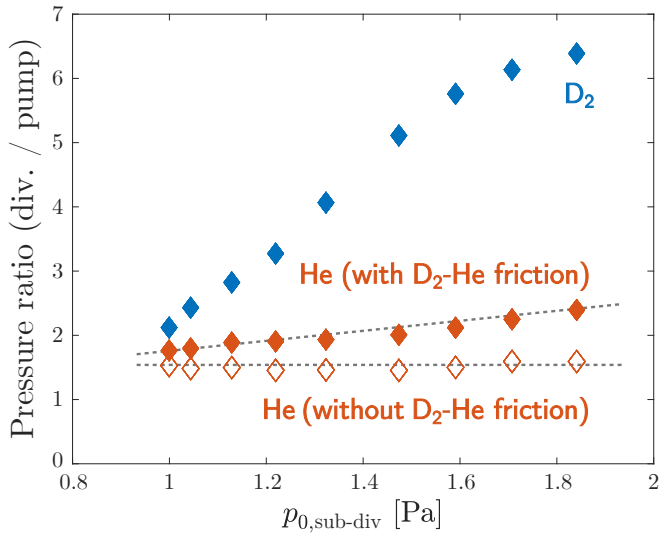

Figure 5.13: Simulated pressure drops between sub-divertor chamber and pump chamber for D_2 molecules and He atoms, as function of the total subdivertor gas pressure, with and without the D_2-He collisions activated.

Figure 5.13 shows the simulated pressure drops as function of the total subdivertor neutral pressure. The blue points refer to the D_2 gas, while the red filled and empty points refer to the He gas, with and without including the D_2-He collisions, respectively.

The D_2 gas flow shows a strong dependence on the total pressure. Since the pipe duct, which emulates the resistance given by physical obstacles, is fixed, this may be only attributed to a viscosity effect. The simulated trend is in qualitative agreement with the experimental observations (Figure 3.7).

The subdivertor pressure drop for the He gas is, generally, lower than for the D_2 gas. This is readily explained by the ab-

sence of the sink effect due to the cryopump for He atoms, whose flow towards the pump chamber is, therefore, less intense. Without collisions with the D_2 molecules, the pressure drop would be independent on the total pressure. The inclusion of such collisions results in an increase with the total pressure, with a trend which qualitatively follows that of the D_2 gas. This indicates, as expected, some degree of entrainment of the helium gas flow into the viscous deuterium gas flow. The degree of entrainment is, however, relatively low even at high pressures, as the pressure drop for the He gas remains lower than the one for the D_2 gas.
We conclude that, although an impact of neutral friction on the He gas flow in the AUG subdivertor is visible, the consequent enhancement of helium pumping is moderate. Therefore, this is not able to fully compensate for the lack of cryopumping, which is required for an efficient exhaust.

5.3.5 Validity of the simulation results

The SOLPS-ITER simulations presented in this Chapter show a good agreement with the experiment, at least in terms of numerical solutions for background plasma and neutral gas flows. The main deficiency is given by an important underestimation of the divertor retention for helium, which is determined by phenomena related to the plasma solutions. The absence of $\boldsymbol{E} \times \boldsymbol{B}$ and diamagnetic drifts in the plasma transport equations may play a role. It is observed that drifts enhance the asymmetry between inner and outer divertor, both in terms of ion fluxes and temperature [215]. With drifts activated, increased ion fluxes and lower temperatures at the inner target and reduced ion fluxes and higher temperatures at the outer target are observed [216]. Additionally, modelling several experimentally observed phenomena such as e.g. the formation of a high-field side high density front is possible only with drifts activated [217]. This may have an impact on both the stagnation surface of the He ion flow and the ionization front of recycled He atoms, whose competition determines divertor retention.
Nonetheless, there are indications that the absence of drifts is not sufficient to explain the discrepancy in the simulated He compression with the experiment. Namely, in the same simulations, the agreement with the experimental divertor compression for D and N is much better. Further aspects which may contribute to explain the discrepancies for the case of He are the following:

- No experimental information is available about radial helium transport in the SOL, because of the technical difficulties in measuring impurity densities in regions with open field lines with methods such as charge-exchange recombination spectroscopy. For this reason, the anomalous particle diffusivity set for He ions in the simulations presented here was the same as for D ions. Empirically tuning the intensity of radial He transport may help to achieve higher He densities in the divertor.
- The coefficients describing collisional parallel transport of He ions in the SOL used in the simulations presented here were derived in [218, 219]. They are based on a simple Zhdanov closure of the Braginskii equations [220], and calculated assuming a nearly zero mass ratio between main ions and impurity ions. Whereas this may be reasonable for heavier impurities, it may generate inaccuracies in the description of collisional helium transport. Recently, improved coefficients valid for arbitrary plasma mixtures were calculated [221] and implemented in SOLPS-ITER [222], in which the masses of main and impurity ions are comparable. The application of such improved coefficients in ITER simulations lead to weaker thermal forces and stronger friction forces on He ions. This results in the stagnation surface being shifted towards upstream, i.e. in an enlargement of the region with forward flow. As shown in this Chapter, He compression is very sensitive to the exact location of the stagnation surface of the He ion flow. Therefore, including such an improved treatment

may contribute to a further increase of the simulated He compression. This would bring the simulated values closer to the experimental ones.

- Including non-resonant CX collisions between He atoms and D ions would imply a relevant decrease of the mean free path of recycled He atoms, which is relevant only at very low electron temperatures (< 1.5 eV) and high D ion densities (cf. Fig. 2.12). It is unlikely that this would have any effect on the ionization of He atoms recycled in the SOL plasma. However, it is possible that the presence of a thin, high density, low temperature layer in the PFR shields the SOL plasma from the He atoms reflected from the roof baffle or from the subdivertor region, increasing the simulated He compression. Determining whether this really happens requires performing simulations which include these collisions.

Additional recent progress in the development of SOLPS-ITER may further contribute to achieve more realistic plasma solutions. Among these, e.g., the implementation of a new numerical scheme for the solution of the B2.5 equations involving a 9-point stencil [223], the possibility of using a B2.5 grid extended towards the main wall [224] and a self-consistent treatment of turbulence-driven anomalous SOL transport [225].

The simulations performed for this thesis aimed to identify the most important physics mechanisms which are relevant for the interpretation of helium transport and recycling in the divertor, and to characterize how these mechanisms are affected by the divertor scenario. Despite the quantitative discrepancies, the results are qualitatively consistent with the experimental observations. The lower He compression in the subdivertor region, w.r.t. that of D, indicates a poor He enrichment and, generally, a non efficient transport of He atoms towards the pumps. This is explained by the high first ionization energy of He atoms [147], which causes a very different recycling behavior of He atoms w.r.t. that of other impurities such as N and Ar [42, 43, 44]. The simulated characteristics of the neutral gas flows, which indicate a non negligible friction between the He and D_2 gases which however does not produce a full entrainment, are also in line with the experiment.

Chapter 6

Conclusions and outlook

The achievement of a positive power balance in a burning D-T plasma relies on an efficient removal of He "ash", as the accumulation of thermalized He ions would dilute the fusion fuel [24, 25, 26] and degrade the confinement properties [29]. Helium exhaust from tokamaks is determined by multiple physics aspects: ion transport in magnetized plasmas, atomic processes, plasma-material interactions and rarefied gas flow dynamics. Understanding the underlying mechanisms is the only way to develop operational scenarios for burning plasmas favourable for helium exhaust and compatible with the requirements of core confinement and power exhaust [10, 11]. Additionally, it supports the choice of wall materials and geometry for the plasma-facing components and the design of the pumping systems in future fusion reactors [48, 49].

For this purpose an experimental investigation of helium exhaust was performed at the ASDEX Upgrade (AUG) tokamak in the course of this work. We measured the time evolution of the He concentration both in the plasma and in the exhaust gas in He-seeded H-modes for different divertor plasma scenarios, namely different divertor neutral pressures and divertor detachment states. This was a revision of similar experiments performed in the past at AUG [78, 79, 80]. New experiments were motivated by a renewed divertor geometry [91] and the transition from a full-carbon wall to a reactor-relevant full-tungsten wall [92, 93] since the previous investigation. The experiments allowed to quantify how efficiently helium is transported towards the divertor and retained in the subdivertor volume as function of the divertor plasma scenario. Key ingredients for the experimental analyses were reliable measurements of the absolute impurity ion density in the plasma, through charge exchange recombination spectroscopy [121, 123], and He partial pressure measurements in the exhaust gas within the vacuum vessel, performed for the first time at AUG through an in-vessel optical Penning gauge [134].
The experimental investigation was complemented by a thorough numerical modelling to interpret the experimental observations and provide reasonable extrapolations towards future devices. We employed different numerical frameworks for the modelling of different aspects of helium exhaust. A novel multi-reservoir impurity particle balance model was applied to interpret the observed dynamic behavior of helium during plasma discharges and to quantify the relative impact of long-term wall storage and active pumping. This is an extension of the plasma transport model originally contained in the Aurora code [50] with a wall recycling model which realistically simulates plasma-wall interactions and long-term wall storage. This development was motivated by the need to assess the impact of the tungsten, which is known to have a high retention capability of He atoms [37], on the experimentally observed exhaust dynamics. On the other hand, we used the SOLPS-ITER code package [51] to interpret the mechanisms determining helium transport and recycling in the divertor and to assess their dependence on the divertor plasma and exhaust gas characteristics.

Referring to the Section 1.2.3, for an efficient exhaust, helium must be (1) *quickly transported from the core towards the divertor*, (2) *neutralized and recycled at the plasma-facing material surfaces*, (3) *retained within the subdivertor volume*, and (4) *efficiently collected by an active pumping system*. In the course of this work, we studied each of these processes experimentally and numerically, yielding the following conclusions:

1. In agreement with previous studies [78], helium exhaust at AUG is observed to be not constrained by core transport phenomena. The characteristic times describing core confinement of He ions are much shorter than those describing the active pumping. Radial transport in the inner core is mainly driven by turbulence [141], which prevents He ions from accumulating in the core in plasma conditions typical of AUG.
2. The full-tungsten wall of AUG cannot be considered as fully recycling for helium. Because of the efficient retention of He atoms in tungsten [37] the wall surfaces do not saturate within the time of a plasma discharge, and absorb a large amount of He atoms. The retained atoms can be released due to ion-bombardment-driven erosion. This constitutes a constant source of He particles for the plasma even when no external injection is performed. In this sense, the wall surfaces act as a particle reservoir filling up with He particles and releasing them in a following time. The net effect is delaying the permanent removal, i.e. through active pumping, of individual He particles from the system.
3. Divertor retention of recycled He atoms, quantified through the He compression, was experimentally found to improve with divertor neutral pressure. On the other hand, a slower removal rate is observed when the divertor transits to a strongly detached regime. Consistently, a degradation of divertor retention with a strongly detached divertor is observed in the performed SOLPS-ITER simulations. Both experiments and simulations indicate a poor He enrichment in the subdivertor region, close to the minimum threshold desired for ITER [9]. This indicates a non efficient transport of helium towards the pumps compared to that of deuterium. The SOLPS-ITER simulations indicate that the high ionization energy of He atoms is the key mechanism determining its poor divertor enrichment [147]. This also explains the very different recycling behavior of helium and other impurities such as nitrogen and argon [42, 43, 44].
4. The inefficient active pumping systems at AUG, where the cryopump does not remove He atoms [102], constitute a further hindrance to helium exhaust. The available pumping speed of the turbomolecular pumps is much weaker than that of the cryopump in removing other gas species [101]. Such poor pumping capability of He atoms would be incompatible with the requirements of a burning plasma [24, 25, 26], when the behavior of AUG is extrapolated towards a fusion reactor. The performed SOLPS-ITER simulations suggest that inter-species friction between the He gas flow and the much more intense D_2 gas flow in the subdivertor region, although non negligible, does not enhance helium pumping much.

The experimental and numerical results on helium exhaust achieved in this work enable predictions towards fusion reactors. Several important implications in view of reactor operations may be drafted.
In the newly developed multi-reservoir particle balance model, the walls had a major impact on both the general dynamics of helium in the system, and on the simulated helium transport in the plasma edge. This suggests that analytical and numerical models for impurity transport and exhaust may produce misleading results if plasma-wall interaction is not properly taken into account, at least when wall saturation is not reached. Whereas this is quantitatively more relevant for the case of helium in a tungsten tokamak, similar effects cannot be ruled out for other combinations of impurity and wall material. It is recommended for impurity transport studies to evaluate whether the assumption of a purely recycling wall is valid.

On the other hand, the experimental and numerical observations about divertor retention of recycled He atoms agree with earlier studies at AUG with different divertor geometry and wall material [78, 79, 80]. This indicates that divertor retention mostly depends on the divertor plasma characteristics (e.g. pressure and temperature), rather than on the technical characteristics of the device. This justifies the extrapolation of the observed behavior towards future fusion reactors. For this reason, the room for optimization of divertor retention of helium in a reactor is limited. Any operational divertor plasma scenario is indeed constrained by the requirements of power exhaust [10, 11], which must be achieved simultaneously with those of helium exhaust. For example, whereas full detachment is needed for power exhaust, it may lead to reduced He neutral pressures in the divertor.
The most relevant room for optimization of helium exhaust is therefore given by a proper design of the pumping systems. Extrapolating our results towards a reactor shows the unlikelihood of fulfilling the requirements of a stationary burning plasma only employing turbomolecular pumps, because of their limited pumping speed. Employing cryopumps which actively remove He atoms, e.g. through activated charcoal coating [46] or argon-frost [47], could be essential to fulfil this requirement.

Further efforts can strengthen the results achieved in this work, from both experimental and numerical points of view.
The performed experimental studies were limited to an assessment of helium exhaust in the most basic divertor plasma scenarios, i.e. type-I ELMy H-modes. To assess the compatibility of helium exhaust with the requirements of power exhaust, in view of reactor operations, investigations should be extended to other scenarios investigated at AUG [226]. Among these, ELM-suppressed H-modes through resonant magnetic perturbations (RMPs) [227], I-modes [228], negative triangularity plasmas [229] and ELM-free H-modes such as the EDA H-mode, [230], the quasi-continuous exhaust (QCE) regime [231], the X-point radiating (XPR) regime [232] and the compact radiative divertor (CRD) regime [233], can be considered.
Investigations in alternative divertor configurations, such as the X-divertor and the snowflake divertor [234] may be also performed in the near future at AUG, after the installation of a new upper divertor with in-vessel coils [235, 236]. Future upper divertor studies at AUG will also benefit from the presence of a new cryopump coated with activated charcoal to trigger helium cryosorption [237]. This will be a unique possibility to study and develop power-exhaust-relevant scenarios in a device with efficient helium pumping, which is the necessary to lay the foundations of operational scenarios for ITER and DEMO.
Furthermore, the SOLPS-ITER modelling can be improved to achieve a better agreement with the experimental divertor retention for helium, through the inclusion of drifts [215], an improved treatment of collisional helium transport [222] and the activation of non-resonant CX collisions in the atomic physics model. Helium transport and recycling can be also simulated in alternative divertor configurations [238] for predictive and interpretative purposes in view of the forthcoming upper divertor operations at AUG.

Bibliography

[1] J.P. Freidberg, "Plasma physics and fusion energy", 2008, *Cambridge University Press.*

[2] S. Chapman, T.G. Cowling, "The mathematical theory of non-uniform gases", 1939, *Cambridge University Press.*

[3] H.-S. Bosch and G.M. Hale, "Improved formulas for fusion cross-sections and thermal reactivities", 1992, *Nucl. Fusion*, **32**, 611.

[4] L. Spitzer, "Physics of fully ionized gases", 1962, *John Wiley and Sons.*

[5] U. Stroth, "Plasmaphysik", 2018, *Springer.*

[6] V.D. Shafranov, "Equilibrium of a toroidal plasma in a magnetic field", 1963, *J. Nucl. Energy, Part C Plasma Phys.*, **5**, 251.

[7] J. Wesson, "Tokamaks", 2011, *Oxford University Press.*

[8] R.A. Pitts *et al*, "Fusion: The way ahead", 2006, *Phys. World*, **19**, 20.

[9] A. Loarte *et al*, "Progress in the ITER Physics Basis - Power and particle control", 2007, *Nucl. Fusion*, **47**, S203.

[10] H. Zohm *et al*, "On the physics guidelines for a tokamak DEMO", 2013, *Nucl. Fusion*, **53**, 073019.

[11] M. Wischmeier, "High density operation for reactor-relevant power exhaust", 2015, *J. Nucl. Mater.*, **463**, 22-29.

[12] D. Naujoks, "Plasma-material interaction in controlled fusion", 2010, *Springer.*

[13] B. Lipschultz *et al*, "Plasma–surface interaction, scrape-off layer and divertor physics: implications for ITER", 2007, *Nucl. Fusion*, **47**, 1189.

[14] R. Parker *et al*, "Plasma-wall interactions in ITER", 1997, *J. Nucl. Mater.*, **241-243**, 1-26.

[15] J.P. Gunn *et al*, "Surface heat loads on the ITER divertor vertical targets", 2017, *Nucl. Fusion*, **57**, 046025.

[16] P.C. Stangeby, "The plasma boundary of magnetic fusion devices", 2000, *CRC Press.*

[17] C.S. Pitcher and P.C. Stangeby, "Experimental divertor physics", 1997, *Plasma Phys. Control. Fusion*, **39**, 779.

[18] F. Wagner *et al*, "Regime of improved confinement and high beta in neutral-beam-heated divertor discharges of the ASDEX tokamak", 1982, *Phys. Rev. Lett.*, **49**, 1408.

[19] F. Wagner *et al*, "Development of an edge transport barrier at the H-Mode transition of ASDEX", 1984, *Phys. Rev. Lett.*, **53**, 1453.

[20] F. Ryter *et al*, "Survey of the H-mode power threshold and transition physics studies in ASDEX Upgrade", 2013, *Nucl. Fusion*, **53**, 113003.

[21] H. Zohm *et al*, "Edge localized modes (ELMs)", 1996, *Plasma Phys. Control. Fusion*, **38**, 105.

[22] S.I. Krasheninnikov *et al*, "Divertor plasma detachment", 2016, *Phys. Plasmas*, **23**, 055602.

[23] S.I. Krasheninnikov and A.S. Kukushkin, "Physics of ultimate detachment of a tokamak divertor plasma", 2017, *J. Plasma Phys.*, **83**, 155830501.

[24] D. Reiter *et al*, "Burn condition, helium particle confinement and exhaust efficiency", 1990, *Nucl. Fusion*, **30**, 2141.

[25] D. Reiter *et al*, "Stationary burning: Analysis of profile effects on the required exhaust efficiency and the permitted helium particle confinement time", 1990, *J. Nucl. Mater.*, **176-177**, 756-762.

[26] D. Reiter *et al*, "Helium removal from tokamaks", 1991, *Plasma Phys. Control. Fusion*, **33**, 1579.

[27] J.D. Lawson, "Some criteria for a power producing thermonuclear reactor", 1957, *Proc. Phys. Soc. B*, **70**, 6.

[28] T. Pütterich *et al*, "Determination of the tolerable impurity concentrations in a fusion reactor using a consistent set of cooling factors", 2019, *Nucl. Fusion*, **59**, 056013.

[29] A. Kappatou *et al*, "Energy confinement and performance of pure helium plasmas and helium seeded deuterium plasmas", 2018, *27th IAEA Fusion Energy Conference, Gandhinagar.*

[30] D.C. McDonald *et al*, "ELMy H-modes in JET helium-4 plasmas", 2004, *Plasma Phys. Control. Fusion*, **46**, 519.

[31] F. Ryter *et al*, "H-mode threshold and confinement in helium and deuterium in ASDEX Upgrade", 2009, *Nucl. Fusion*, **49**, 062003.

[32] P. Manas *et al*, "The confinement of helium tokamak plasmas, impact of electron heating, turbulent transport and zonal flows", 2019, *Nucl. Fusion*, **59**, 014002.

[33] J. Hillesheim *et al*, "Implications of JET-ILW L-H transition studies for ITER", 2018, *27th IAEA Fusion Energy Conference, Gandhinagar.*

[34] U. Plank *et al*, "H-mode power threshold studies in mixed ion species plasmas at ASDEX Upgrade", 2020, *Nucl. Fusion*, **60**, 074001.

[35] T. Pütterich *et al*, "ELM flushing and impurity transport in the H-mode edge barrier in ASDEX Upgrade", 2011, *J. Nucl. Mater.*, **415**, S334-S339.

[36] E.J. Doyle *et al*, "Progress in the ITER Physics Basis - Plasma confinement and transport", 2007, *Nucl. Fusion*, **47**, S18.

[37] K. Schmid *et al*, "The implications of high-Z first-wall materials on noble gas wall recycling", 2007, *Nucl. Fusion*, **47**, 984.

[38] R. Neu *et al*, "Tungsten: an option for divertor and main chamber plasma facing components in future fusion devices", 2005, *Nucl. Fusion*, **45**, 209.

[39] A. Kärcher *et al*, "The influence of displacement damage on helium uptake and retention in tungsten", 2023, *Nucl. Mater. Energy*, **34**, 101370.

[40] V. Rohde *et al*, "Wall retention of deuterium and gaseous impurities in all tungsten ASDEX Upgrade", 2009, *Plasma Phys. Control. Fusion*, **51**, 124033.

[41] P.C. Stangeby and J.D. Elder, "Impurity retention by divertors I. One dimensional models", 1995, *Nucl. Fusion*, **35**, 1391.

[42] L. Xiang *et al*, "Modeling of argon seeding in ASDEX Upgrade H-mode plasma with SOLPS5.0", 2017, *Nucl. Mater. Energy*, **12**, 1146-1151.

[43] I.Y. Senichenkov *et al*, "On mechanisms of impurity leakage and retention in the tokamak divertor", 2019, *Plasma Phys. Control. Fusion*, **61**, 045013.

[44] F. Hitzler *et al*, "Impurity transport and divertor retention in Ar and N seeded SOLPS 5.0 simulations for ASDEX Upgrade", 2020, *Plasma Phys. Control. Fusion*, **62**, 085013.

[45] A. Kallenbach *et al*, "Impurity seeding for tokamak power exhaust: from present devices via ITER to DEMO", 2013, *Plasma Phys. Control. Fusion*, **55**, 124041.

[46] D.W. Sedgley, "Development and application of charcoal sorbents for cryopumping fusion devices", 1989, *Fusion Eng. Des.*, **10**, 217-222.

[47] J. Kim *et al*, "Helium pumping by argon frosting on a 4.5 K surface", 1990, *J. Vacuum Sci. Technol. A*, **8**, 3084-3087.

[48] R.A. Pitts *et al*, "Physics basis and design of the ITER plasma-facing components", 2011, *J. Nucl. Mater.*, **415**, S957-S964.

[49] G. Federici *et al*, "Overview of the DEMO staged design approach in Europe", 2019, *Nucl. Fusion*, **59**, 066013.

[50] F. Sciortino *et al*, "Modeling of particle transport, neutrals and radiation in magnetically-confined plasmas with Aurora", 2021, *Plasma Phys. Control. Fusion*, **63**, 112001.

[51] R. Schneider *et al*, "Plasma edge physics with B2-Eirene", 2006, *Contrib. Plasma Phys.*, **46**, 3-191.

[52] R. Dux, "Impurity transport in ASDEX Upgrade", 2003, *Fusion Sci. Technol.*, **44**, 708-715.

[53] R. Dux, "Impurity transport in tokamak plasmas", 2004, *IPP report 10-27*.

[54] H.P. Summers *et al*, "Ionization state, excited populations and emission of impurities in dynamic finite density plasmas: I. The generalized collisional–radiative model for light elements", 2006, *Plasma Phys. Control. Fusion*, **48**, 263.

[55] Open-ADAS website. https://open.adas.ac.uk/.

[56] R. Balescu, "Transport processes in plasmas, vol. 1 - Classical transport", 1988, *North Holland*.

[57] R. Balescu, "Transport processes in plasmas, vol. 2 - Neoclassical transport", 1988, *North Holland*.

[58] D. Fajardo *et al*, "Analytical model for collisional impurity transport in tokamaks at arbitrary collisionality", 2022, *Plasma Phys. Control. Fusion*, **64**, 055017.

[59] R. Balescu, "Aspects of anomalous transport in plasmas", 2005, *CRC Press*.

[60] F.F. Chen, "Resistive overstabilities and anomalous "diffusion"", 1965, *Phys. Fluids*, **8**, 912-919.

[61] F. Romanelli, "Ion temperature-gradient-driven modes and anomalous ion transport in tokamaks", 1989, *Phys. Fluids B: Plasma Physics*, **1**, 1018–1025.

[62] S.C. Prager, A.K. Sen and T.C. Marshall, "Dissipative trapped-electron instability in cylindrical geometry", 1974, *Phys. Rev. Lett.*, **33**, 692.

[63] S.I. Braginskii, "Transport processes in a plasma", 1965, *Reviews of Plasma Physics*, **1**, 205-311.

[64] J. Neuhauser *et al*, "Modelling of impurity flow in the tokamak scrape-off layer", 1984, *Nucl. Fusion*, **24**, 39.

[65] W.O. Hofer and J. Roth, "Physical processes of the interaction of fusion plasmas with solids", 1996, *Academic Press*.

[66] W. Eckstein, "Physical sputtering and reflection processes in plasma-wall interactions", 1997, *J. Nucl. Mater.*, **248**, 1-8.

[67] K. Schmid *et al*, "Impact of gyro-motion and sheath acceleration on the flux distribution on rough surfaces", 2010, *Nucl. Fusion*, **50**, 105004.

[68] J.P. Biersack and W. Eckstein, "Sputtering Studies with the Monte Carlo Program TRIM.SP", 1984, *Appl. Phys. A*, **34**, 73-94.

[69] W. Eckstein, "Backscattering and sputtering with the monte-carlo program TRIM.SP", 1994, *Radiat. Eff. Defects Solids*, **130-131**, 239-250.

[70] HYDHEL database. https://www.eirene.de/Documentation/documentation.html.

[71] R.J. Goldston, "A simple neutral density profile calculation for tokamaks with $\lambda_{\mathrm{mfp}} \ll a$", 1978, *Plasma Physics*, **20**, 1199.

[72] K. Shimizu *et al*, "A review on impurity transport in divertors", 1997, *J. Nucl. Mater.*, **241-243**, 167-181.

[73] J.M. Lafferty, "Foundations of vacuum science and technology", 1998, *John Wiley and Sons*.

[74] M. Abdou *et al*, "Physics and technology considerations for the deuterium–tritium fuel cycle and conditions for tritium fuel self sufficiency", 2021, *Nucl. Fusion*, **61**, 013001.

[75] M. Groth *et al*, "Noble gas enrichment studies at JET", 2001, *J. Nucl. Mater.*, **290-293**, 867-871.

[76] M. Groth *et al*, "Helium and neon enrichment studies in the JET Mark IIAP and Mark IIGB divertors", 2002, *Nucl. Fusion*, **42**, 591.

[77] K.-D. Zastrow *et al*, "Helium exhaust experiments on JET with Type I ELMs in H-mode and with Type III ELMs in ITB discharges", 2005, *Nucl. Fusion*, **45**, 163.

[78] H.-S. Bosch *et al*, "Particle exhaust studies in ASDEX Upgrade", 1997, *Plasma Phys. Control. Fusion*, **39**, 1771.

[79] H.-S. Bosch *et al*, "Noble gas exhaust with a strongly baffled divertor in ASDEX-Upgrade", 1999, *J. Nucl. Mater.*, **266-269**, 462-466.

[80] H.-S. Bosch *et al*, "Helium transport and exhaust with an ITER-like divertor in ASDEX Upgrade", 2001, *J. Nucl. Mater.*, **290-293**, 836-839.

[81] A. Sakasai *et al*, "Helium exhaust in divertor–closure configuration with W-shaped divertor of JT-60U", 2001, *J. Nucl. Mater.*, **290-293**, 957-961.

[82] M.R. Wade *et al*, "Helium exhaust studies in the DIII-D tokamak", 1995, *J. Nucl. Mater.*, **220-222**, 178-182.

[83] M.R. Wade *et al*, "Impurity enrichment studies with induced scrape-off layer flow on DIII-D", 1998, *Nucl. Fusion*, **38**, 1839.

[84] E.T. Hinson *et al*, "Enhanced helium exhaust during edge-localized mode suppression by resonant magnetic perturbations at DIII-D", 2020, *Nucl. Fusion*, **60**, 054004.

[85] D.P. Coster *et al*, "B2-EIRENE modelling of He compression and enrichment", 2001, *J. Nucl. Mater.*, **290-293**, 845-848.

[86] D. Reiser *et al*, "Helium compression analysis for ASDEX Upgrade with fluid and kinetic codes", 2001, *J. Nucl. Mater.*, **290-293**, 953-956.

[87] A.S. Kukushkin *et al*, "Effect of conditions for gas recirculation on divertor operation in ITER", 2007, *Nucl. Fusion*, **47**, 698.

[88] G.W. Pacher *et al*, "ITER operation window determined from mutually consistent core–SOL–divertor simulations: definition and application", 2008, *Nucl. Fusion*, **48**, 105003.

[89] H.D. Pacher *et al*, "Modelling of the ITER reference divertor plasma", 2011, *J. Nucl. Mater.*, **415**, S492-S496.

[90] H.D. Pacher *et al*, "Impurity seeding in ITER DT plasmas in a carbon-free environment", 2015, *J. Nucl. Mater.*, **463**, 591-595.

[91] R. Neu *et al*, "Properties of the new divertor IIb in ASDEX Upgrade", 2002, *Plasma Phys. Control. Fusion*, **44**, 1021.

[92] R. Neu *et al*, "Plasma wall interaction and its implication in an all tungsten divertor tokamak", 2007, *Plasma Phys. Control. Fusion*, **49**, B59.

[93] R. Neu *et al*, "Overview on plasma operation with a full tungsten wall in ASDEX Upgrade", 2013, *J. Nucl. Mater.*, **438**, S34-S41.

[94] R.A. Pitts *et al*, "Physics basis for the first ITER tungsten divertor", 2019, *Nucl. Mater. Energy*, **20**, 100696.

[95] A. Zito *et al*, "Investigation of helium exhaust dynamics at the ASDEX Upgrade tokamak with full-tungsten wall", 2023, *Nucl. Fusion*, **63**, 096027.

[96] A. Herrmann and O. Gruber, "ASDEX Upgrade - Introduction and overview", 2003, *Fusion Sci. Technol.*, **44**, 569-577.

[97] J. Neuhauser *et al*, "Edge and divertor physics in ASDEX Upgrade", 2003, *Fusion Sci. Technol.*, **44**, 659-681.

[98] R. Neu *et al*, "Plasma-wall interaction and first-wall materials in ASDEX Upgrade", 2003, *Fusion Sci. Technol.*, **44**, 692-707.

[99] B. Streibl *et al*, "Machine design, fueling and heating in ASDEX Upgrade", 2003, *Fusion Sci. Technol.*, **44**, 578-592.

[100] T. Härtl *et al*, "Status and perspectives of the ASDEX Upgrade gas inlet system", 2015, *Fusion Eng. Des.*, **96-97**, 265-268.

[101] V. Rohde *et al*, "Gas balance in ASDEX Upgrade with tungsten first wall", 2009, *J. Nucl. Mater.*, **390-391**, 474-477.

[102] B. Streibl *et al*, "Operational behaviour of the ASDEX Upgrade in-vessel cryo pump", 2001, *Fusion Eng. Des.*, **56-57**, 867-872.

[103] F. Leuterer *et al*, "The ECRH system of ASDEX Upgrade", 2001, *Fusion Eng. Des.*, **56-57**, 615-619.

[104] J.-M. Noterdaeme *et al*, "The ASDEX upgrade ICRH antenna", 1994, *Fusion Eng. Des.*, **24**, 65-74.

[105] A. Stäbler *et al*, "Design of the neutral beam injection system for ASDEX Upgrade", 1988, *15th Symposium on Fusion Technology, Utrecht.*

[106] M. Kikuchi, "A note on the Mirnov signal analysis in tokamaks", 1986, *Nucl. Fusion*, **26**, 101.

[107] P.J. McCarthy *et al*, "The CLISTE interpretive equilibrium code", 1999, *IPP report 5-85.*

[108] P.J. McCarthy, "Analytical solutions to the Grad–Shafranov equation for tokamak equilibrium with dissimilar source functions", 1999, *Phys. Plasmas*, **6**, 3554–3560.

[109] H. Murmann *et al*, "The Thomson scattering systems of the ASDEX Upgrade tokamak", 1992, *Rev. Sci. Instrum.*, **63**, 4941-4943.

[110] I.H. Hutchinson, "Principles of plasma diagnostics", 2002, *Cambridge University Press.*

[111] B. Kurzan and H.D. Murmann, "Edge and core Thomson scattering systems and their calibration on the ASDEX Upgrade tokamak", 2011, *Rev. Sci. Instrum.*, **82**, 103501.

[112] E. Wolfrum *et al*, "Fast lithium-beam spectroscopy of tokamak edge plasmas", 1993, *Rev. Sci. Instrum.*, **64**, 2285-2292.

[113] J. Schweinzer *et al*, "Reconstruction of plasma edge density profiles from LiI(2s-2p) emission profiles", 1992, *Plasma Phys. Control. Fusion*, **34**, 1173.

[114] R. Fischer *et al*, "Probabilistic lithium beam data analysis", 2008, *Plasma Phys. Control. Fusion*, **50**, 085009.

[115] M. Willensdorfer *et al*, "Characterization of the Li-BES at ASDEX Upgrade", 2014, *Plasma Phys. Control. Fusion*, **56**, 025008.

[116] S.K. Rathgeber *et al*, "Estimation of edge electron temperature profiles via forward modelling of the electron cyclotron radiation transport at ASDEX Upgrade", 2013, *Plasma Phys. Control. Fusion*, **55**, 025004.

[117] R.C. Isler, "An overview of charge-exchange spectroscopy as a plasma diagnostic", 1994, *Plasma Phys. Control. Fusion*, **36**, 171.

[118] E. Viezzer *et al*, "High-resolution charge exchange measurements at ASDEX Upgrade", 2012, *Rev. Sci. Instrum.*, **83**, 103501.

[119] R.M. McDermott *et al*, "Extensions to the charge exchange recombination spectroscopy diagnostic suite at ASDEX Upgrade", 2017, *Rev. Sci. Instrum.*, **88**, 073508.

[120] M. Cavedon *et al*, "A fast edge charge exchange recombination spectroscopy system at the ASDEX Upgrade tokamak", 2017, *Rev. Sci. Instrum.*, **88**, 043103.

[121] R.M. McDermott *et al*, "Evaluation of impurity densities from charge exchange recombination spectroscopy measurements at ASDEX Upgrade", 2018, *Plasma Phys. Control. Fusion*, **60**, 095007.

[122] R.J. Fonck *et al*, "Determination of plasma-ion velocity distribution via charge-exchange recombination spectroscopy", 1984, *Phys. Rev. A*, **29**, 3288.

[123] A. Kappatou *et al*, "A forward model for the helium plume effect and the interpretation of helium charge exchange measurements at ASDEX Upgrade", 2018, *Plasma Phys. Control. Fusion*, **60**, 055006.

[124] S. Potzel *et al*, "Electron density determination in the divertor volume of ASDEX Upgrade via Stark broadening of the Balmer lines", 2014, *Plasma Phys. Control. Fusion*, **56**, 025010.

[125] S.S. Henderson *et al*, "Determination of volumetric plasma parameters from spectroscopic N II and N III line ratio measurements in the ASDEX Upgrade divertor", 2018, *Nucl. Fusion*, **58**, 016047.

[126] D. Brida *et al*, "Heat flux pattern in detached L-modes and ELM mitigated H-modes with rotating magnetic perturbations in ASDEX Upgrade", 2017, *Nucl. Fusion*, **57**, 116006.

[127] M. Weinlich and A. Carlson, "Flush mounted probes in ASDEX Upgrade", 1996, *Contrib. Plasma Phys.*, **36**, 53-59.

[128] M. Weinlich and A. Carlson, "Flush mounted Langmuir probes in an oblique magnetic field", 1997, *Phys. Plasmas*, **4**, 2151-2160.

[129] G. Haas and H.-S. Bosch, "In vessel pressure measurement in nuclear fusion experiments with ASDEX gauges", 1998, *Vacuum*, **51**, 39-46.

[130] A. Scarabosio *et al*, "Measurements of neutral gas fluxes under different plasma and divertor regimes in ASDEX Upgrade", 2009, *J. Nucl. Mater.*, **390-391**, 494-497.

[131] A. Drenik *et al*, "Detection of ammonia by residual gas analysis in AUG and JET", 2017, *Fusion Eng. Des.*, **124**, 239-243.

[132] Extrel MAX QMS specifications.
https://www.process-insights.com/products-3/products-industrial/mass-spectrometers-gas-analyzers/max-qms-flange-mounted-system/.

[133] F.M. Penning, "Die glimmentladung bei niedrigem druck zwischen koaxialen zylindern in einem axialen magnetfeld", 1936, *Physica*, **3**, 873-894.

[134] T. Kremeyer *et al*, "Wisconsin In Situ Penning (WISP) gauge: A versatile neutral pressure gauge to measure partial pressures in strong magnetic fields", 2020, *Rev. Sci. Instrum.*, **91**, 043504.

[135] D.L. Hillis *et al*, "Deuterium-tritium concentration measurements in the divertor of a tokamak via a modified Penning gauge", 1997, *Fusion Eng. Des.*, **34-35**, 347-351.

[136] S. Vartanian *et al*, "Simultaneous H/D/T and ^{3}He/^{4}He absolute concentration measurements with an optical Penning gauge on JET", 2021, *Fusion Eng. Des.*, **170**, 112511.

[137] H.-S. Bosch *et al*, "Invariance of divertor retention on external particle flow in detached ASDEX Upgrade discharges", 1996, *Phys. Rev. Lett.*, **76**, 2499.

[138] A. Kallenbach *et al*, "Developments towards an ELM-free pedestal radiative cooling scenario using noble gas seeding in ASDEX Upgrade", 2021, *Nucl. Fusion*, **61**, 016002.

[139] R. Fischer *et al*, "Integrated Data Analysis of profile diagnostics at ASDEX Upgrade", 2010, *Fusion Sci. Technol.*, **58**, 675-684.

[140] R. Fischer *et al*, "Bayesian modelling of fusion diagnostics", 2003, *Plasma Phys. Control. Fusion*, **45**, 1095.

[141] A. Kappatou *et al*, "Understanding helium transport: experimental and theoretical investigations of low-Z impurity transport at ASDEX Upgrade", 2019, *Nucl. Fusion*, **59**, 056014.

[142] M. Cavedon *et al*, "Pedestal and E_r profile evolution during an edge localized mode cycle at ASDEX Upgrade", 2017, *Plasma Phys. Control. Fusion*, **59**, 105007.

[143] P.E. Lhuillier *et al*, "Helium retention and early stages of helium-vacancy complexes formation in low energy helium-implanted tungsten", 2013, *J. Nucl. Mater.*, **433**, 305-313.

[144] L. Pentecoste *et al*, "Low energy and low fluence helium implantations in tungsten: Molecular dynamics simulations and experiments", 2016, *J. Nucl. Mater.*, **470**, 44-54.

[145] V. Rohde *et al*, "Wall conditioning in ASDEX Upgrade", 2007, *J. Nucl. Mater.*, **363-365**, 1369-1374.

[146] A. Kallenbach *et al*, "Non-boronized compared with boronized operation of ASDEX Upgrade with full-tungsten plasma facing components", 2009, *Nucl. Fusion*, **49**, 045007.

[147] A. Kallenbach *et al*, "Divertor enrichment of recycling impurity species (He, N_2, Ne, Ar, Kr) in ASDEX Upgrade", *Submitted to Nucl. Fusion.*

[148] A. Kallenbach *et al*, "Divertor power load feedback with nitrogen seeding in ASDEX Upgrade", 2010, *Plasma Phys. Control. Fusion*, **52**, 055002.

[149] F. Reimold *et al*, "Experimental studies and modeling of complete H-mode divertor detachment in ASDEX Upgrade", 2015, *J. Nucl. Mater.*, **463**, 128-134.

[150] P.A. Schneider *et al*, "Observation of different phases during an ELM crash with the help of nitrogen seeding", 2014, *Plasma Phys. Control. Fusion*, **56**, 025011.

[151] M.G. Dunne, "Impact of impurity seeding and divertor conditions on transitions, pedestal structure and ELMs", 2017, *Nucl. Fusion*, **57**, 025002.

[152] R. Schneider *et al*, "Role of divertor geometry on detachment in ASDEX Upgrade", 1999, *J. Nucl. Mater.*, **266-269**, 175-181.

[153] J. Roth *et al*, "Divertor retention for recycling impurities", 1992, *Nucl. Fusion*, **32**, 1835.

[154] G. Meisl *et al*, "Implantation and erosion of nitrogen in tungsten", 2014, *New J. Phys.*, **16**, 093018.

[155] G. Meisl *et al*, "Nitrogen retention in ASDEX Upgrade", 2015, *J. Nucl. Mater.*, **463**, 668-671.

[156] K. Behringer, 1987, *Rep. JET-R 87(08)*.

[157] P.C. Stangeby and J.D. Elder, "Calculation of observable quantities using a divertor impurity interpretive code, DIVIMP", 1992, *J. Nucl. Mater.*, **196-198**, 258-263.

[158] K. Schmid *et al*, "An integrated model of impurity migration and wall composition dynamics for tokamaks", 2011, *J. Nucl. Mater.*, **415**, S284-S288.

[159] K. Schmid *et al*, "Quantitative modeling of fuel retention in the JET-C and JET-ILW wall configurations by WallDYN and predictions for ITER", 2015, *J. Nucl. Mater.*, **463**, 66-72.

[160] G. Meisl *et al*, "Simulating the nitrogen migration in Be/W tokamaks with WallDYN", 2016, *Phys. Scr.*, **T167**, 014079.

[161] F. Sciortino *et al*, "Experimental inference of neutral and impurity transport in Alcator C-Mod using high-resolution x-ray and ultra-violet spectra", 2021, *Nucl. Fusion*, **61**, 126060.

[162] T. Nishizawa *et al*, "Non-parametric inference of impurity transport coefficients in the ASDEX Upgrade tokamak", 2022, *Nucl. Fusion*, **62**, 076021.

[163] O. Linder *et al*, "Self-consistent modeling of runaway electron generation in massive gas injection scenarios in ASDEX Upgrade", 2020, *Nucl. Fusion*, **60**, 096031.

[164] L.L. Lao *et al*, "Reconstruction of current profile parameters and plasma shapes in tokamaks", 1985, *Nucl. Fusion*, **25**, 1611.

[165] R. Dux *et al*, "Main chamber sources and edge transport of tungsten in H-mode plasmas at ASDEX Upgrade", 2011, *Nucl. Fusion*, **51**, 053002.

[166] L. Casali *et al*, "Modelling of nitrogen seeding experiments in the ASDEX Upgrade tokamak", 2018, *Phys. Plasmas*, **25**, 032506.

[167] E. Viezzer *et al*, "Dynamics of the pedestal transport during edge localized mode cycles at ASDEX Upgrade", 2020, *Plasma Phys. Control. Fusion*, **62**, 024009.

[168] W. Eckstein, "Computer simulation of ion-solid interactions", 1991, *Springer*.

[169] W. Eckstein, "Calculated sputtering, reflection and range values", 2002, *IPP report 9-132*.

[170] M. Wischmeier *et al*, "High recycling outer divertor regimes after type-I ELMs at high density in ASDEX Upgrade", 2007, *J. Nucl. Mater.*, **363-365**, 448-452.

[171] S. Brezinsek *et al*, "Characterisation of the deuterium recycling at the W divertor target plates in JET during steady-state plasma conditions and ELMs", 2016, *Phys. Scr.*, **T167**, 014076.

[172] F.M. Laggner *et al*, "Divertor, scrape-off layer and pedestal particle dynamics in the ELM cycle on ASDEX Upgrade", 2018, *Plasma Phys. Control. Fusion*, **60**, 025002.

[173] A. Drenik *et al*, "Evolution of nitrogen concentration and ammonia production in N_2-seeded H-mode discharges at ASDEX Upgrade", 2019, *Nucl. Fusion*, **59**, 046010.

[174] A. Kallenbach *et al*, "Plasma surface interactions in impurity seeded plasmas", 2011, *J. Nucl. Mater.*, **415**, S19-S26.

[175] W. Fundamenski *et al*, "A model of ELM filament energy evolution due to parallel losses", 2006, *Plasma Phys. Control. Fusion*, **48**, 109.

[176] D. Moulton *et al*, "Quasineutral plasma expansion into infinite vacuum as a model for parallel ELM transport", 2013, *Plasma Phys. Control. Fusion*, **55**, 085003.

[177] C. Guillemaut *et al*, "Ion target impact energy during type I edge localized modes in JET ITER-like wall", 2015, *Plasma Phys. Control. Fusion*, **57**, 085006.

[178] T. Eich *et al*, "On the asymmetries of ELM divertor power deposition in JET and ASDEX Upgrade", 2009, *J. Nucl. Mater.*, **390-391**, 760-763.

[179] M. Küstner *et al*, "The influence of surface roughness on the angular dependence of the sputter yield", 1998, *Nucl. Instrum. Methods Phys. Res. B*, **145**, 320-331.

[180] C. Cupak *et al*, "Sputter yields of rough surfaces: Importance of the mean surface inclination angle from nano- to microscopic rough regimes", 2021, *Appl. Surf. Sci.*, **570**, 151204.

[181] A. Hakola *et al*, "Long-term erosion of plasma-facing materials with different surface roughness in ASDEX Upgrade", 2014, *Phys. Scr.*, **T159**, 014027.

[182] C.C. Klepper *et al*, "Design of a diagnostic residual gas analyzer for the ITER divertor", 2015, *Fusion Eng. Des.*, **96-97**, 803-807.

[183] C.C. Klepper *et al*, "Extending helium partial pressure measurement technology to JET DTE2 and ITER", 2016, *Rev. Sci. Instrum.*, **87**, 11D442.

[184] C. Day *et al*, "The vacuum systems of ITER", 2008, *Vacuum*, **83**, 773-778.

[185] R.J.H. Pearce *et al*, "Gas species, their evolution and segregation through the ITER vacuum systems", 2012, *Vacuum*, **86**, 1725-1730.

[186] R.J.H. Pearce *et al*, "The ITER divertor pumping system, design evolution, simplification and performance", 2013, *Fusion Eng. Des.*, **88**, 809-813.

[187] X. Bonnin *et al*, "Presentation of the new SOLPS-ITER code package for tokamak plasma edge modelling", 2016, *Plasma Fusion Res.*, **11**, 1403102.

[188] S. Wiesen *et al*, "The new SOLPS-ITER code package", 2015, *J. Nucl. Mater.*, **463**, 480-484.

[189] B.J. Braams, "Computational studies in tokamak equilibrium and transport", 1986, *Ph.D. Thesis*.

[190] M. Baelmans, "Code improvements and applications of a two-dimensional edge plasma model for toroidal fusion devices", 1993, *Ph.D. Thesis*.

[191] D. Reiter, "Randschicht-konfiguration von tokamaks: entwicklung und anwendung stochastischer modelle zur beschreibung des neutralgastransports", 1984, *Ph.D. Thesis*.

[192] D. Reiter *et al*, "The EIRENE and B2-EIRENE codes", 2005, *Fusion Sci. Technol.*, **47**, 172-186.

[193] E. Kaveeva *et al*, "SOLPS-ITER drift modelling of JET Ne and N-seeded H-modes", 2021, *Nucl. Mater. Energy*, **28**, 101030.

[194] N. Horsten *et al*, "Validation of SOLPS-ITER simulations with kinetic, fluid, and hybrid neutral models for JET-ILW low-confinement mode plasmas", 2022, *Nucl. Mater. Energy*, **33**, 101247.

[195] H. Wu *et al*, "SOLPS-ITER modeling of ASDEX Upgrade L-mode detachment states", 2021, *Plasma Phys. Control. Fusion*, **63**, 105005.

[196] A. Zito *et al*, "Numerical modelling of an enhanced perpendicular transport regime in the scrape-off layer of ASDEX Upgrade", 2021, *Plasma Phys. Control. Fusion*, **63**, 075003.

[197] I.Y. Senichenkov *et al*, "Approaching the radiating X-point in SOLPS-ITER modeling of ASDEX Upgrade H-mode discharges", 2021, *Plasma Phys. Control. Fusion*, **63**, 055011.

[198] O. Pan *et al*, "SOLPS-ITER simulations of an X-point radiator in the ASDEX Upgrade tokamak", 2023, *Nucl. Fusion*, **63**, 016001.

[199] E.T. Meier *et al*, "Drifts, currents, and power scrape-off width in SOLPS-ITER modeling of DIII-D", 2017, *Nucl. Mater. Energy*, **12**, 973-977.

[200] W. Dekeyser *et al*, "SOLPS-ITER modeling of the Alcator C-Mod divertor plasma", 2016, *Plasma Fusion Res.*, **11**, 1403103.

[201] M. Wensing *et al*, "SOLPS-ITER validation with TCV L-mode discharges", 2021, *Phys. Plasmas*, **28**, 082508.

[202] E. Kaveeva *et al*, "SOLPS-ITER modelling of ITER edge plasma with drifts and currents", 2020, *Nucl. Fusion*, **60**, 046019.

[203] F. Subba *et al*, "SOLPS-ITER modeling of divertor scenarios for EU-DEMO", 2021, *Nucl. Fusion*, **61**, 106013.

[204] A.S. Kukushkin *et al*, "Finalizing the ITER divertor design: The key role of SOLPS modeling", 2011, *Fusion Eng. Des.*, **86**, 2865-2873.

[205] D. Reiter *et al*, "Non-linear effects on neutral gas transport in divertors", 1997, *J. Nucl. Mater.*, **241-243**, 342-348.

[206] AMJUEL database. https://www.eirene.de/Documentation/documentation.html.

[207] C. May, "Neutralgasströmugen in Fusionexperimenten bei endlichen Knudsenzahlen", 1997, *Ph.D. Thesis*.

[208] S. Varoutis *et al*, "Simulation of neutral gas flow in the JET sub-divertor", 2017, *Fusion Eng. Des.*, **121**, 13-21.

[209] V. Kotov *et al*, "Numerical study of the ITER divertor plasma with the B2-EIRENE code package", 2007.

[210] P.L. Bhatnagar, E.P. Gross and M. Krook, "A model for collision processes in gases. I. Small amplitude processes in charged and neutral one-component systems", 1954, *Phys. Rev.*, **94**, 511.

[211] P. David *et al*, "Optimization of the computation of total and local radiated power at ASDEX Upgrade", 2021, *Nucl. Fusion*, **61**, 066025.

[212] P. Manz *et al*, "The diffusion limit of ballistic transport in the scrape-off layer", 2020, *Phys. Plasmas*, **27**, 022506.

[213] M. Bernert *et al*, "The X-Point radiating regime at ASDEX Upgrade and TCV", 2023, *Nucl. Mater. Energy*, **34**, 101376.

[214] U. Stroth *et al*, "Model for access and stability of the X-point radiator and the threshold for marfes in tokamak plasmas", 2022, *Nucl. Fusion*, **62**, 076008.

[215] A.V. Chankin, "Classical drifts in the tokamak SOL and divertor: models and experiment", 1997, *J. Nucl. Mater.*, **241-243**, 199-213.

[216] L. Aho-Mantila *et al*, "Assessment of SOLPS5.0 divertor solutions with drifts and currents against L-mode experiments in ASDEX Upgrade and JET", 2017, *Plasma Phys. Control. Fusion*, **59**, 035003.

[217] F. Reimold *et al*, "The high field side high density region in SOLPS-modeling of nitrogen-seeded H-modes in ASDEX Upgrade", 2017, *Nucl. Mater. Energy*, **12**, 193-199.

[218] E. Sytova *et al*, "Impact of a new general form of friction and thermal forces on SOLPS-ITER modelling results", 2018, *Contrib. Plasma Phys.*, **58**, 622-628.

[219] E. Sytova *et al*, "Derivation of the friction and thermal force for SOLPS-ITER multicomponent plasma modeling", 2020, *Phys. Plasmas*, **27**, 082507.

[220] V. Zhdanov, "Transport processes in multicomponent plasma", 2002, *Taylor and Francis*.

[221] S.O. Makarov *et al*, "Equations and improved coefficients for parallel transport in multicomponent collisional plasmas: Method and application for tokamak modeling", 2021, *Phys. Plasmas*, **28**, 062308.

[222] S.O. Makarov *et al*, "Impact of the improved parallel kinetic coefficients on the helium and neon transport in SOLPS-ITER for ITER", 2022, *Contrib. Plasma Phys.*, **62**, e202100165.

[223] W. Dekeyser *et al*, "Implementation of a 9-point stencil in SOLPS-ITER and implications for Alcator C-Mod divertor plasma simulations", 2019, *Nucl. Mater. Energy*, **18**, 125-130.

[224] W. Dekeyser *et al*, "Plasma edge simulations including realistic wall geometry with SOLPS-ITER", 2021, *Nucl. Mater. Energy*, **27**, 100999.

[225] W. Dekeyser *et al*, "A self-consistent κ-model for anomalous transport due to electrostatic, interchange-dominated $\boldsymbol{E} \times \boldsymbol{B}$ drift turbulence in the scrape-off layer and implementation in SOLPS-ITER", 2022, *Contrib. Plasma Phys.*, **62**, e202100190.

[226] U. Stroth *et al*, "Progress from ASDEX Upgrade experiments in preparing the physics basis of ITER operation and DEMO scenario development", 2022, *Nucl. Fusion*, **62**, 042006.

[227] W. Suttrop *et al*, "Experimental conditions to suppress edge localised modes by magnetic perturbations in the ASDEX Upgrade tokamak", 2018, *Nucl. Fusion*, **58**, 096031.

[228] T. Happel *et al*, "The I-mode confinement regime at ASDEX Upgrade: global properties and characterization of strongly intermittent density fluctuations", 2017, *Plasma Phys. Control. Fusion*, **59**, 014004.

[229] T. Happel *et al*, "Overview of initial negative triangularity plasma studies on the ASDEX Upgrade tokamak", 2023, *Nucl. Fusion*, **63**, 016002.

[230] L. Gil *et al*, "Stationary ELM-free H-mode in ASDEX Upgrade", 2020, *Nucl. Fusion*, **60**, 054003.

[231] G.F. Harrer *et al*, "Quasicontinuous exhaust scenario for a fusion reactor: The renaissance of small edge localized modes", 2022, *Phys. Rev. Lett.*, **129**, 165001.

[232] M. Bernert *et al*, "X-point radiation, its control and an ELM suppressed radiating regime at the ASDEX Upgrade tokamak", 2021, *Nucl. Fusion*, **61**, 024001.

[233] T. Lunt *et al*, "Compact radiative divertor experiments at ASDEX Upgrade and their consequences for a reactor", 2023, *Phys. Rev. Lett.*, **130**, 145102.

[234] M. Kotschenreuther *et al*, "Magnetic geometry and physics of advanced divertors: The X-divertor and the snowflake", 2013, *Phys. Plasmas*, **27**, 102507.

[235] T. Lunt *et al*, "Proposal of an alternative upper divertor in ASDEX Upgrade supported by EMC3-EIRENE simulations", 2017, *Nucl. Mater. Energy*, **12**, 1037-1042.

[236] I. Zammuto *et al*, "The new ASDEX Upgrade upper divertor for special alternative configurations: Design and FEM calculations", 2021, *Fusion Eng. Des.*, **171**, 112468.

[237] G. Schall *et al*, "Design and operation of the in vessel cryopump for the new upper divertor in ASDEX Upgrade", 2021, *Fusion Eng. Des.*, **166**, 112316.

[238] O. Pan *et al*, "SOLPS-ITER modeling with activated drifts for a snowflake divertor in ASDEX Upgrade", 2020, *Plasma Phys. Control. Fusion*, **62**, 045005.

Publications

The activities carried out in the framework of this thesis contributed, directly or indirectly, to the following publications on peer-reviewed journals.

Publications as first author:

- **A. Zito**, M. Wischmeier, D. Carralero, P. Manz, I. Paradela Pérez, M. Passoni and the ASDEX Upgrade team, "Numerical modelling of an enhanced perpendicular transport regime in the scrape-off layer of ASDEX Upgrade", 2021, *Plasma Phys. Control. Fusion*, **63**, 075003.
- **A. Zito**, M. Wischmeier, A. Kappatou, A. Kallenbach, F. Sciortino, V. Rohde, K. Schmid, E.T. Hinson, O. Schmitz, M. Cavedon, R.M. McDermott, R. Dux, M. Griener, U. Stroth and the ASDEX Upgrade team, "Investigation of helium exhaust dynamics at the ASDEX Upgrade tokamak with full-tungsten wall", 2023, *Nucl. Fusion*, **63**, 096027.

Publications as co-author:

- P. Manz, C. Hufnagel, **A. Zito**, D. Carralero, M. Griener, T. Lunt, O. Pan, M. Passoni, B. Tal, M. Wischmeier, E. Wolfrum and the ASDEX Upgrade team, "The diffusion limit of ballistic transport in the scrape-off layer", 2020, *Phys. Plasmas*, **27**, 022506.
- P.T. Lang, B. Plöckl, M. Bernert, A. Bock, R. Dux, A. Kallenbach, V. Rohde, M. Siccinio, W. Suttrop, **A. Zito** and the ASDEX Upgrade team, "Targeting a versatile actuator for EU-DEMO: Xenon doping of fueling pellets", 2021, *Fusion Sci. Technol.*, **77**, 42-50.
- A. Kallenbach, P.T. Lang, M. Bernert, R. Dux, T. Eberl, T. Gleiter, R.M. McDermott, C. Piccinni, B. Plöckl, V. Rohde, **A. Zito** and the ASDEX Upgrade team, "Argon doped pellets for fast and efficient radiative power removal in ASDEX Upgrade", 2022, *Nucl. Fusion*, **62**, 106013.
- P.T. Lang, L.R. Baylor, C. Day, R. Dux, R.M. McDermott, T. Giegerich, T. Gleiter, A. Kallenbach, B. Plöckl, V. Rohde, **A. Zito** and the ASDEX Upgrade team, "Admixed pellets for fast and efficient delivery of plasma enhancement gases: Investigations at AUG exploring the option for EU-DEMO", 2023, *Fusion Eng. Des.*, **196**, 114020.
- A. Kallenbach, R. Dux, S.S. Henderson, C. Tantos, M. Bernert, C. Day, R.M. McDermott, V. Rohde, **A. Zito** and the ASDEX Upgrade team, "Divertor enrichment of recycling impurity species (He, N_2, Ne, Ar, Kr) in ASDEX Upgrade H-modes", *Submitted to Nucl. Fusion.*

Acknowledgements

These acknowledgements are not going to be short. Whereas being concise has never been my thing, the main reason for this is that many people need to be acknowledged, for helping me achieve this goal. And they need to be acknowledged in a proper and grateful way.

This may seem weird but I think that, as a very first thing, who most deserve to be acknowledged are authors and co-authors of the 238 papers, theses and textbooks which I cited throughout this entire work. If it is true that one can see further only by standing on the shoulder of giants, well, then none of this work would have been possible without the contribute to science of those who came before me, and laid the foundations for me to build my own, personal contribute to science.

Coming to those who directly entered this piece of life of mine, firstly I would like to express by deep gratefulness to my academic supervisor at IPP and TUM, Prof. Dr. Ulrich Stroth, who ultimately made all of this possible. Thanks for your support, for your strong and constant presence, and for your equally strong and constant criticism, whenever it was needed. I do remember that, when I was already in delay with this thesis, you begged me to stop working and start writing, saying that what I had was already sufficient. Still, I kept working because I was convinced that the small, additional piece of work I wanted to do was genuinely essential for completing the structure of this thesis and giving it its own consistency. Instead of getting upset - which might have been a deserved reaction - you told me that I was an independent scientist. This is still the greatest source of pride that the academic world has reserved to me, up to date.

I would like to thank my day-to-day supervisor, Dr. Marco Wischmeier. You have put trust into me, and have followed and supported me during these years. The inspiring discussions had together have strongly contributed in expanding my knowledge and my horizons in such an interesting and challenging research field.

I would also like to thank Dr. Athina Kappatou for the general support provided to me during these years, for having introduced me to the world of the ASDEX Upgrade experiments, for providing me accurate He ion density measurements for all my experiments and, most of all, for the idea which firstly gave birth to this thesis project.

Among the entire ASDEX Upgrade team, I am particularly grateful to Dr. Arne Kallenbach for his wise and farsighted management of our experiments and the original conceptual development of the multi-reservoir particle balance model which constitutes the biggest result of this thesis. A huge thank you is in order also to Dr. Francesco Sciortino for letting me contribute to the development of Aurora and for guiding me through the learning process of Python, Fortran and some nice and useful coding tricks. I also thank Dr. Klaus Schmid for performing the calculation of the surface coefficients employed in my model.

My knowledge about experiments and diagnostics has hugely benefited from the contribute of several experts, in particular Dr. Volker Rohde for the AUG vacuum systems, Dr. Thomas Schwarz-Selinger for the mass spectrometers, Dr. Marco Cavedon, Dr. Rachael McDermott, Dr. Ralph Dux and Dr. Michael Griener for plasma spectroscopy in all its different fashions, Dr.

Matthias Bernert and Dr. Pierre David for plasma bolometry, Dr. Rainer Fischer, Dr. Dirk Stieglitz and Dr. Balázs Tal for integrated data analysis and midplane plasma profiles, and Dr. Dominik Brida for the divertor Langmuir probes. Additionally, although pellet experiments did never enter directly my personal investigation, I would like to acknowledge the fruitful collaboration born in these years with Dr. Peter Lang and Dr. Bernhard Plöckl.

From the numerical point of view, my knowledge and understanding of plasma edge modelling has hugely benefited from the fruitful discussions with Dr. Ou Pan, Dr. Tilmann Lunt, Dr. David Coster and Sergei Makarov.

Outside the framework of the thesis-related work, I owe a huge thank you to those who contributed to make IPP a nice place to work, in particular Francesco, Lennart, Klara, Teo, Maxi, Andrés, Davide, Marco, Benedikt, Andreas, Daniel W., Daniel F., Tabea and Oleg. A special acknowledgement must be reserved to Ulrike, as you put up with me during this last period in such a genuine and caring way, even when I was kinda "difficult" to put up with. I am not sure that I would have made it without you. Thank you all so much for being more friends than colleagues.

Finally, I owe a special and immeasurable thankfulness to all the people that, during my life and my studies, believed in me, because I would only have been a shadow of the man I am now without the teachings you gave me, the trust you placed in me, and the moments spent together during these years.

Thanks to my whole family, for always supporting me in whatever I did and for always respecting my choices. Thanks because from you I have always received more love than I have ever deserved.

During almost 29 years I have met many people, from so many different places. Maybe too many. For this reason, if I recognize that I can feel some of these people still close to me, in any place and in any moment, then these are people that will be with me forever, and in which I can place a total and unconditional trust.

Therefore thanks to my old friends from Imola, in particular Tommi, Paolino, Liuc, Dade, Jonj and Quentin, for the simplicity with which we are still all together as if these 15 years have never passed, and for remaining always interested in my life.

Thanks to Irene and Betta, because you promised that you would have always been there for me, and you kept that promise, and because, even after waiting so, so, so, so, so many hours, days, weeks, at the end you always answer my messages.

Thanks to all those friendships that, although started sharing studies between Bologna and Milano, continued even thereafter, demonstrating their genuineness, in particular with Gerri, Laura and Izzu. After all these years I am still amazed by the trust you put in me in moments of my life in which, maybe, I was less worthy of trust as I might be now.

Thanks also to all those friendships started living together in a same place, in particular with Cello and Gabri, for the constant and wise support you have given to me throughout these years.

Thanks to my fellow gamers of the COviD-MW2 brigade (including campers, tubers and cheaters), companions of many life-or-death battles, for giving a sense to all those lonely lockdown evenings.

Thanks to Francesco and Sara, because you made me feel somehow at home also here in Munich during these - often difficult - years.

And thank you, Francesca, because many things have happened to both of us in these years, but your superpower of being able to profoundly shape the course of my life has not faded away, and this has contributed to make me the person I am now.